Automated Quantification of Human Alpha Rhythms

A Thesis Submitted for the Degree of
Doctor of Philosophy

by

Alan King Ip Chiang

School of Physics
and
Brain Dynamics Center

The University of Sydney

August 2010

Declaration of originality

To the best of my knowledge, this thesis contains no copy or paraphrase of work published by another person, except where duly acknowledged in the text. Likewise, this thesis contains no material which has been presented for a degree at The University of Sydney or any other university.

Alan King Ip Chiang

Included papers and attribution

Chapters 2, 3, and Appendix C are based on the following papers:

Chapter 2 **Automated characterization of multiple alpha peaks in multi-site electroencephalograms**
A.K.I. Chiang, C.J. Rennie, P.A. Robinson, J.A. Roberts, M.K. Rigozzi, R.W. Whitehouse, R.J. Hamilton, E. Gordon
Journal of Neuroscience Methods (2008), **168**:396–411.

I was primarily responsible for this work, with an overall contribution of about 80%.

Chapter 3 **Age trends and sex differences of alpha rhythms**
A.K.I. Chiang, C.J. Rennie, P.A. Robinson, S.J. van Albada, C.C. Kerr
Submitted to *Clinical Neurophysiology*.

I was primarily responsible for this work, with an overall contribution of about 80%.

Appendix C **Neurophysiological changes with age probed by inverse modeling of EEG spectra**
S.J. van Albada, C.C. Kerr, A.K.I. Chiang, C.J. Rennie, P.A. Robinson
Clinical Neurophysiology (2010), **121**:21–38.

I contributed to the data analysis, and reviewing of this work, with an overall contribution of about 5%.

Acknowledgements

This work would not had been possible without the generous support and help from the following people:

Firstly my supervisors Professor Peter Robinson, Doctor Chris Rennie, and briefly Doctor Sacha van Albada, who all spent substantial time in detail editing of all parts of the thesis and provided assistance whenever it is needed. Fellow members of the complex system group, in particular Dr Cliff Kerr for his excellent insights to matlab and latex.

To all the people that had the (mis)fortunate of sharing an office with me: Audrey Lobos, Mark Hertzberg, Peter Domachuck, Emily Perks, Paul Leopardi, Yin Hu, and more recently Daniel Graham, Xuelong Zhao, Tim Patten, (and I sincerely apologize for any office mates whom I did not mention) for your patience, company, and aid through the various stages of my candidature. Special mention of Hong Nguyen, who endured my pestering from first year until he had enough and left for Japan.

My parents, Heather and Bernard Chiang, who nurtured my scientific curiosity from a young age, allowing me the freedom to pursuit my interest, and stood by my side through the better and worse of my decisions and actions. My brother King and his girlfriend Kelly, as well as my cousin Wing Man, who put up with living with me.

Finally my two closest friends and their better halves, Leo Leung and Angie Lau, Clement Lun and Katrina Chau, who help dragged me out of the house so I did not become a recluse. My martial art buddies who kept my body in (barely) reasonable shape to get through this ordeal.

On a more technical note, the work on the method section was supported by the Australian Research Council and a University of Sydney Sesqui grant. I thank Homi Bahramali and Ilario Lazzaro for their contributions to the EEG database of 100 healthy subjects that was drawn on in this study. The work on the result section was supported by the Australian Research Council. I also acknowledge the support of the Brain Resource International Database (under the auspices of Brain Resource; www.brainresource.com) for data acquisition and processing. And I sincerely thank the individuals who gave their time to take part in the study.

Summary

This thesis seeks to quantify human alpha rhythm in order to obtain better measures to test theoretical models of neurodynamics, with potential clinical applications for the method of identification.

An automated algorithm is developed in Chapter 2 to facilitate collection of objective data from an expanded alpha band (4–14 Hz) in a large number of subjects. This method avoids subjective bias inherent to traditional visual identification of the alpha activity, produced multiple peak information (if multiple peaks exist) that is absent in qEEG measures, and uses information from multiple electrode sites to eliminate spurious peaks. This method is tested and validated on 100 subjects.

In addition to traditional measures of alpha activities such as the frequency and amplitude, further measures were devised to better quantify the alpha rhythm and its spatial characteristics. Background spectra in the alpha range are also characterized.

In Chapter 3 the algorithm is applied to a large (1498 subjects) database of normal healthy subjects of approximately equal number in each sex, as well as a large span in age (6–86 years), in order to establish typical parameter ranges. Analysis is done comparing the age and the topological trends that are known variants in the alpha rhythm. Investigations are also performed to test for potential sex differences and/or lateralities. Key results are that double alpha peaks are resolved in a large proportion of the subjects ($\approx$50%), while single alpha peak cases are likely to be double-peak cases in which the two peaks are not resolved. Age trends in measures of alpha activity show increase of alpha frequency from childhood to adolescence, a plateau in adulthood, and a slight decline in old age; a decrease in alpha amplitude in old age is also observed. These findings are consistent with previous literature and provide better statistics. Topological distribution of the alpha activity on the head is also explored, with little lateral asymmetry observed. No statistically significant differences between the sexes are found.

The C++ code that was developed and utilized in this thesis is included in Appendix B. It is provided on disk and is available online.

A study carried out on the same group of subjects to determine age-related trends of EEG parameters produced by model fitting is included in Appendixes C, to provide a comparison between the methods and highlights corresponding results.

Contents

Chapter 1

Introduction

In this chapter we discuss motivations for the quantification of the alpha rhythm, the most prominent type of brain activity measured in the electroencephalogram (EEG) and also introduce a number of concepts in neuroscience, in particular neurophysiology, that provide a background for the thesis. In Section 1.1 we discuss the interest and incentives behind the study of the alpha rhythm, as well as some of the challenges involved in its analysis. Section 1.2 describes in broad terms some of the basic structure that is relevant in both clinical applications and modeling of the alpha rhythm. This is followed by discussion of the EEG in Section 1.3. Section 1.4 describes some of the techniques that are employed in the field for the analysis of EEG signals, and finally in Section 1.5 a brief overview of alpha rhythm characteristics.

1.1 Motivation

In the broadest terms, the study of the brain is hoped to reveal to us some of the secrets of the human mind. The heart was initially thought to be the seat of the human mind, with the brain merely being a cooling device for hot blood, which was suggested by Aristotle to be the source of human rationality (Finger, 2001). Later Galen showed that the brain is connected to all the muscles in the body via nerve cells (Rocca, 2003), but it is only at Galvani's discovery that a dead frog's leg responds to electricity, and hence nerve cells communicate through electrical signals, that we can place the start of modern neuroscience (Piccolino, 2006).

The investigation of the brain is hampered by a multitude of factors. The first is that the span of the activities of the brain covers multiple orders of magnitude, from the cells to the whole brain, and beyond the brain a network of neurons that is spread throughout the body (Bullock, 2002). The huge span in the activities of the brain begs the question of how to measure activities in the appropriate scale (Nunez and Srinivasan, 2006).

Experimental designs are an inherent problem with neuroscience. The brain in general cannot be switched off with precision during the course of an experiment. An isolated region's activity can be suppressed or enhanced with Transcranial Magnetic Stimulation (TMS) or electrical impulses applied through deep electrodes. This leads to mapping of the brain for specific functions. Unfortunately currently TMS lacks in precision (Wassermann et al., 2008), groups of neurons are activated based on the proximity to the magnetic source. Deep electrodes offers more precise manipulation (Guo et al., 2007) but are highly invasive. Hence, precise linking of specific neurons to exact experimental outcomes or measurements are generally not possible.

Difficulties exist in both measurements and their interpretations. EEGs are currently one of the cheapest, and simplest ways to measure brain activity, with electrical potentials measured on the scalp. EEG has very high temporal resolution, but the spatial resolution is somewhat lacking, 1–2 cm at best: because the measurement is taken on the scalp, signals from the neuron are attenuated by the separation between the generation and measuring sites, and spatial information is masked by volume conduction within the brain and its surrounding tissues (Nunez and Srinivasan, 2006; Niedermeyer and Lopes da Silva, 2004). Magnetoencephalography (MEG) is similar to EEG but magnetic field instead of electric potentials are measured which results in less distortion of the signal, but the very weak source signal of the brain requires magnetic shielding which limits its general use. Near-Infrared Spectroscopy (NIRS) (Nagai et al., 2007), Position Emission Topography (PET) (Fox and Mintun, 1989) and functional Magnetic Resonance Imaging (fMRI) (Hennig and Koch, 2003) all rely on assumptions that blood flows and/or metabolic activities measures brain activities indirectly. Figure 1.1 shows the spatial and temporal resolution, as well as the invasiveness of some of the measurement techniques.

Interpretation of the measurements are also difficult. With NIRS (Hoshi et al., 2001), PET (Jueptner and Weiller, 1995), and fMRI (Arthurs and Boniface, 2002), brain activity is measure by a proxy, which requires further modeling of blood flow and its interaction with neuronal tissues to interpret the underlying activity itself (Buxton and Frank, 1997). Even with EEG and MEG, where the measurement is a direct consequence of neuronal activities, their sensitivities are to different anatomical regions of the cortex and different components of the respective fields (Mosher et al., 1993; Gener and Acar, 2004): EEG is sensitive in both tangential and radial component, and MEG only measure the tangential component (Nunez and Srinivasan, 2006; Niedermeyer and Lopes da Silva, 2004). Source localization of EEG and MEG, or the determination of the source of the activity is also a problem with no unique solution. Independent of the type of measurement, the “forward” (Hallez et al., 2007) and

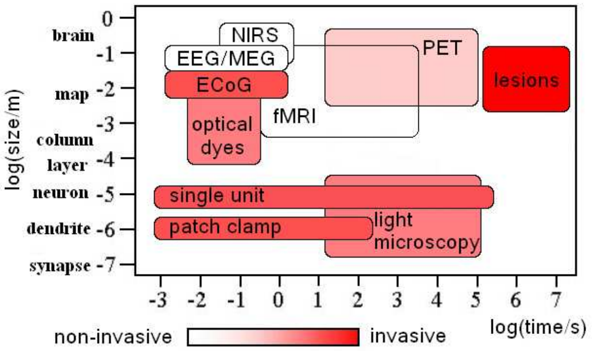

Figure 1.1: A schematic showing the approximate temporal and spatial resolution of some current techniques. The darker color represents a more invasive techniques. Courtesy A. Galka.

"inverse" problems (Pascual-Marqui, 1999) are central to the interpretations of neurological data since the exact relationship between the activity generated in the brain and measured on the scalp is unclear. (The "forward" problem is the calculation of the EEG signal with known source locations and a known model, whereas the "inverse" problem is locating the source of the activity from experimental results.)

The electrical activity of the brain has long been used as a diagnostic tool for brain function and state since its discovery in the late 19^{th} century by Caton (1875). The ability to measure the electrical activity in the brain by means of electrodes on the head is a handy tool to study brain function as it is noninvasive and easy to apply. Since the earliest work in the field by Berger (1929), the alpha rhythm had been noted as the most prominent component of human EEG from the scalp of a normal health awake human adult (with their eyes closed). There are theories where the alpha rhythm represents a "resting state" for the brain which is primed for novel visual stimuli (Moosmann et al., 2003). Classically alpha rhythm had been described as a singular rhythm in the defined frequency bounds. Previous research (Feshchenko et al., 2001; Kolev et al., 2002; Tsai et al., 2006) has shown there exist the possibilities of multiple rhythms within the alpha frequency band of brain physiological activity, the alpha frequency is highly dependent on the individual's age (Surwillo, 1961; Marshall et al., 2002; Stroganova et al., 1999), and that the alpha frequency might "split" according to some theoretical considerations (Robinson et al., 2003b). Details of the alpha rhythm and related alpha band activities would be discussed in Section 1.5. Higher resolution of the details in the alpha rhythm and their quantification will assist in constraining and refining of theoretical models.

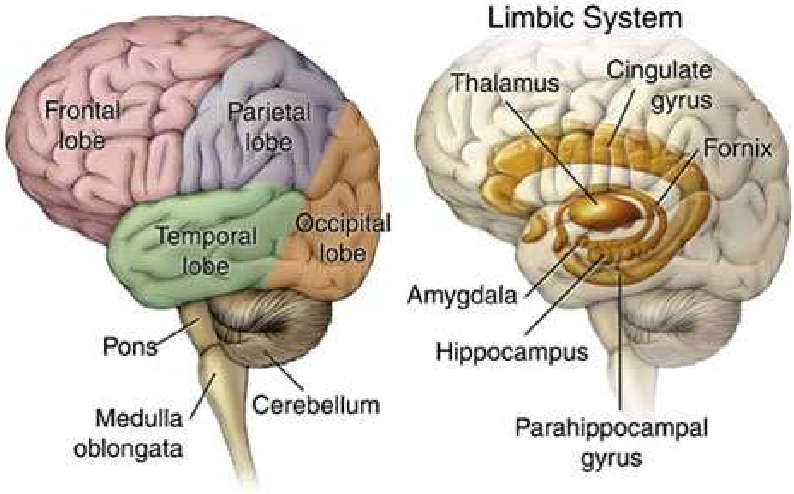

Figure 1.2: A schematic of the brain, on the left shows the cerebellum, comprising the frontal, parietal, temporal, and occipital lobes, as well as the cerebellum and the brain stem pons and medulla oblongata. On the right shows the thalamus, cerebellum and hippocampus, associated with the limbic system. Adapted from http://www.sadclinic.com/the_brain.html.

1.2 Brain physiology

1.2.1 Overall structure

The adult human brain is approximately one and a half kilograms of soft, pink tissues primarily made up of over one hundred billion neurons (Purves, 2000), glia, and blood vessels. Each neuron is linked to others by up to 10^5 synaptic connections. Surrounding the brain are three layers of protective membrane, and the brain is bathed in a clear cerebrospinal fluid which protects it from varying pressure, such as impact, and transports chemicals within the nervous system (Kandel et al., 2000).

Viewed externally, the brain can be divided into three distinct but connected parts: cerebrum, cerebellum and brain stem, shown in Fig. 1.2. The cerebrum is a large, almost symmetrical pair of hemispheres which sit at the top. The cerebellum (little brain) consists of two smaller hemispheres located at the back of the cerebrum. The brain stem is a central core that gradually merges into the spinal cord, exiting through an opening at the base of the skull. There are two other major parts of the brain; the thalamus and hypothalamus; which

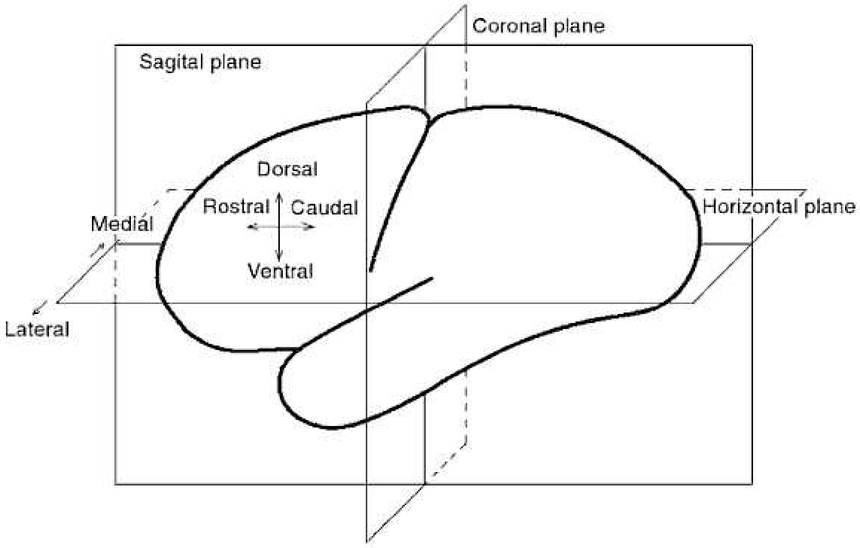

Figure 1.3: Anatomical terms used in neuroscience in reference to different physical dimension and directions in the brain. The brain is cut by horizontal, sagital, and coronal planes. Direction (medial – lateral, dorsal – ventral, rostal – caudal) are depicted by arrows (Kropotov, 2009)

lie in the midline above the brainstem and underneath the cerebrum (Kandel et al., 2000).

Figure 1.3 shows a number of specific naming convention describing location of different anatomical structures of the brain. The anatomical terms are generally confusing in neurobiology, since the relative positions are inferred from the head, and the brain lies within the head. Anterior – posterior, or rostal – caudal direction is defined as from the head to the other end of the body, but in the brain it is usually referred to as the front / back direction. Similarly the dorsal – ventral direction is defined as the spinal column to the belly, but in the case of the brain it is the top / bottom of the brain. Locations are also associated with the respective lobes (frontal, occipital), which simplifies identification.

1.2.2 Neuron

For our purpose, the most important type of cell in the brain is the neuron, which is capable of sending signals to other neurons over long distances. A neuron is made up of several distinctive structures: dendrite, soma, axon, axon (or presynaptic) terminal and myelin sheath. A schematic diagram of a typical neuron is shown in Fig. 1.4. A dendrite is a bushy, branching extension of a

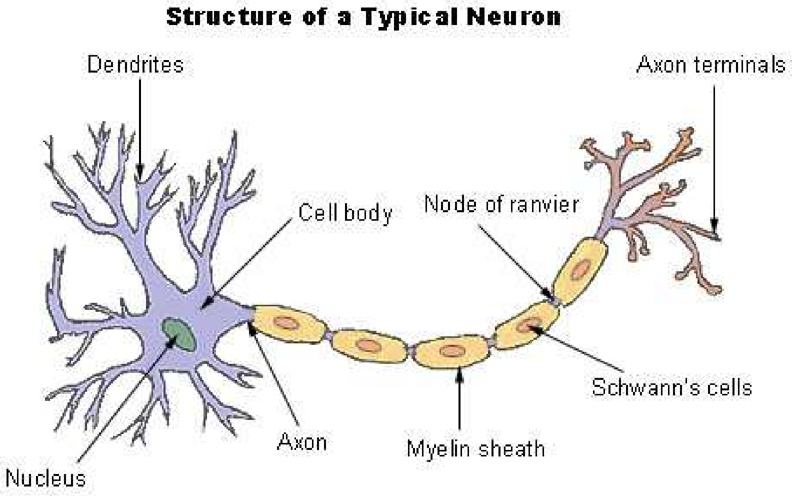

Figure 1.4: Schematic representation of a typical neuron, with the structural parts labeled. Adapted from http://en.wikipedia.org/wiki/Neuron.

neuron that receives messages and conducts impulses towards the cell body. It is generally around 200 μm in length. The cell body contains the ribosome and other sub-cellular parts which do the metabolic work of cells and is also called the soma. The cell body ranges from 5 – 100 μm in diameter (Purves, 2000). The axon is the extension of a neuron, ending in branching terminal fibers, through which chemical messages are released to other neurons, muscles or glands. It can stretch up to 20 cm across the brain (Purves, 2000). The myelin sheath is a insulating layer of fatty cells segmentally encasing the axons of many neurons and vastly increasing the transmission speed of neural impulses (Carlson, 1999; Kandel et al., 2000; Koch, 1999). The junction between the axon tip of the sending neuron and the dendrite or cell body of the receiving neuron is called the synapse. There are approximately a 10^{14} synapses, and 10^6 kilometers of neural interconnection in the brain (Nolte, 1993). When many cell bodies are close together, the cut tissue is pinkish-gray in color and is called *gray matter*. Where axons are clustered or layered together, the myelin sheathing gives a white shiny appearance to the cut tissue, which is called *white matter*. There are many types of neurons, differentiated by the shape of their dendritic tree and axon, among other characteristics. Neurons are electrically polarized, with a slightly negative voltage call the resting potential of approximately -70 mV relative to outside the cell, due to the electrochemical gradient created and maintained by sodium-potassium (Na-K) pumps embedded in the cell membrane.

Presynaptic action potentials cause release of neurotranmitters into the synaptic cleft, which open postsynaptic ion channels in the dendritics membrane. Resulting currents cause voltage perturbations that propagate down dendrites to where they are summed at the soma. The structure and branching of a neuron's dendrites, as well as the availability and variation in voltage-gated ion conductances, strongly influences how it integrates the input from other neurons, particularly those that input only weakly. This integration is both temporal, involving the summation of stimuli that arrive in rapid succession; as well as spatial, via the aggregation of excitatory and inhibitory inputs from separate branches (Stuart et al., 2008).

Action potentials are short spikes in the membrane potential that propagate along axons. This occurs when the soma voltage exceeds a threshold. A brief wave of depolarization then originates at the axonal hillock and travels down the axon, to the axonal terminals, causing neurotransmitters to be released at synapses, in turn stimulating downstream neurons (Kandel et al., 2000; Koch, 1999). When firing occurs, voltage gated sodium channels in the membrane of the neuron open, an inward current of sodium ions occurs, and as a result, the potential spikes (up to around +50 mV). Potassium channels which open slower result in an efflux of potassium ions that contributes an outward current that counteracts the depolarization. After a brief overshoot, or hyperpolarization. the neuron's potential returns to its resting level (Koch, 1999). This voltage change is shown in Fig. 1.5. This is follow by refractory periods: an absolute refractory period is when it is impossible for a stimulus to triggered another firing, and relative refractory period where another firing is trigger only by a stronger than usual stimulus. The refractory periods are dependent on properties of the sodium and potassium channel molecules. The sodium channel enters an inactive state after closing, and cannot be made to open, resulting in the absolute refractory period. Even when the sodium channels revert to their resting state the potassium channel remains open, increasing the threshold value, resulting in the relative refractory period. The refractory period also enforces the one-way propagation of action potential. It is important to note that the amplitude of an action potential is independent of the amount of current the produced it, therefore they are said to be *all-or-none*, and the frequency of the action potential can encode the intensity of a stimulus (Purves et al., 2007).

The signal from the firing propagates down the axons, with a wave of depolarization follow by repolarization and refraction, and only travels in one direction. The speed of propagation is determined by the myelination level, and size of the axon, with a higher level of myelination and larger diameter axons having a faster transmission speed. At the end of the axon are synapses, which transfer the transmission to downstream neurons in one of two ways: (i)

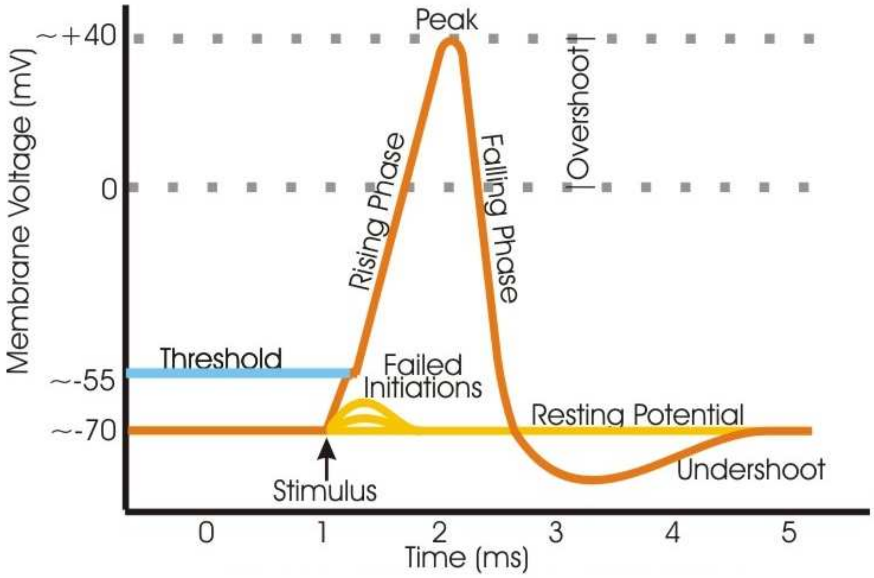

Figure 1.5: A schematic of action potential. If there is insufficient stimulation the neuron would not fire (Failed initiations). Only when the level of stimulation is above the threshold potential, would trigger a "firing". Adapted from http://scienceblogs.com/clock/2006/06/bio101_lecture_6_physiology_re.php.

Electrical synapses or gap junctions directly pass the action potentials to the dendrites of the next cell, is of a higher speed, and can support two-way communication. (ii) Chemical synapses releases chemical signals which is picked up by downstream dendrites, and is a one-way transmission (Kandel et al., 2000).

Neurons can influence other neurons in two main ways: when there is a depolarization of the postsynaptic cell membrane the effect is termed excitatory, bringing the postsynaptic neurons closer to its firing threshold. A hyperpolarization of the postsynaptic membrane is the other alternative, and is termed inhibitory, because it keeps the membrane potential more negative than the threshold potential, and suppresses postsynaptic activity (Gutnick and Mody, 1993).

1.2.3 Cerebrum

Most of the high level brain functions take place in the cerebrum, which is comprised of two large hemispheres, that make up approximately 85% of the brain's weight. The convoluted exterior surface of the cerebrum is called the cerebral cortex. It is made up of a thin (2-3 mm thick) folded grayish layer of cell bodies known as *gray matter*, beneath which is a mass of fibers called the *white matter*. The convolutions are made up of ridge-like bulges call *gyri*, separated by small grooves called *sulci* and larger grooves called *fissures*. This extensive convolution enables a very large surface area of the brain cortex of approximately 0.3 m^2 to fit inside the head (Kandel et al., 2000).

Each hemisphere is divided into five lobes by a few major sulci: the frontal, parietal, temporal, and occipital lobes on the exterior; and the insular cortex deep on the brain's lateral surface, with the lateral sulcus separating the temporal and parietal lobe dorsally, shown in Fig. 1.2. Many of the areas of the cerebral cortex have been mapped to specific functions such as vision, hearing, speech, emotion, language, and other aspects of perception (Kandel et al., 2000; Niedermeyer and Lopes da Silva, 2004).

1.2.4 Thalamus and hypothalamus

The thalamus and hypothalamus lie underneath the cerebrum and connect the cerebrum to the brain stem, shown in the cross-sectional view in Fig. 1.2. The thalamus consists of two rounded masses of gray tissue, made up of millions of neurons grouped into a dozen nuclei. It is the main relay station for incoming and outgoing signals: all sensory input to the brain, except the sense of olfaction, passes through to nuclei of the thalamus before reaching the cortex (Carlson, 1999). The thalamus processes and relays sensory information selectively to various parts of the cerebral cortex, as one thalamic point may reach one or several regions in the cortex (Steriade et al., 1997).

The hypothalamus lies beneath the thalamus on the midline at the base of the brain. It receives many inputs from the brain stem and regulates many of the body's vital drives and activities, as well as controlling the function of internal organs via the autonomic nervous system (Steriade et al., 1997).

1.2.5 Brainstem and cerebellum

The cerebellum also has a cortex much like the cerebrum: unfolded it is approximately the size of one hemisphere of the cerebrum. As in the cerebrum the outer layer of cortical gray matter surrounds a deeper layer of white matter and groups of cells called nuclei. The cerebellum coordinates voluntary movements by fine tuning commands from the motor cortex in the cerebrum. Furthermore, it maintains posture and balance by controlling muscle tone and sensing the position of the limbs (Kandel et al., 2000).

From an evolutionary perspective the brain stem is the most primitive part of the brain. It is responsible for sustaining the basic functions of life, such as cardiac and respiratory activity. The topmost structure of the brain stem is called the midbrain. This contains major relay stations for neurons transmitting signals to the body from the main part of the brain and vice versa (Ghez and Fahn, 1985; Llinas et al., 2004).

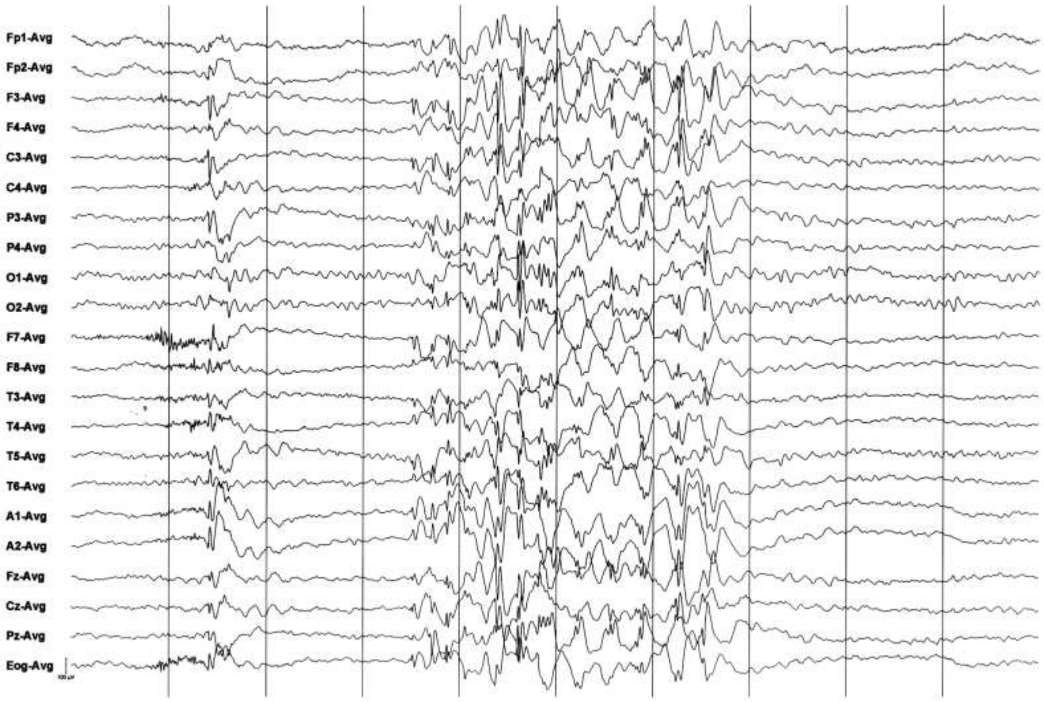

Figure 1.6: A time series EEG trace, noted the EOG is also taken to help with artifact removal. Adapted from http://www.dauwels.com/SESToolbox/Faq.html.

1.3 Electroencephalograms

Electrical activity arises from the signal pulses of neurons (Niedermeyer and Lopes da Silva, 2004). EEG measures this fluctuating electrical potentials that arise from brain activity, along with MEG providing one of the few quantitative measurements of cortical activity and the only noninvasive one with high time resolution. Figure 1.6 shows an example of an EEG time series. In some cases where the measurements are taken directly on the cortex itself, they are referred to as electrocorticograms (ECoGs).

There are several distinctive features in a power spectrum of an EEG. A key phenomenon is the alpha rhythm, first seen by Berger (1929), where an peak in the power spectrum is observed near a frequency of 10 Hz, detected when the subject is awake with a lack of visual stimulus (Gleitman, 1993). The alpha rhythm is known to be a large scale phenomenon detectable across the cortex. Various psychiatric conditions are also correlated with power levels of several frequency bands (Niedermeyer and Lopes da Silva, 2004).

An electrode on the scalp for EEGs generally provides an estimate of neural activity over a region containing 10^7 – 10^9 neurons (Nunez and Srinivasan, 2006). Reflecting the activity of cortical neuron close to the electrode. A much higher spatial resolution can be obtained via the use of ECoGs, at the cost of the extreme invasiveness. Since the brain is not uniform, EEGs vary with the location of the electrodes.

Unfortunately, the spatial resolution of the EEGs is poor, due to various factors such as the volume conduction of electrical signal in the tissues between the cortex and the scalp where the measurements are taken, which acts to smear finer scales (Nunez and Srinivasan, 2006). The temporal resolution of EEGs is quite high, of the order of one millisecond (Carlson and Baskiet, 1997). This enables chronometry of active regions, complementary to other techniques such as magnetic resonance imaging (MRI), providing a direct measure of activities, and physiologically localizing potential source(s) of the activities.

Since the cortex is active in all states barring death, in both awake and sleep states (Freeman, 2001), there is the problem of background activity, in which apparently random firing of neurons provides a background noise during periods of little action (Niedermeyer and Lopes da Silva, 2004). Some researchers believe that low amplitude, scalp EEG frequency components about 20 Hz are typically indistinguishable from muscle-related electrical artifacts, but the latter can be largely eliminated if the subject remains motionless and relaxed during the measurements (Deuschl and Eisen, 2000).

EEGs have been phenomenologically correlated with known brain states as well as mental illness, but a lot of the finer features of EEGs are not understood. Quantitative treatment of the physical mechanisms that generate these phenomena is potentially of great importance to clinical and cognitive research.

1.3.1 Recording procedures

An electrode cap is used for all the recordings examined in this thesis. It provides a simple mechanism to take into account the variability of head size and shape (including asymmetries), the location of the respective electrodes are evaluated in ratio in respect to the nasion and inion distance (nose to the base of the skull) medially, and from the top of one ear to the other laterally. The voltage fluctuation against a reference are recorded by the electrodes.

The convention we used in this paper follows the 10–20 system, as shown in Fig. 1.7. It is based on the iterative subdivision of arcs on the scalp starting from craniometric reference points: Nasion (Ns), Inion (In), Left (PAL) and right (PAR) pre-auricular points. The intersection of the longitudinal (Ns-In) and lateral (PAL-PAR) is named the Vertex. Designation of the electrode positions are in accordance with traditional anatomical of the various lobes of the brain which the electrode are placed over, except in the case of the central region, sensorimotor area. Even subscripts denotes the right hemisphere and odd subscripts denotes the left hemisphere, while midline electrodes had been

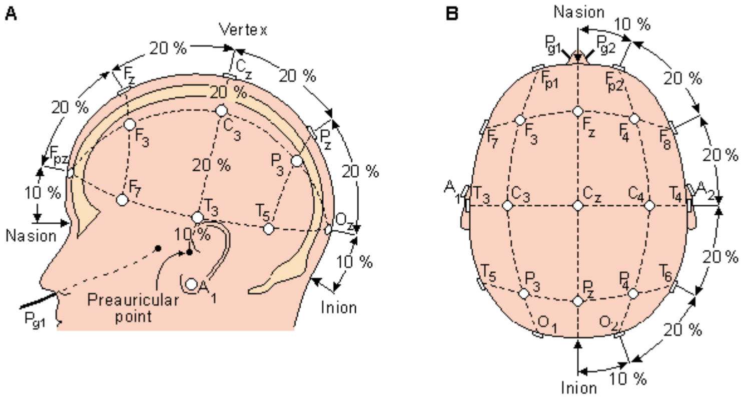

Figure 1.7: Schematic representation of the standardized placement of scalp electrodes in the 10-20 system. Distance is in percentage of the 10/20 range between the Nasion and Inion, as well as fixed points. (A) shows the side view, and (B) shows the top view of the head. Adapted from http://www.bci2000.org/wiki/index.php/User_Tutorial:EEG_Measurement_Setup.

designated as z for *Zentral* (German for *central*) (Niedermeyer and Lopes da Silva, 2004).

The choice of the reference electrode can significantly affects the data (Yao et al., 2005). Ideally a choice of a reference that is neural in respect to the electrode(s) in interest. Topographical distortion would result from a poor choice of reference electrode. There can be either 1 or 2 reference electrodes, physical reference can be used as vertex (C_z), linked-ears, linked-mastoids (rounded protusion of bone just beind the ear), ipsilateral ear (electrode referenced to ear on the same side), contralateral ear (electrode referenced to ear on the opposite side), bipolar reference (each channel represent the difference between two adjacent electrodes), and tip of nose. Reference free recording techniques can also be employed, one of which the reference signal is taken as the average of all the electrodes, or the common average reference (Sanei and Chambers, 2007). Common average reference derivation generally have a lower amplitude than physical references (Binnie, 2003), due to the fact that the absolute deviation of any electrode would be lowered by its own component in the reference, hence electrodes with large voltage changes contaminate the average. Removal of problematic electrodes from the common average reference are possible, but there are limits in this removal since the common average reference reliability depends on the number of electrodes used.

1.3.2 Physiological basis

EEG represents a recording of field potentials on the surface of the scalp, hence it predominately reflects the activity of the cortical neurons closer to the measuring electrode. The orientation of the EEG electrodes in respect to the neuron structure means EEG are sensitive to synchronous neuronal activation in the sulci and the top of the gyri. Deeper structures of the brain do not contribute directly to the surface EEG. The waveform measured on the surface depends on the orientation and distance of the source signal, which is generally composed of the activity of thousands to millions of neurons (Nunez and Srinivasan, 2006).

1.3.3 EEG spectral features

In general the EEG spectrum is often broken down into different frequency ranges for analysis, with is attributed to various physiological functions. Delta rhythm is general that of below 3.5 Hz, Theta 4–7.5 Hz, Alpha 8–13 Hz, Beta 14–30 Hz, and Gamma above 30 Hz. The Greek letters used did not result from the spectral allocation of the frequency bands but rather the historical sequence in which the rhythms were discovered. These frequency ranges are only approximations and are for adult humans. Moreover, these ranges are not fixed but relative, for example: delta rhythm lies below the alpha rhythm, and beta frequency is approximately twice that of alpha frequency.

In the alpha frequency range there exist a number of rhythms: (a) the classical alpha rhythm in the waking state. Primarily associated with visual stimuli, it is attenuated by visual, auditory, tactile, and other somatosensory stimuli and mental activities, though most pronounced is the blocking effect of eye opening (Niedermeyer and Lopes da Silva, 2004). Alpha rhythm declines with the approach of drowsiness, and is used to gauge vigilance. (b) Mu rhythm lies in the higher alpha frequency range. Its topological distribution, and associated physiological origins differ to that of the classical alpha rhythm. It is also termed “central alpha”, “rolandic alpha” or “somatosensory alpha rhythm” in the motor and somatosensory cortex. It is blocked by active (voluntary), passive, or reflexive movements, as well as light tactile stimuli (Niedermeyer and Lopes da Silva, 2004). (c) There is also a “third rhythm” in the lower alpha frequency range, thought associated to auditory stimuli, mainly observed in the temporal section of the head. Alpha rhythms also vary spatially, namely frontal and occipital alpha rhythm mentioned in the literature. A more detailed description of the Alpha rhythm is presented in Sec. 1.5.

The delta frequencies are generally present in adults in slow wave sleep, in babies, and some continuous attention tasks. Delta oscillations of cortical and thalamic origins had been separated in human EEGs, with the removal or the disconnection of the thalamus enhances delta activity recorded from the scalp

(Kropotov, 2009).

Theta frequency is normally seen in young children, also in drowsiness or arousal in older children or adults, and associated with activation and metabolic increases in the medial frontal area and anterior cingulate cortex. It increases with memory load, and is thought to have hippocampal origins (Kropotov, 2009). The hippocampus, anatomically an elaboration of the edge of the cerebral cortex (Amaral and Lavenex, 2006), is located inside the medial temporal lobe, beneath the cortical surface. It has the shape of a curved tube, which had been analogized to a seahorse, hence the name. It is thought to be involved in memory functions.

Beta activity appears in both eyes-open and eyes-closed states, is closely linked to motor behavior, and is generally attenuated during active movement (Niedermeyer and Lopes da Silva, 2004). At least two distinct beta rhythms can be separated: rolandic beta rhythm, located over the motor sensory strip, and frontal beta rhythm. EEG power in the beta band is also associated with cortical activation (Cook et al., 1998).

Gamma rhythms are low amplitude and difficult to measure at the scalp, these frequencies may represent binding of different population of neurons together into a network certain cognitive or motor function (Kropotov, 2009).

1.4 Quantification methods

Analysis of EEG signals is an ongoing problem. Measurement of EEG varies widely on inter- and intra-subject bases, and is dependent on various parameters, some of which cannot be easily controlled or measured. In order to obtain the salient data, we need to first isolate the possible parameters of variation prior to analysis.

EEG often contain activities of extracerebral origins, which may resemble cerebral activity. These artifacts are often subtle and are required to be recognized prior to analysis in order to prevent inaccurate interpretations of the EEG. Holmes et al. (2006) summarized these artifacts can be broadly separated into *nonphysiologic* and *physiologic*. *Nonphysiologic artifact* are signals caused by influence outside of the patient, such as amplifier noise, or improperly applied electrodes. *Physiologic artifact* refers to activities generating electrical field that arise from the subject's body other than the brain: (a) Electrocardiogram: The heart generates an electrical field that is measured on the surface of the body with a magnitude of ≈1 mV. Distant electrocardiographic activity is often detect at the temporal and ear leads. (b) Pulse: A synchronous artifact due to placement of the electrode on or adjacent to a pulsating artery. (c) Eye movement: EEG changes due to eye movement can be modeled electrophysiologically with the eye as a dipole with negativity at the retina and positivity at the cornea. (d) Eye blinks: Probably the most common artifact, a combination of the movement of the eye and the movement of the eyelid over the cornea. (d) Movement of the tongue (glossokinetic potential): The tongue is modeled as a dipole, positive at the tip. (e) Sweat: Perspiration can cause a change in the impedance between the electrode and the scalp. Slow waves (≤ 1 Hz) can be seen in the presence of sweat over a small area, because interaction of the electrolytes in the sweat and the electrode gel or paste can form a battery effect. Sweating over large areas of the scalp can result in short circuits, or low amplitude tracings (Binnie, 2003).

Secondly there are known parameters that changes of the morphology of the EEG spectrum and need to be recorded for each subject (Holmes et al., 2006). (a) Age: Since EEG is known to change rapidly with the neural maturity, this is especially critical in examination of cases of infant and childhood EEG. (b) States: EEG varies with mental state, such as awake, drowsy, sleep, or coma. It is also possible to gauge clues about a state by examining EEG artifacts such as muscle or eye movements. (c) Skull defects: Considering measurements of EEG are done on the surface of the scalp, the signal can potentially attenuate differently by orders of magnitude if there are by breaches in the skull (e.g., due to imperfect closure between skull bones). (d) Clinical History: Clinical interpretation of the EEG is reliant on a medical history of the subject, where medication and/or previous neurological conditions affects the results.

1.4.1 Time series analysis

Historically, analyzing the variation of voltage readings from electrodes with respect to time has been the most direct and common way to visualize and investigate EEG. This is the most common form of EEG analysis, where the clinician or experimentalist visually examine the time series signal, noting various items of interest (Binnie, 2003), and focusing on differences between normal and abnormal patterns. A summary in Holmes et al. (2006) of these items of interest that are investigated: (a) Background activities, mainly rhythm, where frequency and amplitudes are noted with the respective electrode placement to infer functional significances. (b) Synchrony between electrodes of similar location are noted, as well as the shape of the waveforms. (c) Symmetries of activities between the hemisphere of the brain are also examined, and are expected in normal subjects. (d) Paroxysmal features such as spikes or short waves [sharply contoured transient waveforms of relatively short ($\approx$70 ms), and longer duration, respectively)], and seizure patterns. (e) Location of the activities are also note, whether it is focal (limited to one region), or occurs over a wide area. (f) Continuity or intermittency of activities is dependent on the percentage of time it is present. Continuous when it occurs without interruption for prolong periods, discontinuous or intermittent when it appears only from time to time (Duffy et al., 1989).

A number of the deficiencies are associated with traditional EEG time series analysis. Firstly that it is highly subjective, dependent on the skills of the particular clinician or experimentalist. The reliance on visual inspection makes it extremely labor intensive, and the descriptions are highly qualitative. Examination on only the time series data is also problematic: it is easy to overlook low amplitude or frequency effects. Combination of frequencies also obscure details. For example, if two activities have frequencies close to each other it would produce a beating effect, where the signal seems to be fluctuating on and off. This modern signal analysis in other areas of science and engineering have moved to more objective and quantifiable measurements rather than qualitative descriptions based in time series.

1.4.2 Quantitative EEG

Quantitative EEG (qEEG) is the general term for the analysis of EEG by measuring specific parameters, rather than traditional qualitative description.

Since EEGs are often marked with changes in frequency contents, orthogonal transform such as fast Fourier transform (FFT) are employed to gather frequency information of the EEG. Data are average over a segment in such a transform so temporal information is lost, but the resultant frequency power spectrum allows for easily identifiable changes in frequency. A short time Fourier transform (STFT) can be used to analyze successive short epochs, but there is a trade off between time and frequency resolution: namely the frequency resolution is proportional to the time duration. Wavelets can also used instead of orthogonal transforms. Unlike the FFT, the wavelet transform does not utilize sinusoidal functions but a “mother” wavelet, where this wavelet is stretched or shrunk to fit to the size of the period of the rhythmic structure being examined. Hence the resolution of the wavelet is dependent on the period that is examined, where smaller periods would have a higher time resolution compared to the larger periods. This enables a combination of both the spectral and time analysis to study nonstationary phenomenon keeping resolution where it is needed (Akay, 1998).

Although technically the term qEEG could encompass all methods of parameterizing EEG, in both clinical and research settings qEEG is generally used to denote analyses base on band power, spectral peak parameters, coherence, and asymmetry (Kropotov, 2009). Band power measures the total power over a given frequency range, not identifying any spectral features such as peaks. Ratios between power on different frequency bands are often used, due to the large variabilities of absolute amplitudes of EEG spectra. Spectral peaks are usually identified by a single frequency where power in a given band is maximal. Coherence measures degrees in which EEG waveforms are in phase with each other. Asymmetry measures the electrical activity in one hemisphere relative to the other (Niedermeyer and Lopes da Silva, 2004).

These qEEG analytical methods are unable to capture the full characteristics of the signal. For band power measurements, the detailed information a specific frequency peaks is ignored and only the total power within the given frequency band is examined. This has several the potential problems: firstly the physiologically relevant frequency band are not fixed but varies between individuals(Moretti et al., 2004); secondly the frequency peaks are indicative of resonance in the system, so quantifying them is important in gaining understanding of the system as a whole (Nuwer, 1988). Multiple peaks are known to do coexist in a frequency range (Andrew and Pfurtscheller, 1997; Pfurtscheller et al., 1997), so the measurements of only the higher peak in spectral peak analysis may not adequately represent activities in the given range entirely.

1.4.3 Independent component analysis

Independent component analysis (ICA) is a special case a group of statistical technique referred to as blind source separation. It resolves EEG or MEG signals to its potential components, by assuming there are temporally independent sources with negligible propagation delays from the source to the electrodes, and the summation of the potentials arising from the different parts of the scalp is linear at the electrode. It then finds the independent components by maximizing the statistical independence of the estimated components. The result of the analysis is a decomposition of a list of independent components (Comon, 1994; Delorme and Makeig, 2004).

Generally ICA cannot determine the number of of source signals, a uniquely correct ordering of the source signals, nor the proper scaling (including sign) of the source signals. It is different from another statistical technique known as Principle Component Analysis (PCA) where the components are orthogonal, since independent source signals is not necessarily orthogonal (Naik and Kumar, 2009).

1.4.4 LORETA

Low resolution brain electromagnetic tomography (LORETA) is frequently used for analyzing brain activity. It is an attempt to solve the “inverse” problem (i.e. locating the source of the activity from experimental results) which in general has nonunique solutions. An approximate determination of the distribution of the source of neuronal activity is obtained by analyzing EEG data using a 3-dimensional model of the brain under electrophysiological and neuroanatomical constraints, with neighboring cortical areas produce similar local field potentials. The cortex is modeled as a collection of volume elements in a digital brain atlas (Pascual-Marqui et al., 2002).

1.5 Alpha rhythm

The alpha rhythm is the most prominent feature observed in the human EEG, as first noted by Berger (1929). The official definition of the alpha rhythm by the International Federation of Societies for Electroencephalography and Clinical Neurophysiology (IFSECN) is a rhythm at 8-13 Hz occurring during wakefulness over the posterior regions of the head, generally with higher voltage over the occipital area. Amplitude is variable but is mostly below 50 μV for adults. It is best seen with eyes closed and under conditions of physical relaxation and relative mental inactivity, and is blocked or attenuated by attention, especially visual and mental efforts (IFSECN, 1974) (Niedermeyer and Lopes da Silva, 2004). Here it should be noted that suppression of the alpha rhythm by attention or mental effort varies greatly between individuals and experimental conditions (Shaw, 2003).

A more recent updated definition of the alpha rhythm points out some clear distinctions, particularly “use of term alpha rhythm must be restricted to those rhythms that fulfill these criteria. Activities in the alpha band with differ from the alpha rhythm as regards their topography and/or reactivity, should either have specific appellations (for instance: the mu rhythm) or should be referred to as rhythms of alpha frequency, or alpha activity” (Deuschl and Eisen, 2000). This definition highlights the problems associated with definition of a single frequency as the alpha rhythm, since the separation of the particular components is often difficult if not impossible (Pineda, 2005).

Also the frequency criterion of 8–13 Hz proposed by the IFSECN (now known as the IFCN) is not always applicable, for instance in young children and infants, who generally have alpha peaks in lower frequency ranges (Berger, 1929; Lindsley, 1936; Smith, 1941).

1.5.1 Individual differences

Alpha rhythm varies widely between individuals and even within an individual. Power measurements in all EEGs are strongly affected by a multitude of factors, from morphologies of the head to the interelectrode distances. In addition to the above mentioned factors, alpha power and frequency are well known to change with sensory, motor and cognitive loads, as well as age, state of attention or state of arousal, and some studies suggest small sex differences (Benninger et al., 1984; Shaw, 2003).

Age trends

Alpha power and frequency change with age in a nonlinear way. Age related changes in the alpha frequency had been well documented since the early age of EEG research (Lindsley, 1936), with frequency increases from about 7 Hz at an age of about 2 years, to about 10 Hz during adulthood (Niedermeyer and Lopes da Silva, 2004), then a gradual decline throughout adulthood. Stroganova et al. (1999) showed that infants have a lower dominant alpha rhythm compared to adults, regarded as precursors of the adult alpha rhythm. The age trends for elderly subjects is not as clear, due to additional factors other than natural decline of cell functions: some of the subjects would be present with age-related brain pathology.

The blocking of the alpha rhythm varies in strength, is not always complete, and in some cases can be totally absent, especially in the case of alpha blocking due to mental effort. The amplitude ratio between eyes close and eyes open voltage amplitude had been reported to decline with age (Niedermeyer and Lopes da Silva, 2004).

1.5.2 Functional significance

Alpha rhythm was proposed as an “idling” EEG activity, because sensory information processing in a specific area switches off alpha rhythm in that area. The power of alpha activity is inversely correlated to metabolic function of the corresponding area (Kropotov, 2009). This hypothesis was tested by Ergenoglu et al. (2004) and found that the sensory threshold for visual stimuli are reflected in the alpha rhythm of the EEG.

Alpha-band activity in the EEG varies with cognitive and memory performance (Berger, 1929; Bengston and Schaie, 1999; Clark et al., 2004; Klimesch et al., 2007) and is potentially a tool to gauge intelligence (Posthuma et al., 2001). Increases in alpha band activity at frontal and temporal sites are observed in short-term memory tasks (Klimesch, 1999). This increase does not contradict the attenuation of the alpha rhythm with mental effort, as the height of the alpha peak decreases concurrently with the increase in overall alpha band power - a case in which standard qEEG does not capture the change well. The posterior alpha rhythm is most prominent in the relaxed waking state, so can serve as a tool for the assessment of arousal (Niedermeyer and Lopes da Silva, 2004).

The complete absence of alpha rhythm is generally termed as *low voltage records*, since alpha rhythm present as the largest amplitude in EEG in the normal case. *Low voltage records* are found in families of alcoholic and drug addicts (Kropotov, 2009). A reduction of the alpha frequency can occur in demented patients or due to exogenous intoxication (e.g., alcohol) (Samson-

Dollfus et al., 1997).

Alpha frequency systematically changes with age and cognitive impairment (Bengston and Schaie, 1999). Thus, alpha frequency can serve as a diagnostic tool for the onset of dementia (Samson-Dollfus et al., 1997). Some psychiatric disease results in a reduction of alpha frequency, such as schizophrenia (Karson et al., 1988), Alzheimer's disease (Coben et al., 1983), Attention Deficit and Hyperactivity Disorder (ADHD) (Swartwood et al., 2003), and epilepsy (Niedermeyer, 1997). Physiological deficiencies also affects the alpha rhythm, for example hyponatremia and hypernatremia (low and high levels of sodium, respectively) suppress the alpha rhythm (Holmes et al., 2006).

In the general population the alpha rhythm is quite symmetrical between the left and right side of the head, with EEG patterns of similar frequency and amplitude (Kropotov, 2009). Asymmetry greater than 50% might be an indication of pathology. There are some indication of asymmetrical power involvement of the frontal cortex in emotional reaction (Davidson, 2004), though due to the small variation in the difference between the EEG power at the left and right side, methodological problems exist in the analysis (Hagemann, 2004).

There are numerous drug effects on the alpha rhythm, some of which are listed in Table 1.1.

1.5.3 Additional alpha measures

The basic measures of alpha rhythm are its frequency, amplitude, and the width of the given alpha peak. With the inclusion of multiple peaks we can generalize to multiple sets of peak parameters (frequency, amplitude and width) for each of the alpha peaks.

Although the literature is mainly concerned with single alpha frequencies, there has been some work on the expansion of the measures taken. Individual alpha frequency (IAF) is one such measure, proposed by Klimesch (Shaw, 2003; Klimesch, 1997). In this approach, using visual inspection the peak and its closest troughs are measured for each recording electrode site, the means of the respective troughs are obtained from all the electrodes and the weighted spectral estimate of each site is used to evaluate the IAF. A number of subbands to alpha are also defined relative to the IAF: lower 1 alpha (IAF - 4 Hz), lower 2 alpha (IAF - 2 Hz), and upper alpha (IAF + 2 Hz). This subdivision enables further analysis of the alpha band.

Coherence is also used to measure alpha activity (Beaumont et al., 1978; Schoppenhorst et al., 1980). Investigations into structural organization of EEG by the measures of coherence between activities from different part of the head. Pairs of signals with high coherence may have arisen from the same generating process.

Table 1.1: Table of dependence of the alpha rhythm on a non exhaustive list of drugs. The quantities f_α and A_α indicates the frequency and amplitude of the alpha rhythm, respectively.

Type	Drug name	Effect on f_α
Antiepileptic	Benzodiazepines	$--$
	Phenyotin	$--$
	Carbamazepine	$--$
	Barbiturate	$--$
	Valproate	$--$
	Ethosuximide	$--$
Psychotropic	Tricyclic	$--$
	Major Tranquilizers	$--$
	CNS stimulants	$+$
	Lithium *	$-$
Neuroleptics	Sedative	$--$
	Non-sedative	$-$
Antidepressants		$-$
Psychostimulants	LSD type	$+$
	Amphetamine	$-$
Anxiolytics		$-$
Hypnotics		$-$
Nootropics		$-$
Street	Cocaine	$+$
key: + increase, − decrease, ++ strong increase, − − strong decrease the asterisk * indicates that A_α also decreases in this case		

1.5.4 Origins

The theory of the origin of alpha rhythm is still a hotly debated topic. There are three main theories: (a) alpha rhythm is due to a pacemaker type mechanism, where neurons with an intrinsic firing rate fire in synchrony to produce the observe rhythm (Niedermeyer and Lopes da Silva, 2004), (b) the rhythm is due to oscillations of spatial cortical eigenmodes (Nunez, 1995; Wright and Liley, 1996), and (c) resonance in the corticothalamic system, with the frequency close to the resonance frequency of corticothalamic loops. This thesis investigates the phenomena of splitting or multiple peaks in the alpha rhythm, which corresponds to a different explanation for each of the theories: (a) a separate pacemaker would be needed for each spectral peak, (b) a degeneracy of the eigenmode from cortical asymmetries (Nunez, 1995), and (c) nonuniformities in the time delay of the corticothalamic loop (O'Connor and Robinson, 2004).

This lack of consensus in the generation mechanism, along with the difficulties in scaling up current techniques (namely visual inspection) to larger population of subjects, motivates the development of better, objective, and automated quantifications of the alpha rhythm. Only with a large sample of objective alpha rhythm parameters we can further examine and test competing theories of alpha rhythm generation mechanism. This thesis provides the method in facilitate investigation in this area, although exploration of the link between the mechanism and the data is left for future work.

1.6 Structure of the thesis

In Ch. 2 a detailed description of a method developed specifically for the automatic identification of multiple alpha rhythm is presented. A test case of 100 clinically healthy subjects was used to validate the method and show that it not only corresponds well to human identification of the alpha rhythm parameters from the power spectrum in cases of clear alpha peak: frequency, amplitude, and width; but it also handles cases of not distinct alpha peak, and provides a more accurate and objective method for estimating these quantities.

Chapter 3 utilizes the method presented in Chapter 2 on a larger group of 1498 clinically healthy subjects. The aims are to establish population values for alpha parameters, to verify the existence of double alpha peaks, and to examine the age and sex trends of the alpha rhythm parameters. The choice of the subjects is common with other studies that extracted parameters associated with the generation of alpha rhythm in some theories of alpha generation, such as the time delay in the corticothalamic loop t_0 (Roberts and Robinson, 2008b), in independent ways; one of these studies is presented in the Appendix C (van

Albada et al., 2010). Finally, Chapter 4 briefly summarizes the results and outlines some possible future research directions.

Chapter 2

Alpha peak characterization algorithm

2.1 Abstract

The identification of alpha rhythm in the human electroencephalogram (EEG) is generally a laborious task involving visual inspection of the spectrum. Moreover the occurrence of multiple alpha rhythms is often overlooked. This chapter seeks to automate the process of identifying alpha peaks and quantifying their frequency, amplitude and width as a function of position on the scalp. Experimental EEG were fitted with parametrized spectra spanning the alpha range, with results categorized by multi-site criteria into three distinct classes: no distinguishable alpha peak, a single alpha peak, and two alpha peaks. The technique avoids visual bias, integrates spatial information, and is automated. We show that multiple alpha peaks are a common feature of many spectra.

2.2 Introduction

Correlations of the electroencephalogram (EEG) with brain functions are widely used diagnostically, and are inferred to be closely connected to brain dynamics, information processing, cognition, and states of arousal (Niedermeyer and Lopes da Silva, 2004). The alpha rhythm was first identified in humans by Berger (1929) as the most prominent feature in the EEG. The normal alpha rhythm varies in amplitude, frequency, morphology, and spatial distribution from one individual to the other. It also varies with time, and some individuals with a normally functioning brain never show an alpha rhythm (Niedermeyer and Lopes da Silva, 2004). Development and verification of an improved automated method for quantification of alpha activities is the core aim of this chapter.

In the literature there are descriptions of several rhythms within the conventional adult alpha frequency range of 7-13 Hz (Niedermeyer, 1997). Generally the alpha rhythm is present in the relaxed awake state, with the conventional alpha rhythm more prominent in the eyes-closed state than with eyes open. The conventional alpha rhythm is associated with the visual cortex, "central alpha" or rolandic mu rhythm with the sensorimotor cortex, and the so-called tau rhythm with the auditory cortex (Niedermeyer and Lopes da Silva, 2004). As with the conventional alpha, which is blocked by visual stimuli, the mu rhythm is blocked by movements (Niedermeyer, 1997), and the tau rhythm is blocked by auditory stimuli. Thus in the traditional alpha rhythm range there could exist a number of peaks, each differently modulated by experimental conditions and associated with a particular region of the brain (Samson-Dollfus et al., 1997). It is possible for more than one alpha rhythm to be present in a single recording. Splitting of the alpha peak into two sub-peaks, separated by up to 1-2 Hz, has been found to occur in the normal population (Nunez and Srinivasan, 2006; Robinson et al., 2001a).

Alpha band activity in the EEG varies with cognitive and memory performance (Berger, 1929). Increases in alpha band activity at frontal and temporal sites are observed in short-term memory tasks (Klimesch, 1999). A relaxed waking state is the optimal condition for the posterior alpha rhythm, so EEG can serve as a tool for the assessment of arousal (Niedermeyer and Lopes da Silva, 2004). A reduction of the alpha frequency can indicate exogenous intoxication (e.g., alcohol) or occur in demented patients (Samson-Dollfus et al., 1997). Alpha frequency also systematically changes with age, as has been well documented since Smith (1941), which suggests that alpha frequency is an indicator of neural maturation or myelination. Thus alpha frequency can serve as a diagnostic tool for onset of dementia (Samson-Dollfus et al., 1997), neural maturation (Klimesch et al., 1993), and potentially intelligence (Posthuma et al., 2001), cognitive states (Klimesch et al., 2007) and memory performance (Clark et al., 2004).

The mechanisms for the generation of the alpha peaks are still controversial. Proposed mechanisms include: (i) Pacemakers located in a small portion of the brain, each with a characteristic frequency and with projections to the cortex. Although intrinsically bursting neurons do exist, which are capable of entrainment via local coupling, a major problem with this theory is that it is an ad hoc explanation of why various resonances exist, a new pacemaker is needed for every peak and sub-peak (Robinson et al., 2003b; Nunez and Srinivasan, 2006, Ch 2). Secondly, the transition from wake to sleep involves concurrent activation and deactivation of peaks, a pattern which is not explained by pacemaker theory (Robinson et al., 2003b). (ii) A second proposed mechanism involves spatial cortical eigenmodes, where the splitting of the alpha peak would result from breaking of the degeneracy between modes caused by cortical asymmetry (Nunez and Srinivasan, 2006, Ch 11), though the predicted result appears contrary to observation (Robinson et al., 2001a). (iii) A third mechanism for multiple alpha peaks arises from nonuniformities of the time delay in resonant corticothalamic loops (Robinson et al., 2001c, 2003b), which usually leads to two dominant peaks, even when the local alpha frequency is continuously varying across the brain.

Better characterization of alpha peaks via objective measurements of frequencies, powers, peak widths, and other parameters will potentially help distinguish between the above generation mechanisms. All this motivates the present attempt to improve on existing methods for alpha peak quantification.

The identification of the alpha rhythm is generally done visually: a trained scorer inspects the EEGs (either in time series or power spectra), identifies, and quantifies the alpha peak based on personal or laboratory-specific operational criteria for which there are incomplete standardization. This is a time-consuming and subjective process, further complicated by factors such as noise, the presence or absence of certain peaks at some of the sites, and broad-band background signals. This chapter thus seeks to find an objective automated algorithm for the identification and characterization of peaks.

There have been numerous attempts to automate information extraction from EEGs, including use of time domain analysis (Hjorth, 1970), applications of fractal dimensions (Arle and Simon, 1990; Pritchard, 1992), statistical measures (Nakamura et al., 1992), wavelet transforms (Schiff et al., 1994), and adaptive neural networks (Herrmann et al., 2001; Huupponen et al., 2002). Time domain analysis describes the characteristics of an EEG trace with descriptive parameters based on time series data using a statistical approach. This technique does not attempt to compete with human identification, but rather provides parameters that may be useful in quantifying subtle changes in the EEG, and which may be correlated with physiological variables (Hjorth, 1970). Arle and Simon (1990) applied fractal dimension to EEG analysis for the detection of transients and showed that the quasi-random background EEG has a different fractal dimension to transient deterministic data, which is useful in isolating transient signals. The wavelet transform provides an alternative to the Fourier transform in EEG analysis. Statistical measures have been used to extract similar information to the traditional visual analysis using periodograms from the EEG data (Nakamura et al., 1992), but only a single alpha peak was considered and the channels were treated separately. The frequency and the amplitude of the alpha peak were found using adaptive neural networks (Herrmann et al., 2001), but work to date only considered the possibility of a single alpha peak.

In contrast to the above techniques, the method developed in this chapter extracts detailed measures for the background spectrum as well as for each alpha peak: its frequency, amplitude, and peak width. These have direct links to the physiology of the generation mechanism. These peak parameters can potentially help to distinguish the mechanism of generation. The possibility of multiple alpha peaks raises the problem of distinguishing a single alpha peak, whose frequency changes spatially, from the case of multiple spatially separate sources. The method developed in this chapter is capable of resolving such smooth spatial variations in frequency as well as multiple peaks, thus aiding identification. The method is based on codification of visual inspection, and analysis spanning all the electrodes to help eliminate artifacts.

The structure of this chapter is as follows: In Sec. 2 we outline subject demographics, EEG collection criteria, and our alpha quantification and classification algorithms. In Sec. 3 we present the parameters extracted from the spectrum from the categorization of a 100 normal subjects. In Sec. 4 we summarize the main results.

2.3 Method

2.3.1 Subjects and EEG

EEG data used in this chapter were selected from a database previously collected by the Brain Dynamics Center, Westmead Hospital, Australia. In compiling the data, EEG recordings of healthy adult subjects from the general community were obtained with the appropriate ethical clearances and informed consent (Bahramali et al., 1999). The data selected for this study include 100 subjects (49 females and 51 males) with mean ages of 44 years (SD = 16 years) and 45 years (SD = 15 years), respectively. The EEGs were acquired as part of a wider battery of electrophysiological tests. Only the EEG measures from the eyes-closed state were used in this study. The subjects were asked to rest quietly with their eyes closed for the two minute duration of the task and were awake and non-drowsy throughout the recordings. An electrode cap using the International 10-20 system of scalp sites with 19 electrodes was used to acquire the EEG data. EEGs were recorded at a 250 Hz sampling rate through a SynAmps amplifier using a linked earlobe reference and a low-pass third order Butterworth filter with −6 dB point at 50 Hz. Ocular artifacts were corrected offline according to the method of Gratton et al. (1983). For further details see Bahramali et al. (1999).

The electroencephalogram was first divided into successive 8.192 s segments, which were windowed, Fourier transformed, modulus squared, and averaged to produced one power spectrum per recording site. Deviations of >100 μV from the mean caused the segment to be rejected prior to transformation.

2.3.2 Alpha quantification method

The alpha rhythm is characterized by state dependence and complex topography that is inconsistent across individuals, posing significant challenges to automatic quantification. Our method addresses the need for unbiased and robust quantification of alpha power, frequency, and topography. The general approach described here is to fit parametric functions to the spectra from each recording site, then combine the parameters from all sites to produce a simple topographically-informative summary of the size and shape of each alpha peak. The algorithm involves several stages and many optimized features, which are detailed in subsequent sections.

The spectra are fitted using a nonlinear algorithm with a series of criteria to identify peaks and their associated parameters: frequency, amplitude, and width. Since the data from different sites contain spatial trends, we cannot simply average the data from all sites. However, we interrelate data from multiple sites to reduce the effects of noise and increase the accuracy of the alpha peak parameters obtained.

A summary of the fitting process is shown in the flowchart in Fig. 2.1. We explain in detail the workings of the method in this section, following the order of the steps involved. An overview of our approach is provided in Sec. 2.2.1. In Sec. 2.2.2 we expand on how the background trend is evaluated, and in Sec. 2.2.3 the identification and quantification of the peaks are discussed in greater detail. In Sec. 2.2.4 we discuss a key distinguishing feature of the method: how information from multiple electrodes is used in order to verify and refine peak parameters at each site, allowing the program to rule out spurious peaks and resolve finer details than is possible with visual inspection or single electrode data alone, and how different types of peaks are classified.

General Approach

Figure 2.2 shows a spectrum with two peaks, at 8 and 10 Hz, and a background that piece-wise approximates a power-law relationship. Our goal is to codify the identification and quantification of these components, including spatial trends, in a way resembling that used in visual interpretation of data.

In order to determine the parameters of the alpha peaks we fit a parametrized spectrum, a function which has the key features identified in Fig. 2.2, to the *logarithm* of the power spectrum [i.e., to $\log P(f)$]. Use of the logarithm provides a better fit to the data. Since it is necessary to have dimensionless quantities in order to take the logarithm, we define:

$$\log P(f) = \log \left[P_{raw}(f)/P_0 \right], \tag{2.1}$$

where P_{raw} is the raw power and $P_0 = 1\ (\mu V)^2\ \mathrm{Hz}^{-1}$. The function used in the

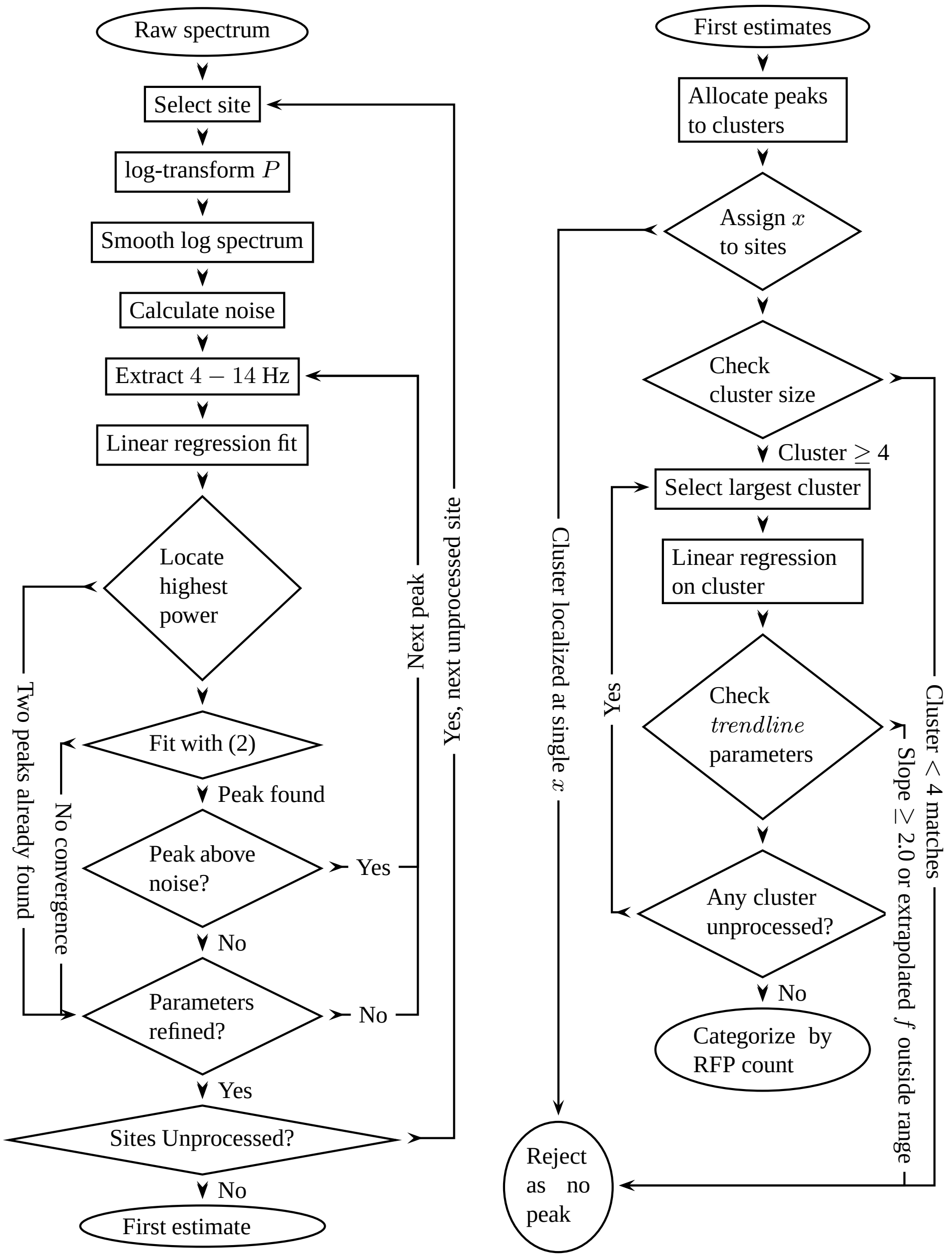

Figure 2.1: The flowchart of the decision process used in our method. (a) Fitting of the peaks to the experimental spectrum. (b) The decision process in which data from multiple sites are used to distinguish between a robustly fitted peak (RFP) and noise. Refer to text for details of the steps.

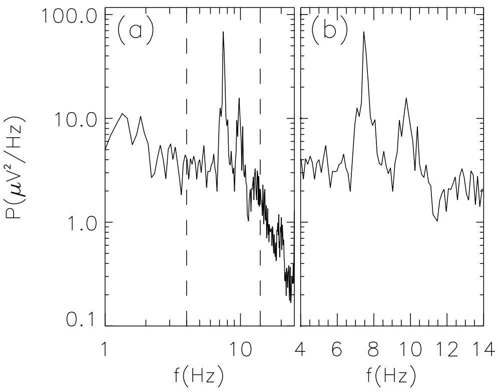

Figure 2.2: An example of a log-transformed power spectrum: (a) the spectrum from 1 to 25 Hz with both axes logarithmic, and (b) the same spectrum with a linear frequency axis in the region of interest [4 to 14 Hz, between the dotted lines in (a)].

fit is then:

$$\begin{aligned}\log P(f) \quad \approx \quad & A_1 \exp\left(\frac{-(f-f_1)^2}{\Delta f_1^2}\right) \\ & + A_2 \exp\left(\frac{-(f-f_2)^2}{\Delta f_2^2}\right) \\ & + B - C \log f, \end{aligned} \tag{2.2}$$

where A_1, f_1, and Δf_1 are the amplitude, frequency, and width of the first peak, A_2, f_2, and Δf_2 are the corresponding quantities for the second peak, B is the normalization of the background spectrum, and C is the exponent in a power-law approximation to the background spectrum,

$$P_{bg}(f) = e^B f^{-C}. \tag{2.3}$$

An apparent problem with (2.2) is that for any set of parameters A_1, f_1, Δf_1, A_2, f_2, Δf_2, B and C, an equally good fit occurs if the subscripts are swapped, with $1 \Longleftrightarrow 2$. This is not a problem in practice as a later sorting process deals with this ambiguity. Of more significance are three limiting cases: (i) indeterminacy of the amplitude A_1 or A_2 when the frequency $f_1 \approx f_2$ and width $\Delta f_1 \approx \Delta f_2$, which results when two peaks merge into one; (ii) indeterminacy of the first or second peak parameters $f_{1,2}$ and $\Delta f_{1,2}$ when $A_{1,2} \approx 0$, when one peak disappears or is negligible and (iii) indeterminacy of $A_{1,2}$ and B when Δf_1 or $\Delta f_2 \to \infty$, causing the peaks to flatten into the background. In all three cases the problem is ill-conditioned due to over-parameterization.

Accordingly, a stepwise approach is adopted when analyzing experimental data. Rather than fitting all eight parameters of (2.2) to the experimental spectrum in a single step, the background component $B - C \log f$ is fitted in the region of interest first. A peak is then located by identifying the highest residual power after subtracting the background trend. This principal peak is fitted to the original spectrum with the background component identified in the previous step included, whilst allowing the parameter B, the normalization, to vary (but keeping C, the slope, fixed). A second peak is identified by repeating the process: the principal peak parameters and C are fixed, and other parameters are allowed to vary. This approach can be used to determine any number of peaks per site, but we limit the number of fitted peaks to two since we see no robust evidence of more, and we do not wish to fit random peaks produced by noise. The Levenberg-Marquardt method (Press et al., 1995) is used to fit (2.2) to $\log P(f)$ by minimizing the mean-square deviation between the two.

The final phase is to apply criteria to integrate information from multiple electrode sites to refine the initial peak parameter estimates, to further rule out any spurious fits, and to obtain global descriptions of alpha characteristics.

Smoothing and Background Identification

In our algorithm, with the provisional peak as the highest residual power in the range, noise can potentially produce an extremum which lies far from any actual peak. For this reason smoothing is applied to the experimental spectrum (Step 4 in Fig. 2.1a) prior to searching for a provisional peak by taking a boxcar average spectrally. The following function describes the smoothing process:

$$(\log P)'_i = \sum_{n=-k}^{k} \frac{\log P_{i+n}}{2k+1}. \tag{2.4}$$

where k points are included either side of the frequency of interest. The smoothing is calculated in $\log P$ as with the rest of the fitting routine. In our case the width of the boxcar is 1.83 Hz. The smoothed spectrum has a second use: the RMS difference between the raw and smoothed spectra is taken as an indication of noise (Step 5 in Fig. 2.1a), and used later in the algorithm. We then truncate the spectrum to $4 - 14$ Hz, to isolate the part relevant to alpha (Step 6 in Fig. 2.1a).

In this chapter we approximate the background spectrum in the range $4 - 14$ Hz by a single power-law, Eq. (2.3), implying:

$$\log P_{bg}(f) = B - C \log f. \tag{2.5}$$

Table 2.1: Parameters in the iterative fit shown in Fig. 2.3. Row (a) corresponds to the first pass of the algorithm or Fig. 2.3(a), in which only the background spectrum fitted. Row (b) and Fig. 2.3(b) are the result of fitting the first peak. Row (c) and Fig. 2.3(c) are the result from fitting the second peak. The last row is the result of several further iterations of steps (a)-(c).

	A_1	f_1	Δf_1	A_2	f_2	Δf_2	B	C
(a)	0	0	0	0	0	0	2.59	−0.59
(b)	2.40	7.52	0.45	0	0	0	2.40	−0.59
(c)	2.40	7.52	0.45	1.53	9.80	0.57	2.25	−0.59
	2.51	7.53	0.52	1.56	9.80	0.60	2.20	−0.59

A first estimate of the background is obtained by fitting the form (2.5) to the log-transformed truncated spectrum using linear regression. This is conveniently achieved by setting $A_1 = A_2 = 0$ in Eq. (2.2) (Step 7 in Fig. 2.1a). With the identification of peaks in the later steps the value of parameter B is further refined.

Peak Quantification

The peak fitting routine (Fig. 2.1a) finds and fits one peak at a time, reducing the number of variables in order to decrease the possibility of a false fit. The algorithm uses the amplitude and frequency of the largest peak in the residual spectrum to initialize A and f (Step 8 in Fig. 2.1a). Peak width, Δf, is initialized to 1 Hz. The three peak parameters and B are then fitted to the data, while keeping earlier peak parameters (if any) and C fixed (Step 9 in Fig. 2.1a). If this peak is found to be above the noise threshold then the process is repeated for a second peak (Step 10 in Fig. 2.1a). The algorithm is looped (Step 11 in Fig. 2.1a) to refine the parameter estimates until the residual spectrum has no more peaks distinguishable from noise or two peaks have already been found, and B changes by less than 1% in successive iterations. All the sites are processed in the same manner (Step 12 in Fig. 2.1a) resulting in the first estimate of the parameters for all sites.

Figure 2.3 demonstrates the first three steps and a final result of this iterative fitting algorithm, while Table 2.1 shows the corresponding parameters. The intermediate steps in the convergence of the parameters are left out for clarity. The algorithm initially fits the background spectrum: see (a) in Fig. 2.3 and in Table 2.1. Iterative fitting to successive peaks of smaller amplitude is shown in (b) and (c) in Fig. 2.3 and in Table 2.1. Note in the right column of (b) in Fig 2.3 there is a marked decrease in amplitude of the highest peak in the previous residual spectrum (a) in Fig 2.3. The peaks judged visually to be at 7.45 and 9.64 Hz are slightly shifted from the fitted peaks of 7.53 and

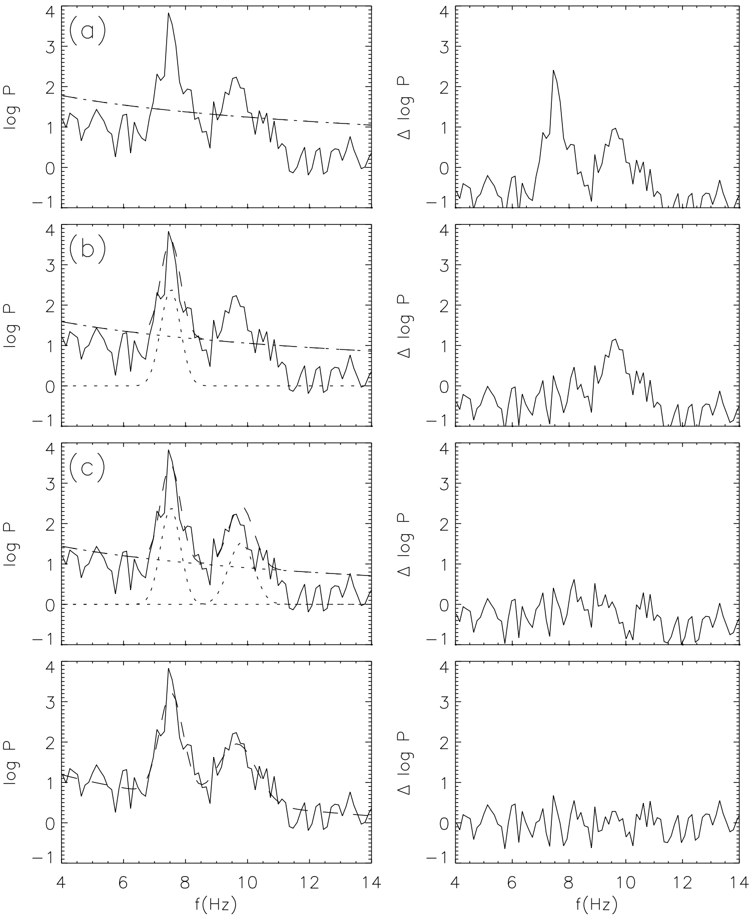

Figure 2.3: Iterations of fitting by components to refine parameters. In the left column the solid line represents the raw spectra, dotted lines represent its individual components (i.e., peaks or background), and dashed lines represent the total fitted spectrum. The right column shows the residual spectra. (a) Fitting the background. (b) Fitting one peak with refinements to the background. (c) Fitting a second peak in addition to further refining the background parameters. Last row shows the final fit and the residual spectrum after several further iterations of steps (a)-(c).

9.80 Hz, due to a combination of (i) the slope of the background shifting the apparent frequency and (ii) the discrete nature of the experimental spectrum. The average value for the residual spectrum of (b) and (c) is below zero as a result of the algorithm fitting mainly to the peak rather than the background, but is corrected when steps (a)–(c) are iterated. The last row of Fig. 2.3 and Table 2.1 shows the final result of iterations.

Peak Verification

Once fits are obtained from all recording sites, several complications become apparent: (i) peaks due to spatially separated sources may overlap to the extent that the fitting algorithm cannot distinguish them, (ii) noise may obscure or eliminate valid peaks, or may be mistaken for a peak, and (iii) the morphology and frequency of the alpha peak can vary from site to site. All these mean that the provisional scores need to be refined. Fortunately this is possible by assuming that frequency, as a function of position, varies only slowly if at all. Thus, the next step – a key distinguishing feature of our method – is to determine which of the provisional peaks have plausible topography by requiring local continuity, consistent both with an extended source and with a small number of discrete sources. Here the term “source” does not imply a discrete pacemaker-type source, but encompasses all types of generation mechanism. Even with a continuous change in the parameters of a generation mechanism, two discrete peaks can emerge (Robinson et al., 2003b).

The frequency of a source is unaffected by volume conduction or neural projection. Thus, looking for peaks of similar frequency spanning multiple sites provides a powerful means to identify the spectral peak due to a real source, although it works best when there is just one source frequency. This requirement of spatial continuity is also valuable in dealing with complications (i)-(iii) above.

Ambiguous cases in category (i) above can often be resolved by considering spatial topography. If we assume two similarly shaped peaks generated from two spatially distinct sources, and if the frequency difference of the peaks is sufficiently large, then they appear as two distinct peaks, as shown in Fig. 2.4(a). However, when the frequency difference decreases while maintaining the same amplitudes, the two peaks merge into a single peak with a shoulder [Fig. 2.4(b)], and further decreasing the frequency difference results in a single peak. Similarly, for a small difference in frequency, as the relative amplitude of the second peak decreases, the resultant spectrum changes from a double peak, to a single peak with a shoulder, as shown in Fig. 2.4(c), and eventually to a single peak.

In the case of two peaks, whose frequency separation is less than their width, the resultant spectrum resembles a single peak. The originating sources

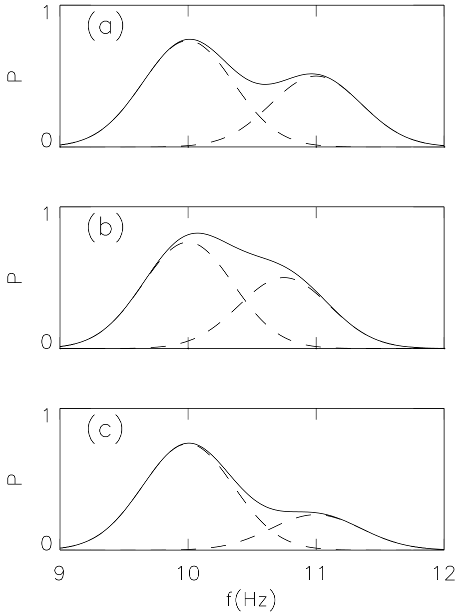

Figure 2.4: Possible morphologies resulting from a superposition of two peaks. The dashed lines are component peaks and the solid lines the resultant spectrum from the combination of the two peaks. (a) Two peaks with different amplitudes, with frequency separation of 1 Hz. (b) Two peaks with the same amplitudes as in (a) but at frequency separation of 0.75 Hz. (c) Two peaks with the same frequencies as in (a), but with amplitude of the higher frequency peak decreased to half the value in (a).

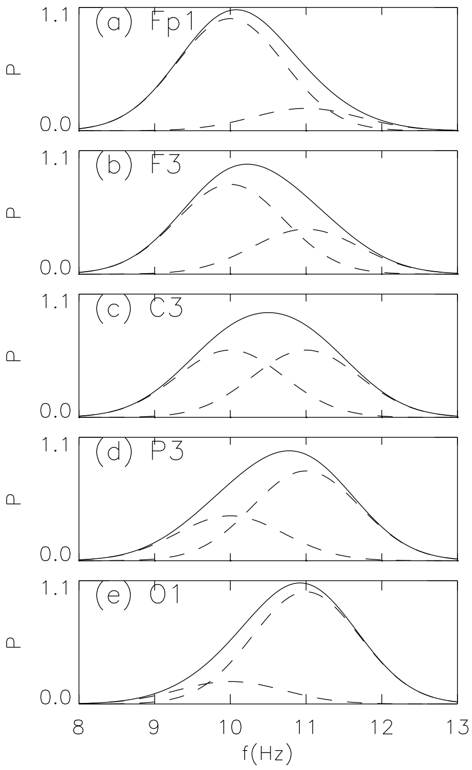

Figure 2.5: Demonstration of how the combination of two peaks with fixed frequencies (here 10 and 11 Hz with 1 Hz widths) can produce a spatially continuously varying overall peak frequency. This diagram shows the resultant spectrum at different locations, assuming the peak with frequency 10 Hz is predominantly generated at the Fp1 site and the 11 Hz peak is predominantly generated at the O1 site, each with amplitude decreasing with the distance from its predominant site. The dashed lines shows the component peaks, and the solid lines show the resultant spectra.

are typically propagated to other sites, decreasing in signal amplitude through neural projection or volume conduction. For generators in both the frontal and the occipital lobes of the brain, the peak frequency could appear to be changing continuously between these sites, as shown by the example in Fig. 2.5. The frequency versus position relation will be referred to as the linear *trendline* of the alpha peak. Potentially the true local frequency could also be changing, depending on the mechanism (recall that our approach does not assume any particular generation mechanism). Trendlines are a simple means to describe all anticipated cases, and require only mild assumptions.

The peaks from all sites of a single subject identified by the above fitting algorithm are pooled, ranked in order of increasing frequency, and separated

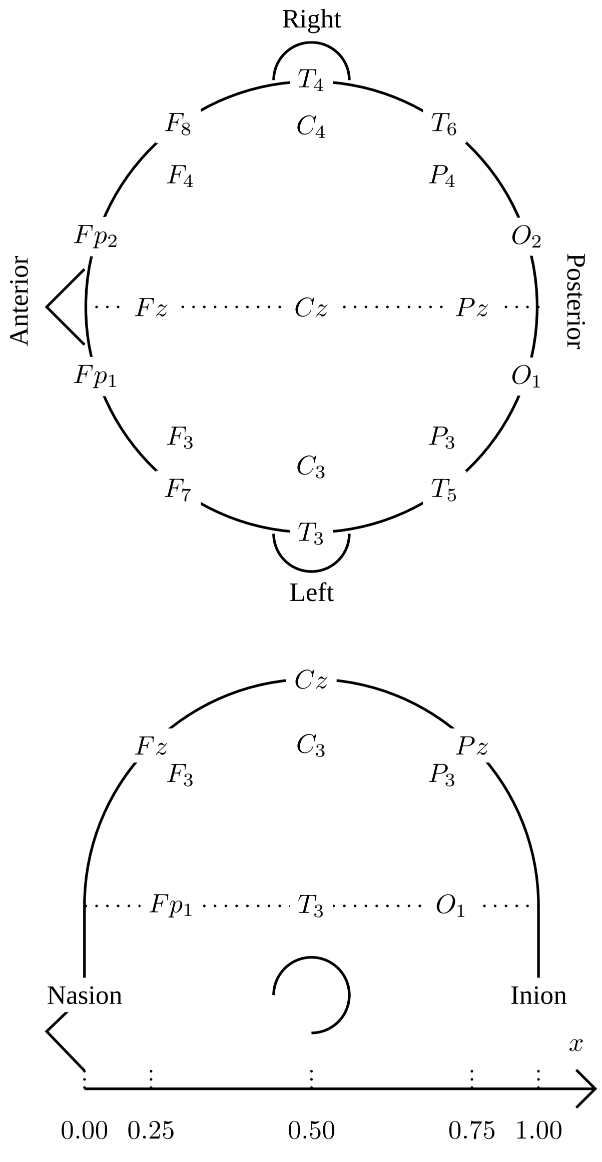

Figure 2.6: Schematics of the placement of the electrodes, showing their nominal frontal-occipital positions, x. The x distances follow the circumference of the head rather than the linear diameter.

into clusters of similar frequency by examining the absolute frequency difference between frequency-wise adjacent peaks. To construct these clusters the average of the absolute frequency difference is evaluated; and if the adjacent peaks are separated by more than the average of the absolute frequency difference, then the peaks are placed in different clusters (Step 2 in Fig. 2.1b). Sites are assigned an x value (Step 3 in Fig. 2.1b), the frontal-occipital location of the site normalized to the value of 0 at $Fp_{1,2}$ and to 1 at $O_{1,2}$, as depicted in Fig 2.6. Any cluster of fewer than four peaks is rejected as likely being due to noise (Step 4 in Fig. 2.1b) and clusters that are restricted in a single x location are likewise rejected. We first select the largest cluster (Step 5 in Fig. 2.1b) and perform a linear regression between frequency and x to work out the trend within the cluster (Step 6 in Fig. 2.1b). Clusters are rejected if the frequency difference is greater than 2 Hz between transverse rows, or the extrapolated frontal and occipital frequencies from the linear regression parameters are outside the 4–14 Hz range of interest (Step 7 in Fig. 2.1b). Progressively smaller clusters are then examined in the same way (Step 8 in Fig. 2.1b), until we have selected up to two clusters or all have been rejected.

We define a robustly fitted peak (RFP) to be a peak that conforms to the criteria set by the above algorithm, and we classify a set of spectra from a subject by the numbers of RFPs resulting from the above verification method (Step 9 in Fig. 2.1b).

Resolving problematic cases

Spectral noise is a common problem with EEG data. An additional complication in the present context is the occasional absence of any well-defined alpha peaks, even after considering both the frequency and spatial domains.

In order to classify the alpha band spectra robustly, the algorithm is designed to reject several types of spectrum with no observable alpha peak: (i) The peak identification mechanism rules out any peak whose amplitude is below the noise threshold that is determined by the variability of the given spectrum (Step 10 in Fig. 2.1a). (ii) When the numerical fitting fails to converge, which implies a noisy spectrum, the provisional peak is rejected (Step 9 in Fig. 2.1a). (iii) More subtly, if the set of spectra from a single subject does not have a set of frequencies or trends that is common to sufficiently many of the sites, (≥ 4 sites in this algorithm; Step 4 in Fig. 2.1b), or the variability of the alpha peak at a single x location is too large (Step 7 in Fig. 2.1b) then the parameters for such subjects are rejected due to lack of significant alpha peaks. All the above cases are interpreted as corresponding to no robustly observable alpha peak in the spectrum.

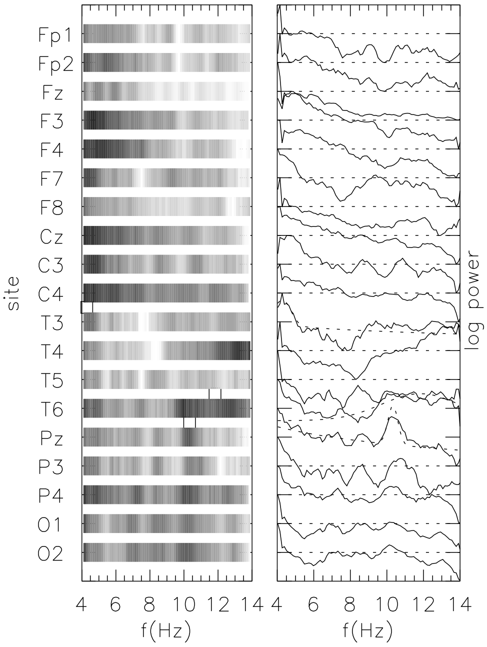

Figure 2.7: Example of a Class 0 set of spectra from a subject with no clear alpha peak. The left column contains grayscale plots in which the shade corresponds to power, with darker being higher and sites are as labeled. The right column shows corresponding normalized logarithmic power spectra, where the dotted lines are the fitted curves and the solid lines are the actual spectra from the subject. Squares above the grayscale plots mark peaks that were fitted with the peak quantification algorithm. Normalization differs slightly from site to site in this illustrative figure.

2.4 Results

The results of the categorization of the EEG data from 100 subjects specified using the algorithm detailed in Sec. 2 are described here. We observe several distinct classes of spectra, as distinguished by the number of RFPs.

In this section we consider Classes with 0, 1, and 2 RFPs, respectively within a subject's spectra. An example of each Class and some basic statistics of the results are presented. Since this section focuses on the method, not the wider implications of the results to specific hypotheses, a full statistical analysis is beyond its scope. Detailed applications will be pursued in subsequent publications.

2.4.1 Class 0: No robustly fitted alpha peak

In this class the peak frequency of the various sites shows no distinct pattern, or candidate peaks are similar in size to the noise fluctuations in the spectrum. We regard such spectra as having no clear alpha peak.

Six of the 100 subjects are in Class 0, with an example shown in Fig. 2.7. In this example very few sites yield an alpha peak in the fitting step (only at the Pz, T6, and T3 electrode sites was a peak successfully fitted), though no clusters of peaks across sites are found of sufficient size to yield a RFP. Visually there are two weak peaks at about 9 and 11 Hz, which are consistent across several sites (P3, Pz, T5, and C3), but these peaks are not successfully separated from the noisy background.

2.4.2 Class 1: Single robustly fitted alpha peak

The sets of spectra in this class show a single approximately linear trend of the alpha frequency with respect to x. A total of 57 of the 100 subjects belong to Class 1, with Fig. 2.8 illustrating a set of spectra for a subject from this class. This example shows a very sharp alpha peak near 9.5 Hz. The fitting algorithm found a miscellaneous peak other than the RFP (at T4 electrode site), but it was eliminated in the verification process. The algorithm result agrees with visual inspection, which does not reveal any obvious extra peaks.

Histograms of the RFP frequencies are presented in Fig. 2.9, for all subjects in Class 1. Most of the subjects have a higher frequency for the occipital sites compared to the frontal sites, the distributions of peak frequency have similar width, and are mostly right skewed. Histograms of the RFP frequency show little left-right variation, so the analysis of the trend is focused here on a representative slice to the left of the central sagittal plane: the Fp1, F3, C3, P3, and O1 sites.

The standard errors of the mean are $0.12, 0.14, 0.16, 0.16$, and 0.15 Hz for the Fp1, F3, C3, P3, and O1 sites, respectively. There is a slight linear trend with respect to the x location:

$$f = [(0.48 \pm 0.17)\, x + (8.81 \pm 0.10)]\, \mathrm{Hz}, \tag{2.6}$$

where the uncertainties shown are ± one standard error. The positive gradient reflects that the occipital frequency is generally larger than the frontal frequency, but with $p = 0.065$ is only approaching significance. The skewness of the histogram is smallest near the frontal pole.

Histograms of the peak amplitude, A, as defined in Eq. (2.2), show little left-right variation, so are plotted in Fig. 2.10 only for the slice defined above. Note the peak amplitude is not the total logarithmic power at the particular

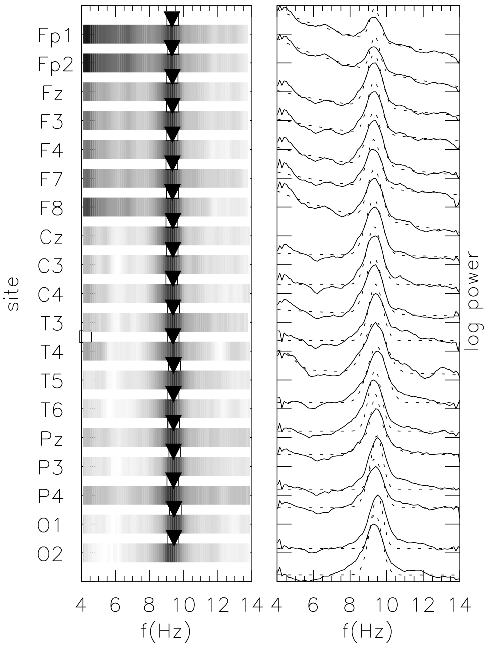

Figure 2.8: Example of a Class 1 set of spectra, plotted as in Fig. 2.7 with the left showing the grayscale plots and the right showing normalized power spectra. In the left column squares and triangles denote the peaks found via the peak quantification process and the results from the peak verification algorithm respectively, with the vertex of the triangle pointing down to the RFP expected frequency. In the right column dotted curves represent the fits and solid curves are the experimental spectra.

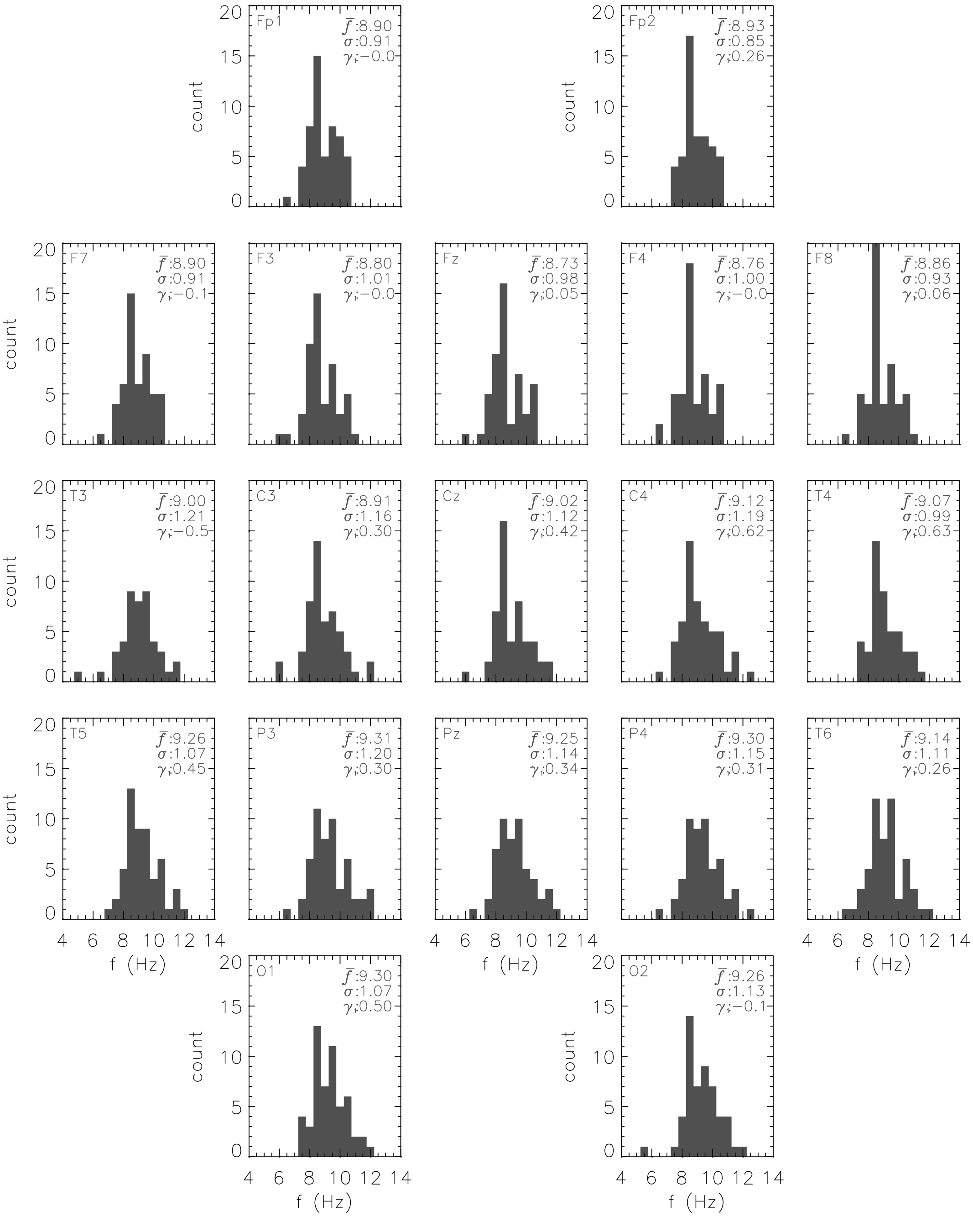

Figure 2.9: Histograms of fitted frequencies for subjects in Class 1. At the top left corner of each histogram is the name of the site, and the top right corner shows the average $\overline{f}$ in Hz, standard deviation σ in Hz, and skewness γ of the histogram.

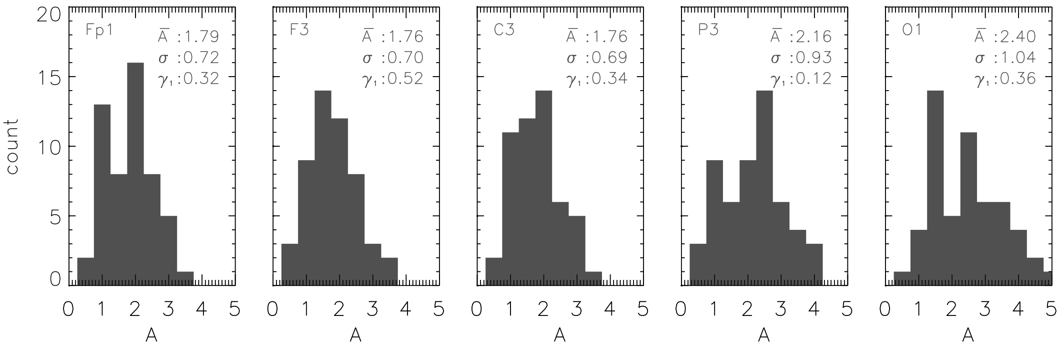

Figure 2.10: Histograms of the fitted amplitude parameter A for subjects in Class 1 at sites along a sagittal slice (Fp1, F3, C3, P3, and O1). At the top left corner of each histogram is the name of the site, and the top right corner shows the average $\overline{A}$, standard deviation σ, and skewness γ of the histogram.

frequency but is in essence the difference between the peak and the background spectrum, and is a dimensionless number. We observe that the peak amplitudes have a broader distribution and a higher average at the back of the head than the front of the head, and are skewed to the right. The standard errors of the mean are $0.10, 0.10, 0.10, 0.13$, and 0.14 for the Fp1, F3, C3, P3, and O1 sites, respectively. The averages at Fp1, F3, and C3 are similar ($1.79, 1.76$, and 1.76, respectively) and less than at the more occipital sites, P3 and O1 (2.16 and 2.40, respectively).

The Q-factor is an indication of the quality of resonance in the system, or the sharpness of the peak, irrespective of its amplitude. In this chapter we define $Q = f_0/\Delta f$, where f_0 is the resonance frequency and Δf is the width of the peak as defined previously. Histograms of Q show little or no significant left-right variation, so are shown only for the slice defined above. The standard errors on the mean are $1.14, 0.85, 0.65, 0.63$, and 0.73 for the Fp1, F3, C3, P3, and O1 sites, respectively. Figure 2.11 shows the resonance of the system is sharpest lowest about the middle of the head (C3, $\overline{Q} = 7.36$), with all the histograms highly right skewed. The highest Q values were $53, 27, 23, 26$, and 27 at Fp1, F3, C3, P3, and O1, respectively.

We next examine the frequency difference between the frontal and occipital site. A trendline is obtained from linear regression of the dominant cluster for each subject – the same trendline used in the peak verification step. Best fits of the frequencies from the trendline $f_{trend}(x)$ at the frontal $[f_F = f_{trend}(0)]$ and occipital $[f_O = f_{trend}(1)]$ locations are used, instead of the actual frequency (if found). Figure 2.12 shows the histogram of the frequency difference ($f_O - f_F$ or δf) between the fitted frequency f_O at the occipital site and the corresponding

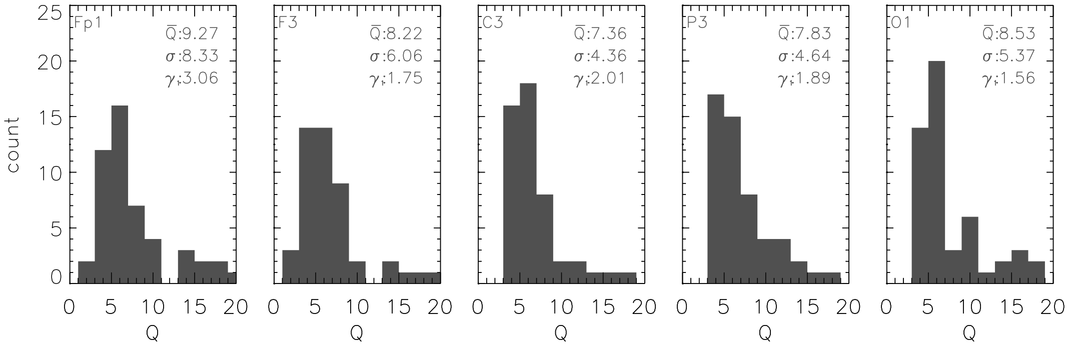

Figure 2.11: Histograms of the fitted Q-factor for subjects in Class 1 at site along the sagittal slice previously defined. Q is a dimensionless quality. At the top left corner of each histogram is the name of the site, and the top right corner shows the average $\overline{Q}$, standard deviation σ, and skewness γ of the histogram. The range is truncated at $Q = 20$ for clarity.

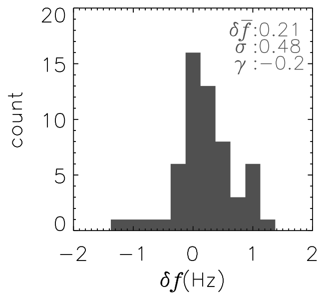

Figure 2.12: Histogram of the difference in fitted frequency $\delta f = f_O - f_F$ between the frontal and the occipital sites of the subjects with one robustly fitted peak. The top right corner shows the mean $\overline{\delta f}$ in Hz, standard deviation σ in Hz, and skewness γ of the histogram.

frequency f_F at the frontal site for each subject. This distribution is slightly left skewed ($\gamma \approx -0.7$), and has a slightly positive average frequency difference ($\overline{\delta f} = 0.21$ Hz) reflecting a generally higher frequency at occipital sites, with a standard error of the mean of 0.06 Hz. A total of 54% of subjects in this class have a higher occipital frequency compared to the frontal frequency, 28% have frequency difference of < 0.25 Hz corresponds to the 0 Hz bin, and the remaining 18% have a lower occipital frequency.

2.4.3 Two robustly fitted alpha peaks (Class 2)

Two distinct alpha peaks can be identified in the spectra for a given subject of this class. The remaining 37 of the 100 subjects belong to Class 2. Figure 2.13 illustrates a set of spectra from a subject in this class. This example shows sharp alpha peaks at roughly 8 and 9.5 Hz, although with some gaps. The algorithm failed to fit a secondary peak at the F7, F4, and T3 sites but then interpolated a peak of frequency consistent with the trendline. The final result from the algorithm agrees with visual inspection of the set of spectra. As illustrated by this example, our algorithm reduces variance in results by adjusting values that are plausibly affected by noise.

The parameters examined below are considered in clusters of similar frequency – the same clusters utilized in the peak verification step. Only the two most populous clusters are considered, and we distinguish the two clusters by their average frequency. The cluster with the higher frequency is usually the one with the higher number of counts.

Histograms of the RFP frequencies are compiled in Fig. 2.14, for all subjects in Class 2. The histograms show both the cluster with the higher average frequency (shaded) and the lower average frequency (outline). The lower average frequency cluster tends to have a smaller number of fitted peaks in each site and a higher spread in frequency compared to the higher average frequency cluster shown in Fig. 2.14. Looking at the same slice just left of the central sagittal plane (Fp1, F3, C3, P3, and O1 sites) as previously, the standard errors of the mean are $0.13, 0.21, 0.20, 0.17$, and 0.13 Hz for the higher average frequency cluster and $0.22, 0.18, 0.26, 0.28$, and 0.30 Hz for the lower average frequency cluster at the respective sites. For the higher average frequency cluster the trend is

$$f = [(0.31 \pm 0.20)\, x + (9.82 \pm 0.14)]\, \mathrm{Hz}, \tag{2.7}$$

where the uncertainties shown are ± one standard error. For the lower average frequency cluster the trend is

$$f = [(-0.33 \pm 0.48)\, x + (8.07 \pm 0.24)]\, \mathrm{Hz}. \tag{2.8}$$

In both case the gradient term is significant, with a p-value of 0.22 and 0.54

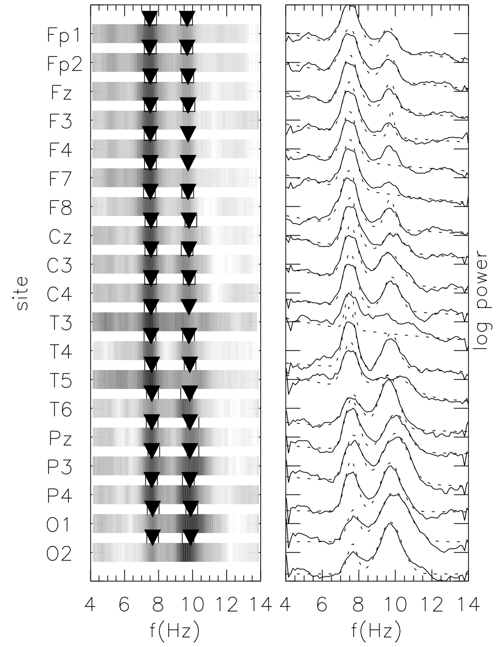

Figure 2.13: Example set of Class 2 spectra, plotted as in Fig. 2.8 with the left showing the grayscale plots and the right showing normalized power spectra.

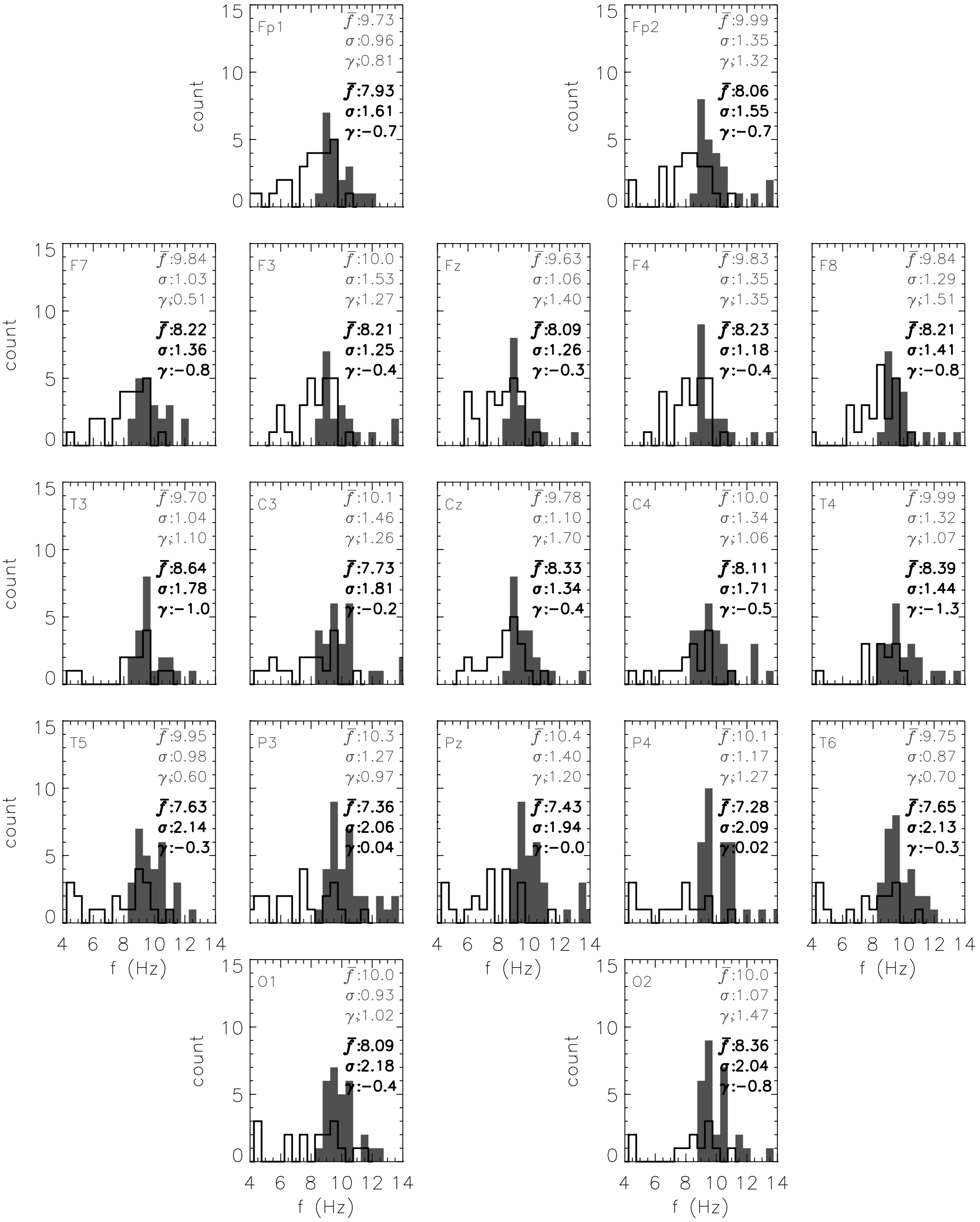

Figure 2.14: Histograms of the fitted frequencies for subjects with two robustly fitted peaks. The shaded histograms are for the clusters with higher frequency, and the outlined histograms are for the clusters with lower frequency. At the top left corner of each histogram is the name of the site, and the top right corner shows the average $\overline{f}$ in Hz, standard deviation σ in Hz, and skewness γ. The lighter colored (upper number set) indicating the figures for the higher frequency, and the darker colored (lower number set) for the lower frequency.

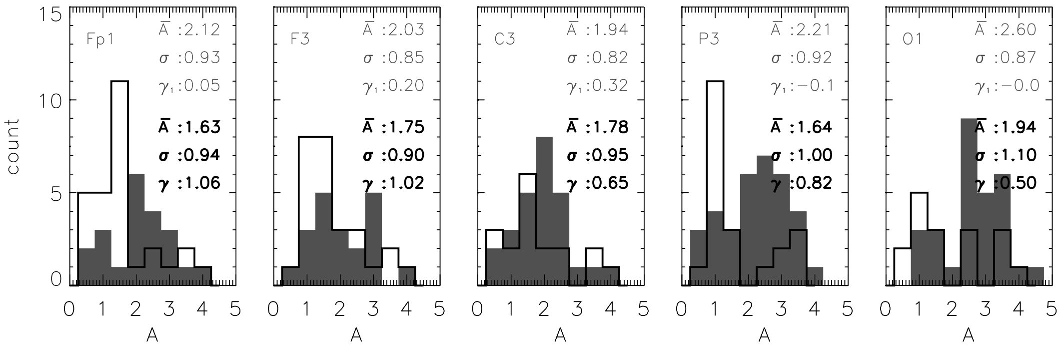

Figure 2.15: Histograms of fitted A for subjects in Class 2 at site along the sagittal slice previously defined. The shaded histograms are for the cluster with higher frequency, and the outlined histogram shows the cluster with lower frequency. At the top left corner of each histogram is the name of the site, and the top right corner shows the average $\overline{A}$, standard deviation σ, and skewness γ of the respective histograms.

for the higher average frequency and lower average frequency case, respectively.

As in Class 1, histograms of the fitted A, frequency, and Q-factor show little left-right variation, so the plots for the RFP power and Q-factor (Fig. 2.15 and 2.16, respectively) are only shown at the Fp1, F3, C3, P3, and O1 sites. The standard errors of the mean for the higher average frequency cluster are $0.20, 0.19, 0.16, 0.16$, and 0.16 and the lower average frequency cluster $0.18, 0.17, 0.21, 0.22$, and 0.27 for the respective sites. We observe that $\overline{A}$ is slightly higher at the back for both the higher and lower frequency clusters, similar to the corresponding case in Class 1.

The Q-factor histograms in Fig. 2.16, show that the resonance of the system is least sharp at about the middle of the head for the case of higher average frequency, similar to the case in Class 1. Otherwise the histograms show little trend in the average, standard deviation, or skewness vs x. The standard errors of the mean for the higher average frequency clusters are $0.28, 2.50, 0.93, 0.56$, and 0.68 and for the lower average frequency clusters are $0.77, 0.77, 1.16, 1.12$, and 2.45 for Fp1, F3, C3, P3, and O1 sites, respectively. The higher frequency cluster generally has a higher Q value, but the high variability in Q limits what we can infer from the data. The highest Q for the higher average frequency cluster are $21, 20, 26, 34$, and 29 for the Fp1, F3, C3, P3, and O1 sites, respectively, and the highest Q values for the lower average frequency cluster are $28, 27, 18, 21$, and 17, respectively.

Figure 2.17(a) shows the frequency difference between the occipital site and the frontal site ($f_O - f_F$), in the same format as in Class 1. The higher

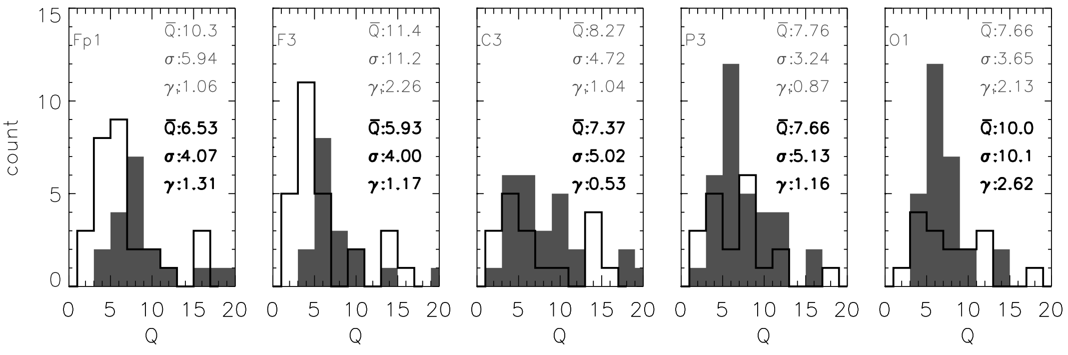

Figure 2.16: Histograms of Q-factor for subjects in Class 2 at site along the sagittal slice previously defined, Q is a dimensionless quantity. The shaded histograms are for the cluster with higher frequency, and the outlined histogram shows the cluster with lower frequency. At the top left corner of each histogram is the name of the site, and the top right corner shows the average $\overline{Q}$, standard deviation σ, and skewness γ of the respective histograms. The range is truncated at $Q = 20$ for clarity.

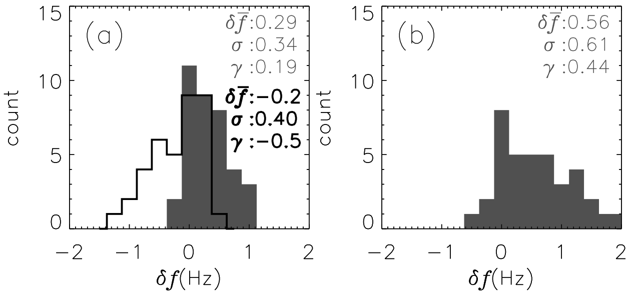

Figure 2.17: Histogram of the difference in frequency $\delta f = f_O - f_F$ between the frontal and the occipital site of the subjects with two robustly fitted peaks, where the shaded histograms indicates the cluster with higher frequency, and the outlined histogram shows the cluster with lower frequency. (b) Histogram of the difference in frequency of the extrapolated trends calculated from the highest A peaks. For both histograms the top right corner shows the mean $\overline{\delta f}$ in Hz, standard deviation σ in Hz, and the skewness γ of the respective histograms.

average frequency cluster has more cases with a positive dependence on x: $\overline{\delta f} = 0.29$, with standard error of the mean 0.06, and is right skewed ($\gamma = 0.19$). There are 30% of subjects with frontal and occipital frequency within 0.25 Hz ($|f_O - f_F| < 0.25$ Hz), 5% with the frontal frequency greater than the occipital frequency ($f_O < f_F$), and 65% having the occipital frequency greater than that of the frontal frequency ($f_O > f_F$). In contrast the lower average frequency cluster has more cases with a negative dependence on x: $\overline{\delta f} = -0.20$, with standard error of the mean 0.07, and is left skewed ($\gamma = -0.5$). There are 24% of subjects with $|f_O - f_F| < 0.25$ Hz, 49% with $f_O < f_F$, and 27% with $f_O > f_F$.

A brief comparison with commonly used methods is shown in Fig. 2.17(b). This histogram is derived from extrapolated frequencies for the front and the back of the head from selecting the peak with highest A of the two cluster and discarding the other. We can observe that it has a significantly different distribution to the corresponding cases above. It shows a significant shift with more higher frequencies towards back of the head ($\overline{\delta f} = 0.56$), standard error of the mean 0.10, and is right skewed ($\gamma = 0.44$). There are 22% of the subjects in the 0 bin, 70% with $f_O < f_F$, and 8% with $f_O > f_F$.

2.5 Summary and discussion

We have developed and verified a method of alpha peak identification that is based upon codifying the visual identification of alpha peaks and its multi-site aspects. Systematizing and automating visual estimation processes results in a method that not susceptible to visual bias. The algorithm further addresses problems listed in the Introduction on the wide inter- and intra-individual variability of the EEG by enforcing smooth spatial variation of frequency and utilizing data from multiple electrode sites. The results include sets of Robustly Fitted Peaks (RFPs), peak parameters, and a classification determined by the number of RFPs in the spectra.

The strength of this method lies in codifying visual inspection, which avoids the ambiguity of “black-box” methods utilized in some other types of analyses and provides an intuitive understanding of the algorithm and the interpretation of the subsequent results. Rather than being restricted to the narrow traditional alpha band (7-13 Hz) the algorithm explores a slightly expanded band range (4-14 Hz), since lower frequencies are needed in the examination of alpha peaks for studies in infants, children, and adolescents (Niedermeyer, 1997).

The method can cope with key difficulties mentioned in the Introduction and illustrated in previous sections: (i) peak frequency estimates are unaffected by the visual bias by the slope due to the background spectrum, as illustrated in Fig. 2.3. (ii) Information from multiple sites is used to eliminate spurious peaks and identify real peaks. The multi-site method also accommodates inherent variability of EEG across different subjects, by requiring consistency of a peak within each subject. (iii) It allows for spatial variations in alpha frequency, which can arise from two spectrally nearby frequencies as illustrated in Fig. 2.4, or as an inherent property of the alpha rhythm. (iv) Identification of more than one alpha peak within the chosen frequency range is possible. (v) Most importantly it allows for scaling to much larger sample size without the subjectivity or the labor of visual inspection.

In Sec. 3 our method was illustrated by applying it to the EEGs of 100 healthy subjects. We separated the subjects into three categories, indicated by the number of RFPs in the spectra, to ease comparison and to highlight the importance of the often-neglected secondary peak in the alpha band. The main results were: (i) 6 subjects showed no significant alpha peak (Class 0), 53 subjects showed one RFP (Class 1), and the remaining 42 subjects showed two RFP (Class 2). This highlights the importance of the identification of the secondary alpha peak, as it is present in approximately 40% of the subjects sampled, a point not previously recognized in the literature. (ii) Quantification of the frequency difference between frontal and occipital sites: trends were indistinguishable from zero in Eqs. (2.6)–(2.7), but non-zero in the stronger tests shown in Figs. 2.12 and 2.17. (iii) The predominance of higher frequency in the occipital sites compared to the frontal sites is seen in Figs. 2.12 and 2.17, confirms previous findings in the literature. (iv) In individual sites the frequency distributions have similar standard deviations and are mostly right skewed (Fig. 2.9 and the higher average frequency cluster in 2.14). (v) Generally higher amplitudes are recorded for occipital sites compared to the frontal sites (Figs. 2.10 and 2.15). (vi) For Class 1, the Q-factor histograms in Fig. 2.11 suggest the alpha resonance is weakest at the vertex of the head. Similar results are shown in the corresponding case in Class 2 (Fig. 2.16), but the high standard deviation in the results indicates a bigger sample is needed. And most significantly (vii) we note the importance of considering multiple alpha peaks, rather than restricting scoring to a single peak measure. In previous studies, if there were two peaks in the alpha range it was common practice that the alpha peak with the higher power chosen, to the exclusion of all others. Our results imply that this will yield misleading results.

In our data we found it necessary to fit at most two alpha peaks, but the program can easily be extended to encompass more peaks, as predicted in the case of large variability in the nonuniformities in a corticothalamic resonance model (Robinson et al., 2003b). This fitting algorithm can also be extended to any other rhythm, for example beta, with minimal modifications. The technique discussed in this chapter is compatible with all physiological generation mechanisms since it does not use model-based constraints. With refined sets of parameters obtained using this algorithm it may be possible to differentiate between generation mechanisms, and more accurately pinpoint any alpha frequency changes associated with changes of state.

One proviso is that the algorithm describe here mainly focuses on the anterior-to-posterior trends, as we found that these to be dominant. This reduces the sensitivity to any trends from left to right. It is possible, with little modification in the algorithm, to include more general frequency consistency/-continuity conditions, and thereby further explore the spatial topography of the alpha frequency. More detailed topographic studies and other applications of the method with better statistics will be presented in future: our aim here is chiefly to illustrate the method.

Chapter 3

Age and sex trends

3.1 Abstract

An investigation was carried out on the age trends, sex differences, and splitting of alpha peaks of the EEG spectrum in the healthy population, using an automated multi-site algorithm to parametrize the alpha rhythm in 1498 healthy subjects aged 6 to 86 years. Alpha peaks identified from multiple electrode sites were organized into clusters of similar frequencies whose sex differences and age trends were investigated. Significant age-related trends were observed for frequency, position, and amplitude of dominant alpha peaks. Occipital sites had alpha clusters of higher average frequency, higher power, and greater presence across the scalp. Frequency and power differences were found between the sexes. In particular observed increases in alpha frequency in children and decreases in the elderly were consistent with those from earlier studies. Distinct alpha rhythms were prevalent (≈45%), thus investigations which only examine the alpha frequency with the highest peak power can produce misleading results. The strong dependence of alpha frequency on age and anterior-posterior position indicates use of a fixed alpha frequency band is insufficient to capture the full characteristics of the alpha rhythm. This study allows for establishment of typical alpha rhythm parameter ranges (including power and frequency) in the healthy population, and quantifies the variation in alpha frequency across the scalp. The automated characterization enables objective evaluations of alpha band activities over large samples. These findings are potentially useful in testing theories of alpha generation, where splitting of the alpha rhythm has been theoretically predicted to occur in individuals with large differences in axon length between anterior and posterior corticothalamic loops.

3.2 Introduction

The alpha rhythm is the most prominent feature observed in the human electroencephalogram (EEG), and is strongest when the subject is in an eyes-closed relaxed state (Niedermeyer and Lopes da Silva, 2004). It is suppressed by attention or mental effort, though this attenuation varies greatly between individuals and experimental conditions (Shaw, 2003). The normal alpha rhythm varies in amplitude from one individual to another, and a small minority of people with normal brain function do not show an alpha rhythm (Niedermeyer and Lopes da Silva, 2004). An alpha-free low voltage EEG may also develop in adult life in certain clinical conditions such as Huntington's chorea (Scott et al., 1972). Activity is still present in the alpha band, but there is not necessarily a spectral peak, which is required for the identification of the alpha rhythm. The frequency of the alpha rhythm increases from approximately 3–5 Hz at birth until an adult value near 10 Hz is reached at around 20 years of age (Marshall et al., 2002), followed by a slow decrease thereafter (Dustman et al., 1999a). There are mixed reports of changes in the alpha rhythm in adulthood (Duffy et al., 1984; Niedermeyer and Lopes da Silva, 2004). However, recent studies with large sample sizes have found dominant alpha frequencies to decease with age in adults independent of pathology (Aurlien et al., 2004b; van Albada et al., 2010). Alpha rhythm is observed across the entire scalp, and there is some evidence that its frequency is anticorrelated with head size (Nunez and Srinivasan, 2006), though a recent MRI study by Valdés-Hernández et al. (2010) suggests it may instead be independent. A reduction of the alpha frequency can occur in demented patients or due to exogenous intoxication (e.g., with alcohol) (Samson-Dollfus et al., 1997). Alpha frequency systematically changes with cognitive impairment (Bengston and Schaie, 1999).

Various peaks in the alpha band have been noted in the literature. One distinction is between frontal and occipital alpha, as determined by the location where the peak is most prominent; another is between "fast" and "slow" alpha (higher and lower frequency, respectively) (Klimesch, 1999). Generally, the alpha peak frequency is lower at frontal electrodes than at occipital electrodes. Frontal-occipital frequency differences in alpha peaks can result in overlapping double peaks ("split-alpha"), which are distinguishable given a sufficiently large frequency difference. Split alpha peaks have been found to occur in the healthy population (Chiang et al., 2008; Nunez and Srinivasan, 2006), and arise naturally in a theoretical model of the generation of the alpha rhythm (Robinson et al., 2003b). Additional rhythms in the alpha band are "central alpha" or rolandic mu rhythm from the sensorimotor cortex, and tau rhythm from the auditory cortex (Niedermeyer and Lopes da Silva, 2004), which might be related to a "third" rhythm discovered by Niedermeyer (1997). As with conventional alpha, which is blocked by visual stimuli, mu and tau rhythms are blocked by movements and auditory stimuli, respectively. The "third" rhythm is blocked by cognitive activities but not consistently by auditory stimuli. Thus, a number of rhythms contribute to the traditional alpha band, each differently modulated by experimental conditions and associated with a particular region of the brain (Samson-Dollfus et al., 1997).

There have been mixed reports of sex differences of the alpha rhythm in the healthy population. Matthis et al. (1980), Díaz de León et al. (1988), Harmony et al. (1990), and Benninger et al. (1984) found significant differences between males and females. Girls were found to have a maturational lag in the increase of alpha frequency in EEG compared with boys, which disappears around adolescence (Clark et al., 2004). Some studies have suggested earlier maturation in girls (Petersén and Eeg-Olofsson, 1971), while others failed to find differences between male and female alpha frequency in EEG (Cohn et al., 1985).

In this chapter we examine sex and developmental/aging trends in the alpha rhythm over a wide range of ages, in a sample of 1498 subjects with roughly equal proportions of males and females. A relatively large number of subjects in the range 6–20 years allows detailed examination of age and sex differences during childhood and adolescence, when developmental neurological changes are rapid. The age range extends to 86 years, thus also allowing examination of the later phases of maturation and aging. Despite the concentration at young ages, the number of subjects in the older age range is significantly larger than in most comparable studies.

For processing the large number of subjects involved, we use our recent automated method for the characterization of alpha peaks (Chiang et al., 2008), which has the advantages of being objective and reproducible compared to traditional methods. The method analyzes spectra in two stages: first, spectra from individual sites are fitted; second, information is used from the first stage analysis at multiple electrodes to produce a reduced set of peak parameters that are spatially consistent across electrodes. It is specifically designed to deal with cases of multiple overlapping alpha peaks. This technique avoids visual bias, integrates spatial information, and can be scaled up to large groups of subjects.

The remainder of this chapter is organized as follows: Section 3.3 briefly outlines the data collection methods, and the algorithm used to determine alpha peak parameters; Section 3.4 describes age trends and sex differences in these parameters; and Section 3.5 discusses the implications of these findings.

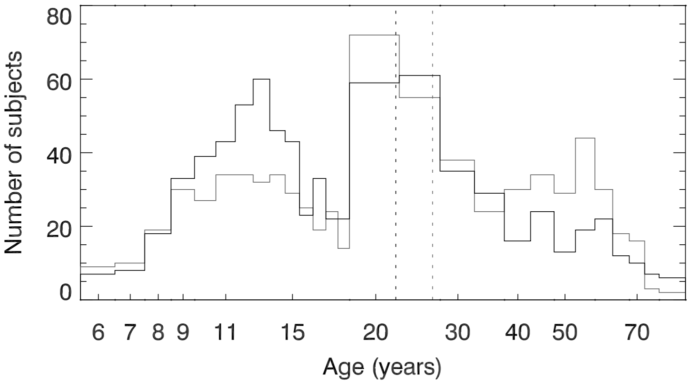

Figure 3.1: Histogram of subjects versus age, with single-year bins for ages < 20 years, 5-year bins for ages ≥ 20 and < 80, and a single bin for ages ≥ 80 years, which results in a similar number of subjects in each bin. Note the age axis is logarithmic. Female and male subjects are indicated by the gray and black lines, respectively. Mean ages are shown by the vertical dotted lines.

3.3 Methods

In this section we present details of the acquisition and processing of the data. Sections 3.3.1 and 3.3.2 describe the subject demographics and EEG collection procedure, respectively. Sections 3.3.3 and 3.3.4 illustrate the automated algorithm used to extract peak parameters from spectra. Additional details on the peak-fitting algorithm can be found in Chiang et al. (2008). Section 3.3.5 describes the statistical analysis.

3.3.1 Subjects

The EEG recordings used in this study were obtained from the BRAINnet website (www.brainnet.net), and are a subset of the Brain Resource International Database, an archive of electrophysiological and psychophysiological measures, demographics, and psychometric tests (Gordon et al., 2005). A group of 1498 subjects was used, comprising 735 females and 763 males, ranging from 6 to 86 years of age. Subjects were healthy, without any known history of brain injury, mental illness, substance abuse, psychological, psychiatric, neurological, or genetic disorders, or other medical conditions that could influence the normality of the EEG. Figure 3.1 shows the distribution of age in each sex. The large number of subjects in all age bins allows for detailed comparisons between different age and sex groups.

3.3.2 Recording procedure

Participants were seated in a sound- and light- attenuated room. An electrode cap was used to acquire data from the Fp1, Fp2, F7, F3, Fz, F4, F8, FC3, FCz, FC4, T3, C3, Cz, C4, T4, CP3, CPz, CP4, T5, P3, Pz, P4, T6, O1, Oz, and O2 electrode sites, although only the 19 standard sites in the International 10–20 system for sites were used for further analysis. Subjects were asked to rest quietly with their eyes closed for the two-minute duration of the task. Horizontal eye movements were recorded with electrodes placed 1.5 cm laterally to the outer canthus of each eye. Vertical eye movements were recorded with electrodes placed 3 mm above the middle of the left eyebrow and 1.5 cm below the middle of the left bottom eyelid. A continuous acquisition system (NuAmps), with a sampling rate of 500 Hz, was used in the collection of EEG. Skin resistance was kept below 5 kΩ and a 100 Hz low-pass filter was applied prior to digitization. All scalp EEG channels were referenced to the average of A1 and A2 (mastoids), and were corrected offline for EOG artifact using a technique based on that of Gratton et al. (1983).

The EEG time series were first divided into successive 8.192 s segments, which were mean subtracted, windowed, Fourier transformed, modulus squared, and averaged to produce one power spectrum per recording site. Deviations of the EEG in any channel by more than ±250 μV from the mean caused the segment to be rejected prior to transformation, because such extreme potentials indicate artifacts. A subject is discarded when all the segments were rejected. In our sample, EEG spectra from 42 of the 1498 subjects were discarded by this criterion, leaving 1456 subjects for analysis.

3.3.3 Peak parameters

The algorithm analyzes the power spectra for a given subject in two stages, as illustrated in Fig. 3.2. The first stage uses the parametrized spectral form:

$$\begin{aligned}\log_{10} P(f) \approx\ & E_1 \exp\left(\frac{-(f-f_1)^2}{w_1^2}\right) + E_2 \exp\left(\frac{-(f-f_2)^2}{w_2^2}\right) \\ & + G - H \log_{10} f, \end{aligned} \qquad (3.1)$$

where f is measured in Hz. In Eq. (3.1) Gaussian peaks are parametrized by amplitudes E_n, central frequencies f_n, and widths w_n, where the subscript n denotes the peak of interest. This form is numerically fitted over an expanded alpha range (4–14 Hz) of each of the experimental EEGs. The parametrized

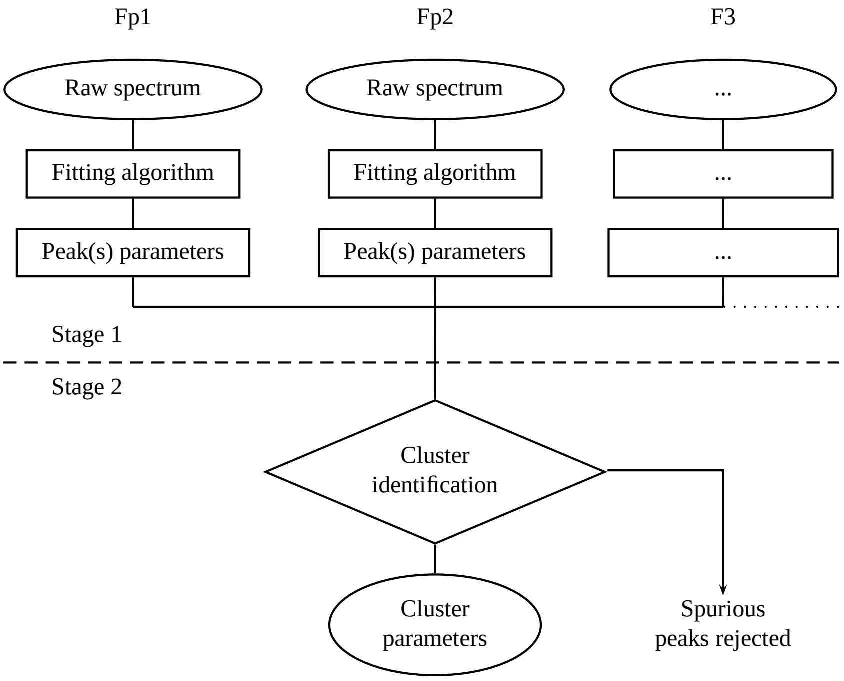

Figure 3.2: Schematic showing the stages involved in the estimation of cluster parameters. Stage 1 involves the fitting of individual sites to Eq. (3.1), and extracting the peak parameters. These parameters are collated, refined, and analyzed collectively in stage 2 to produce the cluster parameters. The final cluster parameter are what is being examined in this chapter. Further details can be found in Chiang et al. (2008).

spectrum includes a power-law background component:

$$\begin{aligned} P_{bkg}(f) &= 10^{G-H\log_{10} f}, \\ &= 10^{G} f^{-H}, \end{aligned} \qquad (3.2)$$

where 10^G is the normalization and H is the index of the power-law. The absolute amplitude L_n of the peak n is given by:

$$L_n = 10^{E_n+G-H\log_{10} f_n}, \qquad (3.3)$$

and we can define amplitude of the peak corrected for background power to be:

$$K_n = L_n - P_{bkg}(f_n). \qquad (3.4)$$

The second stage selectively collates these fits across all the sites, to rule out noise and to identify robust alpha peak “clusters”. A cluster comprises a set of spatially contiguous and spectrally similar alpha peaks. In practice either 0, 1, or 2 clusters are found to be adequate to account for observations. Advantages of this technique include avoidance of visual bias, integration of spatial information, and the ability to handle large amounts of data. Further details of the algorithm are found in Chiang et al. (2008).

Figure 3.3 illustrates the results of the fitting algorithm. Figure 3.3a shows fitted parameters associated with an individual spectrum. Note that the heights E_n are measured relative to the power-law background. Figure 3.3b indicates how clusters were identified. Seven schematic spectra from different recording sites are plotted, with one site (black line) lacking the peak at f_1, and several sites having smaller peaks that were discarded. Criteria are applied in the frequency and spatial domains to extract a small number of clusters from the set of spectral fits (Chiang et al., 2008). In practice, this results in no more than two clusters. For the case with two clusters, the clusters may or may not be spatially overlapping; i.e., spectra may or may not contain two peaks at any particular site.

3.3.4 Cluster parameters

Once identified, the main characteristics of each cluster can be compactly described by only a few parameters: frequency, position, spatial extent, and average peak power. In this section we give precise definitions for these quantities.

The frequency f of each cluster is defined as the mean frequency of its constituent peaks. The value of f may in principle fall anywhere in the range of frequencies used by the algorithm (4–14 Hz). The weighted occipitality X of a cluster is defined as a sum of the position of its constituent peaks weighted by

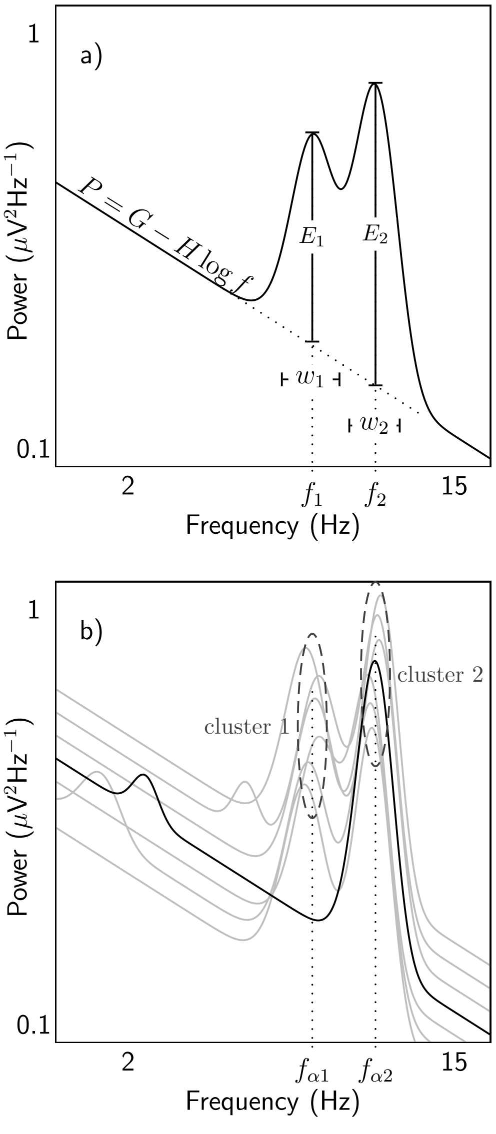

Figure 3.3: Illustration of spectral fits. Both axes are shown in logarithmic scale. (a) Schematic of the fitted values for one recording site. (b) Schematic of clustering in a spectrally consistent manner, with lines representing spectra from different sites.

their corrected amplitude K_n. The location of an electrode corresponding to the location of Fpz (in between Fp1 and Fp2) is defined as $X = 0$ and that of Oz as $X = 1$. The parameter X allows us to distinguish frontal and occipital alpha peaks, and intermediate cases where relevant. The laterality Y of a cluster is defined similarly to X, with the leftmost electrode defined to be at $Y = -0.4$ and the rightmost electrode defined to be at $Y = 0.4$, retaining the difference of 0.2 between closest adjacent electrodes as is defined for occipitality. The spatial extent s is determined as the number of sites displaying at least one peak from the cluster. The value of the cluster size s lies in the range 4–19; the lower bound arises because any cluster with a peak visible in fewer than 4 sites is not considered robust. The average peak power P is taken to be the average value of K_n [see Eq. (3.4)] within the cluster.

3.3.5 Curve fitting and statistical analysis

In this section we discuss two specific curve fitting methods that were used in this thesis. Section 3.3.5 describes the fitting of smooth asymptotically linear functions to quantify age trends. Section 3.3.5 considers the distribution of frequency differences between clusters for two-cluster cases, to which a Gaussian function is fitted.

Age trend fitting

Age trends were approximated using a functional form that was chosen based on the following observations: (i) some parameters show non-normal distributions; (ii) the median typically shows approximately linear trends at young and old ages; (iii) there was substantial variation in the age ranges over which trends were nonlinear; (iv) the transition from "development" to "aging" occurs gradually, with intermediate slopes in early adulthood; and (v) the median never showed more than one clear turning point for any of the parameters. This motivated a fitting function that is smooth, asymptotically linear, and has a second derivative of constant sign. A functional form that meets these criteria and has only a small number of parameters is given in van Albada et al. (2010):

$$y = Cx + (C - A)\tau \log\left(1 + \exp[-(x - I)/\tau]\right) + D, \tag{3.5}$$

$$I = \frac{B - D}{C - A}, \tag{3.6}$$

where x is the age, τ is a width parameter quantifying the age range over which the slope changes considerably, and A, B, C, and D are free parameters. Since fits were relatively insensitive to τ, this parameter was fixed at 3 years, which yielded good fits. Equation (3.5) represents a smooth interpolation between two

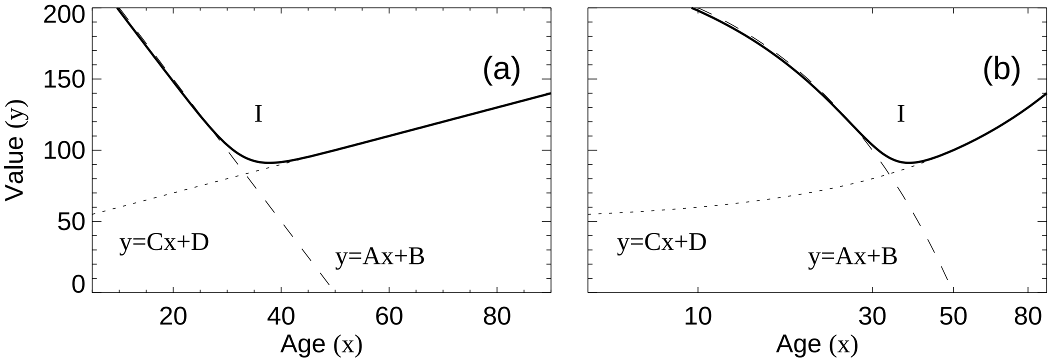

Figure 3.4: Example of the function given by Eq. (3.5) with negative A and positive C (solid line). The asymptotic linear trends $y = Ax + B$ (dashed) and $y = Cx + D$ (dotted) intersect at $x = I$. The linear graph is shown in (a), and (b) shows the age axis logarithmically for later comparisons.

straight lines, $y = Ax + B$ for $x \to -\infty$ and $y = Cx + D$ for $x \to \infty$. These lines intersect at I, the breakpoint age, which is also the point of maximum rate of change in slope for the interpolated fit. Figure 3.4 illustrates the functional form.

In order to track the median rather than the mean, fits were performed by minimizing the mean absolute difference (MAD), rather than squared deviations, between fitted and measured values. Optimization was achieved using a downhill simplex method (Nelder and Mead, 1965), with starting conditions determined by linear least-square fits to the age ranges 6–15 and 40–86 years. Confidence intervals for the variables and fits were obtained by bootstrapping with 1000 resamplings.

Gaussian fits

The distribution of alpha frequencies was well described by a Gaussian (see Sec. 3.4.1). Since the distribution obtained by subtracting the variates from two independent Gaussian distribution with arbitrary means and variances is also Gaussian, the difference Δf for double-peak cases is also expected to follow a Gaussian distribution. However, the distribution actually obtained may be different, due to cases with unresolvably small Δf being misidentified as single-peak cases. To check whether this occurred, we fitted a Gaussian to the histogram of Δf, taking into account only (positive or negative) values of Δf, for which resolvability of the two peaks was good. The difference between this theoretical Gaussian distribution and the actual distribution of Δf represents cases that theoretically have two closely spaced peaks but in practice may be classified as having a single peak. The number of such cases was compared with the actual number of single clusters found. A confidence interval for the number of cases potentially misidentified as having a single peak was obtained by bootstrapping with 1000 resamplings.

The cutoff values of Δf for the Gaussian fit were chosen based on the following considerations: (i) taking a large cutoff could leave insufficient data to produce a reliable fit, and (ii) taking a small cutoff would underestimate the number of cases incorrectly classified as having a single peak. The compromise used in this section is to take the Δf corresponding approximately to the peaks of the bimodal histogram as the cutoff values.

3.4 Results

First, we discuss the removal of outliers from the data. Second, we examine various ways of differentiating between clusters. Third, age trends of the cluster alpha parameters are presented. Finally, the cluster parameters are examined for sex differences.

3.4.1 Parameter distributions and outliers

Our algorithm examines an expanded alpha range (4–14 Hz) to accommodate the known variations of alpha frequency with age (in particular, lower alpha frequency in childhood and adolescence). In addition to the true alpha peaks, peaks may be found that are not due to alpha rhythms within this frequency range, such as the low-end beta rhythm and the theta rhythm. In this section we identify these cases and eliminate them from our subsequent analysis.

The algorithm described in Sec. 3.3.3 was applied to 1456 subjects, with 42 others rejected for having excessively noisy EEG spectra. Each of these yielded either zero, one, or two sets of cluster parameters (f, X, Y, s, and P), of which only f and X were used in outlier rejection. Figure 3.5 shows the distribution of the occipitality X of each cluster against its averaged frequency f. The majority of the clusters are grouped in a central band. Other than the central grouping we see two distinct groups of clusters: (a) a group of clusters with low f, distinct from the central band of clusters, and (b) a group of clusters with high f, which show less distinct separation from the central band. The points near the two frequency limits do not appear to follow the linear trend displayed by the central group of clusters; hence, these points probably represent outliers. We can identify the outliers by frequency cutoffs at 13 Hz and 5 Hz. After removing outliers, there were 41 subjects with no discernible clusters, 744 subjects with one cluster, and 671 subjects with two

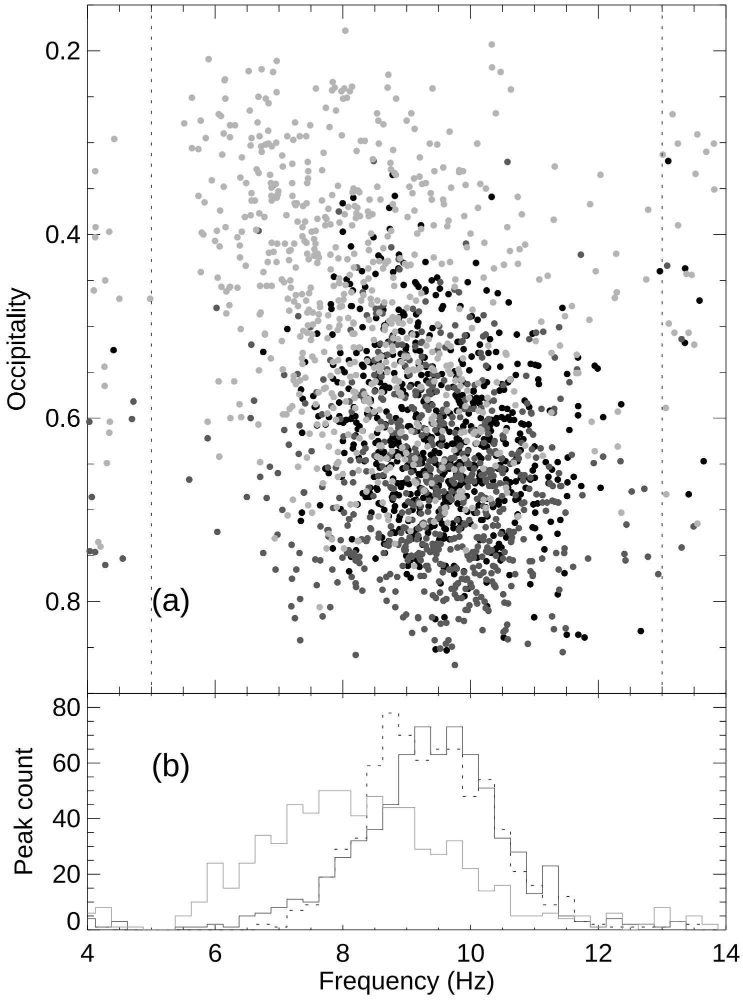

Figure 3.5: Scatter plot of alpha peak clusters in the f-X plane, with the top of the diagram indicating the front of the head. (a) Black, dark gray and light gray circles, respectively, denote one-cluster peaks, peaks of higher spatial extent from the two-cluster case, and peaks of lower spatial extent from the two-cluster case. The dotted lines show the upper and lower constant frequency cutoff. (b) Histogram of the frequency distribution of peaks. The dotted line represents one-cluster peaks, while the dark and light gray solid lines correspond to the peaks of higher and lower spatial extent from the two-cluster case, respectively.

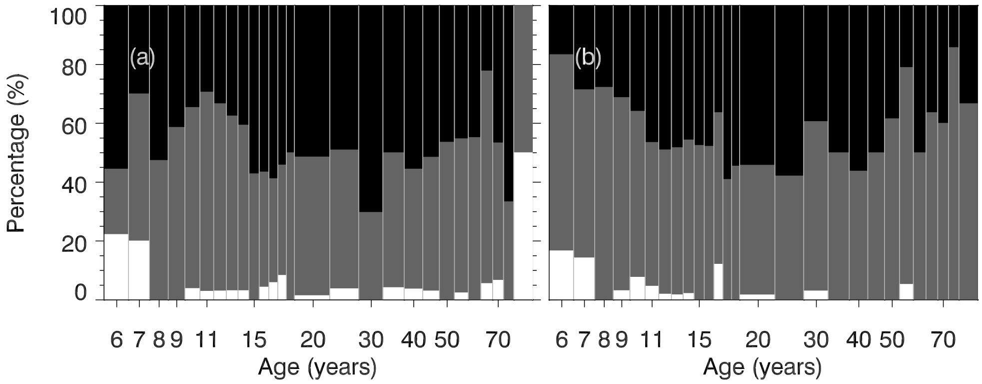

Figure 3.6: Percentage of alpha peak clusters in each age bin, as in Fig. 3.1. White corresponds to the case with no peak cluster, dark gray to the one peak cluster case, and black to two peak clusters. (a) Females. (b) Males.

clusters, as listed in Table 3.1. Figure 3.6 illustrates the distribution of clusters for male and female subjects in each age bin after the elimination of the outliers.

We can also examine the distribution of the alpha peak frequency in the two clusters. The clusters can be separated by their relative occipitality X, with higher occipitality termed the occipital cluster, and the lower occipitality termed the frontal cluster, with their associated cluster parameters. Note this defintion only relies on the relative anterio-posterior location between the clusters, not the absolute value, so the frontal cluster would be the relatively more frontally located cluster, and vice versa. Figure 3.7 the distribution between the frontal and occipital frequency is plotted. This conforms with data from the literature where the occipital cluster has a higher frequency compared to that of the frontal cluster, although a significant fraction (22%) of the points are above the line of equality ($f_F = f_O$), with the frontal frequency higher than the occipital frequency.

The difference of the power of the frontal and occipital alpha peaks is examined in Fig. 3.8. We can see the distribution of the power is skewed towards a higher occipital peak, as reported in the literature (Inouye et al., 1986), with occipital alpha dominant. However, in approximately 26% of the cases the frontal power is higher than the occipital power.

Figure 3.9 examines whether the frequency ratio and relative power of the two peaks are correlated. While there is a broad scatter, a clear positive correlation is seen. Specifically higher relative occipital frequency is correlated with a higher relative occipital power, as seen in the denser clustering of points toward the top right and bottom left corners.

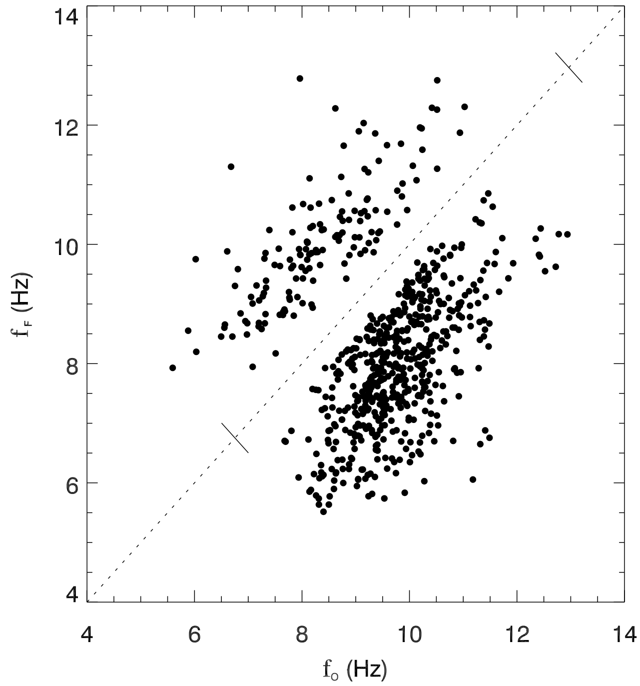

Figure 3.7: Frontal alpha frequency f_F versus occipital alpha frequency f_O in two-cluster cases. The dotted line shows $f_F = f_O$. There is the expected gap around the dotted line since peaks cannot be resolved if they are nearly the same in frequency, the marks on the dotted line indicate the upper and lower bounds of the frequencies of one-cluster cases.

Table 3.1: Breakdown of number of alpha clusters per subject after removal of outliers. N denotes subjects whose EEG was discarded prior to analysis because of excessive time-series noise.

Number of alpha clusters	Female	Male	All subjects	Percentage
N	24	18	42	2.8
0	23	18	41	2.7
1	354	390	744	49.7
2	334	337	671	44.8
Number analyzed (0+1+2)	711	745	1456	97.2
Total	735	763	1498	100.0

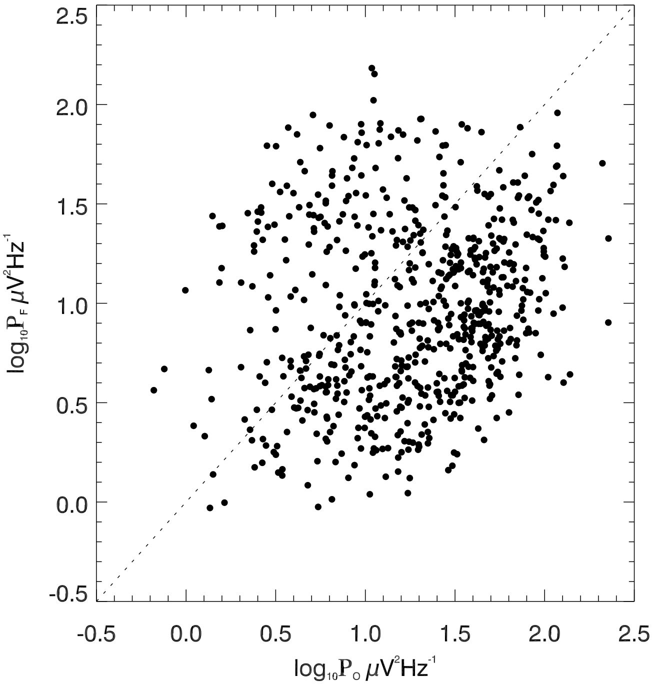

Figure 3.8: Frontal alpha power (P_F) versus occipital alpha power (P_O)in two-cluster cases. The dotted line shows $P_F = P_O$.

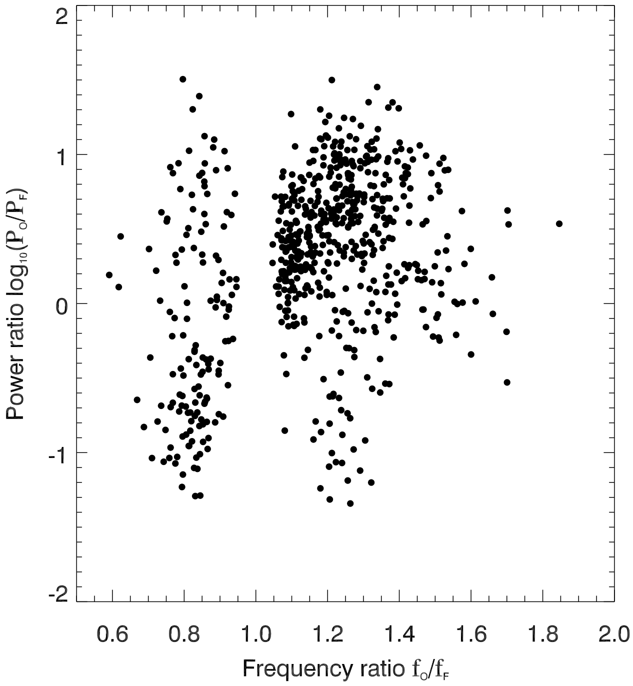

Figure 3.9: Relationship between the frequency ratio (f_O/f_F) and the power ratio (P_O/P_F). A gap at $f_O/f_F = 1$ is due to the lack of resolvability between the two peaks if the frequencies are nearly the same

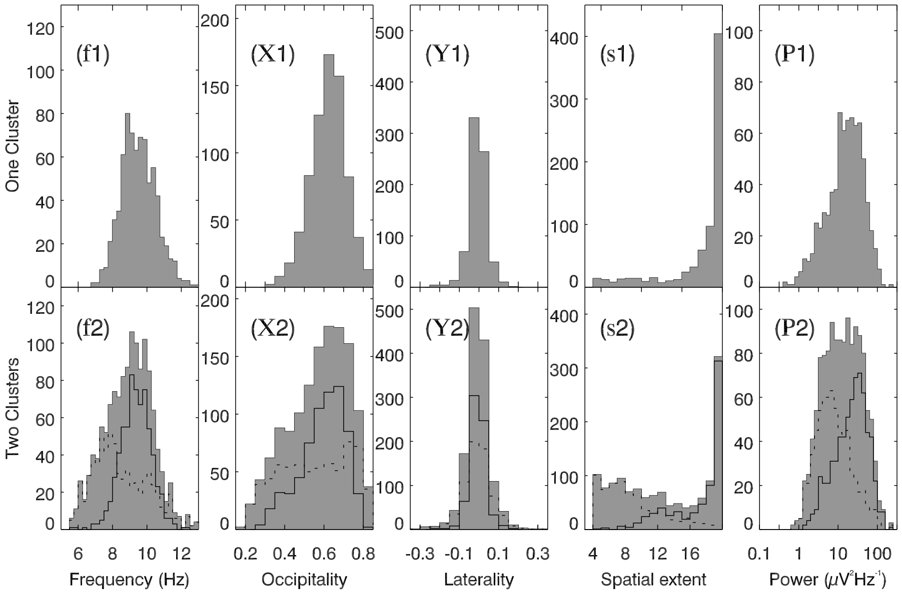

Figure 3.10: Histograms of parameters: alpha peak frequency f, cluster average occipitality X, cluster average laterality Y, spatial extent s, and cluster averaged peak power P. Results for the 744 subjects with one alpha cluster are shown in the upper row, and for the 671 subjects with two clusters are shown in the lower row. In the latter case, the 671 pairs of values are plotted as two separate histograms: one showing the distribution of values (f, X, Y, s, or P) associated with the *spatially smaller* cluster (dashed line); and one showing the distribution associated with the *spatially larger* cluster (solid line). The sum of the two histograms is also plotted (shaded).

The distributions of parameters f, X, Y, s, and P are shown in Fig. 3.10. In all three cases (one alpha cluster and both of the two alpha clusters cases) (i) X tends to be more occipital than frontal, (ii) $|Y| \ll 1$ reflects small lateral differences, and (iii) the frequency distribution is centered at approximately 10 Hz. Compared with the one-cluster cases, the two-cluster cases have (i) a greater proportion of clusters at low frequencies (left side of Fig. 3.10$f2$), (ii) a wider range of positions along the frontal-occipital axis (left and right sides of Fig. 3.10$X2$), (iii) a greater proportion of clusters extending across a small number of electrodes (left side of Fig. 3.10$s2$), and (iv) a greater proportion of clusters having smaller cluster average peak power (left side of Fig. 3.10$P2$). When the two-cluster parameter values are split into two separate distributions (where we arbitrarily choose to split by spatial extent), we find that those distributions describing the cluster of *larger* spatial extent (solid line in row 2 of Fig. 3.10) resemble the one-cluster distributions (row 1 of Fig. 3.10).

3.4.2 Cluster order

The similarity and differences between the one- and two-peak cases in Fig. 3.10 suggest that – where two peaks can be distinguished – one is approximately as in the single peak case, while the other is lower in frequency, more frontal, and smaller in extent and power. However, it is not possible to conclude this from Fig. 3.10 alone, as we cannot infer whether or not all these distinctions are correlated. The following sections thus examine the same set of values as in Fig. 3.10, but after classification by "cluster order", and with the aid of the independent variables of age and sex.

To understand better the contrasting distributions in Fig. 3.10 it helps to distinguish the members of each two-cluster pair. Member clusters can be labelled by their (a) cluster average frequency f, (b) cluster occipitality X, (c) cluster spatial extent s, or (d) cluster averaged peak power P. The laterality parameter Y has been omitted here due to left-right near-symmetry, but is explored in Section 3.4.4. We examine these alternatives below.

Differentiating clusters by their relative (a) f corresponds to separation into cases of fast and slow alpha, (b) X corresponds to separation into occipital and frontal alpha, (c) s corresponds to the dominant/secondary alpha where it is defined as the cluster seen at most/second most number of electrodes, respectively (Chiang et al., 2008), and (d) P gives an indication of the relative strengths of peaks in the clusters. Here we define the "upper" cluster to be the cluster whose differentiating parameter (i.e., f, X, s, or P) has a higher numerical value than that of the "lower" cluster.

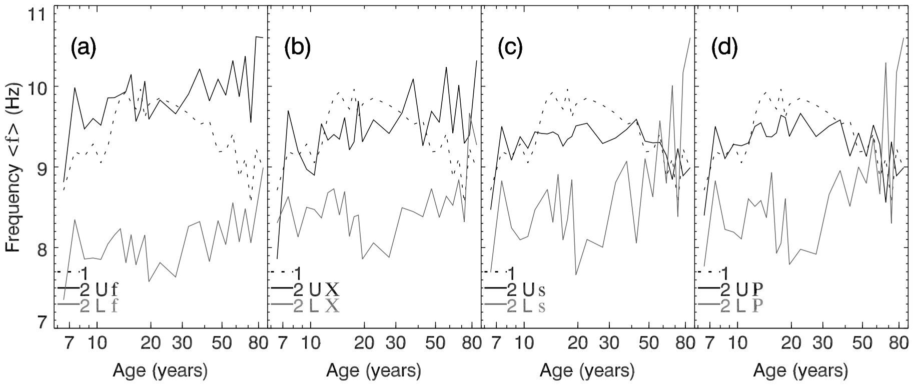

Figure 3.11: Subject cluster frequency averaged in age bins $\langle f \rangle$ versus age (with age bins as indicated in Fig. 3.1). Dotted lines denote the single alpha cluster subjects. The solid lines denote the two-cluster cases, with black the upper and gray the lower clusters. Columns correspond to the method of classification of clusters. The first column (a) shows paired clusters classified by f; in the second (b), third (c), and fourth column (d) the clusters are classified by X, s, and P, respectively. The dotted lines (cases for which only one cluster was found) in all the plots are identical. Errors are roughly uniform across the age ranges except for the extremes where the numbers of subjects are lower.

3.4.3 Age trends

Here we examine the same alpha cluster parameters as shown in Fig. 3.10, but as functions of both age and each of the four classification options described above.

Figures 3.11–3.14 show variations of alpha cluster parameters with age for each of the four ways to classify the paired clusters. To classify the trends, cluster parameters of subjects were averaged within each of the age bins; and this averaging is denoted by angled brackets, $\langle\rangle$. The single cluster trend is shown in these figures, together with both the “upper” and “lower” of the two clusters. For cases where there are two distinguishable clusters, the difference between the pair of values (f, X, s, or P) is roughly consistent in all subpanels in all four figures, which shows that to a large extent the four alternative classifications of pairs are interchangeable. Nevertheless the clearest separation of the upper and lower clusters of the two-cluster case versus any parameter occurs, by definition, when the classification of the groups are determined by the said parameter: these cases are seen in Fig. 3.11(a), Fig. 3.12(b), Fig. 3.13(c), and Fig. 3.14(d). The one-cluster cases are the same in all four frames and serve as a comparison to the two-cluster cases.

We found $\langle f \rangle$ (Fig. 3.11) to have a clear age trend. Single clusters $\langle f \rangle$ are consistent with the trend widely reported in the literature, with the alpha

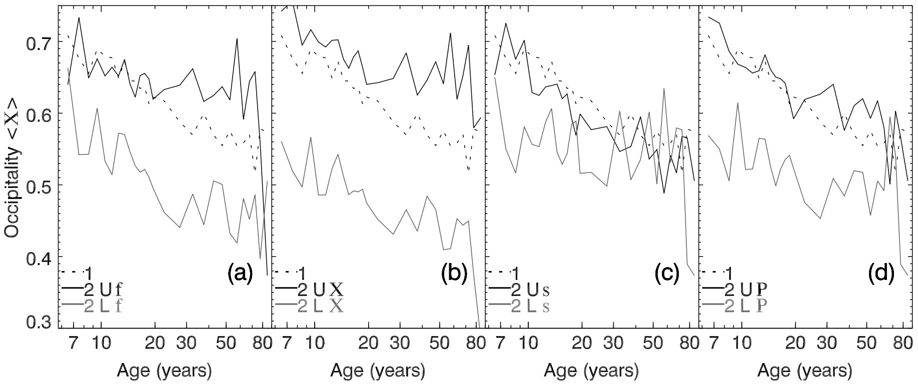

Figure 3.12: Subject cluster occipitality averaged in age bins $\langle X \rangle$ versus age presented in the same format as Fig. 3.11.

frequency increasing up to approximately age 20, and decreasing gradually during adulthood (Niedermeyer and Lopes da Silva, 2004). The single peak trends roughly match those of the upper of the two clusters: the higher-frequency member (Fig. 3.11a), the more occipital member (Fig. 3.11b), the member with greater spatial extent (Fig. 3.11c), and the member with a greater maximum peak power (Fig. 3.11d). Both lower and upper cluster frequency shown in Fig. 3.11a, and corresponding roughly to the frontal and occipital alpha respectively in Fig. 3.11b, remains relatively constant until approximately age 30 and increases slightly at older ages, contrasts clearly with the single-cluster case.

A clear age trend was also observed in mean occipitality $\langle X \rangle$. For one-cluster, and for both upper and lower peaks of the two-cluster cases, there is a consistent decrease of $\langle X \rangle$ with age, indicating that clusters become more frontal with age. This is somewhat surprising in view of age-related increases in frequencies for cases with two clusters, and the generally lower alpha frequencies at frontal sites. Figure 3.12(c) shows that there is no clear correlation between cluster size and occipitality.

The spatial extent $\langle s \rangle$ increases slightly until about age 20 years, and is constant for older ages. The upper and lower clusters are least distinct when the classification is based on X (Fig. 3.13b) again indicating that frontal and occipital clusters extend across comparable numbers of sites. When the classification is based on frequency, the separation of the upper and lower clusters is most distinct at younger ages and less clear at older ages.

The peak power $\langle P \rangle$ is high during early adolescence and declines until approximately age 20, after which the trend levels off for the one-cluster case. The downward trend is persistent in adulthood for both upper and lower two-cluster cases. The separation of the upper and lower clusters in the two-cluster

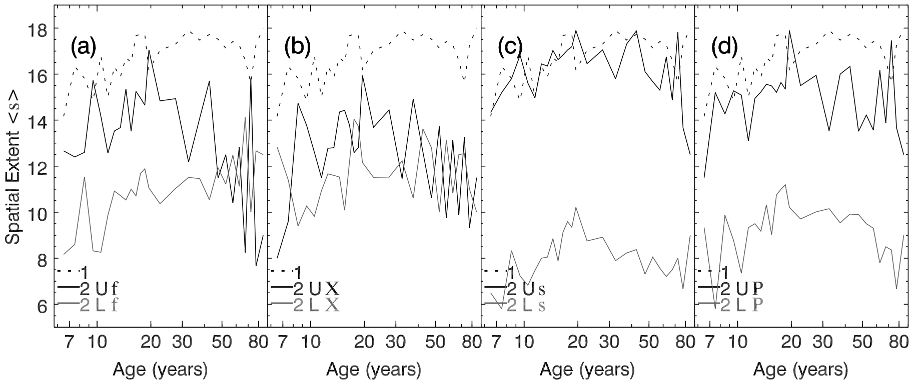

Figure 3.13: Subject cluster spatial extent averaged in age bins $\langle s \rangle$ versus age presented in the same format as Fig. 3.11.

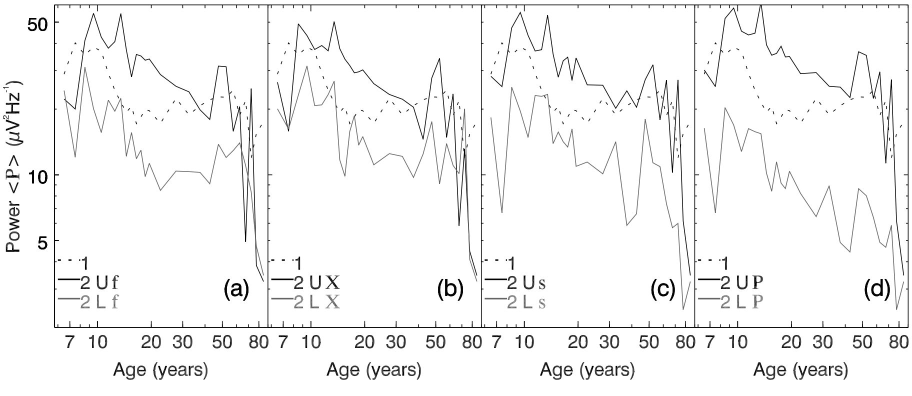

Figure 3.14: Subject cluster power averaged in age bins $\langle P \rangle$ versus age presented in the same format as Fig. 3.11.

Table 3.2: Results of fitting Eq. (3.5) to the age trends and median absolute deviation of the one-cluster case. Parameters A and C, and B and D, are the slopes and intercepts pre and post breakpoint age (I), respectively. Slopes that significantly deviate from zero at the 5% level are highlighted in bold. Parameters are in their respective units (Hz for f, dimensionless for X, Y, s, and $\mu\mathrm{V}^2\mathrm{Hz}^{-1}$ for P.)

		A (yrs^{-1})	B	C (yrs^{-1})	D	I (yrs)
all subjects	f	$\mathbf{0.15\pm0.05}$	8.0 ± 0.4	$\mathbf{-0.020\pm0.004}$	10.3 ± 0.2	14 ± 2
	X	$\mathbf{-(5\pm1)\times10^{-3}}$	0.74 ± 0.02	$-(2\pm6)\times10^{-4}$	0.58 ± 0.04	29 ± 7
	Y	$(3\pm4)\times10^{-3}$	-0.03 ± 0.03	$(0\pm2)\times10^{-5}$	$(0\pm9)\times10^{-4}$	10 ± 6
	s	0.2 ± 0.2	16 ± 2	$-(2\pm9)\times10^{-3}$	19.1 ± 0.3	13 ± 8
	$\log P$	$\mathbf{-0.08\pm0.03}$	2.1 ± 0.2	$(0\pm1)\times10^{-4}$	1.13 ± 0.07	12 ± 3
female	f	$\mathbf{0.18\pm0.07}$	7.6 ± 0.7	$\mathbf{-0.023\pm0.005}$	10.4 ± 0.2	14 ± 2
	X	$-(2\pm3)\times10^{-3}$	0.69 ± 0.05	$-(2.0\pm0.6)\times10^{-3}$	0.67 ± 0.03	10 ± 30
	Y	$(3\pm5)\times10^{-3}$	-0.02 ± 0.03	$(0\pm4)\times10^{-6}$	$(0\pm2)\times10^{-3}$	10 ± 10
	s	0.4 ± 0.4	14 ± 3	$-(4\pm9)\times10^{-3}$	19.1 ± 0.3	13 ± 4
	$\log P$	$\mathbf{-0.10\pm0.04}$	1.8 ± 0.4	$-(2\pm2)\times10^{-3}$	1.26 ± 0.08	6 ± 5
male	f	$\mathbf{0.15\pm0.07}$	8.1 ± 0.4	-0.014 ± 0.009	10.1 ± 0.3	12 ± 4
	X	$\mathbf{-(6\pm1)\times10^{-3}}$	0.74 ± 0.02	$(1.3\pm0.9)\times10^{-3}$	0.48 ± 0.07	38 ± 7
	Y	$(3\pm3)\times10^{-3}$	-0.04 ± 0.03	$(0\pm2)\times10^{-5}$	$(0\pm9)\times10^{-4}$	12 ± 8
	s	$(0\pm2)\times10^{-3}$	19 ± 2	$(0\pm1)\times10^{-3}$	18.9 ± 0.6	80 ± 30
	$\log P$	$\mathbf{-0.06\pm0.02}$	2.1 ± 0.2	$(3\pm3)\times10^{-3}$	0.9 ± 0.2	18 ± 4

case is quite clear for all the parameters, as seen in Fig. 3.14.

In Figs. 3.11–3.14, for the two-cluster cases, the value of the variable plotted for the upper cluster is higher on average than that for the lower cluster. This shows that all four discriminating factors are correlated; i.e., the second peak has lower frequency, is more frontally located, has a smaller spatial extent, and has less power.

3.4.4 Sex differences

This section examines parameter differences between males and females. We first look at the one-cluster case, since it shows the strongest age trends. Second, we examine two-cluster cases classified according to occipitality X to enable a comparison between frontal and occipital alpha peaks. Finally we examine differences in laterality Y.

One-cluster cases

Figure 3.15 shows the one-cluster age trends obtained by fitting functions of the form (3.5) for males and females. Table 3.2 lists the corresponding slopes (A and C), intercepts (B and D), and the breakpoint ages (I). The overall

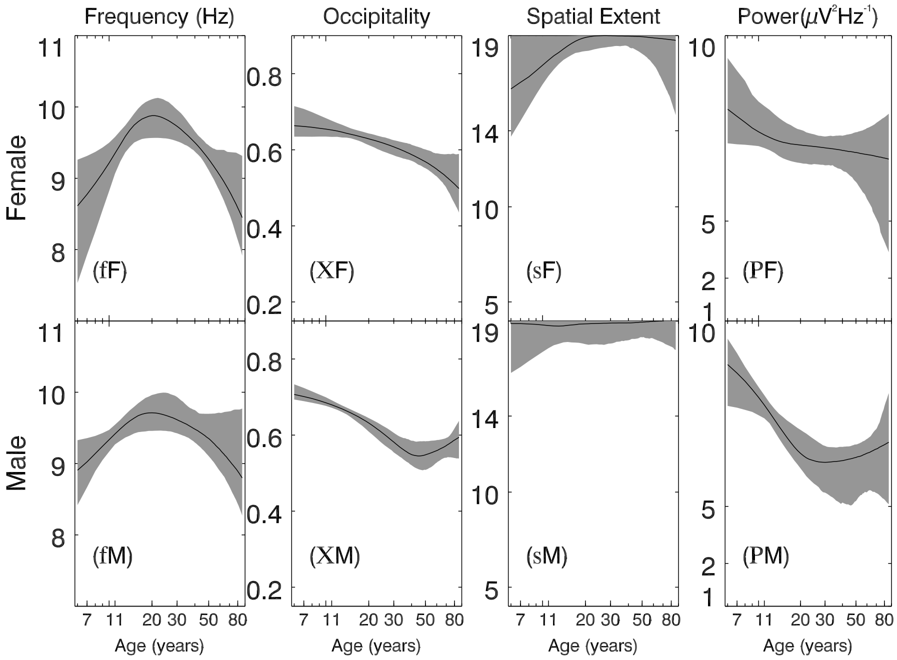

Figure 3.15: Fits of the function given in Eq. (3.5) to the single-cluster parameters (f) frequency, (X) occipitality, (s) spatial extent, and (P) average peak power. The gray patches represent 95% confidence intervals for the fits, and the solid lines indicate the median of the fit, both obtained by bootstrapping. Note for column (c) the maximum extent is strictly bounded by 19, which is the maximum number of electrodes examined.

trends are quite similar for males and females, with the fitted values A, B, C, and D of Table 3.2 for male and female all within error bounds of the fitting.

For f, there was a significant increase with age during development, apparent in both females and males. The subsequent decrease was clearest in females. We can see in the median fit values in Figs. 3.15f that females have a lower alpha frequency compared to that of the male prior to around age 16 (which is approximately the breakpoint age). The trend is reversed with a higher alpha frequency for females compared to males until approximately the age of 40, and reverts back to a males having a higher frequency after that age.

X continues to become more frontal throughout the age range in females, whereas in males it moves more occipitally from about age 40 years onward. Only the male negative asymptotic slope prior to the breakpoint age reached significance (see Figs. 3.15X and Table 3.2).

For s (Figs. 3.15s) females have stronger age trends than males, however both curves are close to the upper bound of 19 electrode sites. This indicates that, if a single cluster is present, it generally extends across all electrodes examined.

Finally, P decreases to a lower level in males than in females in early adulthood, with both males and females showing a significant negative slope prior to the breakpoint age (Figs. 3.15P and Table 3.2). Note that the slopes of P are fitted on a logarithmic scale because of the big variations in P.

Two-cluster cases

Since a clearly superior choice of the cluster ordering did not present itself, we examine ordering of two-clusters only by occipitality. Figures 3.16 and 3.17 illustrate the two-cluster fits with uncertainties, where clusters were ordered according to their occipitality X. Hence the upper and lower clusters correspond to the occipital and frontal cluster, respectively. The parameters of the corresponding fits are listed in Table 3.3.

As noted in Sec. 3.4.1 for males and females combined, for the parameter f neither of the two clusters (Figs. 3.16f and 3.17f) shows the clear frequency reduction in adults that is apparent in the single-cluster cases (Figs. 3.15f). Rather, both frequencies increase over almost the whole age range. Table 3.3 shows that the positive asymptotic slope for the upper cluster reached significance only when both sexes were combined prior to the breakpoint age. No slopes for f reached significance post breakpoint age.

For X we observed that for the occipital (upper) cluster (Figs. 3.16X) becomes more frontal until approximately the breakpoint age (≈ 20) and remains stable afterwards in both sexes. Frontal (lower) clusters (Figs. 3.17XM and 3.17XF, for males and females, respectively), occipitality levels off in males after age 40 years, but continue to become more frontal in females. Only the

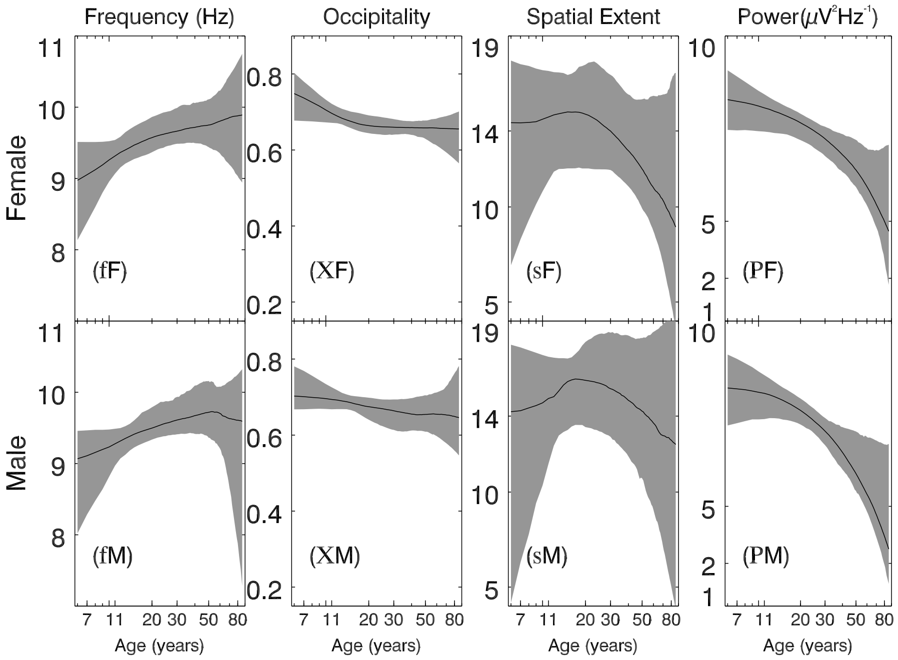

Figure 3.16: Fits of the upper X-ordered (occipital) cluster of two-cluster parameters presented in the same format as Fig. 3.15.

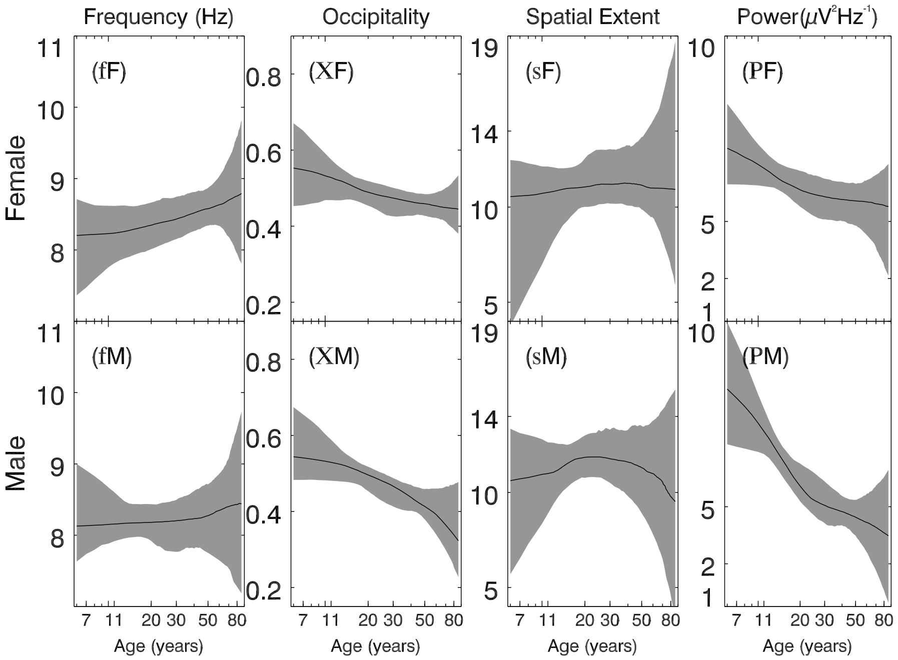

Figure 3.17: Fits of the lower X-ordered (frontal) cluster of two-cluster parameters presented in the same format as Fig. 3.15.

Table 3.3: Parameters ($A-D$ and I) and median absolute deviations of age trends of the function given in Eq. (3.5) for two-cluster cases. Clusters were ordered according to occipitality, so that 'upper' refers to occipital clusters, and 'lower' to frontal ones. Breakpoint ages (I) outside the age range examined (6–86 years), and the associated slope parameters are omitted. Slopes that significantly deviate from zero in the 95% confidence interval are highlighted in bold. Parameters are in their respective units (Hz for f, dimensionless for X, Y, s, and $\mu\mathrm{V}^2\mathrm{Hz}^{-1}$ for P).

			A (yrs^{-1})	B	C (yrs^{-1})	D	I (yrs)
all subjects	upper	f	$\mathbf{0.10\pm0.08}$	8.3 ± 0.8	$(0\pm6)\times10^{-4}$	9.6 ± 0.2	13 ± 5
		X	$\mathbf{-(8\pm4)\times10^{-3}}$	0.79 ± 0.05	$(0\pm5)\times10^{-6}$	0.66 ± 0.03	16 ± 4
		Y	$(0\pm2)\times10^{-4}$	$(0\pm2)\times10^{-3}$	$(0\pm3)\times10^{-5}$	$-(1\pm9)\times10^{-3}$	10 ± 20
		s	0.2 ± 0.4	15 ± 8	-0.07 ± 0.08	16 ± 2	10 ± 20
		$\log P$	–	–	$\mathbf{-0.012\pm0.002}$	1.64 ± 0.06	–
	lower	f	–	–	$(6\pm6)\times10^{-3}$	8.1 ± 0.2	–
		X	$-(2\pm8)\times10^{-3}$	0.64 ± 0.09	$-(1\pm1)\times10^{-3}$	0.50 ± 0.06	20 ± 30
		Y	$(0\pm3)\times10^{-4}$	-0.01 ± 0.02	$(0\pm2)\times10^{-7}$	-0.02 ± 0.01	70 ± 10
		s	0.2 ± 0.3	8 ± 4	-0.03 ± 0.04	13 ± 2	16 ± 9
		$\log P$	$\mathbf{-0.04\pm0.02}$	1.6 ± 0.2	$-(2\pm4)\times10^{-3}$	0.9 ± 0.2	19 ± 6
female	upper	f	0.10 ± 0.09	8.5 ± 0.9	$(3\pm9)\times10^{-3}$	9.6 ± 0.3	11 ± 7
		X	$\mathbf{-0.015\pm0.007}$	0.82 ± 0.07	$-(1\pm4)\times10^{-4}$	0.67 ± 0.02	11 ± 4
		Y	–	–	$(0\pm3)\times10^{-5}$	$-(1\pm9)\times10^{-3}$	–
		s	0.2 ± 0.4	15 ± 7	-0.08 ± 0.09	16 ± 3	10 ± 20
		$\log P$	-0.01 ± 0.01	1.6 ± 0.2	-0.011 ± 0.004	1.6 ± 0.2	10 ± 30
	lower	f	0.02 ± 0.06	8 ± 1	$(6\pm9)\times10^{-3}$	8.3 ± 0.4	10 ± 30
		X	$-(6\pm7)\times10^{-3}$	0.6 ± 0.1	$-(3\pm1)\times10^{-4}$	0.48 ± 0.05	20 ± 10
		Y	$(0\pm5)\times10^{-4}$	$(0\pm3)\times10^{-3}$	$(0\pm3)\times10^{-5}$	-0.02 ± 0.01	10 ± 10
		s	$(0\pm3)\times10^{-3}$	9 ± 4	$(0\pm5)\times10^{-3}$	11 ± 2	10 ± 20
		$\log P$	-0.03 ± 0.03	1.4 ± 0.4	$-(1\pm4)\times10^{-3}$	0.9 ± 0.2	17 ± 9
male	upper	f	0.04 ± 0.05	8.8 ± 0.6	$(0\pm2)\times10^{-3}$	9.9 ± 0.9	20 ± 20
		X	$(0\pm5)\times10^{-4}$	0.76 ± 0.09	$(0\pm1)\times10^{-4}$	0.68 ± 0.06	20 ± 40
		Y	$(0\pm3)\times10^{-4}$	0.01 ± 0.03	$(2\pm6)\times10^{-4}$	$(0\pm2)\times10^{-3}$	10 ± 20
		s	0.2 ± 0.4	13 ± 6	-0.02 ± 0.1	17 ± 3	20 ± 30
		$\log P$	–	–	$\mathbf{-0.015\pm0.003}$	1.7 ± 0.1	–
	lower	f	–	–	$(3\pm7)\times10^{-3}$	8.1 ± 0.2	–
		X	–	–	$-(3\pm1)\times10^{-3}$	0.55 ± 0.04	–
		Y	$(2\pm5)\times10^{-3}$	-0.02 ± 0.03	$(0\pm3)\times10^{-5}$	-0.01 ± 0.01	80 ± 10
		s	0.2 ± 0.3	10 ± 4	-0.05 ± 0.08	13 ± 3	20 ± 10
		$\log P$	$\mathbf{-0.06\pm0.03}$	1.9 ± 0.4	$-(3\pm5)\times10^{-3}$	0.8 ± 0.2	18 ± 5

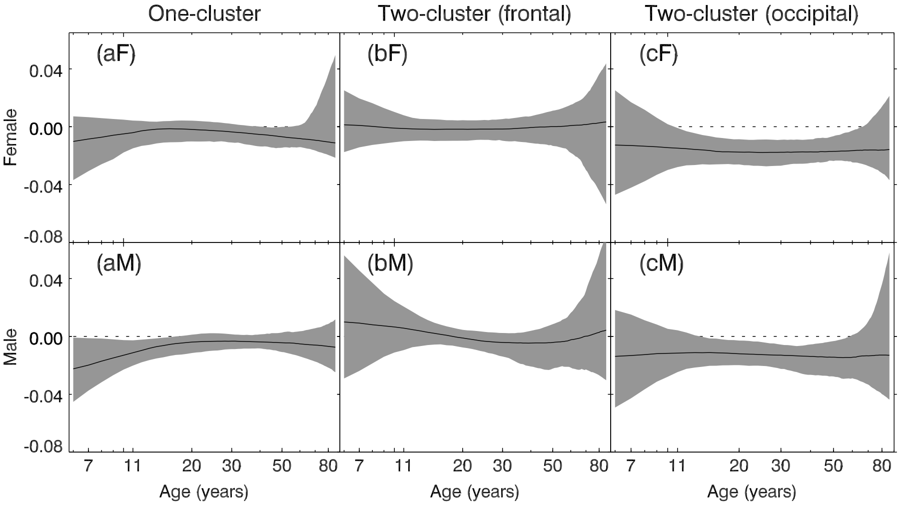

Figure 3.18: Changes of laterality Y across age in the same format as Fig. 3.15, (a) one-cluster case, (b) occipital cluster, and (c) frontal cluster. Positive laterality Y indicates a cluster is right-dominated, where as negative Y indicates a cluster is left-dominated. The zero-line has been indicated

slope for the upper (occipital) cluster in females prior to the breakpoint age reached significance (Table 3.3).

Figures 3.16*s* and 3.17*s* show the changes in spatial extent for occipital and frontal clusters, respectively. For both sexes the occipital cluster appears to become smaller after age 20, whereas the frontal cluster remains relatively stable throughout the age range. However, none of the asymptotic slopes for this parameter reached significance.

Average peak power P of the frontal cluster (Figs. 3.17P) is similar to that in the one-cluster case in both sexes, with males having higher power prior to adolescence, and showing a clearer breakpoint than females. A consistent reduction in average peak power P for both sexes in the occipital cluster is apparent in Figs. 3.16P.

Lateral differences

The laterality values are small, as seen in Fig. 3.10. The parameters of the fitted age trends are listed in Tables 3.2 and 3.3. Figure 3.18aM shows for one-cluster case in males the laterality changes from left dominance (negative Y) at young ages to left-right balance ($Y = 0$) at age 20 years and over, whereas in females (Fig. 3.18aF) the left dominance at young age is much smaller than that of males ($Y \simeq -0.01$). This trend is not clearly seen in either of the

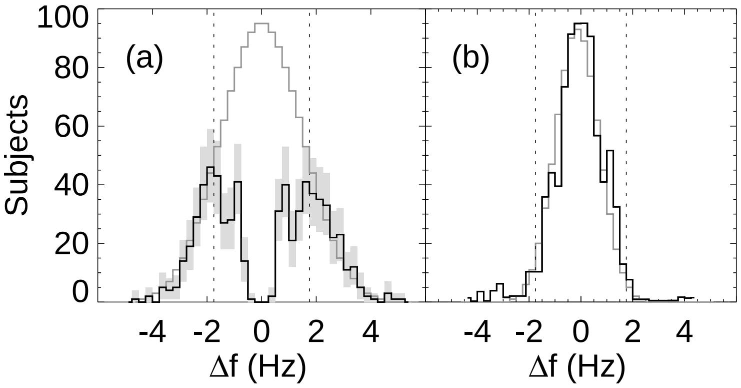

Figure 3.19: Analysis of Δf ordered by laterality (Y). Shown black in (a) distribution of Δf, and (b) residue between fitted and theoretical Δf distribution. Gray plot shows in (a) the fitted Δf distribution omitting the region of ambiguity, and (b) Gaussian fitting of the residue plot. The shaded regions in (a) are the 95% confidence interval obtained by bootstrapping with 1000 iterations. The dotted lines in both plots indicate the $|\Delta f|$ above which peaks were deemed to have good resolvability.

two-cluster cases (Figs. 3.18b and Figs. 3.18c). Figures 3.18c show that the frontal cluster is generally left hemisphere dominated, with the 95% confidence interval below zero between the ages of 16 to 60 for both sexes. The deviation is small however: The value of -0.02 seen in females corresponds to a lateral deviation of only about 0.8 cm.

3.4.5 Are single peaks unresolved double peaks?

In a further analysis of the cluster parameters, subjects with only one alpha cluster are compared to those with two distinguishable clusters. This is motivated by the possibility that the distinction between these two group is artificial; i.e., that all subjects have two peaks, and the one-cluster subjects are simply those with unresolved double peaks. This hypothesis is suggested both by parsimony, and by the fact that if a frontal and an occipital cluster have a small enough frequency difference, it is likely that they will be unresolved and thus conflated into one. We explore this idea here by considering the distribution of f_{single} from the one cluster group, and the distribution of $\Delta f = f_{upper} - f_{lower}$ (where f_{upper} and f_{lower} are the frequency of the upper and lower two-clusters, respectively) from the two cluster group, where the clusters were ordered by laterality Y. Due to the large degree of left-right symmetry of clusters, this ordering leads to a nearly symmetrical distribution of Δf, simplifying the fitting of the Gaussian.

The key idea is that the distribution of Δf for two-cluster cases (Fig. 3.19a) may be attributable to a simple unimodal distribution, which has a deficit around $\Delta f = 0$ due to those cases being having classified as only one cluster. If this is so, the area of the deficit should equal the number of one-cluster cases. The histogram of Δf is shown in Fig. 3.19(a), with a Gaussian fitted to the wings ($|\Delta f| > 1.75$ Hz), and Fig. 3.19(b) shows this residue with a Gaussian fit. The 95% confidence interval for the residue is [586,1078], obtained from fitting a Gaussian to each bootstrap sample and taking the residue. This is consistent with the number of one-cluster cases (671).

3.5 Discussion

We have examined the alpha spectral peak parameters of a large dataset of healthy subjects of both sexes using a recently developed automated method for peak identification and parametrization (Chiang et al., 2008), which groups alpha peaks at different electrodes according to their spectral similarities. This enabled information from multiple electrodes to be rendered in a manageable format. Parameters extracted for each cluster of alpha peaks were frequency f, occipitality X, laterality Y, spatial extent s, and power P. The variations of these parameters with respect to position, age, and sex are explored.

The main findings of this chapter are:

(i) We reproduced several classical results (Niedermeyer and Lopes da Silva, 2004): First the alpha peak is present in most subjects, with only 2.7% of the subjects exhibiting no discernible alpha peak as shown in Table 3.1. Second, the dominant alpha peak as a cluster average is located in the occipital region of the head (Fig. 3.10b); the apparent offset in occipitality is due to the cluster averaging. Third, if a fronto-central alpha peak is present it is generally weaker and has a lower frequency than that of the occipital peak. Fourth, alpha peak frequency changes with age, rising until the teenage years, then slowly declining.

(ii) Multiple alpha peaks are a common feature of spectra and need to be considered in the quantification of the alpha rhythm, with about 45% of subjects exhibiting two discernible alpha peaks. Double alpha peaks not only occur in the obvious case where there exist two clearly distinguishable peaks at a certain sites, but also when distinct frequencies are spatially distinct (Chiang et al., 2008). Our automated algorithm addresses cases with multiple alpha peaks, either at single electrodes, or across sites. A difficulty encountered specific to the multiple peaks was how to distinguish the grouping of peaks. We presented a variety of ways to distinguish the two clusters but no uniquely superior solution presented itself. Hence, ordering of the two-cluster cases by their relative occipitality was employed.

(iii) We observed relationships between the alpha frequency f with the position X of the peak, with lower frequency associated with lower X (i.e., more frontal). Alpha peaks were found to shift to more frontal positions with age. This frontal shifting of the alpha peak could indicate two things: increasing power from frontal sites, or decreasing power from occipital sites. The decrease of average power P with age indicates the latter is the more probable conclusion. This further suggests that both frontal and occipital components increase in frequency with age, that their relative weights shifting from the higher frequency components to the lower frequency components. For the double cluster cases there are greater changes in the frequency, between the old and the young, at the occipital peak than at the frontal peak.

(iv) Alpha cluster parameters change with age, often with different slopes before and after adolescence. We examined age trends of alpha parameters, extracted frequency $\langle f \rangle$, occipitality $\langle X \rangle$, laterality $\langle Y \rangle$, spatial extent $\langle s \rangle$, and averaged power $\langle P \rangle$, and found that most of these parameters varied significantly with age. The frequency and power variations with age are consistent with documented results (Niedermeyer and Lopes da Silva, 2004). In addition we found a slight dominance of the left hemisphere for all the alpha cluster (single cluster, frontal and occipital cluster in the two cluster cases). A breakpoint age was established where the trends in the alpha frequency and the cluster position versus age change, with a typical value from 10–20 years of age.

(v) Figure 3.15f shows males having higher peak frequencies prior to age ≈ 16 years in one-cluster cases, which is consistent with findings in van Albada et al. (2010) where females had a lower alpha frequency on average. Power trends also differ between male and females: Fig. 3.15P shows a larger decrease in males compared with females until age 20 and a small increase until the end of the age range, whereas the females have a smaller and consistent decrease in power through with respect to age. A similar trend can also been seen in Fig. 3.17P with males having a larger decrease in power compared with females.

(vi) The one-cluster case almost always lies between that of the upper and lower two-cluster cases in Figs. 3.11–3.14 (except in the spatial extent of the single cluster case, where the presence of the cluster is visible on almost all the electrodes examined). Figures 3.11–3.14 indicate that frontal and occipital clusters evolve in parallel, so they provide no evidence for separate frontal and occipital alpha generators, a mechanism sometimes postulated for alpha generation. Whilst separate frontal and occipital generators are not totally ruled out, they would have to be affected by aging processes in the same way to account for the observations, which is unlikely. The stronger decrease in the power of the occipital cluster in two-cluster case with age, together with the trend of increase frontality both provide evidence for the hypothesis of one-cluster being a combination of two-clusters. Indeed, detailed analysis of the frequency difference Δf between the clusters in the two-cluster case shows that the one-cluster cases are consistent with being double peaks that cannot be resolved. Age trends for the one-cluster case and the higher cluster in the two-cluster cases are similar, relationships between the higher and lower clusters in the two-cluster cases also consistent with the hypothesis that the one-cluster case is the result of two sources that cannot be resolved.

Several overall conclusions can be drawn from this chapter. First, the automated algorithm is valuable in processing large group of subjects, and produces an easily interpreted parameterization of alpha distribution on the scalp. Second, electrode choice in single electrode studies needs to consider the variations in alpha rhythm frequency with both the electrode position and age. Most importantly, consideration of multiple peaks in the alpha rhythm is essential, given that multiple peaks had been observed in almost half the subjects. Additionally, single peaks may simply be multiple peaks with frequencies too close to be resolved.

This chapter suggest several avenues to pursue in future research: (a) extension of the algorithm on a larger set of electrodes would yield higher quality cluster data for individual subjects. (b) The spatial aspects of the alpha peak are only examined briefly in this chapter; a more thorough analysis between electrodes would enable detailed analysis of variations across the scalp. (c) The present method could complement low resolution brain electromagnetic tomography (LORETA) by functioning as a peak identification and quantification preprocessing stage. (d) Since several common disorders show alterations of alpha activity, including ADHD (alpha asymmetry) and Alzheimer's disease (alpha slowing), a comparison of alpha peak parameters in healthy subjects versus these patient groups is likely to yield clinically important results.

Chapter 4

Conclusions and future directions

The motivation for this thesis was to seek an objective and automated method for quantification of the alpha rhythm. Over the course of this work such a method was developed, tested, and applied to a large scale database. This enabled the construction of a large, reliable, and consistent data set to quantify alpha rhythm in individuals, probe demographical variations with the alpha rhythm, and constrain theories of alpha generation.

4.1 Alpha quantification method

The method developed was summarized in Ch. 2. An algorithm was utilized to overcome a variety of difficulties: the large variability of EEG between individuals even under controlled experimental conditions, high levels of noise in the EEG spectrum, avoidance of visual bias and potential distortions due to a strong background, and spatial topography of alpha peaks in which there are two clusters of peaks across the head but only a single peak in many or all electrodes. In comparison, traditional methods of alpha rhythm analysis through visual inspection of time series are at least partially subjective and idiosyncratic, not to mention extremely laborious.

The algorithm developed employs a two-stage approach:

(i) in the first stage, EEG spectra from all electrodes are individually fitted with a nonlinear fitting algorithm allowing for up to two Gaussian peaks within an expanded alpha range (4-14 Hz), as well as a background power-law trend. The background spectrum is the spectrum in the absence of the alpha peaks. An expanded alpha range was used because of the known variation of the alpha frequency with age, where younger subjects exhibit alpha activities at lower frequency than the classical adult alpha range, as well as allowing for individual variations and permitting better estimation of the background. This fitting also allowed us to evaluated a measure for noise, the difference between the fitted and the experimental spectrum.

(ii) In the second stage, data from all the electrodes are collated, with a focus on the peaks. Peaks with amplitudes below that of the noise level calculated are removed from the analysis, with the remaining peak clusters into groups of spectral similarities. Spatial restrictions are applied to the peaks, where peaks are required to at least span four electrode sites, and present in no less than two different anterio-posterior location, to further removal spurious peaks. The final outcome was that subjects were placed in one of three clusters: (a) no clear and consistent alpha peak, (b) one clear and consistent alpha peak, or (c) two clear and consistent alpha peaks.

Several characteristics of these consistent, or "robust" alpha peak(s) were next extracted to allow for improved quantification. The traditional measures such as frequencies and amplitudes of the alpha peaks were determined, as well as extra parameters of the spatial extent and location of the cluster, and on the background trends. These measurements enabled objective comparisons of alpha activity between electrodes and across subjects.

4.2 Major findings

Firstly, classical trends of changes in the alpha frequency with respect to age were reproduced: (i) the low alpha frequency in young children, rising frequency during adolescence, leveling off during adulthood, and a slight decline in old age, (ii) the decline of alpha power with age, and (iii) the dominance of the occipital alpha peak, with its higher frequency. These results serve to validate the method against traditional methods.

A surprising finding was that the occurrence of two peaks in the alpha range is very common, with around 50% of the subjects clearly exhibiting this phenomenon. Many researchers in the field had noted the presence of multiple rhythms in the alpha frequency ranges, and others have noted that the traditional view of taking the highest powered alpha peak is not sufficient to capture the full characteristics of the activity. The data are also consistent with the theory that double peak is present in the whole population, with single peak case actually consist of unresolved double peaks.

Further measures of alpha activities were developed, to capture its spatial characteristics in addition to the spectral and amplitude information. These measures were also found to vary with age, in Ch. 3; for example the occipitality of the peak cluster decreases with age and it has a lower frequency.

4.3 Future work

With the success of the automated algorithm in characterizing the alpha rhythm, there are some clear further research directions, including improvements to the algorithm:

(i) We limited our search to only two peaks within the given range. A more exhaustive search can determine whether the choice of two peaks is optimal. The current data suggest that a third alpha peak can potentially exist in subjects with two strong groups of "robust" alpha peaks. This also had been suggested as theoretically possible for very large anterior-posterior differences in the time delay in thalamocortical loops (Robinson et al., 2003b).

(ii) Only 19 electrodes were utilized in the current algorithm. By using all 26 electrodes that are available, or even more electrodes in high density recordings, we can potentially increase the sensitivity of the algorithm to peaks of smaller amplitudes, and improve the spatial resolution of the alpha parameters.

(iii) Implementation of a temporal wavelet transform could explore alpha rhythm changes during an experiment (Freyer et al., 2009), testing and validating ideas on stationarity, as well as looking at synchrony and potential spatial propagation of the alpha activity.

(iv) Only eyes-closed data were examined in this study. The same algorithm could be used on eyes-open data, in order to examine persistence of alpha rhythm and changes of the background spectrum between the two states, potentially to separate different rhythms within the alpha frequency range.

(v) The present method only examined the alpha activity range, but other frequency ranges could be consistently and objectively explored with this method. Peaks in delta activity, beta and gamma frequency ranges could be examined in this manner to establish a quantitative understanding throughout the whole EEG frequency range.

(vi) With the establishment of a large control population of subjects, we can quantitatively identify changes to the alpha rhythm under different experimental and clinical conditions, such as during tasks, under drug administration, behavioral and/or cognitive changes, and from disorders. Further investigation in such comparative studies might well establish criteria that can potentially lead to new clinical identification methods or insights into mechanisms of cognition and disorders.

(vii) Aside from these clear clinical potentials of the method, establishment of this large body of objective measurements of alpha activity might potentially help to answer the question of the mechanism of alpha generation, and ultimately the generation of EEG rhythms more generally. Specifically, quantitative measures of alpha rhythm will allow rejection of theories based on empirical evidence.

Appendix A

Power spectra from the 100–subject dataset of Chapter 2

This section contains all power spectra of the 100 subjects used in Ch. 2. The grayscale plots corresponds to the logarithmic power, with darker being higher and sites are as labeled. Normalizations differ slightly from site to site.

Cases with no alpha peak

Example of spectra from subjects with no clear alpha peak. Squares mark peaks that were found via the fitting process.

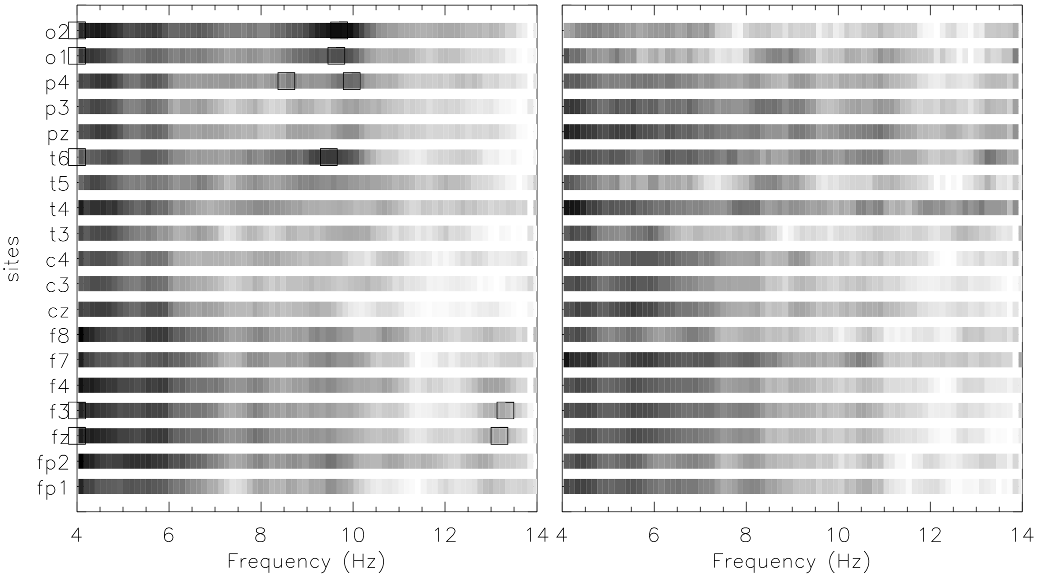

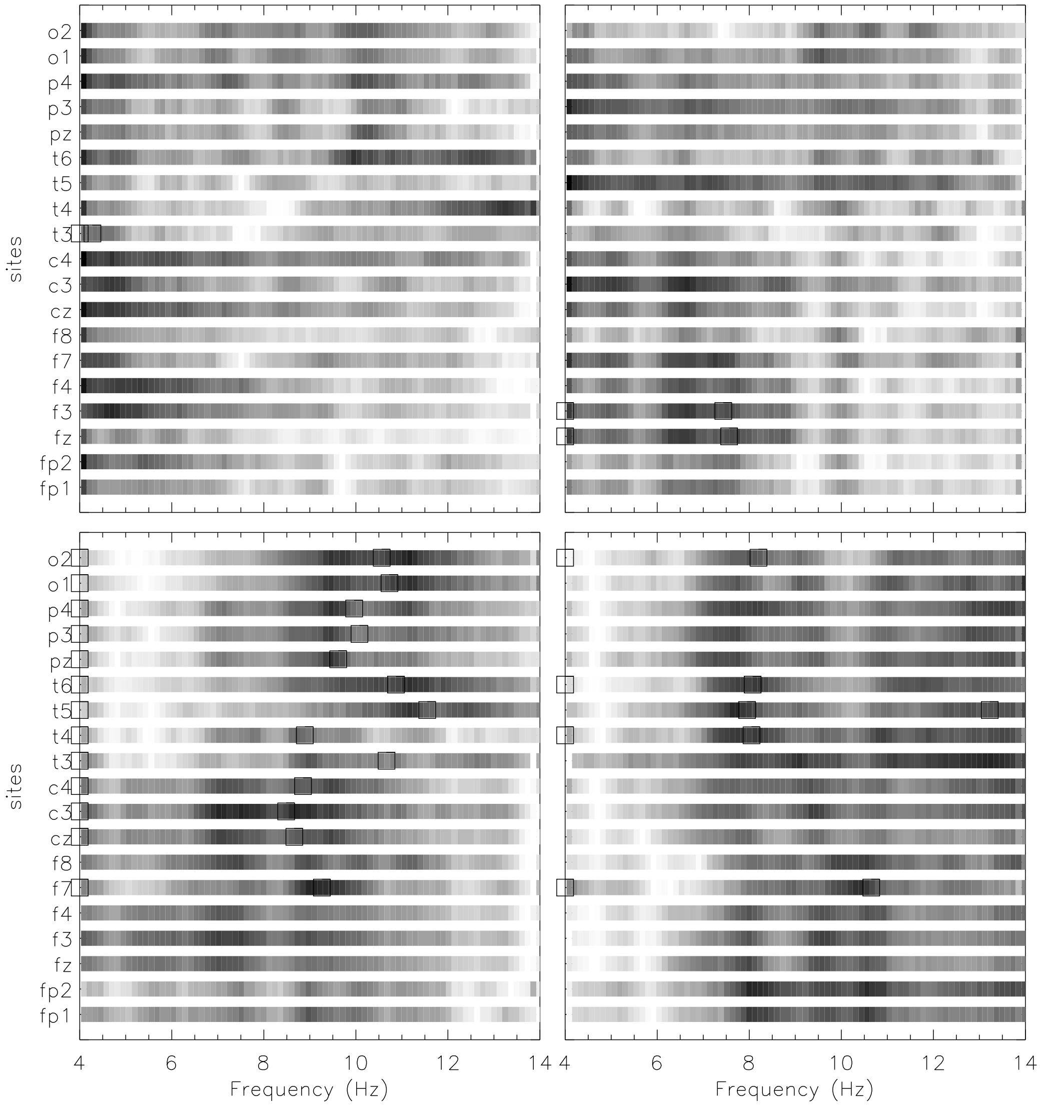
o2
o1
p4
p3
pz
t6
t5
t4
t3
c4
c3
cz
f8
f7
f4
f3
fz
fp2
fp1
sites
4
6
8
10
12
14
Frequency (Hz)

Cases with a single alpha peak

Class 1 set of spectra. Square and crosses mark the peaks found via the fitting process and the verification process, respectively.

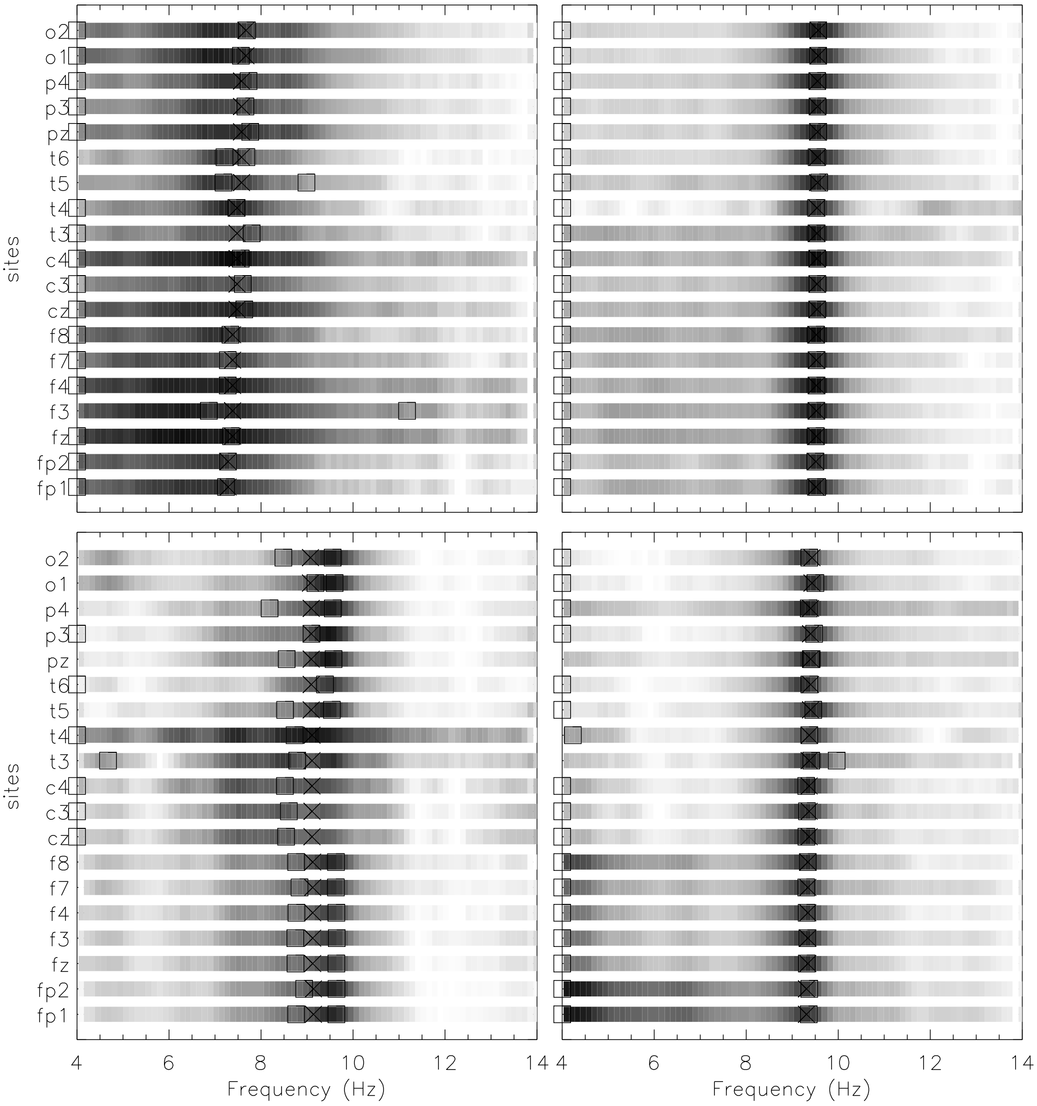

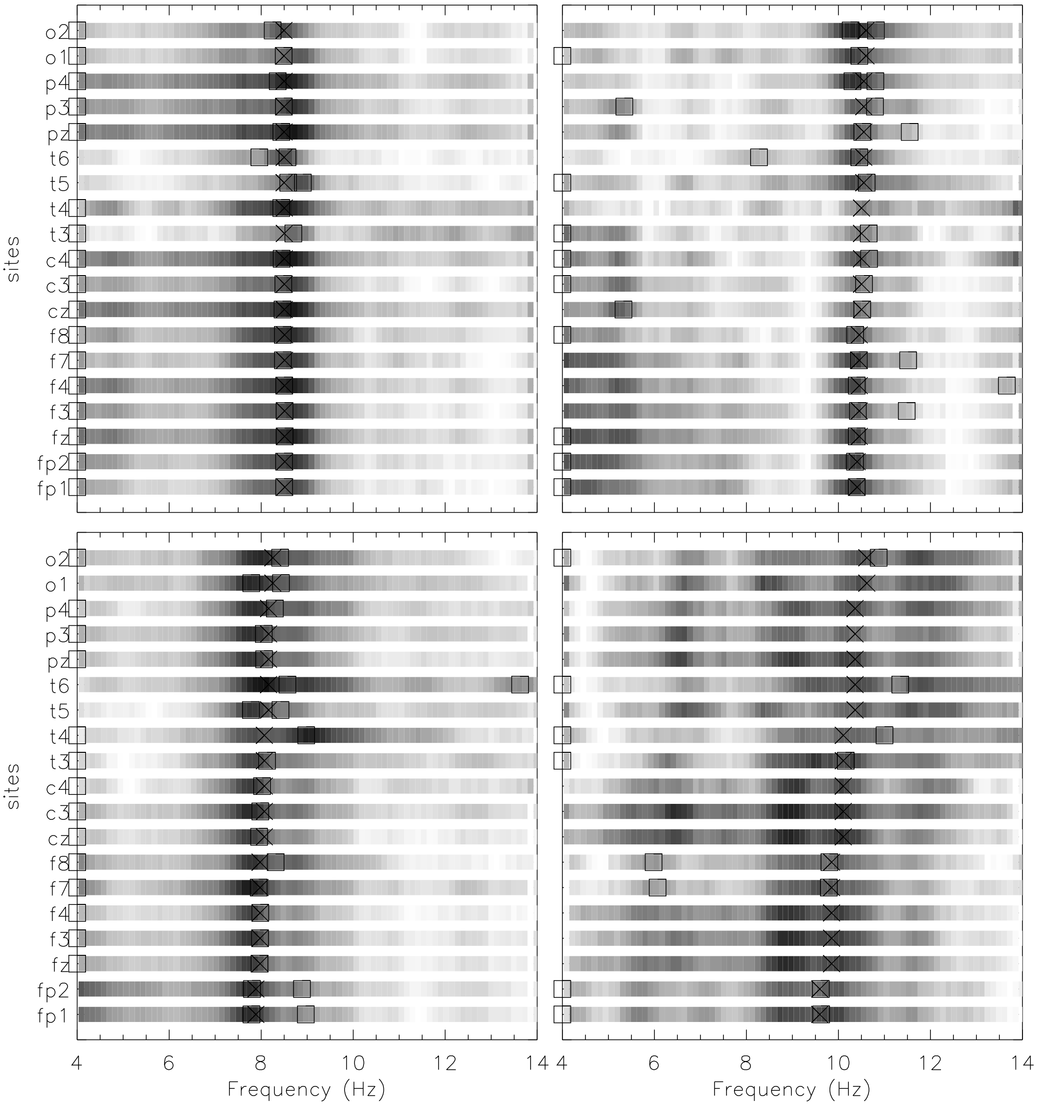
sites
o2
o1
p4
p3
pz
t6
t5
t4
t3
c4
c3
cz
f8
f7
f4
f3
fz
fp2
fp1
4
6
8
10
12
14
Frequency (Hz)

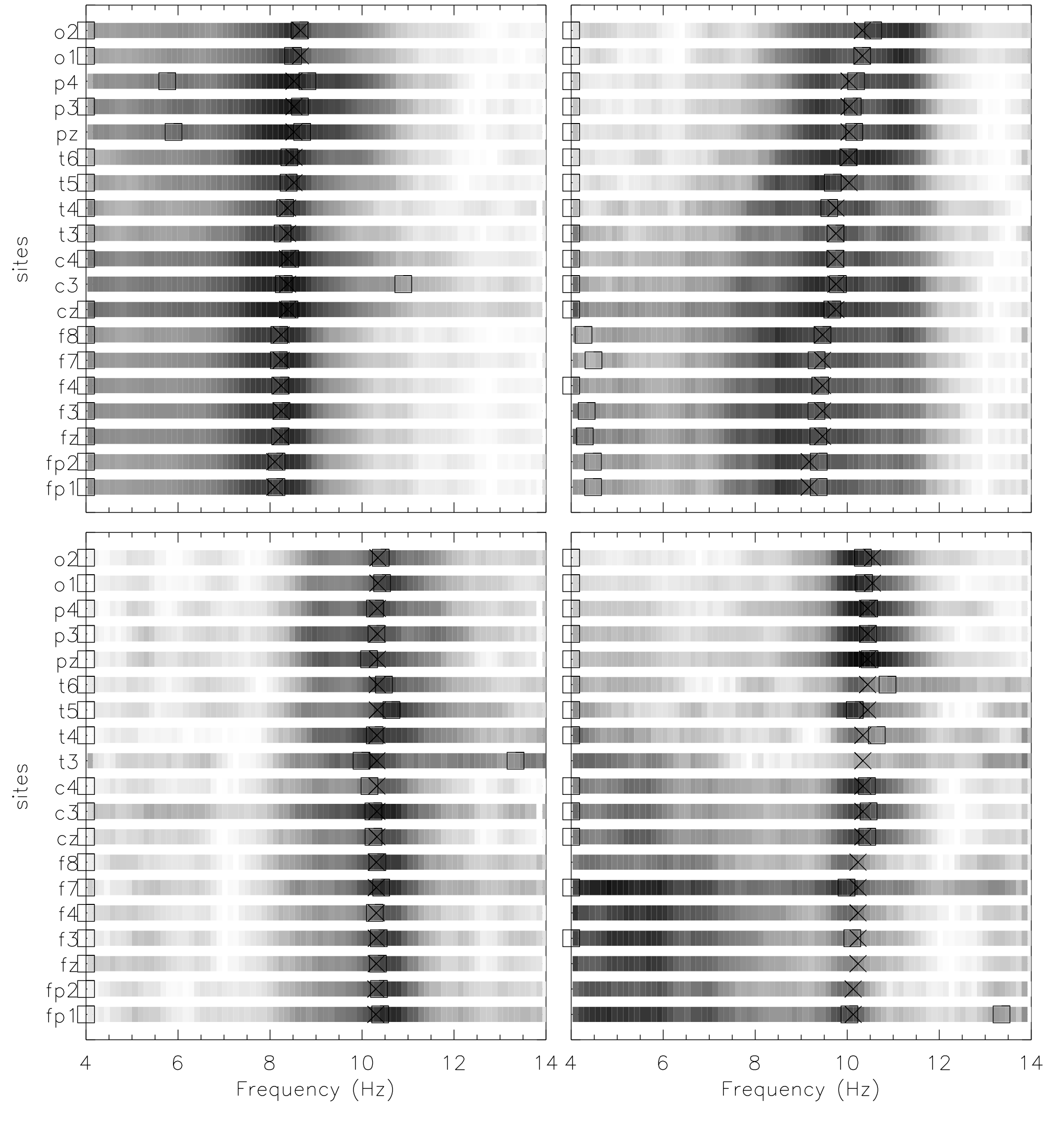
sites
o2
o1
p4
p3
pz
t6
t5
t4
t3
c4
c3
cz
f8
f7
f4
f3
fz
fp2
fp1
4
6
8
10
12
14
Frequency (Hz)

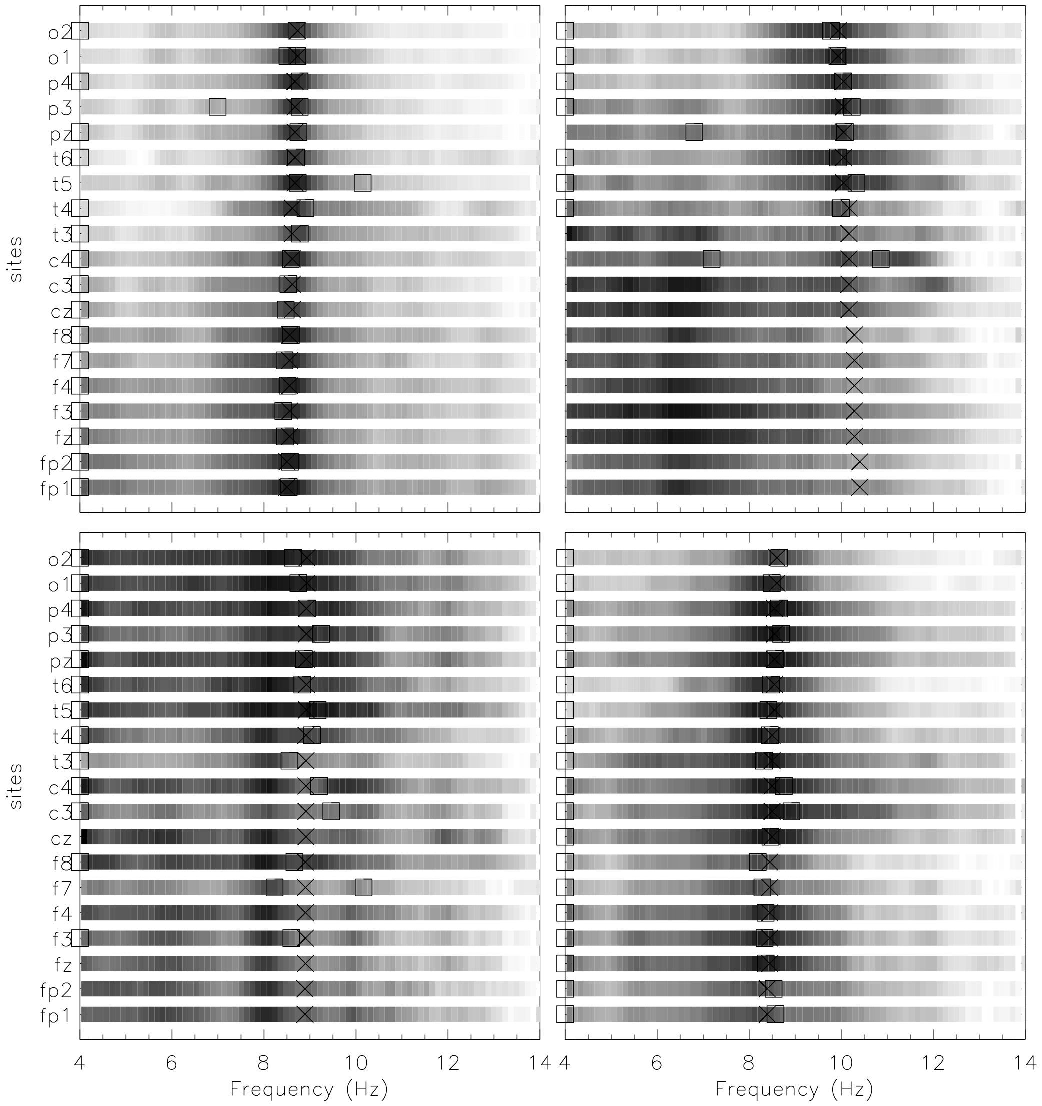
o2
o1
p4
p3
pz
t6
t5
t4
t3
c4
c3
cz
f8
f7
f4
f3
fz
fp2
fp1
sites
4
6
8
10
12
14
Frequency (Hz)


o2
o1
p4
p3
pz
t6
t5
t4
t3
c4
c3
cz
f8
f7
f4
f3
fz
fp2
fp1
sites
4
6
8
10
12
14
Frequency (Hz)

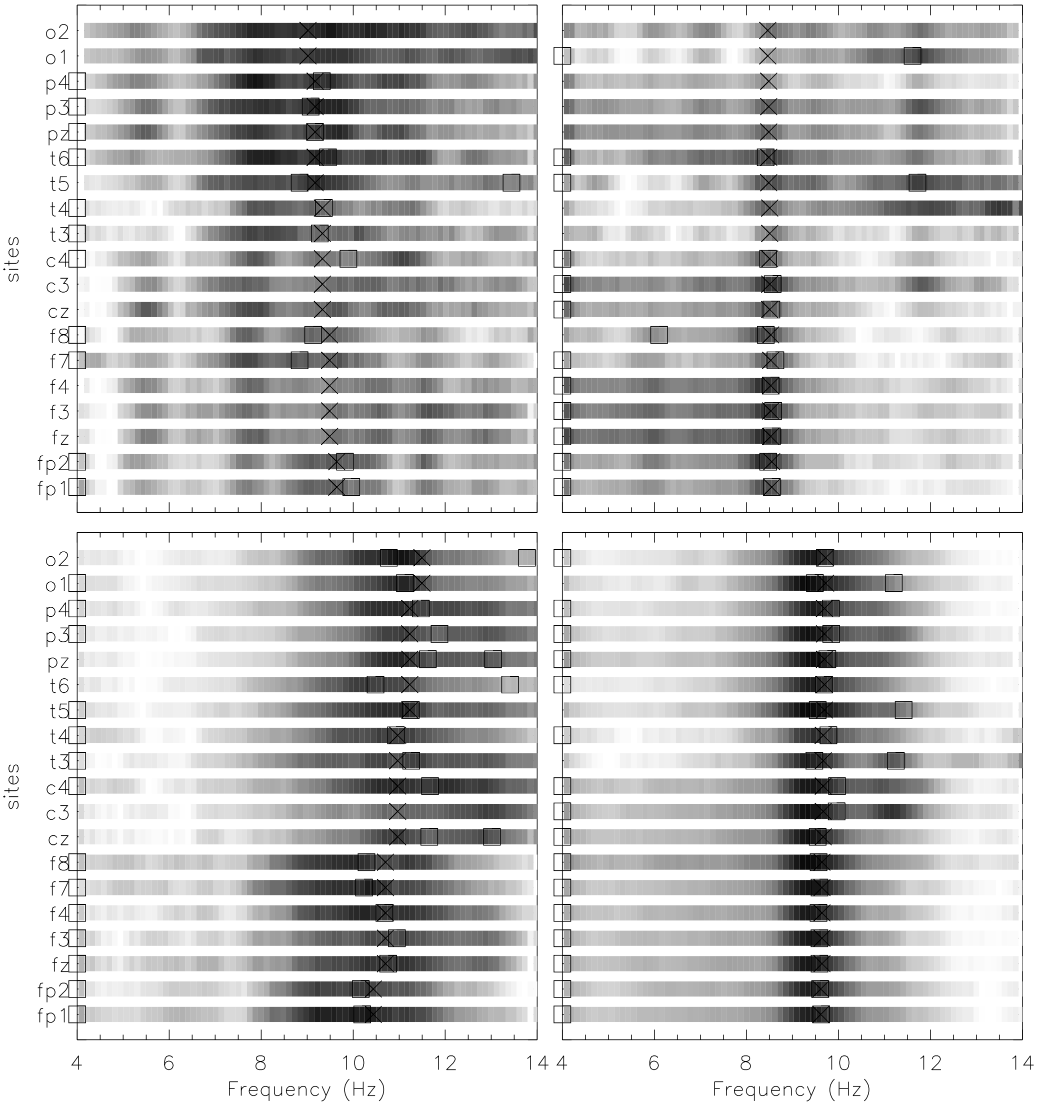
o2
o1
p4
p3
pz
t6
t5
t4
t3
c4
c3
cz
f8
f7
f4
f3
fz
fp2
fp1
sites
4
6
8
10
12
14
Frequency (Hz)

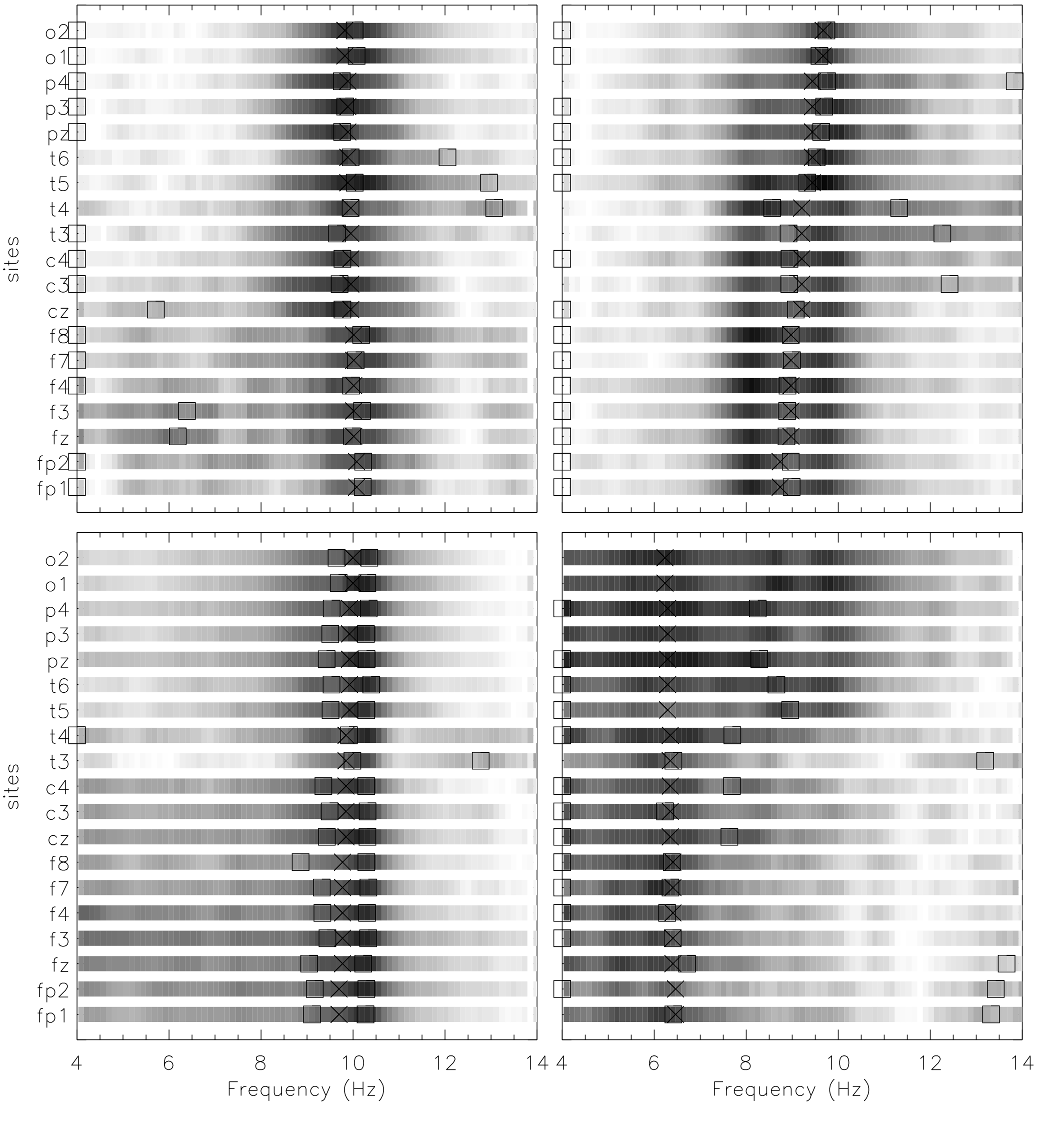
o2
o1
p4
p3
pz
t6
t5
t4
t3
c4
c3
cz
f8
f7
f4
f3
fz
fp2
fp1
sites
4
6
8
10
12
14
Frequency (Hz)

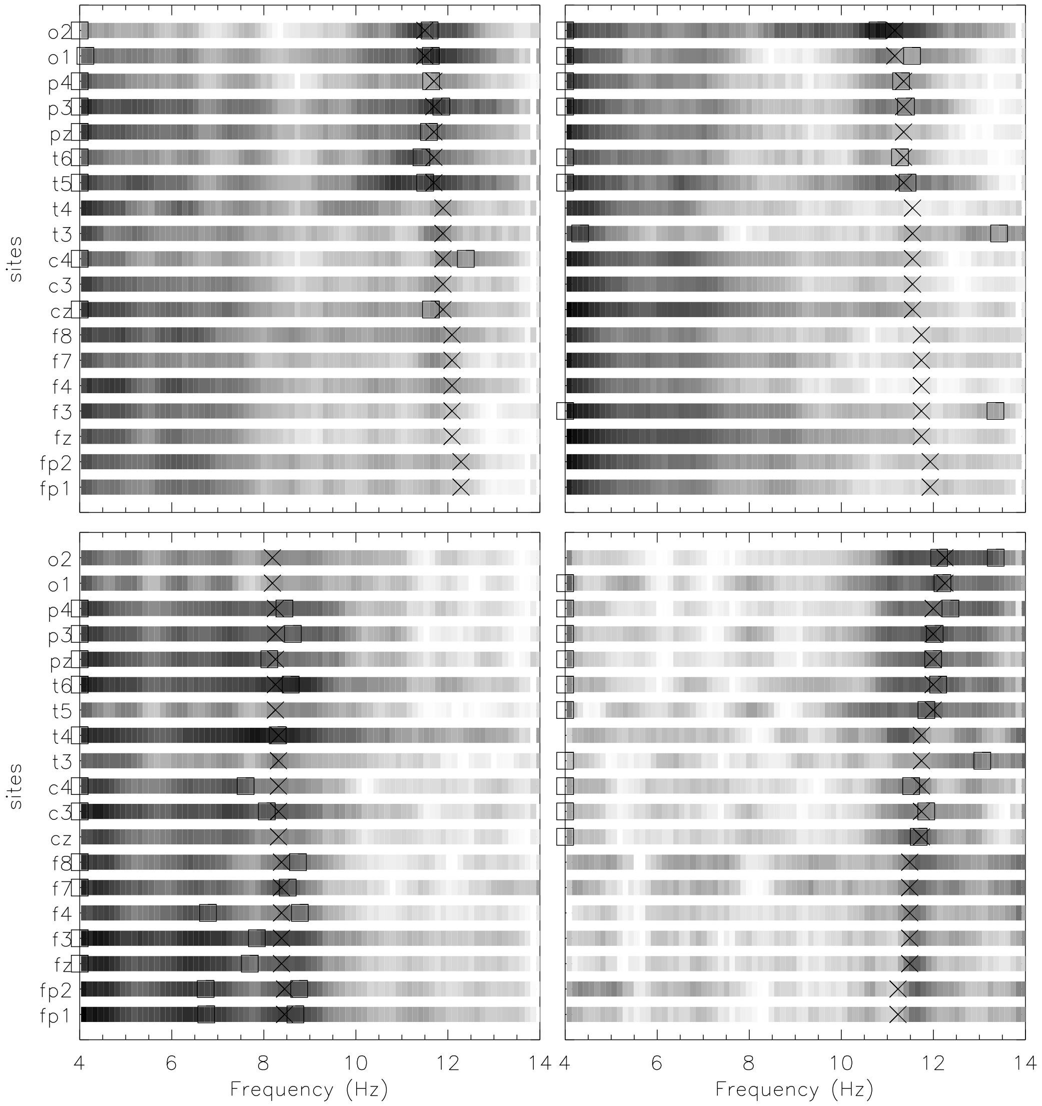
sites
o2
o1
p4
p3
pz
t6
t5
t4
t3
c4
c3
cz
f8
f7
f4
f3
fz
fp2
fp1
4
6
8
10
12
14
Frequency (Hz)

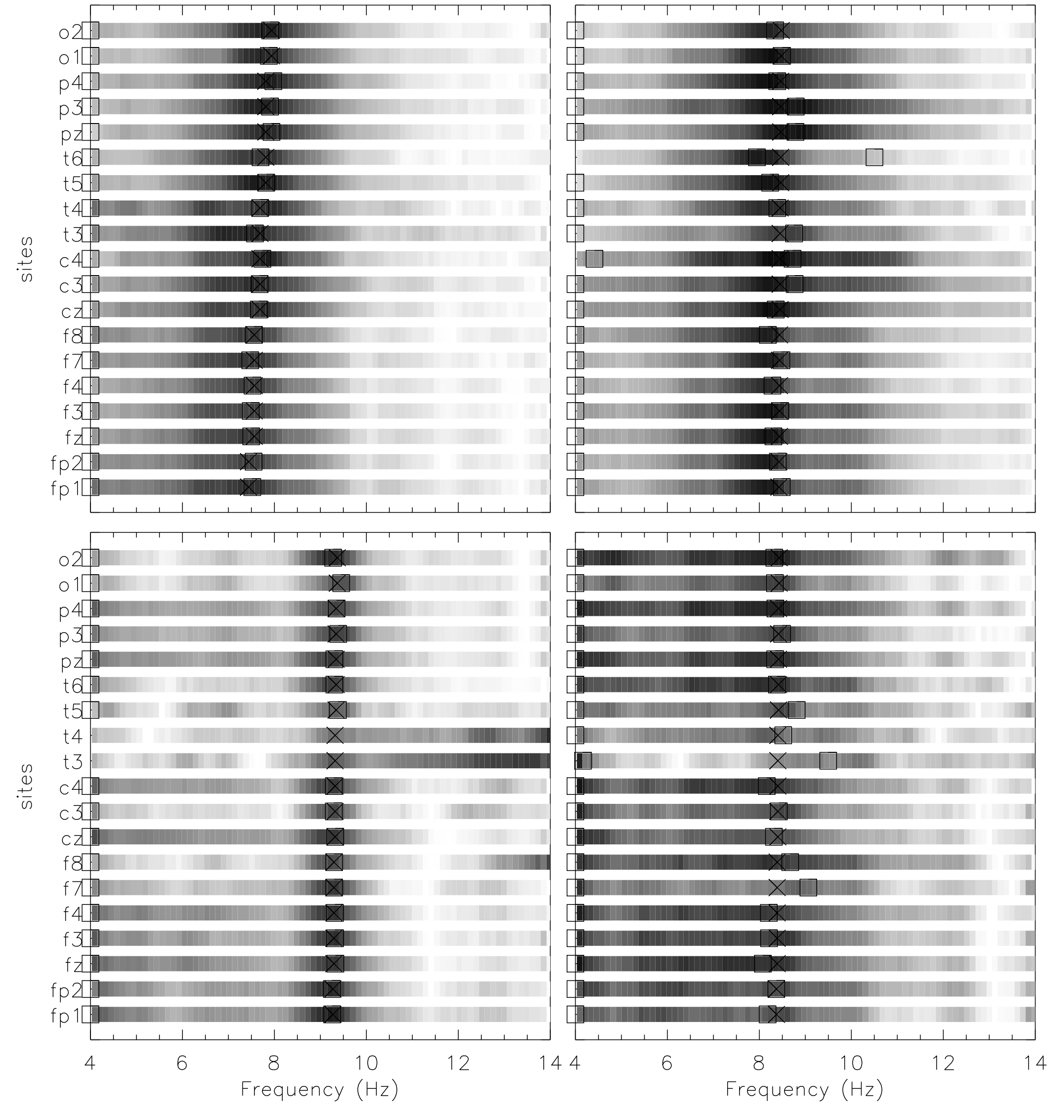
o2
o1
p4
p3
pz
t6
t5
t4
t3
c4
c3
cz
f8
f7
f4
f3
fz
fp2
fp1
sites
4
6
8
10
12
14
Frequency (Hz)

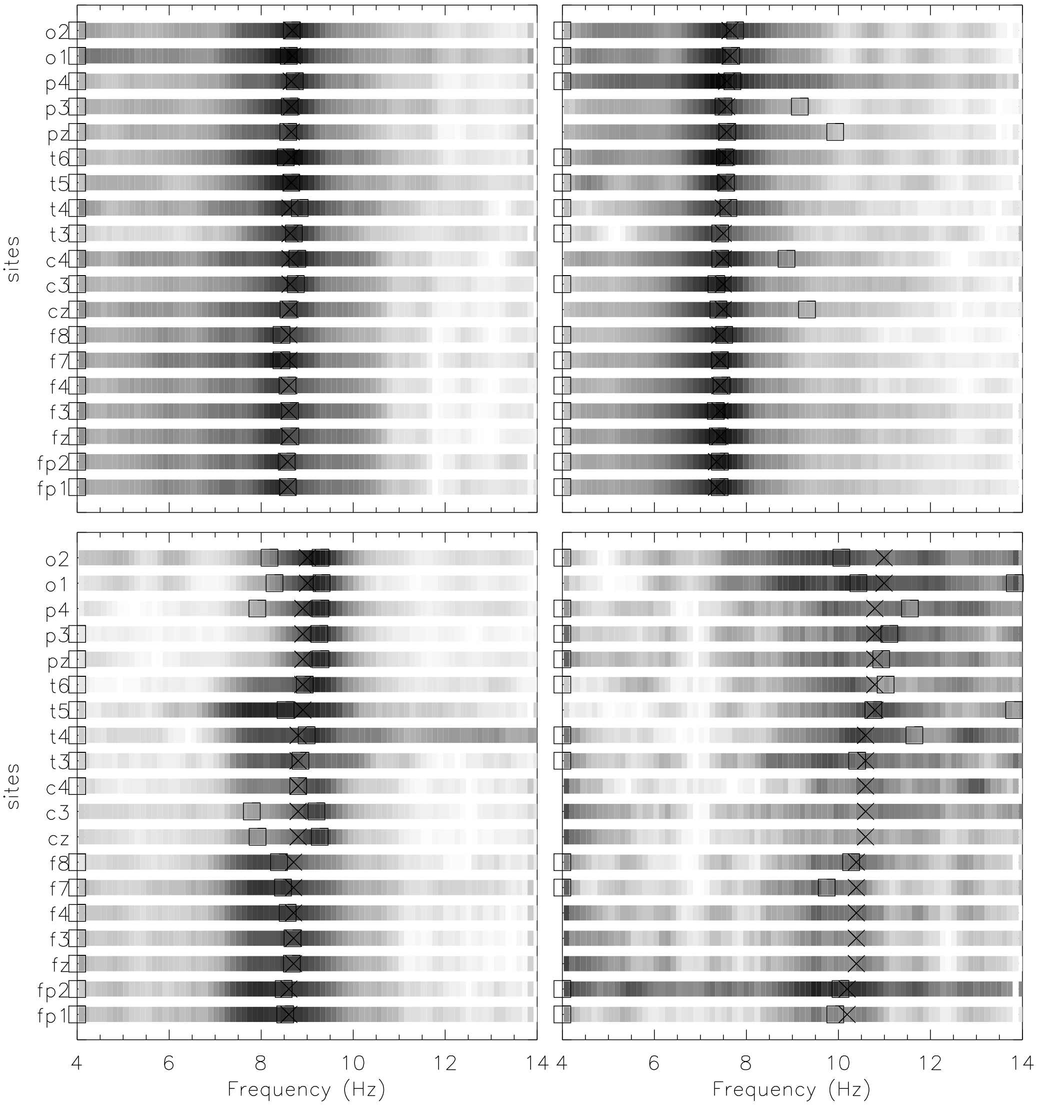
o2
o1
p4
p3
pz
t6
t5
t4
t3
c4
c3
cz
f8
f7
f4
f3
fz
fp2
fp1
sites
4
6
8
10
12
14
Frequency (Hz)

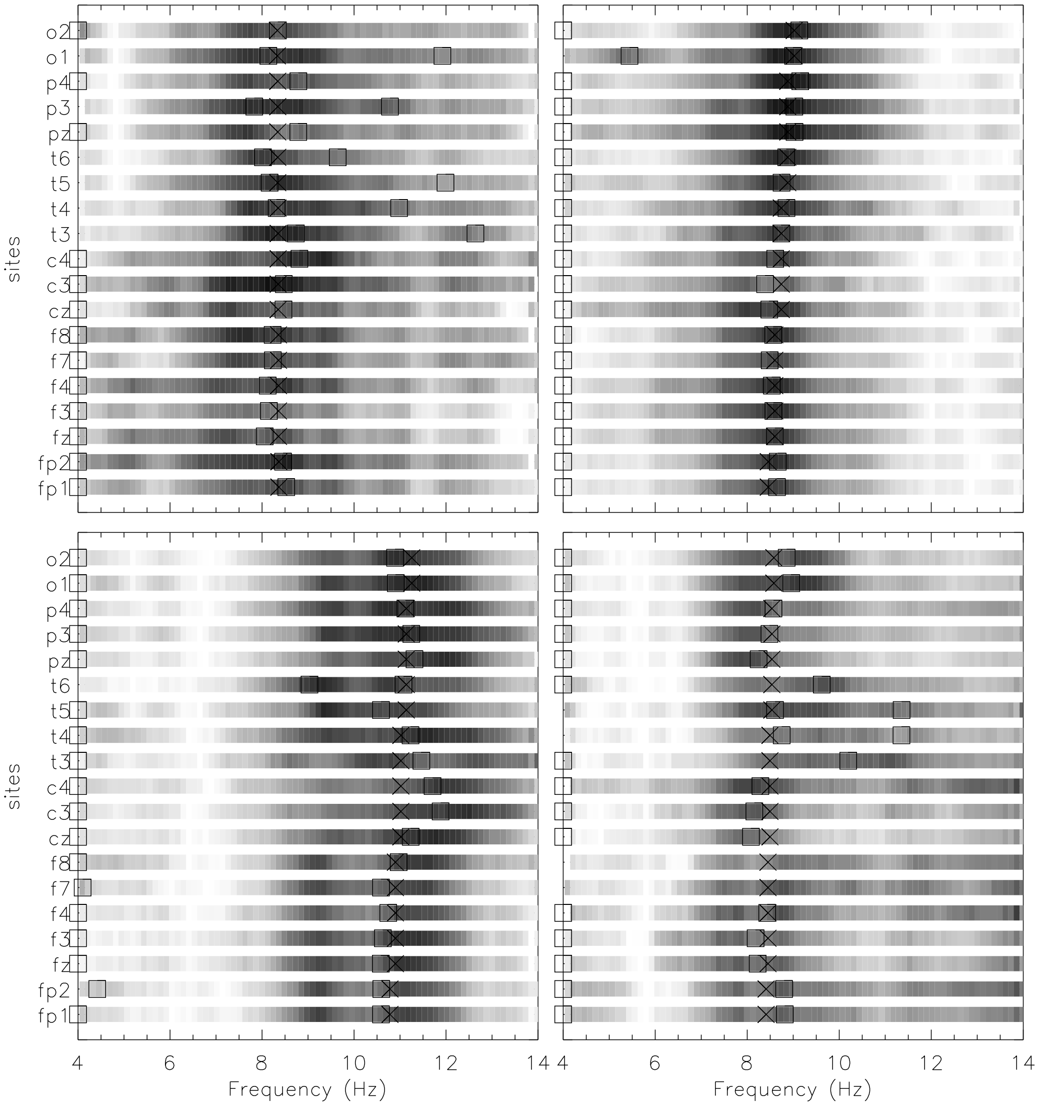
o2
o1
p4
p3
pz
t6
t5
t4
t3
c4
c3
cz
f8
f7
f4
f3
fz
fp2
fp1
sites
4
6
8
10
12
14
Frequency (Hz)

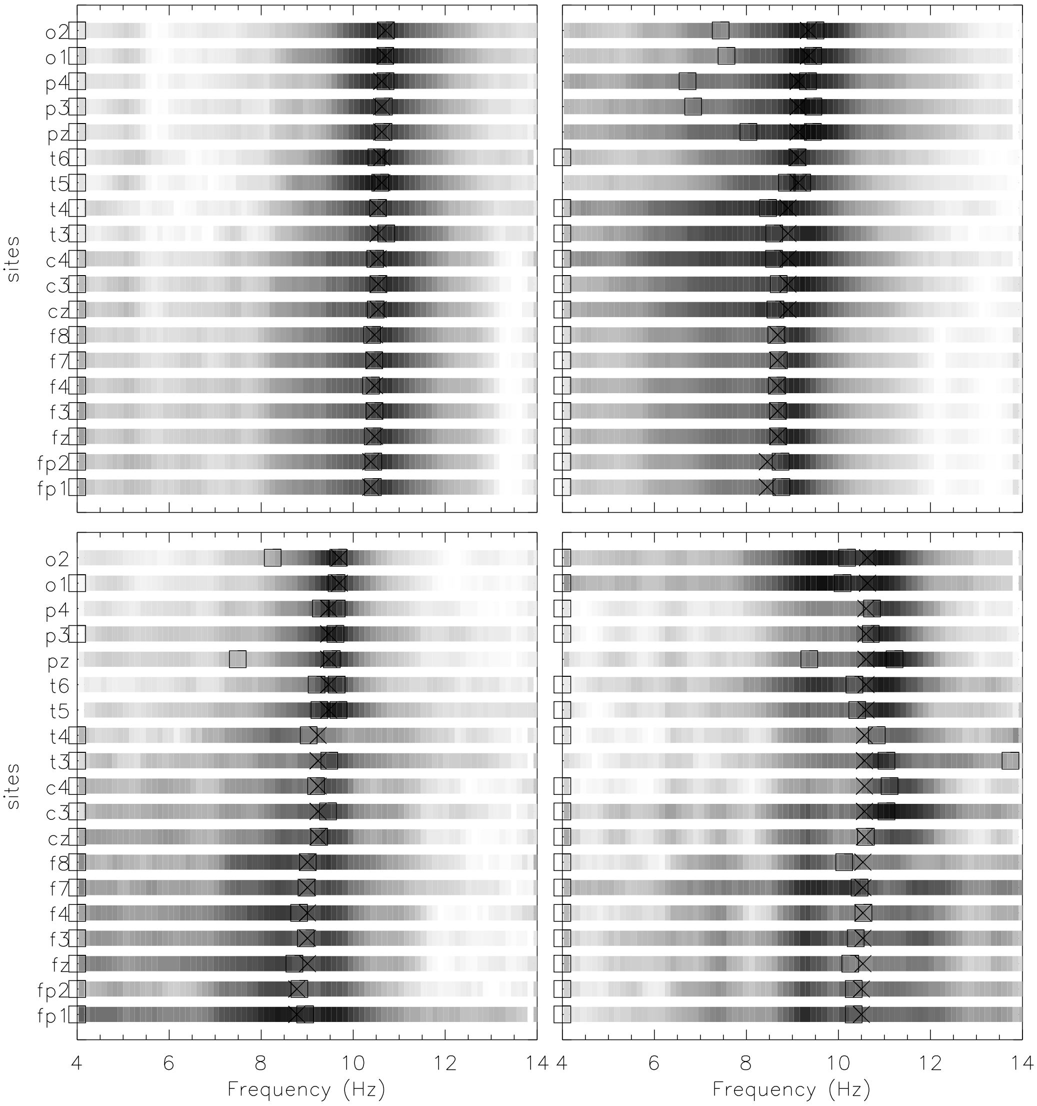
o2
o1
p4
p3
pz
t6
t5
t4
t3
c4
c3
cz
f8
f7
f4
f3
fz
fp2
fp1
sites
4
6
8
10
12
14
Frequency (Hz)

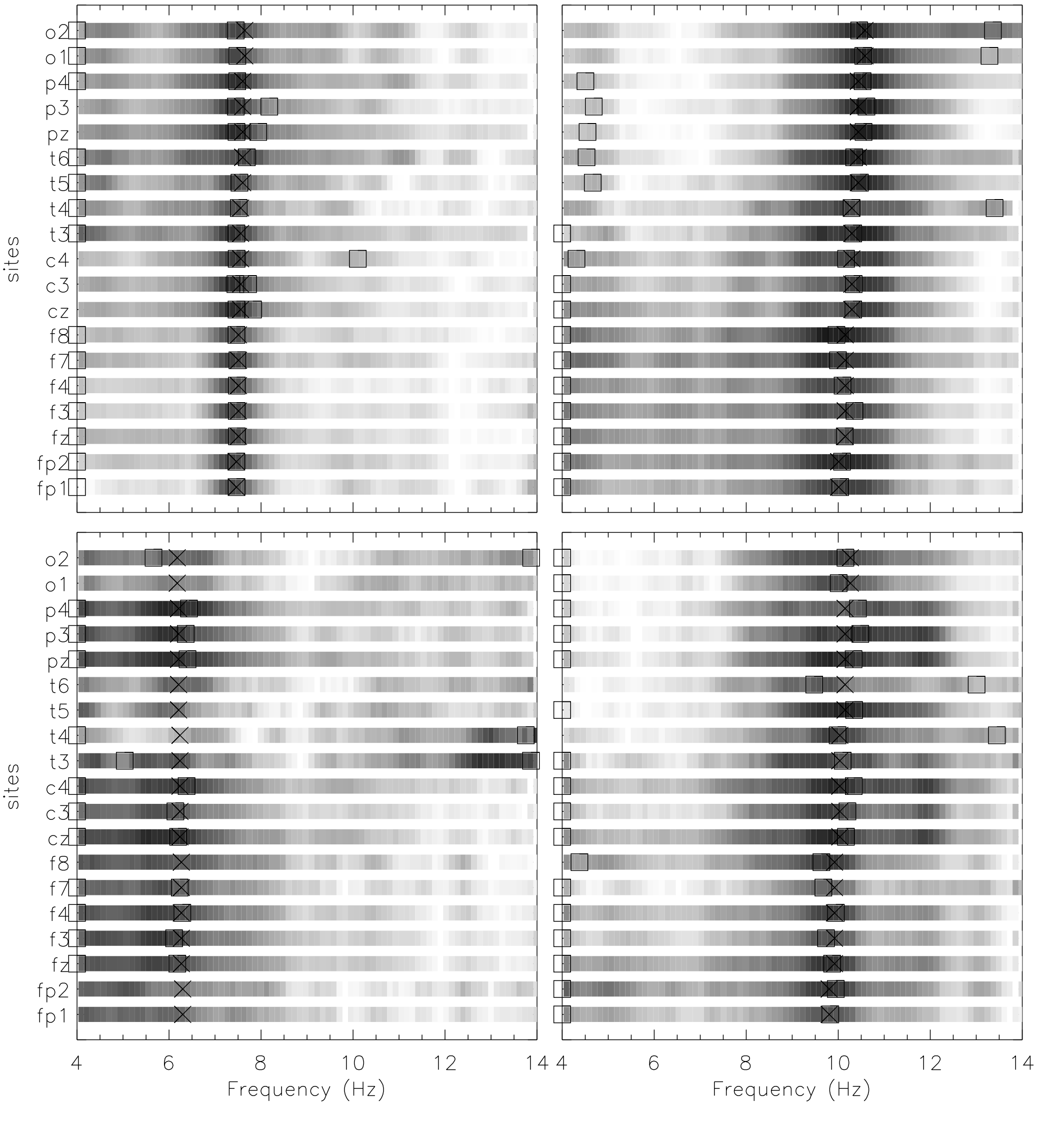
sites
o2
o1
p4
p3
pz
t6
t5
t4
t3
c4
c3
cz
f8
f7
f4
f3
fz
fp2
fp1
4
6
8
10
12
14
Frequency (Hz)

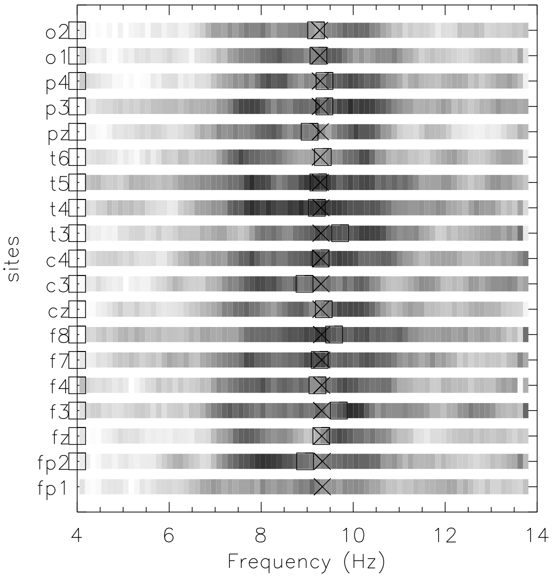

Cases with double alpha peaks

Class 1 set of spectra. Squares and crosses mark the peaks found via the fitting process and the verification process, respectively.

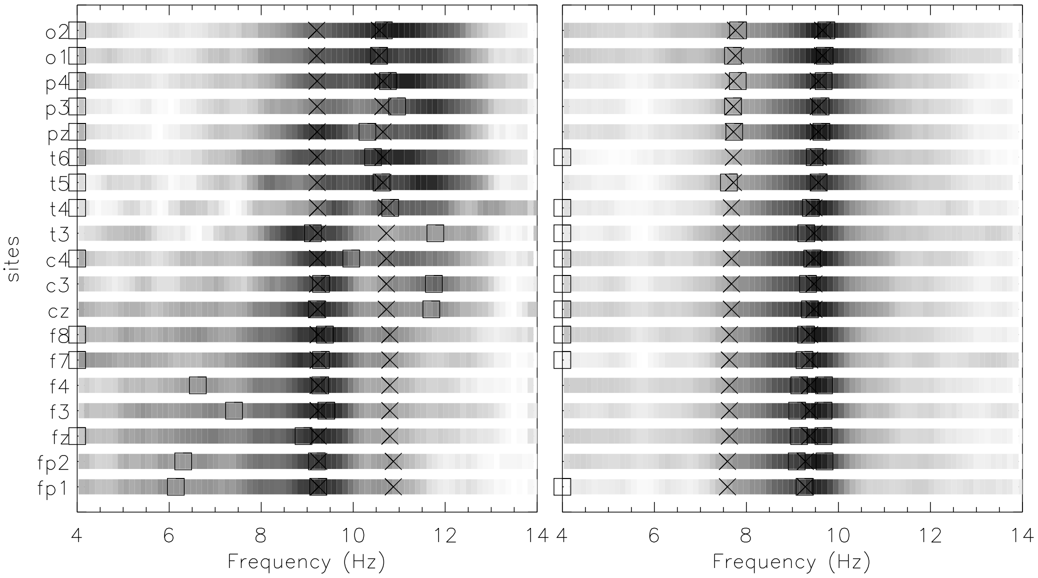

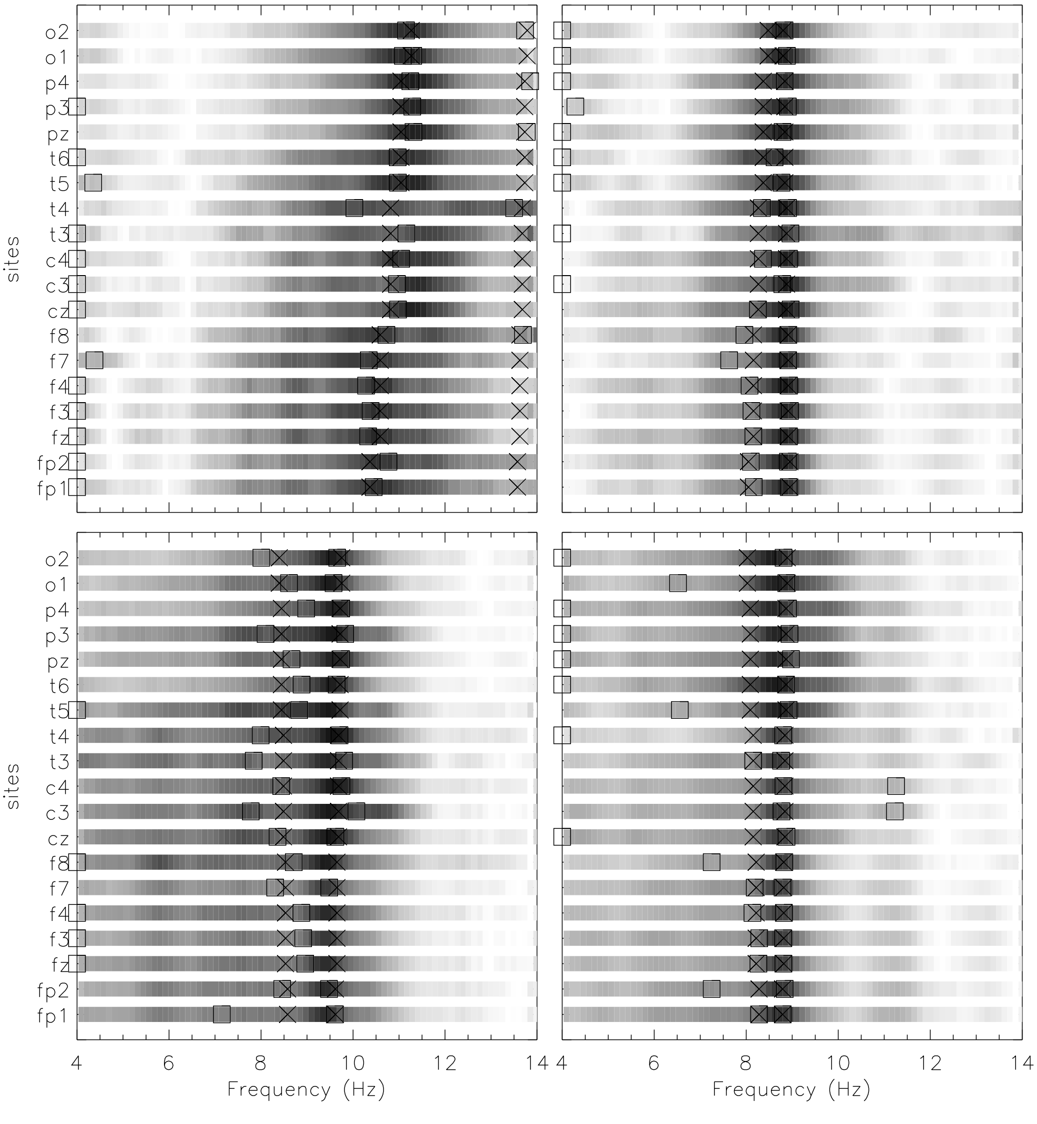
o2
o1
p4
p3
pz
t6
t5
t4
t3
c4
c3
cz
f8
f7
f4
f3
fz
fp2
fp1
sites
4
6
8
10
12
14
Frequency (Hz)

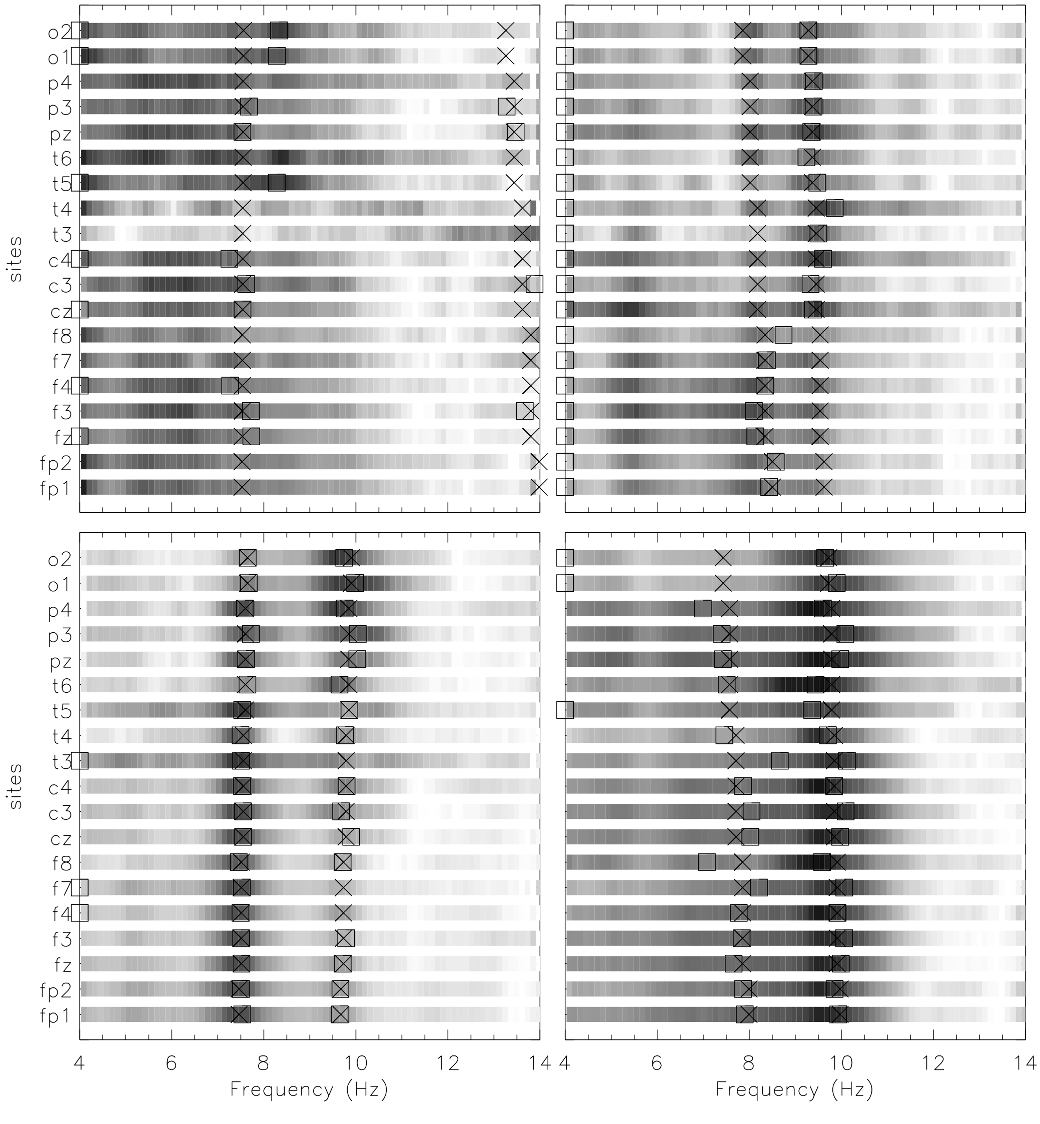
o2
o1
p4
p3
pz
t6
t5
t4
t3
c4
c3
cz
f8
f7
f4
f3
fz
fp2
fp1
sites
4
6
8
10
12
14
Frequency (Hz)

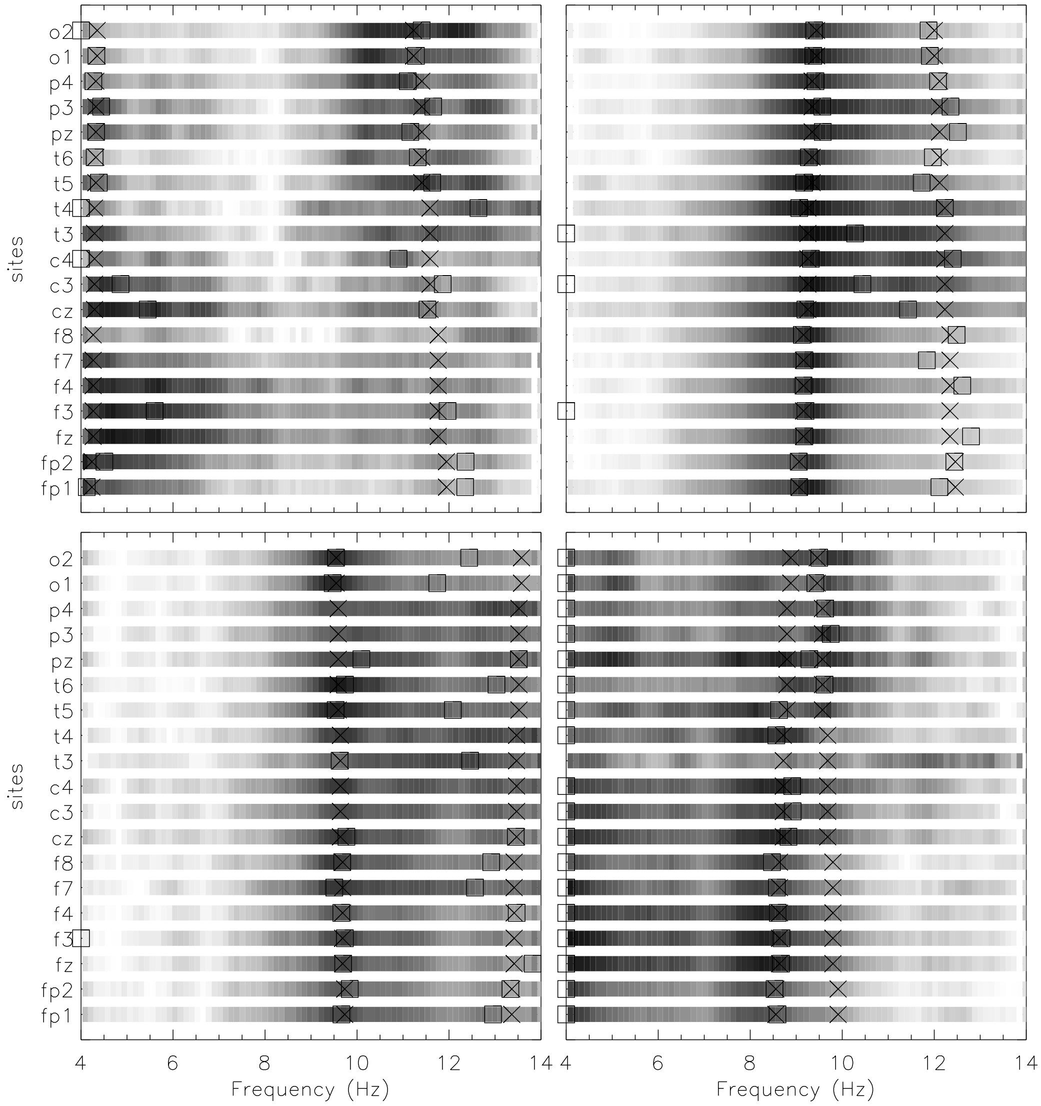
o2
o1
p4
p3
pz
t6
t5
t4
t3
c4
c3
cz
f8
f7
f4
f3
fz
fp2
fp1
sites
4
6
8
10
12
14
Frequency (Hz)

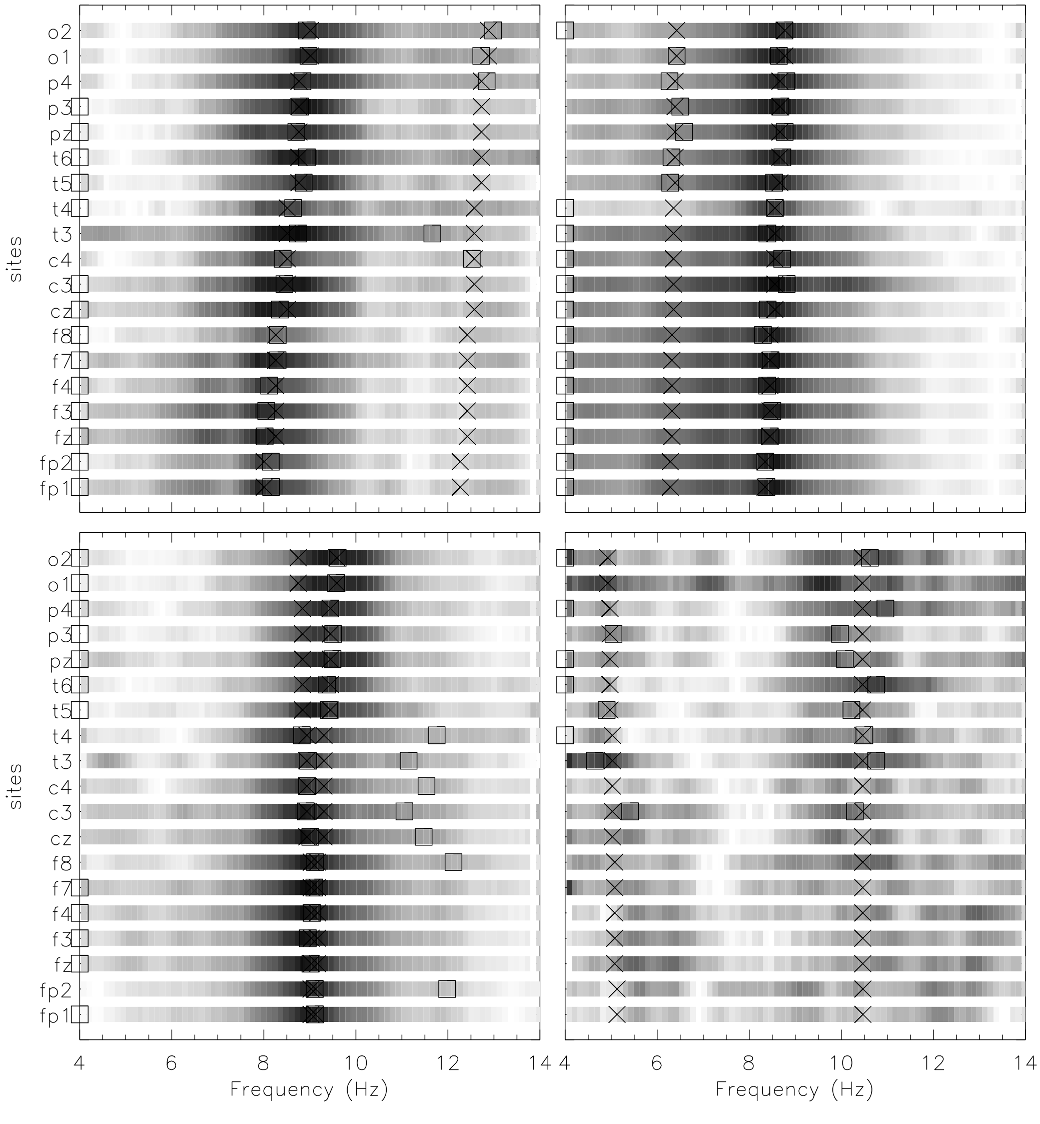
o2
o1
p4
p3
pz
t6
t5
t4
t3
c4
c3
cz
f8
f7
f4
f3
fz
fp2
fp1
sites
4
6
8
10
12
14
Frequency (Hz)

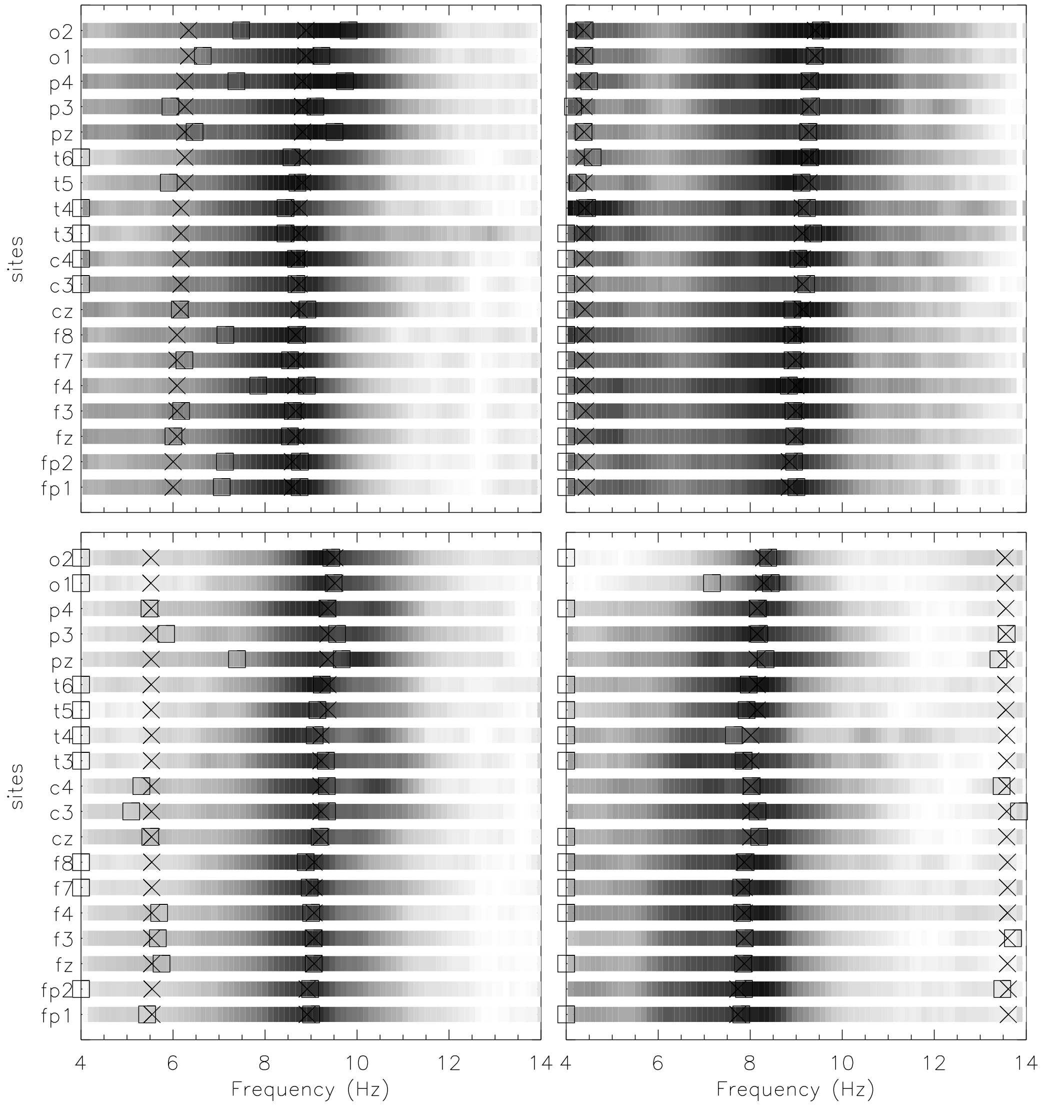
sites
o2
o1
p4
p3
pz
t6
t5
t4
t3
c4
c3
cz
f8
f7
f4
f3
fz
fp2
fp1
sites
o2
o1
p4
p3
pz
t6
t5
t4
t3
c4
c3
cz
f8
f7
f4
f3
fz
fp2
fp1
4
6
8
10
12
14
4
6
8
10
12
14
Frequency (Hz)
Frequency (Hz)

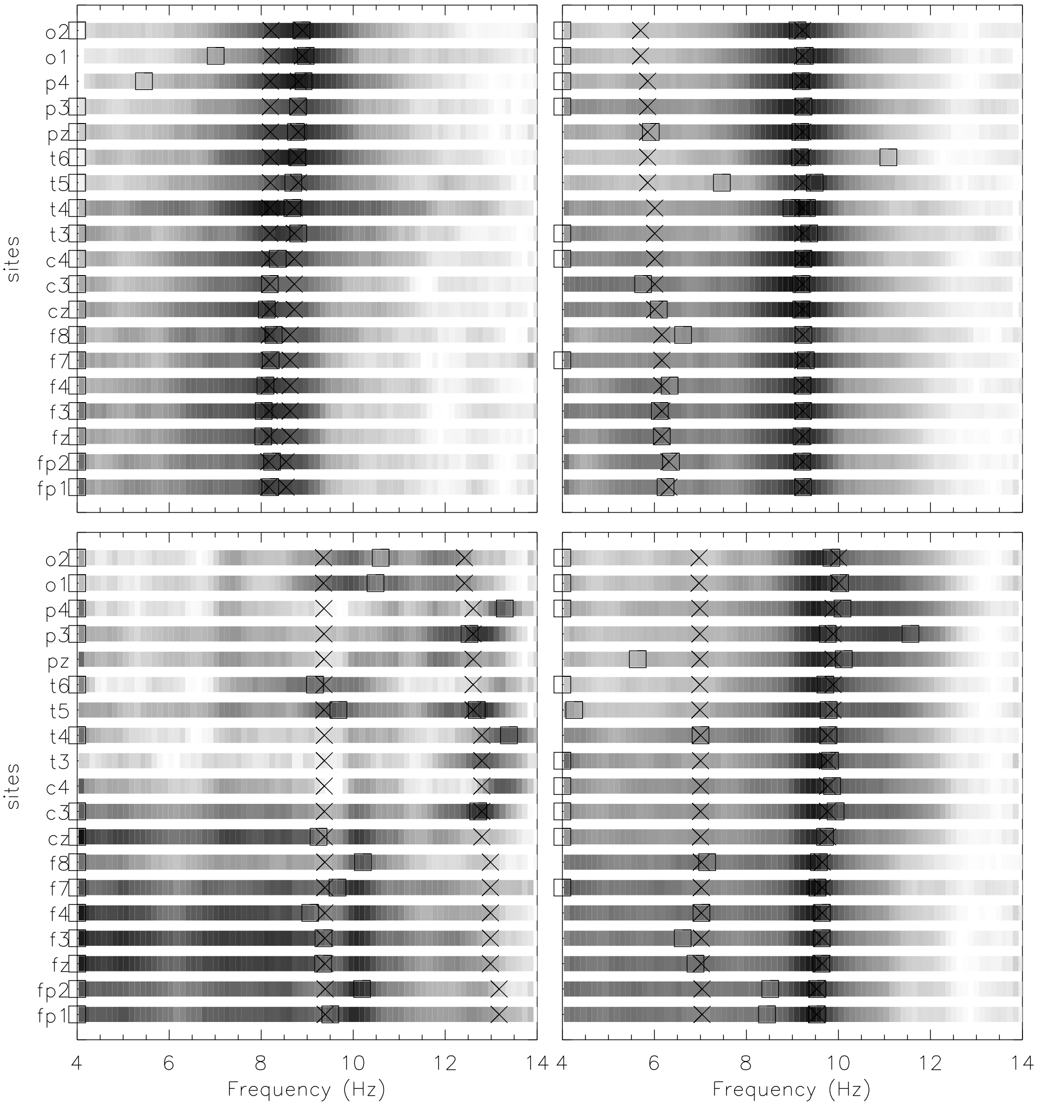
o2
o1
p4
p3
pz
t6
t5
t4
t3
c4
c3
cz
f8
f7
f4
f3
fz
fp2
fp1
sites
4
6
8
10
12
14
Frequency (Hz)

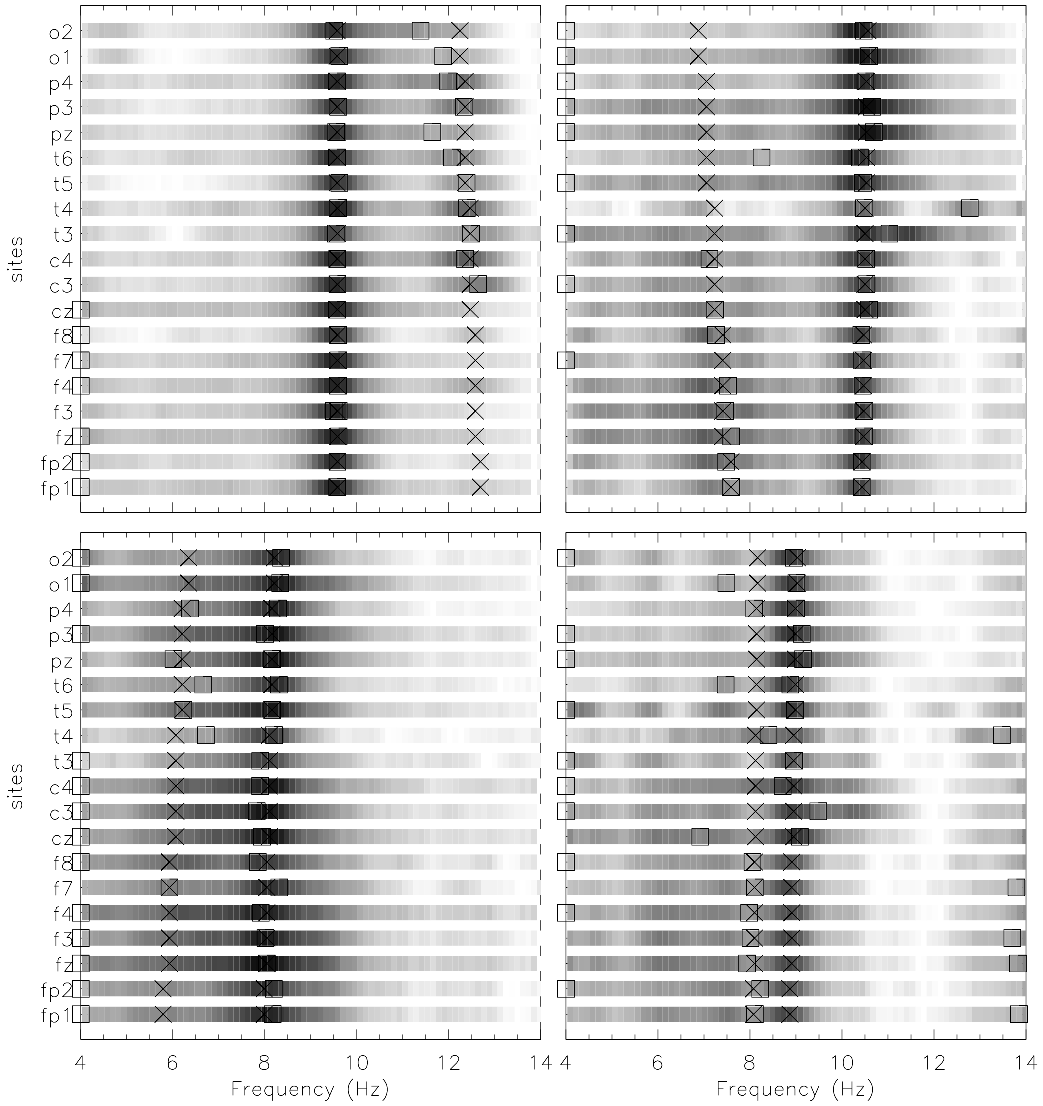
o2
o1
p4
p3
pz
t6
t5
t4
t3
c4
c3
cz
f8
f7
f4
f3
fz
fp2
fp1
sites
4
6
8
10
12
14
Frequency (Hz)

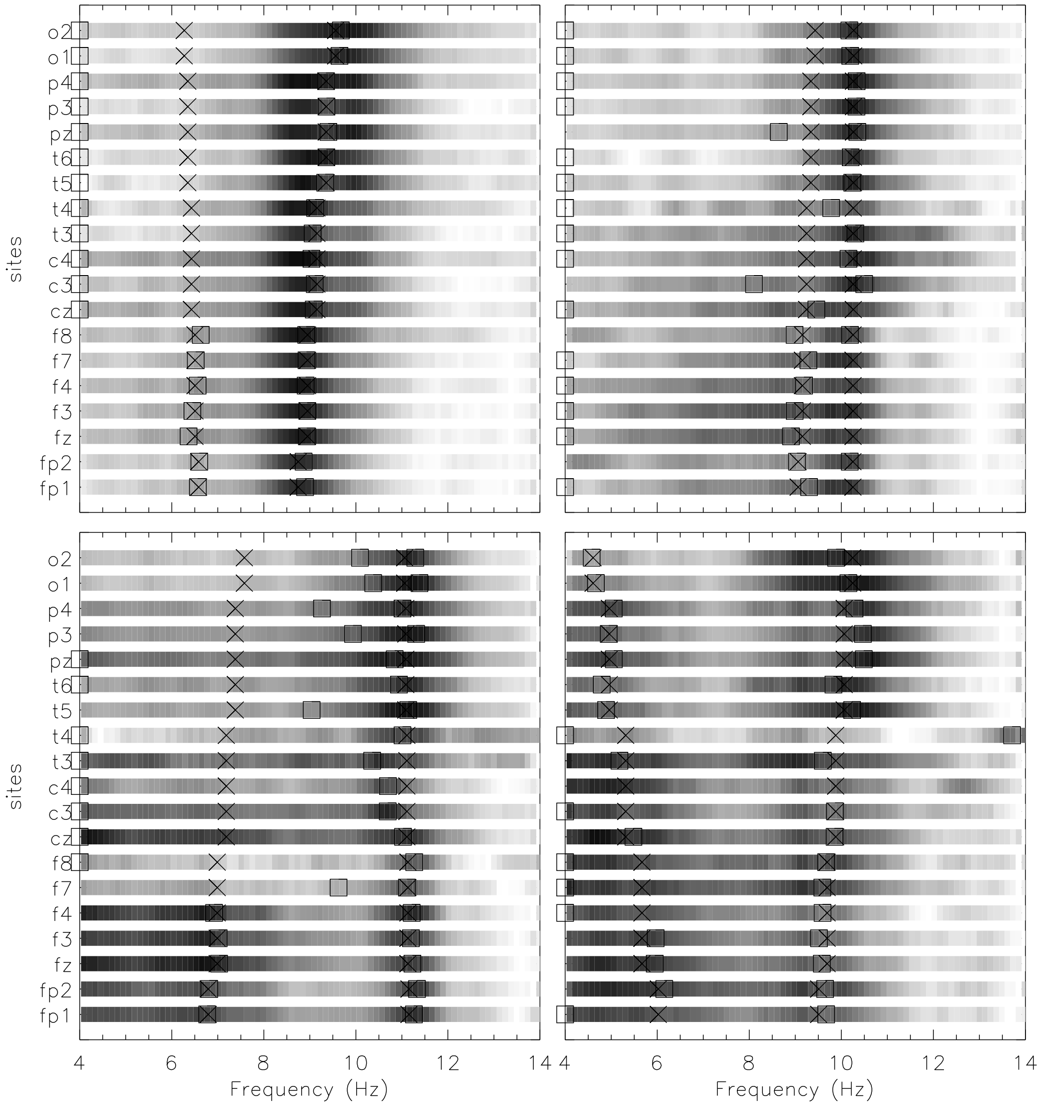
sites
o2
o1
p4
p3
pz
t6
t5
t4
t3
c4
c3
cz
f8
f7
f4
f3
fz
fp2
fp1
4
6
8
10
12
14
Frequency (Hz)

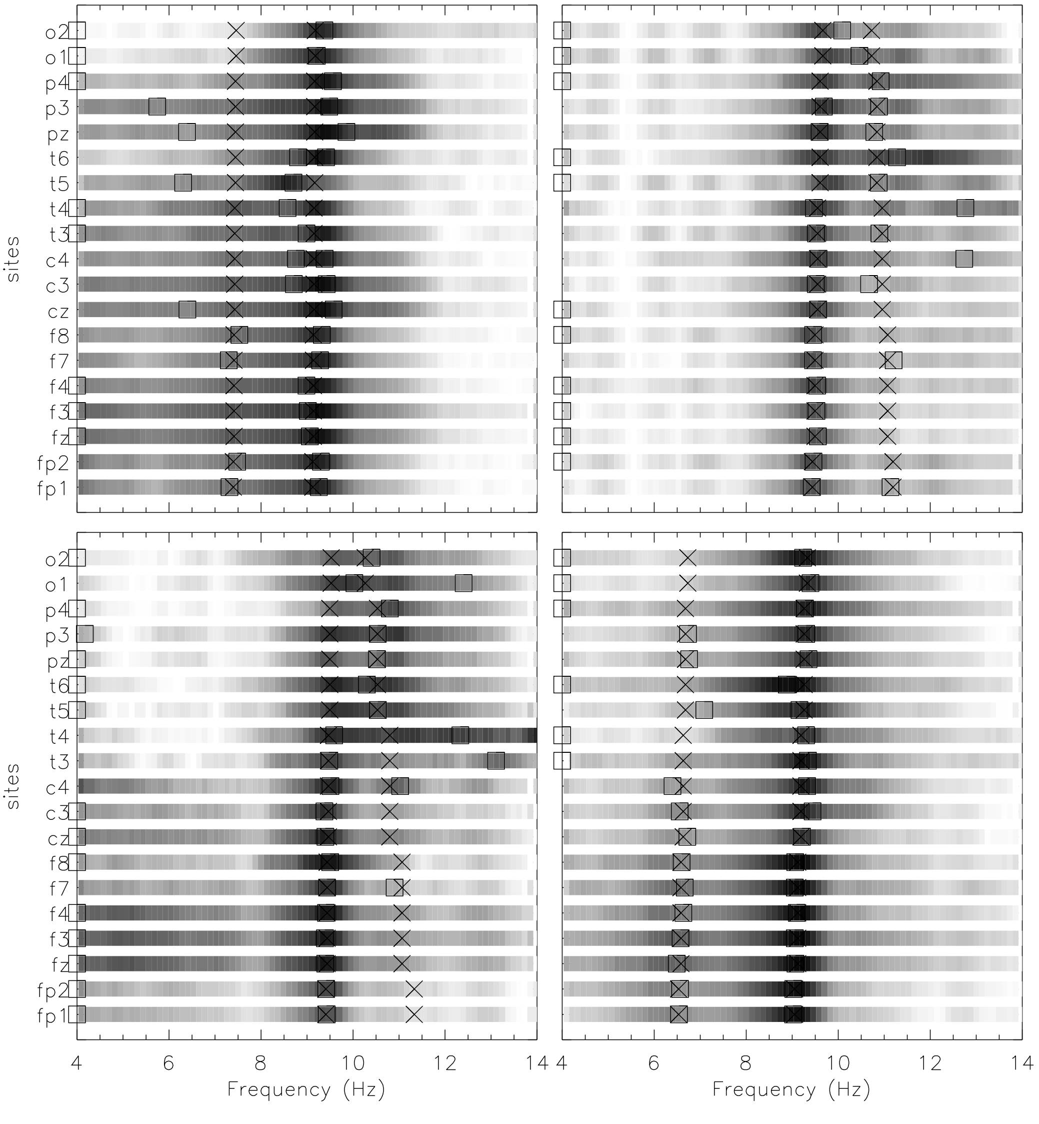
o2
o1
p4
p3
pz
t6
t5
t4
t3
c4
c3
cz
f8
f7
f4
f3
fz
fp2
fp1
sites
4
6
8
10
12
14
Frequency (Hz)

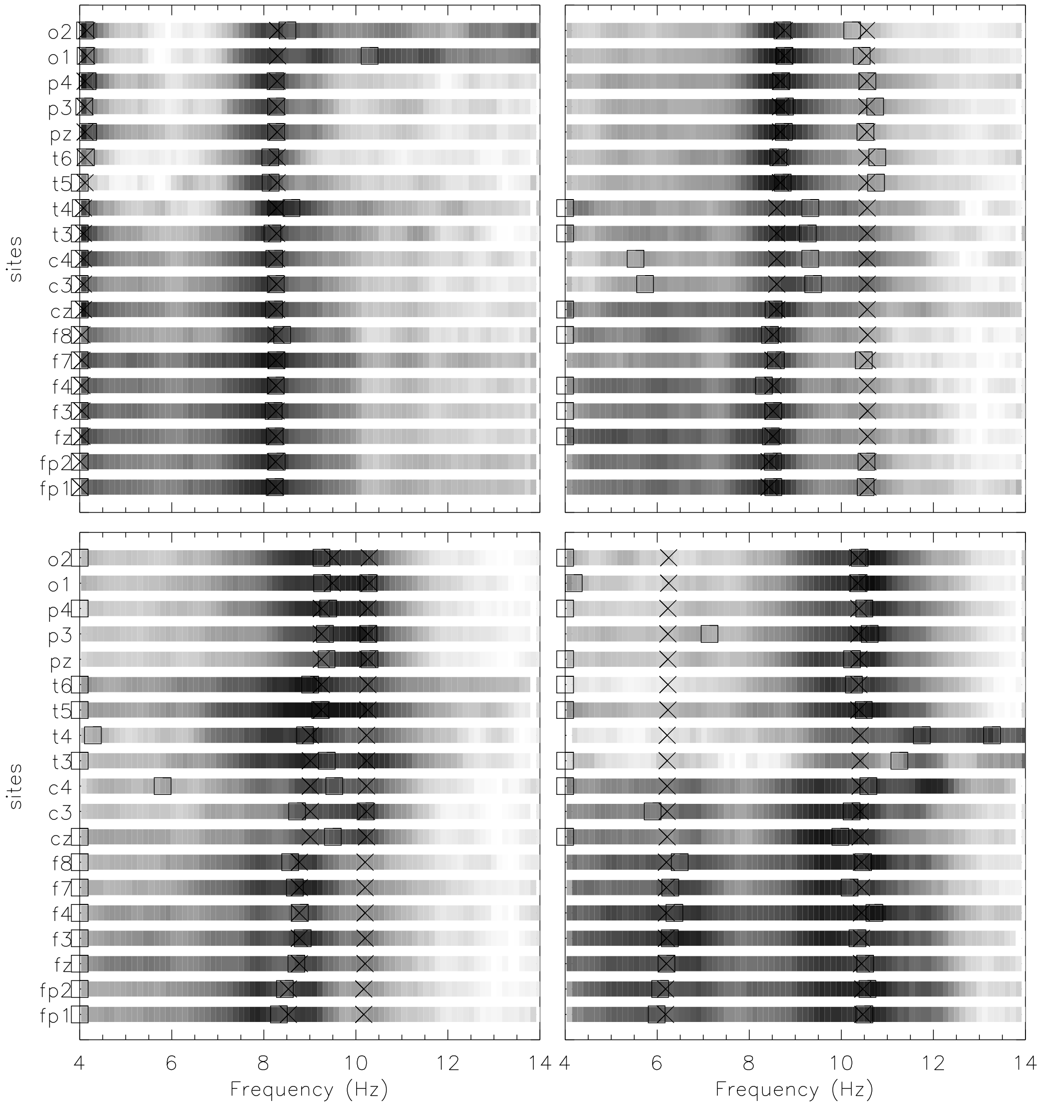
o2
o1
p4
p3
pz
t6
t5
t4
t3
c4
c3
cz
f8
f7
f4
f3
fz
fp2
fp1
sites
4
6
8
10
12
14
Frequency (Hz)

Appendix B

Algorithm for alpha peak quantification

This section contains the C++ code that implements the methods outlined in Ch. 2 and was used subsequently in their verification, and in the production of the results in Ch. 3.

Section B.1 is the code written by myself, Dr. Chris Rennie and Prof. Peter Robinson during the development of the algorithm, Sec. B.2 is the modified code adapted from *Numberical Recipes* (Press et al., 1995). The most updated copy of the code is located:
`http://www.physics.usyd.edu.au/~chiang/gaussfit.tar`.

B.1 Original code

This code implements the steps as listed in Fig. 2.1 in Ch. 2. It is based on a nonlinear fitting of Gaussian peaks and a background spectra, which matches visual inspection in clear cases of alpha peaks and provides automated, objective parameterization more generally. Information from multiple site are utilized to eliminate spurious peaks.

B.1.1 alpha.cpp

Power spectrum were parsed into a format that is readable by the main program in this code, and output of the resultant fitted parameters returned from the main program were formatted.

```
/** \defgroup alpha Standalone wrapper for gaussfit

\brief Program to identify and quantify the
alpha peak in spectra obtained from multiple
scalp sites
```

```
The function multiple_fitting() attempts to fit a
double gaussian fit to the power spectrum (log-log)
along all the site individually and then produce a
value to fit along all the site from the
weight-average of all the site.

To run: \code gaussfit [filename] [number of peaks]
[f1] [f2]
\endcode
where the filename identifies a file containing
multiple spectra, and with the format produced by
\c dumpch, e.g.

@code
   "sleepp3c.eeg sleepp3.prn sleepp3.tag  s-200.0
   w8192.0 a200.0 t0.0 r1 oas"
   ""
   "Sample",     "Freq",          "Fz",          "Cz", ....
   0,           0.00,          10.710,        15.219, ....
   :             :               :             :      ....
   :             :               :             :      ....
 409,          49.93,            7.267,         6.419, ....
@endcode

Two output files are generated:
        filename-ext.par.csv
    containing the fit parameters
        filename-ext.org.csv
    containing the input spectrum
where 'filename-ext' is the input filename minus
its extension (if any).

The general layout of.par.csv files is as follows
@code
0,1,2,3,4,5,6,7,8,9,10,11,12,13,14,15,16,17,18,
1.0, 0.,0.,1.0,0.,0.,1.,2.01,1.19, 0.,0.,0.,0.,0.,
        0.,0.,6.15, 0.00,0.00,
1.0, 0.,0.,2.0,0.,0.,1.,1.83,1.09, 0.,0.,0.,0.,0.,
        0.,0.,6.15, 0.00,0.00,
:
1.0, 1.13,13.90,3.45,0.88,5.74,2.53,0.12,0.64,
        0.00,6.00,-1.00,...,
@endcode
where each row corresponds to a recording site,
and within each row there is
(a) the number of peaks found, usually 1 or 2,
(b) eight parameters containing the peak1
amp+freq+width, peak2 amp+freq+width,
baseline intercept+slope,
```

```
(c) another 3*nLocalPeaks columns containing
group parameters,
(d) 2*nGlobalPeaks columns containing fitted freqs,
and (e) a column of zeros.
*/
/* @{ */

#if defined __unix
#include <fenv.h>      /* feenableexcept */
#endif
#include <math.h>
#include <stdio.h>
#include <stdlib.h>
#include <string.h>

/** \brief default datafile */
#define FILEREAD "cnl037ec.prn"

namespace gaussfit {
void multiple_fitting(const int sitesIP,
        const int number,
        const int nLocalPeaksIP,
        const int nGlobalPeaksIP,
    const double peakspread,
        // [0:number-1]
    const double *freqs,
        // [0:sites-1][0:number-1]
    const double **dataset,
        // [0:sites-1]
    const int *spatialGroup,
    const double minFreq,
    const double maxFreq,
    int& MA_IPOP,
    int &numberOfPeaks,
        // [0:2*mfit-1][0:sites-1]
    double **fparameters,
    double **linearFit,
    double **ipower,
        // [0:nGlobalPeaks-1][0:sites-1]
    double **absolutepower);
}



//----------------------------------------------------------------------------
/** \brief Create a matrix of doubles.

The matrix is addressed as m[row][col], and is
initialized to zero.
```

```
@param rows The first index can be 0; row ; rows-1
@param columns The second index can be 0 ; col ;
        columns-1
@return Reference to initialized array
@see free_matrix
*/
static double **create_matrix(int rows,
        int columns) {
        /* loop index */
    int i;
        /* pointer to new array */
    double **array;
    array =
        (double**)calloc(rows, sizeof(double *));
    for(i=0; i<rows; i++)
        array[i] =
                (double*)calloc(columns, sizeof(double));
    return array;
}



//------------------------------------------------------------------------------
/** \brief Frees a matrix of doubles created by
<tt>create_matrix</tt>.

After the heap memory is released the pointer is set
equal to NULL, to prevent accidental re-use.

@param array Reference to array
@param rows The first index can be 0; row; rows-1
@param columns The second index can be 0; col;
        columns-1
@see create_matrix
*/
static void free_matrix(double **array,
        int rows,
        int columns) {
    int i;                      /* loop index */
    // eliminates -Wunused-parameter warning
    columns = columns;
    for(i=0; i<rows; i++) free(array[i]);
    free(array);
}
```

```
//----------------------------------------------------------------------------
/** \brief the main program,

A filename can be input for the data, if no filename is
specified then the default would be used.
*/
int main(int argc, char *argv[])
{
        // Number of scalp sites: Fp1, Fp2, ... O2
    int sites;
        // Number of frequencies in spectra
    int number;
    int nLocalPeaks; int nGlobalPeaks;
    double minFreq, maxFreq;
        // Upper limit on MA
    const int MA_MAX=50;
    // toggle between normal output and debugging outputs
    int debugFlag=1;
    // Number of parameters (returned by fitting routine)
    int MA;
        // loop indices
    int i,j;
        // returned by peak fitting routine
    int numberOfPeaks;
    // [0:number-1]
    int *sample;
    // [0:number-1]
    double *freqs;
    // [0:sites-1][0:number-1]
    double **dataset;
    // [0:MA-1][0:sites-1]
    double **fittedparameters;
    // [0:nGlobalPeaks-1][0:sites-1]
    double **linearFit;
    // [0:nGlobalPeaks-1][0:sites-1]
    double **ipower;
    // [0:nGlobalPeaks-1][0:sites-1]
    double **absolutepower;
/*      char *columns[] = {"freq",
        "fp1",
        "fp2",
        "fz",
        "f3",
        "f4",
        "f7",
        "f8",
        "cz",
        "c3",
        "c4",
        "t3",
```

```
        "t4",
        "t5",
        "t6",
        "pz",
        "p3",
        "p4",
        "o1",
        "o2"};*/
    char line[320];
    char filenameFFT[FILENAME_MAX];
    char filenameout[FILENAME_MAX];

    double peakspread;

    FILE* eegdata;
    FILE* dataorg;
    FILE* dataparam;

#if defined __unix
    /* Enable some FP exceptions,
        but not FE_INEXACT
        or FE_UNDERFLOW */
    /* (This function is only accessible if
        _GNU_SOURCE is defined) */
    feenableexcept(
        FE_DIVBYZERO |
        FE_INVALID |
        FE_OVERFLOW );
#endif

    /* Scan data file to establish the dimensions
        of the data */
    sites = 19;
    /* This value _properly_ initialized below */
    number = 420;
    // Maximum number of peaks to attempt
    nLocalPeaks = nGlobalPeaks = 2;
    // Default peak width, in Hz
    peakspread = 1.0;
    minFreq = 4.0;
    maxFreq = 14.0;
    // This will updated by multiple_fitting()
    MA = MA_MAX;

    /* For 10/20 sites there are typically 5 spatial
      groups, and spatialGroup[] will consist of 19
      values from the set {-2,-1,0,1,2}, although
      only relative differences matter:
      i.e. values {10,20,30,40,50},
      would lead to the same result. */
```

```
    const int spatialGroup[] = {
        3,3,             //     Fp1 Fp2
        5,5,5,5,5,    // Fz F3 F4 F7 F8
        7,7,7,7,7,    // Cz C3 C4 T3 T4
        9,9,9,9,9,    // T5 T6 Pz P3 P4
        11,11};       //       O1 O2
    if(sizeof(spatialGroup)/sizeof(int) != sites) {
        printf(”#sites=%d␣”
                ”doesn't␣match␣size␣of␣spatialGroup[]\n”
                        ,sites);
        exit(2);
    }

    /* Read spectra */
    if (argc > 1) strcpy(filenameFFT, argv[1]);
    else strcpy(filenameFFT, FILEREAD);
    printf(”%s\n”, filenameFFT);
    eegdata = fopen(filenameFFT,”rt”);
    if(eegdata==NULL) {
        printf(”File␣not␣found\n”);
        exit(0);
    }
    fseek(eegdata,0,SEEK_SET);
    for (int i=1;
        i<=3;
        i++)
        // Skip 3 header lines
        fgets(line, sizeof(line), eegdata);
    for (int j=1;
        fgets(line,sizeof(line),eegdata) != NULL;
        j++)
                // This is the number of points in the spectra
        number = j;
    /* Create arrays */
    sample =
        (int*)calloc(number, sizeof(int));
    freqs =
        new double[number];
    dataset =
        create_matrix(sites, number);
    fittedparameters =
        create_matrix(MA_MAX, sites);
    linearFit =
        create_matrix(nGlobalPeaks,sites);
    ipower =
        create_matrix(nGlobalPeaks,sites);
    absolutepower =
        create_matrix(nGlobalPeaks,sites);

    /* Fill arrays */
```

```
fseek(eegdata,0,SEEK_SET);
for (int i=1;
     i<=3;
     i++)
             // Skip 3 header lines
     fgets(line,sizeof(line),eegdata);
for (j=0;
     fgets(line,sizeof(line),eegdata) != NULL;
     j++)
{
     sscanf (line, "%i,%lf,%lf,%lf,%lf,%lf,%lf,"
             "%lf,%lf,%lf,%lf,%lf,%lf,%lf,%lf,%lf,"
             "%lf,%lf,%lf,%lf,%lf",
          &sample[j],&freqs[j],
          &dataset[0][j],
          &dataset[1][j],
          &dataset[2][j],
          &dataset[3][j],
          &dataset[4][j],
          &dataset[5][j],
          &dataset[6][j],
          &dataset[7][j],
          &dataset[8][j],
          &dataset[9][j],
          &dataset[10][j],
          &dataset[11][j],
          &dataset[12][j],
          &dataset[13][j],
          &dataset[14][j],
          &dataset[15][j],
          &dataset[16][j],
          &dataset[17][j],
          &dataset[18][j]);
}
fclose(eegdata);

gaussfit::multiple_fitting(sites,
                           number,
                           nLocalPeaks,
                           nGlobalPeaks,
                           peakspread,
                           (const double*)freqs,
                           (const double**)dataset,
                           spatialGroup,
                           minFreq, maxFreq,
                           MA,
                           numberOfPeaks,
                           fittedparameters,
                           linearFit,
                           ipower,
```

```
                               absolutepower);

    /* Write parameter file */
    if (debugFlag == 1)
    {
        strcpy(filenameout, filenameFFT);
        i = (strrchr(filenameout,’.’)!= NULL)?
            strrchr(filenameout,’.’)−filenameout:
            strlen(filenameout);
        strcpy(&filenameout[i],”.dbg.csv”);

        dataparam = fopen(filenameout,”w+”);
        for (i = 0; i<=MA+3; i++)
                fprintf(dataparam, ”%i,”,i);
        fprintf(dataparam,”\n”);
        for (i = 0; i<sites; i++)
        {
            fprintf(dataparam,
                ”%f,”,
                (double)numberOfPeaks);
            for (j = 0; j<MA; j++)
                fprintf(dataparam,
                        ”%f,”,
                        fittedparameters[j][i]);
            for (j = 0; j<3; j++)
                fprintf(dataparam, ”%f,”,
                        ((j<nGlobalPeaks)?
                                linearFit[j][i]: 0.0));
            fprintf(dataparam,”\n”);
        }
        fclose(dataparam);
    } else if (debugFlag == 0)
    {
        strcpy(filenameout, filenameFFT);
        i = (strrchr(filenameout,’.’)!= NULL)?
            strrchr(filenameout,’.’)−filenameout:
            strlen(filenameout);
        strcpy(&filenameout[i],”.par.csv”);

        dataparam = fopen(filenameout,”w+”);
        for (int sitecount =0;
                sitecount < sites;
                sitecount++)
        {
            for (int peakcount =0;
                    peakcount < nLocalPeaks;
                    peakcount++)
            {
                fprintf(dataparam, ”%f,”,
                        absolutepower[peakcount][sitecount]);
```

```
                fprintf(dataparam, ”%f,”,
                        ipower[peakcount][sitecount]);
                for (j=0;j<3;j++)
                {
                    fprintf(dataparam, ”%f,”,
                            fittedparameters[j+peakcount*3]
                            [sitecount]);
                }
            }
            fprintf(dataparam,”\n”);
        }
        fclose(dataparam);
    }


    /* Write orig file */
    strcpy(filenameout, filenameFFT);
    i = (strrchr(filenameout,’.’)!= NULL)?
        strrchr(filenameout,’.’)-filenameout:
        strlen(filenameout);
    strcpy(&filenameout[i],”.org.csv”);

    dataorg = fopen(filenameout,”w+”);
    for (i = 0; i<number; i++)
    {
        fprintf(dataorg, ”%f,”,freqs[i]);
        for (j = 0; j<sites; j++)
            fprintf(dataorg, ”%f,”,dataset[j][i]);
        fprintf(dataorg,”\n”);
    }
    fclose(dataorg);

    /* Free arrays */
    free(sample);
    delete[] freqs;
    free_matrix(dataset, sites, number);
    free_matrix(fittedparameters, MA_MAX, sites);
    free_matrix(linearFit, nGlobalPeaks, sites);
    return 0;
}


/* @} */
```

B.1.2 gaussfit.cpp

This is the main working part of the program, with the individual spectra fitted nonlinearly with up to two Gaussian and a background power law. The resultant individually fitted parameters are then analyzed based on their spectral proximity to each other, which results in up two two peak clusters, and their respective parameters are then outputted.

```
/** \defgroup gaussfit Gaussfit: Alpha peak
fitting routine

@brief Routine to identify and quantify the
        alpha peak in spectra obtained from multiple
        scalp sites

It attempts to fit a double gaussian fit to the power
spectrum (log-linear) along all the sites individually
and then produce a value to fit all the sites from
the weighted-average value from all the sites

internal call structure:

\verbatim
multiple_fitting
|
|- ranges
|
|- smooth
|
|- site_guess
|
|- fitting
|     |
|     |- mrqmin (Numerical Recipes)
|
|- peak_sort
      |
      |- simple_clustering
      |            |
      |            |-bubble_sort
      |
      |- bubble_sort
      |
      |- medfit (Numerical Recipes)
\endverbatim


\version
20060628 - Change back to logP_raw=P_fit from
previous version, modify the termination criteria for
the fitting loops to be dependent more on the
repetition of the parameters rather than the hard
value of 100 loops

\version
20060619 - Change the background fitting algorithm
```

```
from utilising the mrqmin routine with initializing
parameters at the endpoint of the region of interest
to a simple linear regression of the log(P) log(f)
spectrum

\version
20060703 - Modify peaksort() to use a 3D matrix
instead of the bitwise operation: to ensure the
extendability of the program beyond 31 sites.
Minor adjustment with the peaksort() routine to
rule out ignorable trends earlier

\version
20061124 - Integrated with changes made to
peaksort()

\version
20070131 - Redo the iterative loop where the
residue is obtain: Instead of taking the residue with
the subsequent problem of negative values simply
leave the parameters in place holding them fixed,
this might be able to solve the previous problem of
fitting the logP_raw = logP_fit because it negates
the problem previously encountered.

\version
20070206 - Re-attempt to implement
logP_raw=logP_fit

\version
20070228 - Revert to logP_raw=P_fit

\version
20070814 - Changed multifitting() so the
convergency criteria depends on all three peak
parameters (power, freq, sd) [inner loop], and the
background param (normalization, power)
[outer loop]

\version
20070815 - Changed the fitting() routine, instead
of quitting the loop when the successive fits chi^2
values are within xx for 10 times in a roll, loop 100
 times where successive fits chi^2 values are
 smaller

\version
20070817 - Clean up the code, remove
unnecessary included functions (fit.c). Rewrote
peaksort(), assign 0->1 instead of 1->5 for
```

```
the sitenumber values, generalise to remove
ambiguities (nPeaks instead of using 2, etc)

\version
20071113 - General cleanup, generalise peaksort()
to be able to take any nPeaks value

\version
20071119 - Modularize bubble_sort, and simple
clustering algorithm, consolidate output file to
par.csv, [mfit+1][site] = groupid, etc

\version
20071204 - Converted to C++, and to use the C++
version of Numerical Recipes

\version
20080423 - Removed bubble_sort, utilizing built in
qsort function

\version
20080507 - Minor bug fixes

*/
/* @{ */

#include <stdarg.h>
#include <stdlib.h>
#include <stdio.h>
#include <stddef.h>
#include <math.h>
#include <string.h>
#include <ctype.h>
#include "nr.h"

namespace gaussfit {

/** Macro for swapping the values in two
        double variables */
#define SWAP(a,b) {
        double temp=(a);(a)=(b);(b)=temp;}
/** Macro for swapping the values in
        two int variables */
#define SWAP_INT(a,b) {
        int temp=(a);(a)=(b);(b)=temp;}

/** \brief Number of parameters describing each
        Gaussian component */
const int nGaussPar = 3;
/** \brief Number of baseline params:
```

```
         intercept, 1st order, 2nd order */
const int nBasePar = 3;
/** \brief Number of group parameters:
         index, nSpatiallyDistinctGroups, avHz */
const int nGroupPar = 3;
/** \brief Constant used to make indexing of
         paramter arrays more readable */
const int power = 1;
/** \brief Constant used to make indexing of
         paramter arrays          more readable */
const int freq = 2;
/** \brief Constant used to make indexing of
         paramter arrays          more readable */
// putting names to the variables
const int sd = 3;
// Number of scalp sites: Fp1, Fp2... O2
static int sites;
// Number of peaks to be fitted (should be 2)
//static int nPeaks;
// Number of peaks to be fitted per spectrum
static int nLocalPeaks;
// Number of peaks to be fitted globally
static int nGlobalPeaks;
// nLocalPeaks*nGaussPar+nBasePar
static int fitparam;
// 2*fitparam
static int MA;
// Resolution of spectra, in Hz, inferred from freqs
static double fresolution;

/** \brief Contains flag, set by NR::gaussj() */
// Singular Matrix error (gaussj.c) check
bool fitsuccess;


/*----------------------------------------------------------------------------------------
  Utility routines copied from Numerical Recipes in C
----------------------------------------------------------------------------------------*/

/** \brief Generalization of the general-purpose
Numerical Recipes exception handler.
*/
static void nrerror(char *fmt, ...) {
    /* construct error messages, and then either throw
       exceptions or print it to stderr -- depending on
       whether BRC/C++ or Unix/C Environment */
    char ErrMsg[512];
    int nc;
    va_list args;
    va_start(args, fmt);
```

```
    nc = vsnprintf(ErrMsg, sizeof(ErrMsg), fmt, args);

    /* nc <0 indicates a formatting or output problem */
    /* nc > sizeof(ErrMsg) indicates buffer too short;
        but is benign */

#ifdef __BCPLUSPLUS__

    if (nc<0)
        throw IseException(
                "Fatal␣error␣in␣gaussfit,␣plus␣vsnprintf␣error");
    else
        throw IseException(ErrMsg);
#else
    fprintf(stderr,"Run-time␣error␣within␣gaussfit..\n");
    if (nc<0)
        fprintf(stderr,
                "Fatal␣error␣in␣gaussfit,␣plus␣vsnprintf␣error");
    else
        fprintf(stderr,"%s\n",ErrMsg);
    fprintf(stderr,"..now␣exiting␣to␣system...\n");
    exit(2);
#endif
}

/** \brief Specific to Numerical recipes array
        allocation routines */
#define NR_END 1
/** \brief Specific to Numerical recipes array
        allocation routines */
#define FREE_ARG char*

/** \brief See Numerical Recipes */
static double *vector(long nl, long nh) {
    /* allocate a double vector with subscript
        range v[nl..nh] */
    double *v;
    v = (double *)malloc((size_t)
        ((nh-nl+1+NR_END)*sizeof(double)));
    if (!v) nrerror("allocation␣failure␣in␣vector()");
    return v-nl+NR_END;
}

/** \brief See Numerical Recipes */
static int *ivector(long nl, long nh) {
    /* allocate an int vector with subscript
        range v[nl..nh] */
    int *v;
    v = (int *)malloc((size_t)
        ((nh-nl+1+NR_END)*sizeof(int)));
```

```
    if (!v) nrerror("allocation␣failure␣in␣ivector()");
    return v-nl+NR_END;
}

/** \brief See Numerical Recipes */
static void free_vector(double *v,
        long nl,
        long nh) {
    /* free a double vector allocated with vector() */
    free((FREE_ARG) (v+nl-NR_END)); nh=nh;
}

/** \brief See Numerical Recipes */
static void free_ivector(int *v,
        long nl,
        long nh) {
    /* free an int vector allocated with ivector() */
    free((FREE_ARG) (v+nl-NR_END)); nh=nh;
}

#undef NR_END
#undef FREE_ARG

/* end of utility routines */




//--------------------------------------------------------------------------------
/** \brief Locates the maximum of an array
@param An array to be examined
@return The index (in the range 0..x.size()-1) of
        the array's maximum
*/
static int maximum(Vec_I_DP &x)
{
    int maxsub=0;
    double max=x[0];
    for (int i=0; i<x.size(); i++)
    {
        if (x[i]>=max)
        {
            max = x[i];
            maxsub = i;
        }
    }
    return maxsub;
}
```

```
//—————————————————————————————————————————————————————————————————————
/** \brief Forces an input value to be positive.

This subroutine returns the absolute value of the input.

@param x the value to be forced to be positive
@return either the input value (if it is already positive),
        or abs(x)
*/
inline double pbound(double x)
{
    /* forcing the value to stay positive */
    return fabs(x);
}



//—————————————————————————————————————————————————————————————————————
/** \brief Forces the gradient value to be positive
        one (to keep consistant of the forced
        positive value.

@param x bounds contains the input values, where
        x is the given value and
        bound is a value used to bound the limit of x,
        both of which is not used in this program
*/
inline double dyda_pbound(double x)
{
    if (x>=0) return 1;
    else return −1;
}



//—————————————————————————————————————————————————————————————————————
/** \brief Smoothing function

Performs a boxcar filter on the specified array.
The length of the (symmetric) boxcar is 2*param+1.

@param array Array to be smoothed
@param param The length of the boxcar filter
        is 2*param+1. The value of this argument must
        be greater of equal to zero.
*/
```

```
static void smooth(Vec_IO_DP &array,
                 const int param)
{
    Vec_DP smoothedarray(array.size());

    for (int i=0; i<array.size(); i++)
    {
        double tempvalues = 0.0;
        int tempcount = 0;
        for (int j= -param; j<=param; j++)
        {
            if (((i+j) >= 0) && ((i+j) < array.size()))
            {
                tempvalues += array[i+j];
                tempcount++;
            }
        }
        smoothedarray[i] = tempvalues/tempcount;
    }

    for (int i=0; i<array.size(); i++) array[i] =
        smoothedarray[i];
}



//--------------------------------------------------------------------------------
/** \brief Produces a fitted spectra given one
        frequency and model parameters.

The equation fitting the spectrum is
\verbatim
y = A*exp(-((x-B)/C)^2) +
          D*exp(-((x-E)/F)^2) +
      G + H*x + I*x^2
\endverbatim
a modified double gaussian, with
A and D being amplitude,
B and E being the central frequency, and
C and F the width; plus an underlying
quadratic spectrum.

a[1:mfit] contains the variables.
a[1] to a[6] contains the variables associated with the
        double gaussian,
a[1] and a[4] being the amplitude,
a[2] and a[5] being the frequency,
a[3] and a[6] being the width of the gaussian peaks
a[7] to a[9] specifies the quadratic parameters,
```

```
a[7] is the constant,
a[8] and a[9] the coefficent of the linear and
        quadratic term respectively.

The higher values of this variable a[i+mfit] is the
bound for the respective variables i, not used in
this program

@param x log10 of a frequency in Hz
@param a set of parameters, [1:2*mfit]
*/
static double fitted(double x,
                     double a[])
{
        // internal variables for calculations
    double curvefit = 0.0, ex, arg;
    for (int i3 = 0;
        i3<nLocalPeaks*nGaussPar;
        i3+=nGaussPar)
    {
                // skip disabled peaks
        if(a[i3+sd]==0.0) continue;
        arg = (x-pbound(a[i3+freq]))/pbound(a[i3+sd]);
        ex = exp(-arg*arg);
        curvefit +=  pbound(a[i3+power])*ex;
    }
    curvefit += a[nLocalPeaks*nGaussPar+1]-
        pbound(a[nLocalPeaks*nGaussPar+2])*log(x);

    return curvefit;
}



//--------------------------------------------------------------------------
/** \brief Evaluates the model spectrum

This routine evaluates the function
\verbatim
  y  =  A*exp(-((x-B)/C)^2) +
        D*exp(-((x-E)/F)^2) +
                G*x^H
\endverbatim
a modified double gaussian, with A and D being
amplitude, B and E being the central frequency, and
C and F an indication of the spread of the
two gaussians; plus an underlying
power-law spectrum.
```

```
@param x Input frequency
@param a Model parameters.
        a[0] to a[5] contains the variables associated with
        the double gaussian, with
        a[0] and a[3] being the amplitude,
        a[1] and a[4] being the frequency,
        a[2] and a[5] being the width,
        a[6] to a[8]    specifies the quadratic parameters,
        where a[6] is the constant,
        a[7] and a[8] the coefficent of the
        linear and quadratic term.
@param y Output frequency
@param dyda Partial derivatives of y with respect to
        each parameter, [0:mfit-1]
*/
static void fgauss(const DP x,
        Vec_I_DP &a, DP &y,
        Vec_O_DP &dyda)
{
    y = 0.0;
    for (int i3 = 0;
        i3 < nLocalPeaks*nGaussPar;
        i3 += nGaussPar)
    {
        // skip disabled peaks
        if(a[i3+sd-1]==0.0) {
            dyda[i3+power-1] = 0;
            dyda[i3+freq-1] = 0;
            dyda[i3+sd-1] = 0;
            continue;
        }

        double arg = (x-pbound(a[i3+freq-1]))/
                pbound(a[i3+sd-1]);
        double ex = exp(-arg*arg);
        double fac =
                pbound(a[i3+power-1])*ex*2.0*arg;

        y += pbound(a[i3+power-1])*ex;
        dyda[i3+power-1] =
                ex*dyda_pbound(a[i3+power-1]);
        dyda[i3+freq-1] =
                fac*dyda_pbound(a[i3+freq-1])/
                pbound(a[i3+sd-1]);
        dyda[i3+sd-1] =
                fac*arg*dyda_pbound(a[i3+sd-1])/
                pbound(a[i3+sd-1]);
    }

    y += a[nLocalPeaks*nGaussPar+1-1]-
```

```
         pbound(a[nLocalPeaks*nGaussPar+2-1])*log(x);
    dyda[nLocalPeaks*nGaussPar+1-1] = 1;
    dyda[nLocalPeaks*nGaussPar+2-1] =
        -dyda_pbound(a[nLocalPeaks*nGaussPar+2-1])*
        log(x);

}



//--------------------------------------------------------------------------------
/** \brief Computes the indices corresponding to the
        given range of freqs

@param datax Input frequency values:
        [0:number-1]
@param number Number of points in datax[]
@param minFreq Lowest frequency of interest,
        e.g. 4 Hz
@param maxFreq Highest frequency of interest,
        e.g. 14 Hz
@param iLo Lower limit of spectral region of interest,
        0..number-1
@param iHi Upper limit of spectral region of interest,
        0..number-1
*/
static void ranges(const double datax[],
        const int number,
    const double minFreq,
    const double maxFreq,
    int &iLo, int &iHi)
{
    // Set range initially to a limiting value
    iLo = iHi = 0;
    for (int i=0; i<number; i++)
    {
        if ((datax[i] <= minFreq) && (iLo<i)) iLo = i;
        if ((datax[i] <= maxFreq) && (iHi<i)) iHi = i;
    }
}



//--------------------------------------------------------------------------------
/** \brief the main fitting routine

This routine takes in the dataset, calculates the fitting
parameters to the modified double gaussian curve,
```

```
calculate the fitted spectrum and return them to the
respective variables.

gues: 1-power 1, 2-freq 1, 3-sd 1, 4-power 2, 5-freq 2,
       6-sd 2, 7-normal, 8-powergrad, 9-powergrad^2

@param dataX are the frequency values:
        [0:number-1] input
@param dataY are the power values:
        [0:number-1] input
@param gues is the initial guess parameters:
        [1:2*mfit] input and modified
@param ia is the mrqmin variable control:
        [1:2*mfit] input
*/
static double fitting(Vec_I_DP &dataX,
        Vec_I_DP &dataY,
        double *gues,
        int *ia)
{
    Vec_DP guesVec(MA);
    Vec_BOOL iaVec(MA);
    for(int i=1; i<=MA; i++) {
        guesVec[i-1] = gues[i];
        iaVec[i-1] = (ia[i]!=0);
    }

    Vec_DP sigVec(dataY.size());
    sigVec = 1.0;

    int itst = 0;
    double alamda = -1;
    double chisq = 0;
 // This is a global variable, modifiable by gaussj()
    fitsuccess = true;

    Mat_DP covar(MA,MA), alpha(MA,MA);

    NR::mrqmin(dataX,
        dataY,
        sigVec,
        guesVec,
        iaVec,
        covar,
        alpha,
        chisq,
        fgauss,
        alamda);

    for (int k=0; ; k++)
```

```
    {
        double chisqck = chisq;
        NR::mrqmin(dataX,
                dataY,
                sigVec,
                guesVec,
                iaVec,
                covar,
                alpha,
                chisq,
            fgauss,
            alamda);
        if (chisq > chisqck) itst = 0;
        else if (fabs(chisq-chisqck) <
                chisq*0.0001) itst++;

        if (!fitsuccess || itst>10) break;
    }

    if (fitsuccess)
    {
        alamda = 0.0;
        NR::mrqmin(dataX,
                dataY,
                sigVec,
                guesVec,
                iaVec,
                covar,
                alpha,
                chisq,
            fgauss,
            alamda);
    }

    for(int i=1; i<=MA; i++)
        gues[i] = guesVec[i-1];

    return chisq;

}



//--------------------------------------------------------------------------------
/** \brief Comparison function for use with
        <tt>qsort</tt>.
@param a One \c int value
@param b Another \c int value
@return Negative if \htmlonly a &lt; b \endhtmlonly
```

```
        zero if \c a==b; Positive if \htmlonly a &gt;
        b \endhtmlonly
*/
int compare_ints(const void *a,
        const void *b)
{
    const int *ia = (const int *)a;
    const int *ib = (const int *)b;
    return (*ia>*ib)-(*ia<*ib);
}



//---------------------------------------------------------------------------------
/** \brief Comparison function for use with
        <tt>qsort</tt>.
@param a One \c int value
@param b Another \c int value
@return Negative if \htmlonly a &lt; b \endhtmlonly
        zero if \c a==b;
        Positive if \htmlonly a &gt; b \endhtmlonly
*/
int compare_dbls(const void *a, const void *b)
{
    const double *ia = (const double *)a;
    const double *ib = (const double *)b;
    return (*ia>*ib)-(*ia<*ib);
}



//---------------------------------------------------------------------------------
/** \brief a simple clustering method

This function works by looking at the difference in
frequency of the spectrally adjacent peaks
*/
int simple_clustering(
        // [1:sizeofx]              in
        double *x,
        // [1:sizeofx]              in/out
        int *xmap,
        // [1:sizeofx]              out
    int *xgroup,
    //                                    in
    int sizeofx,
    //                                    in
    double xres)
```

```
{
    double avgdiff=0.0;
    int totalgroups;

    // rearrange in terms of smallest to largest
    double *xtemp = vector(1,sizeofx);

    for (int i=1; i<=sizeofx; i++) xtemp[i] = x[i];

    qsort(xtemp, sizeofx+1,
        sizeof(double), compare_dbls);

    for (int i=1; i<=sizeofx; i++)
    {
        for (int j=1; j<=sizeofx; j++) if
                (xtemp[j] == x[i]) xmap[j]=i;
    }

    // evaluate the average difference
    // between successive term

    for (int i=1; i<sizeofx; i++)
        avgdiff += fabs(x[xmap[i]]-
                x[xmap[i+1]])/(sizeofx -1);

    /* assign group based on criteria >
    avg diff => new group difference of
    successive term > xresolution * 2 */

    int j = 1;

    for (int i=1; i<=sizeofx; i++)
    {
        xgroup[i] = j;
        if (i < sizeofx)
        {
            if ((avgdiff < fabs(x[xmap[i]]-
                        x[xmap[i+1]])) &&
                (2*xres < fabs(x[xmap[i]]-
                        x[xmap[i+1]]))) j++;
        }
    }

    totalgroups = j;

    return totalgroups;
}
```

```
//----------------------------------------------------------------------
/** \brief Chooses initial values for peak freq and
        amplitude by looking for the peak of the specified
        spectrum.

@param dataX Array of frequency values, in Hz
@param dataY Array of powers corresponding to
        datax
@param initialFreq The frequency, in Hz, of the peak
@param initialPower The spectral power
        corresponding to the peak frequency
*/
void site_guess(Vec_I_DP &dataX,
                Vec_I_DP &dataY,
                double &initialFreq,
                double &initialPower)
{
    int maxysub = maximum(dataY);

    initialFreq = dataX[maxysub];
    initialPower = dataY[maxysub];
}



//----------------------------------------------------------------------
/** \brief Peak verification step

Fitted peaks are verified with information from
multiple electrode sites. only peaks with a span of
at least 4 sites, and 2 'x' position are accepted as
a real peak (in contrast to noise). Trends in the
cluster(s) of peaks are evaluated to produce
the **exfreq estimates

@param param Input: all scores from fitting
        individual spectra.
        Output: some modified version
@param spatialGroup Site locations on arbitrary scale
@return Refined estimate of the number of peaks
*/
int peak_sort(
        double **param, // [0:2*mfit-1][0:sites-1]   in/out
        // [0:sites-1]
        const int *spatialGroup,
        // [0:nGlobalPeaks-1][0:sites-1]
        double **linearFit)
{
```

```
     // output the actual number of peaks
int numberofpeaks=0;
     // number of valid peaks
int validpeakcount=0;
     // total number of clusters
int totalgroups=0;
     // [1:totalgroups]
double *freqgroupavg, *groupcount;
     // [1:totalgroups]
int *siteNumberCount;
double tgrad, tintc, tabdev;
double *freqgroupsd;

/* Inspect spatialGroup[] to determine how
many locations are defined (int nSpatialGroups)
and the values identifing each group
(int spatialGroupValues[nSpatialGroups]).  For
10/20 sites  nSpatialGroups=5 typically, and
spatialGroupValues[]={-2,-1,0,1,2}, although
only relative differences matter:
i.e. values {10,20,30,40,50},
would lead to the same result. */
int nSpatialGroups = 1;
for(int m=1; m<sites; m++) {
     bool found = false;
     for(int mm=0; mm<m; mm++)
          found = found || (spatialGroup[mm]==
               spatialGroup[m]);
     if(!found) nSpatialGroups++;
}
int *spatialGroupValues = new int[nSpatialGroups];
spatialGroupValues[0] = spatialGroup[0];
nSpatialGroups = 1;
for(int m=1; m<sites; m++) {
     bool found = false;
     for(int mm=0; mm<m; mm++)
          found = found || (spatialGroup[mm]==
               spatialGroup[m]);
     if(!found) {
          spatialGroupValues[nSpatialGroups] =
               spatialGroup[m];
          nSpatialGroups++;
     }
}
// Make spatialGroupValues[] monotonic
qsort(spatialGroupValues,
     nSpatialGroups,
     sizeof(int),
     compare_ints);
```

```
int spatialRange=
    spatialGroupValues[nSpatialGroups-1]-
            spatialGroupValues[0];

for (int j=0; j<nLocalPeaks*sites; j++)
{
    if (fabs(param[freq+
            (j/sites)*nGaussPar-1][j%sites]) > 0.0)
    {
        validpeakcount++;
    }
}

/* Arrange frequency from small to large, by
looking at the difference between successive
frequencies and subsequently the average of
the difference. We can rule out any points that
are further than the average of the difference,
and hence put the frequencies in different
groups, and judge which ones are relevent */

if (validpeakcount > 1)
{
    double *freqtemp =
            vector(1,validpeakcount);
    int *freqmark =
            ivector(1,validpeakcount);
    int *freqgroup =
            ivector(1,validpeakcount);
    int *freqmap =
            ivector(1,validpeakcount);

    // for (int m=1; m<=validpeakcount; m++)
    //      freqmap[m] = m;

    // assign frequency to a temp variable
    //      (freqtemp) keep track using freqmark

    for (int j=0,m=1; j<nLocalPeaks*sites; j++)
    {
        if (fabs(param[freq+
                    (j/sites)*nGaussPar-1][j%sites]) >
            0.0)
        {
            freqtemp[m] =
                    param[freq+(j/sites)*nGaussPar-1]
                            [j%sites];
            freqmark[m] = j+1;
            m++;
        }
```

```
    }

    // sort frequencies into clusters (simple method)

    totalgroups = simple_clustering(freqtemp,
            freqmap,
            freqgroup,
            validpeakcount,
            fresolution);

    freqgroupavg = vector(1,totalgroups);
    freqgroupsd = vector(1,totalgroups);
    groupcount = vector(1,totalgroups);
    siteNumberCount = ivector(1,totalgroups);

    // work out group averages / group counts

    for (int j=1; j<=totalgroups; j++)
    {
        // average frequency with each group

        freqgroupavg[j] = 0.0;
        freqgroupsd[j]=0.0;
        groupcount[j] = 0.0;
        for (int m=1;
            m<=validpeakcount;
            m++)
        {
            if (freqgroup[m]==j)
            {
                freqgroupavg[j] +=
                    freqtemp[freqmap[m]];
                groupcount[j] += 1.0;
            }
        }
        freqgroupavg[j] =
            freqgroupavg[j]/groupcount[j];

        for (int m=1;
            m<=validpeakcount;
            m++)
        {
            if (freqgroup[m]==j)
            {
                freqgroupsd[j] +=
                (freqtemp[freqmap[m]]-
                    freqgroupavg[j])*
                    (freqtemp[freqmap[m]]-
                            freqgroupavg[j]);
            }
```

```
    }

    freqgroupsd[j]=
        sqrt(freqgroupsd[j]/groupcount[j]);

    // printf("%f\n", freqgroupsd[j]);

    /* count how many different spatial groups
    contribute to each frequency cluster.  Ignore
    those spread over < 2 spatial groups. */
    const int freqClusterSpatialThreshold = 2;
    siteNumberCount[j] = 0;
    if (groupcount[j] >=
        freqClusterSpatialThreshold) {
        for(int i=0;
                i<nSpatialGroups;
                i++) {
            for (int m=1;
                m<=validpeakcount;
                m++) {
                        int site =
                                (freqmark[
                                        freqmap[m]]-1)
                                %sites;
                        if(spatialGroup[site]==
                                spatialGroupValues[i] &&
                                freqgroup[m]==j) {
                                siteNumberCount[j]++;
                    break;
                }
            }
        }
    }
}

/* Eliminating peaks: we want clusters
to contain at least four peaks, from at least
2 (x) locations */

const int freqClusterSizeThreshold = 4;
const int freqClusterSpatialThreshold = 2;
for (int m=1; m<=validpeakcount; m++)
{
    if ((groupcount[freqgroup[m]]<
                freqClusterSizeThreshold) ||
                (siteNumberCount[freqgroup[m]]<
                freqClusterSpatialThreshold))
    {
        // eliminate group that lies within the criteria
        for (int mm=1;
```

```
                mm<=validpeakcount;
                mm++)
        {
            if (freqgroup[mm] ==
                freqgroup[m])
            {
                // negate freqmark and groupcount to
                // indicate elim
                freqmark[freqmap[mm]] =
                        -abs(freqmark[
                        freqmap[mm]]);
                groupcount[freqgroup[mm]] =
                    -fabs(groupcount[
                    freqgroup[mm]]);
            }
        }
    }
}

// rank the group by their size
int *grouprank = ivector(1,totalgroups);
double *groupcounttemp =
        vector(1,totalgroups);

for (int m=1; m<=totalgroups; m++)
    groupcounttemp[m] = fabs(groupcount[m]);

qsort(groupcounttemp,
        totalgroups+1 ,
        sizeof(double),
        compare_dbls);

for (int i=1; i<=totalgroups; i++)
{
    for (int j=1; j<=totalgroups; j++)
        if (groupcounttemp[i] ==
                fabs(groupcount[j]))
                grouprank[i]=j;
}

for (int m=1; m<=totalgroups; m++)
    if (groupcount[grouprank[m]] < 1)
        grouprank[m]=0;

// get the frequencies in groups
for (int i=1; i<=nGlobalPeaks; i++)
{
    tintc = tgrad = tabdev = 0.0;

    /* 20080507: corrected from totalgroups>i,
```

```
which would result in the algorithm skipping
if there is only 1 group present*/

if (totalgroups>=i)
{
    if (grouprank[totalgroups-(i-1)] != 0)
    {
        Vec_DP trendX((int)
            groupcount[
                    grouprank[totalgroups-(i-1)]]);
        Vec_DP trendY((int)
            groupcount[
                    grouprank[totalgroups-(i-1)]]);

        for (int m=1,
            next=1;
            m<=validpeakcount;
            m++)
        {
            if (freqgroup[m] ==
                    grouprank[totalgroups-(i-1)])
            {
                int j =
                    freqmark[freqmap[m]]-1;
                trendX[next-1] =
                    (double)spatialGroup[j%sites];
                trendY[next-1] =
                    freqtemp[freqmap[m]];
                next++;
            }
        }

        // linear fit to group 1
        NR::medfit(trendX,
            trendY,
            tintc,
            tgrad,
            tabdev);

        /* accept fit if the spatial frequency
        gradient is less than 2Hz per 25%
        division, or 8 Hz across all sites */
        if (fabs(tgrad)*spatialRange<8.0)
            numberofpeaks++;

    }
}

// output linear fit to frequencies
for (int j=0; j<sites; j++)
```

```
            {
                linearFit[i-1][j] = tintc +
                        tgrad*spatialGroup[j];
            }
        }

        // output group parameters to **param
        for (int m=1; m<=validpeakcount; m++) {

            int row = fitparam +
                (abs(freqmark[freqmap[m]])-1)/sites*
                nGroupPar;
            int col =
                (abs(freqmark[freqmap[m]])-1)%sites;
            param[row+0][col] =
                freqgroup[m];
            param[row+1][col] =
                groupcount[freqgroup[m]];
            param[row+2][col] =
                freqgroupavg[freqgroup[m]];
        }

        free_ivector(grouprank,1,totalgroups);

        free_vector(freqtemp,1,validpeakcount);
        free_ivector(freqmark,1,validpeakcount);
        free_ivector(freqgroup,1,validpeakcount);
        free_ivector(freqmap,1,validpeakcount);

        free_vector(freqgroupavg,1,totalgroups);
        free_vector(freqgroupsd,1,totalgroups);
        free_vector(groupcount,1,totalgroups);
        free_ivector(siteNumberCount,1,totalgroups);
    }
    else numberofpeaks = 0;

    delete[] spatialGroupValues;
    return numberofpeaks;
}



//------------------------------------------------------------------------------
/** Routine to check the input arguements of
multiple_fitting(). The various checks are mainly a
guard against un-subtle errors. The compiler will not
be able to pick up all of these.  Also we make explicit
certain requirements like monotonic-increasing,
equally-spaced frequencies.
```

```
@param sites Number of EEG spectra to be fitted
@param number Number of points in each spectrum
@param nLocalPeaksIP <b>Maximum</b> number
        of peaks to attempt to fit per spectrum
@param nGlobalPeaksIP <b>Maximum</b> number
        of peaks to attempt to fit globally
@param peakspread Default peak width in Hz: SD
        of fitted Gaussian
@param freqs Frequencies, in Hz, corresponding
        to spectra
@param spatialGroup Each site is assigned an
        integer that:
        (a) identifies a spatially-close subset of sites; and
        (b) serves as the independent variable in the
        regression in which frequency is the dependent
        variable
@param minFreq Lowest frequency of interest,
        eg 4.0 Hz
@param maxFreq Highest frequency of interest,
        eg 14.0 Hz
@param MA Number of available rows in
        <tt>fparameters</tt>.
*/
void checkInput(int sites,
        int number,
        int nLocalPeaks,
        int nGlobalPeaks,
    double peakspread,
    const double *freqs,
        const int *spatialGroup,
        double minFreq,
        double maxFreq, int& MA) {
    const char *where =
        ”In␣gaussfit::multiple_fitting()”;
    if(sites<=0)
        nrerror(
                ”%s:␣arg␣’sites’␣must␣be␣>␣0”,
                where);
    if(number<=4)
        nrerror(
                ”%s:␣arg␣’number’␣must␣be␣>␣4”,
                where);
    if(nLocalPeaks<=0)
        nrerror(
                ”%s:␣arg␣’nLocalPeaks’␣must␣be␣>␣0”,
                where);
    if(nGlobalPeaks<=0)
        nrerror(
                ”%s:␣arg␣’nGlobalPeaks’␣must␣be␣>␣0”,
```

```
                where);
    if(peakspread<=0)
        nrerror(
                "%s:␣arg␣'peakspread'␣must␣be␣>␣0",
                where);

    for(int i=0; i<number; i++)
        if(freqs[i] < 0)
             nrerror(
                "%s:␣arg␣'freqs[]'␣must␣be␣positive",
                where);
    for(int i=1; i<number; i++)
        if(freqs[i-1] >= freqs[i])
             nrerror(
                "%s:␣arg␣'freqs[]'␣must␣be␣"
                "monotonic␣increasing",where);
    double fresolution =
        (freqs[number-1]-freqs[0])/(number-1);

    for(int i=1; i<number; i++)
            // tolerance, Hz
        if(fabs((freqs[i]-freqs[i-1]) - fresolution) > 0.01)
            nrerror("%s:␣arg␣'freqs[]'␣"
                "must␣increment␣uniformly",where);

    int nSpatialGroups = 1;
    for(int m=1; m<sites; m++) {
        bool found = false;
        for(int mm=0; mm<m; mm++)
            found = found ||
                (spatialGroup[mm]==spatialGroup[m]);
        if(!found) nSpatialGroups++;
    }
    if(nSpatialGroups==1)
        nrerror(
                "%s:␣arg␣'spatialGroup'␣expresses␣"
                "only␣one␣group", where);

    if(minFreq<freqs[0]) nrerror(
        "%s:␣arg␣'minFreq'␣"
        "<␣freqs[0]",where);
    if(maxFreq>freqs[number-1])nrerror(
        "%s:␣arg␣'maxFreq'␣>␣freqs[last]",where);
    if(minFreq>maxFreq) nrerror(
        "%s:␣'minFreq'␣>␣'maxFreq'", where);

    int fitparam = nLocalPeaks*nGaussPar+nBasePar;
    if(MA<fitparam*2) nrerror(
        "%s:␣arg␣'MA'␣must␣be␣>=␣%d",
        where,fitparam*2);
```

```
}



//------------------------------------------------------------------------
/** \brief Calculate the area underneath the spectrum

Evaluate the area under the spectrum within a certain
 frequency range, using the trapezoidal method.

@param freq frequency of interest in Hz
@param sizeoffreqrange range of frequency of
        interest (+-) in Hz
@param dataY Array of frequency
@param dataY Array of powers corresponding to
        datax
*/
double trapezoidal_method(double freq,
                          double sizeoffreqrange,
                          Vec_I_DP &dataX,
                          Vec_I_DP &dataY)
{
    double totalpower=0;
    for (int i=0; i<dataX.size()-1; i++)
    {
        if ((dataX[i] >= freq - sizeoffreqrange)&&
            (dataX[i] <= freq + sizeoffreqrange))
        {
            totalpower=(dataY[i]+dataY[i+1])*
                (dataX[i+1]-dataX[i])/2;
        }
    }

    return totalpower;
}



//------------------------------------------------------------------------
/** \brief Lookup power at a frequency


@param freq frequency of interest in Hz
@param dataY Array of frequency
@param dataY Array of powers corresponding to
        datax
*/
double power_at_freq(double freq,
```

```
                         Vec_I_DP &dataX,
                         Vec_I_DP &dataY)
{
    double power=0.0;
    for (int i=0; i<dataX.size()-1; i++)
    {
        if ((dataX[i+1] >= freq)&&(dataX[i] < freq))
        {
            power=dataY[i];
            break;
        }
    }

    return power;
}



//------------------------------------------------------------------------------------------
/** @brief Estimate alpha peak parameters

Iterate the fitting routine three times, initial and
second is just to refine the fit on each of the
individual parameters, the final fit is with an initial
guess of the weight average parameters across
all the sites.

@param sitesIP Number of EEG spectra to be fitted
@param number Number of points in each spectrum
@param nLocalPeaksIP <b>Maximum</b> number
        of peaks to attempt to fit per spectrum
@param nGlobalPeaksIP <b>Maximum</b>
        number of peaks to attempt to fit globally
@param peakspread Default peak width in Hz: SD of
        fitted Gaussian
@param freqs Frequencies, in Hz, corresponding to
        spectra
@param dataset Input spectra,
        [0:sites-1][0:number-1]
@param spatialGroup Each site is assigned an
        integer that:
        (a) identifies a spatially-close subset of sites; and
        (b) serves as the independent variable in the
        regression in which frequency is the dependent
        variable
@param minFreq Lowest frequency of interest,
        eg 4.0 Hz
@param maxFreq Highest frequency of interest,
        eg 14.0 Hz
```

```
@param MA_IPOP Input: number of available rows in
       <tt>fparameters</tt>.
        Output: number of rows used in
       <tt>fparameters</tt>.
@param numberOfPeaks Global estimate of the
        number of spectral peaks.  This will be
        \htmlonly &le; \endhtmlonly the
        specified maximum \c nGlobalPeaksIP
@param fparameters Fitted parameters organized
        thus: [0:2*mfit-1][0:sites-1]
@param linearFit Spatially linear trend, fitted to
        frequencies: [0:nGlobalPeaks-1][0:sites-1]
*/
void multiple_fitting(const int sitesIP,
        const int number,
    const int nLocalPeaksIP,
    const int nGlobalPeaksIP,
    const double peakspread,
    // [0:number-1]
    const double *freqs,
        // [0:sites-1][0:number-1]
    const double **dataset,
    // [0:sites-1]
    const int *spatialGroup,
    const double minFreq,
    const double maxFreq,
    int& MA_IPOP,
    int& numberOfPeaks,
    // [0:2*mfit-1][0:sites-1]
    double **fparameters,
        // [0:nGlobalPeaks-1][0:sites-1]
    double **linearFit,
        // [0:nGlobalPeaks-1][0:sites-1]
    double **ipower,
        // [0:nGlobalPeaks-1][0:sites-1]
    double **absolutepower)

{
        // width of region of interest
    int count;
    double noiseRMS, error;
    // [1:2*fitparam]
    double *gues, *guesbk;
        // [1:2*fitparam]
    int *ia;
    double chisq, chisqbk;
    // regression param for bkg
    double intercept, gradient, abdeviation;
        // spectral ROI is [iLo,iHo]
    int iLo, iHi;
```

```
// Check that arguments are reasonable
checkInput(sitesIP,
    number,
    nLocalPeaksIP,
    nGlobalPeaksIP,
    peakspread,
    freqs,
    spatialGroup,
    minFreq,
    maxFreq,
    MA_IPOP);

// Update global variables
sites = sitesIP;
nLocalPeaks = nLocalPeaksIP;
nGlobalPeaks = nGlobalPeaksIP;
fitparam = nLocalPeaks*nGaussPar+nBasePar;
MA = fitparam*2;
fresolution =
    (freqs[number-1]-freqs[0])/(number-1);

// Allocate dynamic arrays
gues = vector(1, MA);
guesbk = vector(1,MA);
ia = ivector(1, MA);

ranges(freqs, number, minFreq, maxFreq, iLo, iHi);
count = iHi-iLo+1;
Vec_DP yRes(count);
Vec_DP dataX(count);
Vec_DP dataY(count);
Vec_DP logdataY(count);
Vec_DP logdataYSmoothed(count);

chisqbk = chisq = 0.0;

for (int i=0; i<MA; i++)
     for (int s=0; s<sites; s++)
         fparameters[i][s] = 0.0;

for (int k=iLo; k<=iHi; k++)
    dataX[k-iLo] = freqs[k];

for (int s=0; s<sites; s++)
{
    // initialising arrays
    for (int i=1; i<=MA; i++)
    {
        ia[i] = 0;
```

```
    gues[i] = guesbk[i] = 0.0;
}

for (int k=iLo; k<=iHi; k++)
    logdataYSmoothed[k-iLo] =
        logdataY[k-iLo]=
        log(dataset[s][k]);
smooth(logdataYSmoothed, 7);

// calculating the noise associated
// with current site
error = 0;
for (int k=0; k<count; k++) {
    error += (logdataY[k]-logdataYSmoothed[k])*
             (logdataY[k]-logdataYSmoothed[k]);
}
noiseRMS = sqrt(error/count);


for(int outerLoopCounter = 0;
        outerLoopCounter <= 4; )
{
    // background fitting

    gues[nLocalPeaks*nGaussPar+1] = 0;
    gues[nLocalPeaks*nGaussPar+2] = 0;

    Vec_DP logdataX(count);
    Vec_DP logYDiff(count);
    for (int k=0; k<count; k++) {
        logdataX[k] = log(dataX[k]);
        logYDiff[k] =
                logdataY[k]-fitted(dataX[k],gues);
    }
    // use linear regression to get estimate of
    // slope, intercept
    NR::medfit(logdataX,
        logYDiff,
        intercept,
        gradient,
        abdeviation);

    gues[nLocalPeaks*nGaussPar+1] =
        exp(intercept);
    gues[nLocalPeaks*nGaussPar+2] =
        gradient;

    for (int i=1; i<=MA; i++) ia[i] = 0;

    ia[nLocalPeaks*nGaussPar+1] = 1;
```

```
ia[nLocalPeaks*nGaussPar+2] = 1;

chisqbk = chisq = fitting(dataX,
    logdataY,
    gues,
    ia);

// background fitting completed

// fitting peak(s)
int innerLoopCounter = 0;
for (int nPeakFitsOK=0;
    nPeakFitsOK<=2*nLocalPeaks;
     innerLoopCounter++)
{
    // selecting peak
    int offset =
            (innerLoopCounter%nLocalPeaks)*
            nGaussPar;

    gues[offset+power] = 0;
    gues[offset+freq] = 0;
    gues[offset+sd] = 0;

    for (int k=0; k<count; k++)
        yRes[k] =
            logdataYSmoothed[k]-
            fitted(dataX[k],gues);

    double initialFreq;
    double initialPower;
    site_guess(dataX,
            yRes,
            initialFreq,
            initialPower);

    gues[offset+power] = initialPower;
    gues[offset+freq] = initialFreq;
    gues[offset+sd] = peakspread;
    for (int i=1; i<=MA; i++) ia[i] = 0;
    ia[offset+power] = 1;
    ia[offset+freq] = 1;
    ia[offset+sd] = 1;
    ia[nLocalPeaks*nGaussPar+1] = 1;

    if (gues[offset+power]>noiseRMS)
        chisq = fitting(dataX, logdataY, gues, ia);
    else
    {
        // clear param if guess is too small in
```

```
        // amplitude, break
        gues[offset+power] = 0;
        gues[offset+freq] = 0;
        gues[offset+sd] = 0;
        break;
    }

    // increase iteration count by one if all three
    // peak variables change by less than
    // 0.1% -- or if chisq worsens

    if (((fabs(gues[offset+freq]-
                    guesbk[offset+freq])
            <= 0.001*gues[offset+freq])  &&
        (fabs(gues[offset+power]-
            guesbk[offset+power])
       <= 0.001*gues[offset+power]) &&
        (fabs(gues[offset+sd]-
            guesbk[offset+sd])
       <= 0.001*gues[offset+sd])) ||
       (chisq >= chisqbk))
    {
        nPeakFitsOK++;
        for (int i=1; i<=MA; i++)
            gues[i] = guesbk[i];
    }
    else
    {
        chisqbk = chisq;
        // put good fits into guesbk
        for (int i=1; i<=MA; i++)
            guesbk[i] = gues[i];
    }
}
if (innerLoopCounter==0) break;


// increase iteration count by one if all
// two baseline variables change by
// less than 0.1%

if (fabs(gues[nLocalPeaks*nGaussPar+1]-
    guesbk[nLocalPeaks*nGaussPar+1]) <=
    0.001*fabs(gues[
            nLocalPeaks*nGaussPar+1]) &&
    fabs(gues[
            nLocalPeaks*nGaussPar+2]-
    guesbk[
            nLocalPeaks*nGaussPar+2]) <=
    0.001*fabs(gues[
```

```
                        nLocalPeaks*nGaussPar+2]))
            {
                outerLoopCounter++;
            }

        }

        for (int m=0; m<nLocalPeaks; m++)
        {
            // criteria for bad peaks
            if ((fabs(gues[power+m*nGaussPar])
                < 2*noiseRMS) ||
                (fabs(gues[sd+m*nGaussPar])
                > 4.0*peakspread) ||
                (fabs(gues[freq+m*nGaussPar])
                < dataX[0]) ||
                (fabs(gues[freq+m*nGaussPar])
                > dataX[count-1]) ||
                (fabs(gues[sd+m*nGaussPar])
                < fresolution))
            {
                gues[power+m*nGaussPar] = 0;
                gues[freq+m*nGaussPar] = 0;
                gues[sd+m*nGaussPar] = 0;
            }
        }

        for (int i=0; i<MA; i++)
        {
            if (i != (nLocalPeaks*nGaussPar+0))
                fparameters[i][s] = pbound(gues[i+1]);
            else
                fparameters[i][s] = gues[i+1];
        }
    } // loop over all sites


    numberOfPeaks = peak_sort(fparameters,
        spatialGroup,
        linearFit);

    for (int s=0; s<sites;s++)
    {
        for (int k=iLo; k<=iHi; k++)
                dataY[k-iLo]= dataset[s][k];

        for (int m=0; m<nLocalPeaks; m++)
        {
            if (linearFit[m][s] != 0)
            {
```

```
                                        ipower[m][s]=
                                                trapezoidal_method(
                                                linearFit[m][s],2.0,dataX,dataY);
                                        absolutepower[m][s]=
                                                power_at_freq(
                                                fparameters[m*nGaussPar+1][s],
                                                dataX,
                                                dataY);
                }
            }
    } // loop over all sites


    // Free dynamically allocated arrays
    free_vector(gues, 1, MA);
    free_vector(guesbk, 1, MA);
    free_ivector(ia, 1, MA);

    MA_IPOP = fitparam+
        nGlobalPeaks*
        nGroupPar;
    // return actual number of parameters per site
    return;
}
#undef SWAP

} // end of namespace gaussfit
```

B.2 Code adapted from *Numerical Recipes*

Some modification are perform on the code from *Numerical Recipes* to streamline the algorithm.

B.2.1 mrqmin.cpp

Code for Levenberg-Marquardt gradient descent iterative minimization of a nonlinear function (Press et al., 1995).

```
#include "nr.h"

namespace gaussfit {
    extern bool fitsuccess;      // customization
}

void NR::mrqmin(Vec_I_DP &x,
        Vec_I_DP &y,
        Vec_I_DP &sig,
        Vec_IO_DP &a,
```

```
    Vec_I_BOOL &ia,
    Mat_O_DP &covar,
    Mat_O_DP &alpha,
    DP &chisq,
    void funcs(const DP,
        Vec_I_DP &,
        DP &,
        Vec_O_DP &),
        DP &alamda)
{
        static int mfit;
        static DP ochisq;
        int j,k,l;

        int ma=a.size();
        static Mat_DP *oneda_p;
        static Vec_DP *atry_p,*beta_p,*da_p;
        if (alamda < 0.0) {
                atry_p = new Vec_DP(ma);
                beta_p = new Vec_DP(ma);
                da_p = new Vec_DP(ma);
                mfit=0;
                for (j=0;j<ma;j++)
                        if (ia[j]) mfit++;
                oneda_p = new Mat_DP(mfit,1);
                alamda=0.001;
                mrqcof(x,
                        y,
                        sig,
                        a,
                        ia,
                        alpha,
                        *beta_p,
                        chisq,
                        funcs);
                ochisq=chisq;
                for (j=0;j<ma;j++) (*atry_p)[j]=a[j];
        }
        Mat_DP &oneda=*oneda_p;
        Vec_DP &atry=
                *atry_p,&beta=
                *beta_p,&da=
                *da_p;
        Mat_DP temp(mfit,mfit);
        for (j=0;j<mfit;j++) {
                for (k=0;k<mfit;k++)
                        covar[j][k]=alpha[j][k];
                covar[j][j]=alpha[j][j]*(1.0+alamda);
                for (k=0;k<mfit;k++)
                        temp[j][k]=covar[j][k];
```

```
                oneda[j][0]=beta[j];
        }
        gaussj(temp,oneda);
        for (j=0;j<mfit;j++) {
                for (k=0;k<mfit;k++)
                        covar[j][k]=temp[j][k];
                da[j]=oneda[j][0];
        }
        // customization
        if(gaussfit::fitsuccess==false) return;
        if (alamda == 0.0) {
                covsrt(covar,ia,mfit);
                covsrt(alpha,ia,mfit);
                delete oneda_p;
                delete da_p;
                delete beta_p;
                delete atry_p;
                return;
        }
        for (j=0,l=0;l<ma;l++)
                if (ia[l]) atry[l]=a[l]+da[j++];
        mrqcof(x,
                y,
                sig,
                atry,
                ia,
                covar,
                da,
                chisq,
                funcs);
        if (chisq < ochisq) {
                alamda *= 0.1;
                ochisq=chisq;
                for (j=0;j<mfit;j++) {
                        for (k=0;k<mfit;k++)
                                alpha[j][k]=covar[j][k];
                        beta[j]=da[j];
                }
                for (l=0;l<ma;l++)
                        a[l]=atry[l];
        } else {
                alamda *= 10.0;
                chisq=ochisq;
        }
}
```

B.2.2 mrqcof.cpp

Used by *mrqmin.cpp* to evaluate coefficients.

```
#include "nr.h"

void NR::mrqcof(Vec_I_DP &x,
          Vec_I_DP &y,
          Vec_I_DP &sig,
          Vec_I_DP &a,
     Vec_I_BOOL &ia,
     Mat_O_DP &alpha,
     Vec_O_DP &beta,
     DP &chisq,
          void funcs(const DP,
                    Vec_I_DP &,
                    DP &,
                    Vec_O_DP &))
{
          int i,j,k,l,m,mfit=0;
          DP ymod,wt,sig2i,dy;

          int ndata=x.size();
          int ma=a.size();
          Vec_DP dyda(ma);
          for (j=0;j<ma;j++)
                    if (ia[j]) mfit++;
          for (j=0;j<mfit;j++) {
                    for (k=0;k<=j;k++) alpha[j][k]=0.0;
                    beta[j]=0.0;
          }
          chisq=0.0;
          for (i=0;i<ndata;i++) {
                    funcs(x[i],a,ymod,dyda);
                    sig2i=1.0/(sig[i]*sig[i]);
                    dy=y[i]-ymod;
                    for (j=0,l=0;l<ma;l++) {
                              if (ia[l]) {
                                        wt=dyda[l]*sig2i;
                                        for (k=0,m=0;m<l+1;m++)
                                                  if (ia[m]) alpha[j][k++] +=
                                                            wt*dyda[m];
                                        beta[j++] += dy*wt;
                              }
                    }
                    chisq += dy*dy*sig2i;
          }
          for (j=1;j<mfit;j++)
                    for (k=0;k<j;k++) alpha[k][j]=alpha[j][k];
}
```

B.2.3 covsrt.cpp

Code for rearranging the covariance matrix.

```
#include "nr.h"

void NR::covsrt(Mat_IO_DP &covar,
        Vec_I_BOOL &ia,
        const int mfit)
{
        int i,j,k;

        int ma=ia.size();
        for (i=mfit;i<ma;i++)
                for (j=0;j<i+1;j++)
                        covar[i][j]=covar[j][i]=0.0;
        k=mfit-1;
        for (j=ma-1;j>=0;j--) {
                if (ia[j]) {
                        for (i=0;i<ma;i++)
                                SWAP(covar[i][k],covar[i][j]);
                        for (i=0;i<ma;i++)
                                SWAP(covar[k][i],covar[j][i]);
                        k--;
                }
        }
}
```

B.2.4 gaussj.cpp

Gaussian-Jordan matrix inversion and linear equation solutions.

```
#include <cmath>
#include "nr.h"
using namespace std;

namespace gaussfit {
        // gaussfit customization
    extern bool fitsuccess;
}
void NR::gaussj(Mat_IO_DP &a, Mat_IO_DP &b)
{
        int i,icol,irow,j,k,l,ll;
        DP big,dum,pivinv;

        int n=a.nrows();
        int m=b.ncols();
        Vec_INT indxc(n),indxr(n),ipiv(n);
        for (j=0;j<n;j++) ipiv[j]=0;
        for (i=0;i<n;i++) {
                big=0.0;
```

```
                for (j=0;j<n;j++)
                        if (ipiv[j] != 1)
                                for (k=0;k<n;k++) {
                                if (ipiv[k] == 0) {
                                if (fabs(a[j][k]) >= big) {
                                big=fabs(a[j][k]);
                                        irow=j;
                                    icol=k;
                            }
                          }
                      }
                ++(ipiv[icol]);
                if (irow != icol) {
                        for (l=0;l<n;l++)
                                SWAP(a[irow][l],a[icol][l]);
                        for (l=0;l<m;l++)
                                SWAP(b[irow][l],b[icol][l]);
                }
                indxr[i]=irow;
                indxc[i]=icol;
                // if (a[icol][icol] == 0.0)
                // nrerror("gaussj: Singular Matrix");
                if (fabs(a[icol][icol]) < 1e-12) {
                        // gaussfit customization
                    gaussfit::fitsuccess = false;
                    return;
                }
                pivinv=1.0/a[icol][icol];
                a[icol][icol]=1.0;
                for (l=0;l<n;l++) a[icol][l] *= pivinv;
                for (l=0;l<m;l++) b[icol][l] *= pivinv;
                for (ll=0;ll<n;ll++)
                        if (ll != icol) {
                                dum=a[ll][icol];
                                a[ll][icol]=0.0;
                                for (l=0;l<n;l++) a[ll][l] -=
                                        a[icol][l]*dum;
                                for (l=0;l<m;l++) b[ll][l] -=
                                        b[icol][l]*dum;
                        }
        }
        for (l=n-1;l>=0;l--) {
                if (indxr[l] != indxc[l])
                        for (k=0;k<n;k++)
                                SWAP(a[k][indxr[l]],a[k][indxc[l]]);
        }
}
```

B.2.5 medfit.cpp

Robustly fit data to a straight line using least absolute deviation.

```
#include <cmath>
#include "nr.h"
using namespace std;

DP aa,abdevt;
const Vec_DP *xt_p,*yt_p;

void NR::medfit(Vec_I_DP &x,
          Vec_I_DP &y,
          DP &a,
          DP &b,
          DP &abdev)
{
          int j;
          DP bb,b1,b2,del,f,f1,f2,sigb,temp;
          DP sx=0.0,sy=0.0,sxy=0.0,sxx=0.0,chisq=0.0;

          int ndata=x.size();
          xt_p= &x;
          yt_p= &y;
          for (j=0;j<ndata;j++) {
                    sx += x[j];
                    sy += y[j];
                    sxy += x[j]*y[j];
                    sxx += x[j]*x[j];
          }
          del=ndata*sxx-sx*sx;
          aa=(sxx*sy-sx*sxy)/del;
          bb=(ndata*sxy-sx*sy)/del;
          for (j=0;j<ndata;j++)
                    chisq +=
                              (temp=y[j]-(aa+bb*x[j]),temp*temp);
          sigb=sqrt(chisq/del);
          b1=bb;
          f1=rofunc(b1);
          if (sigb > 0.0) {
                    b2=bb+SIGN(3.0*sigb,f1);
                    f2=rofunc(b2);
                    if (b2 == b1) {
                              a=aa;
                              b=bb;
                              abdev=abdevt/ndata;
                              return;
                    }
                    while (f1*f2 > 0.0) {
                              bb=b2+1.6*(b2-b1);
                              b1=b2;
```

```
                        f1=f2;
                        b2=bb;
                        f2=rofunc(b2);
                }
                sigb=0.01*sigb;
                while (fabs(b2-b1) > sigb) {
                        bb=b1+0.5*(b2-b1);
                        if (bb == b1 || bb == b2) break;
                        f=rofunc(bb);
                        if (f*f1 >= 0.0) {
                                f1=f;
                                b1=bb;
                        } else {
                                f2=f;
                                b2=bb;
                        }
                }
        }
        a=aa;
        b=bb;
        abdev=abdevt/ndata;
}
```

Appendix C

Modeling EEG spectra across age

This study investigates age-associated changes in physiology-based EEG spectral parameters in the healthy population. Eyes-closed EEG spectra of 1498 healthy subjects aged 6–86 years were fitted to a mean-field model of thalamocortical dynamics in a cross-sectional study. Parameters were synaptodendritic rates, cortical wave decay rates, connection strengths (gains), axonal delays for thalamocortical loops, and power normalizations. Age trends were approximated using smooth asymptotically linear functions with a single turning point. Sex differences and relationships between model parameters and traditional quantitative EEG measures were also considered. Age-related changes tend to be most rapid in childhood, generally leveling off at age 15–20 years. Most gains decrease in magnitude with age, as does power normalization. Axonal and dendritic delays decrease in childhood and then increase. Axonal delays and gains show small but significant sex differences. These results demonstrate that mean-field brain modeling allows interpretation of age-associated EEG trends in terms of physiological processes, including the growth and regression of white matter, influencing axonal delays, and the establishment and pruning of synaptic connections, influencing gains, and demonstrates the feasibility of inverse modeling of EEG spectra as a noninvasive method for investigating large-scale thalamocortical dynamics.

C.1 Introduction

Understanding the structural, chemical, and functional changes that accompany brain aging is one of the major goals of research in neuroscience. Structural changes are particularly rapid during childhood, slow down after adolescence, and appear to accelerate again in late adulthood. Although the morphological, chemical, and functional development of the human brain, as well as changes in the electroencephalogram (EEG), have been tracked extensively (Duffy et al., 1993; Gasser et al., 1988; Hartikainen et al., 1992; Kemper, 1994; Polich, 1997; Rossini et al., 2007; Thompson et al., 2000), knowledge of the specific processes underlying changes in the EEG across age is limited.

Growth and pruning processes affect the volumes of the cortical and subcortical gray matter, cerebral white matter, and the corpus callosum. Cranial size increases up to age ∼20, with growth continuing a few years longer in males than in females (Dekaban, 1977; Eichorn and Bayley, 1962). Cortical gray matter volume increases up to adolescence (Giedd et al., 1999), although localized pruning already occurs during childhood (Caviness et al., 1996). The corpus callosum grows considerably between the ages of 3 and 11 years and more slowly up to 15 years (Thompson et al., 2000). Ongoing myelination increases the white matter content of various cortical and other brain areas throughout childhood (Barnea-Goraly et al., 2005; Perrin et al., 2008; Sowell et al., 2004).

After adolescence, a steady decrease in brain volume occurs, which appears to become more severe after about 60–70 years (Haug, 1987; Scahill et al., 2003). This is accompanied by an increase in absolute and relative cerebrospinal fluid volume that commences already in childhood (Gur et al., 1991; Sowell et al., 2002). Although reductions in brain volume were traditionally attributed to neuronal loss, later studies with improved methodology have largely failed to reveal loss of hippocampal or neocortical neurons with age, and have instead attributed decreased brain volume to shrinkage of neurons (Peters, 2002; Rapp and Gallagher, 1996; Rasmussen et al., 1996). An exception is Pakkenberg and Gundersen (1997), who reported a loss of about 10% of neurons in the neocortex of both males and females between age 20 and 90. Thalamic volume also decreases with age, whether due to loss or shrinkage of neurons (Sullivan et al., 2004; Van Der Werf et al., 2001). Although some authors have reported white matter volume to be relatively stable compared to gray matter volume (Passe et al., 1997; Sullivan et al., 2004), others have found white matter volume reductions from about age 50 (Ge et al., 2002; Miller et al., 1980). According to a recent study, white matter shows much greater reductions than gray matter between the ages of 46 and 92 (Piguet et al., 2009).

Small numbers of neuritic plaques and neurofibrillary tangles, characteristic of Alzheimer's disease, accumulate even in normal aging (Morrison and Hof, 1997; Tomlinson et al., 1968). Often, advancing age is further accompanied by reductions in cerebral perfusion, oxygen consumption, and glucose utilization (Kuhl et al., 1982; Pantano et al., 1984; Zemcov et al., 1984). There are also age-related changes in chemical signaling (Gallagher and Colombo, 1995; McEntee and Crook, 1991; Suhara et al., 1991; Volkow et al., 2000).

There are sex differences in brain anatomy and chemistry, and in certain aspects of brain development (Coffey et al., 1998; Cosgrove et al., 2007; De et al., 2001). Female brains have smaller volumes and approximately 16% fewer neocortical neurons at any age than male brains (Caviness et al., 1996; Dekaban and Sadowsky, 1978; Haug, 1987; Pakkenberg and Gundersen, 1997). However, many studies have reported more substantial age-related atrophy or reductions in brain volume in men than in women (Coffey et al., 1998; Cowell et al., 1994; Gur et al., 1991; Tomlinson et al., 1968; Xu et al., 2000), although some have suggested earlier onset or more severe atrophy in women (Hatazawa et al., 1982; Hubbard and Anderson, 1983). It is generally found that a larger percentage of the total volume is occupied by gray matter in women than in men (Cosgrove et al., 2007).

This study aims to provide a new window on brain aging using a model of neuronal activity that incorporates the main structures and connections contributing to the EEG. This approach is based on a mean-field model of thalamocortical dynamics developed over a number of years, primarily by Robinson et al. (1997, 1998, 2001b); Robinson (2003a), and Rennie et al. (1999, 2000, 2002). This model was partly based in turn on work by Nunez (1974, 1995), Wilson and Cowan (1972, 1973), Wright and Liley (1995), and others. Comparisons of model predictions with data have revealed good agreement with a range of features of EEGs, including evoked potentials (EPs) (Chapter c3++Fix), seizure dynamics (Breakspear et al., 2006; Roberts and Robinson, 2008a), spectra (Robinson et al., 2001b; Rowe et al., 2004), coherence and correlations (Robinson, 2003b), and changes with arousal (Robinson et al., 2002). Inverse modeling by fitting to spectra yields parameters including thalamocortical axonal delays, synaptodendritic rates, a damping rate for signals in the cortex, a scaling parameter for spectral power, and connection strengths of the cortex, thalamic relay nuclei, and thalamic reticular nucleus. An advantage of our model is that it provides information on structures as deep as the thalamus without the need for invasive measurements. Moreover, this information is of a different type than would be obtained by most invasive techniques, yielding average properties of large neuronal assemblies and their interconnections, rather than properties of small numbers of individual neurons.

Determining model parameters across age for healthy individuals is useful not only because it demonstrates the feasibility of extracting physiological information from the EEG, but also because it establishes a standard against which to compare clinical groups. Moreover, comparisons with known physiological changes provide a test of the model that can stimulate its further development.

In Sec. C.2 we describe the subjects and data acquisition, the model, and the methods used for fitting and statistical analysis. Section C.3 gives parameter values and age trends, and also addresses sex differences. Section C.4 provides a summary and relates our results to the existing literature.

C.2 Methods

This section outlines the model and methods used in our analysis. Section C.2.1 details the composition of the data set and criteria for inclusion. Section C.2.2 provides an overview of the theoretical model of EEG generation. Section C.2.3 summarizes the procedures for fitting model predictions to empirical spectra. Section C.2.4 describes the statistical techniques used in the analysis of model parameters.

C.2.1 Subjects and EEG recording

The cross-sectional data set was composed of 763 males and 735 females, selected to have EEG and EP data across a range of electrodes, allowing future comparison with model fits to EPs (Chapter c5++Fix), parameters obtained from deconvolution of EPs (Chapter c2++Fix), and detailed fits to alpha peaks (Chiang et al., in preparation). The 1498 subjects overlap with the 1008 previously studied by Williams et al. (2008). Subjects' ages were 6.4–86.6 years for males, and 6.1–82.6 years for females, with age distributions as shown in Fig. C.1. The large number of young subjects allows reliable estimation of age trends over a period of relatively rapid change. Furthermore, the study also included 126 subjects aged 60 years or more, a larger number than considered in most studies of the EEG in aged individuals. All subjects were healthy, without any known history of brain injury; mental illness; substance abuse; psychological, psychiatric, neurological, or genetic disorders; or other medical conditions that could influence the normality of the EEG. More detailed criteria were as in van Albada et al. (2007).

Eyes-closed resting EEGs were recorded by Brain Resource Ltd. (www.-brainresource.com) and made available through the Brain Resource International Database (BRID) (Gordon et al., 2005). Recordings were obtained with a NuAmps amplifier (Neuroscan) at 26 electrode sites according to an extended International 10–20 system. The sampling rate was 500 Hz and average of mastoids was used as a reference. To keep the scope of the study manageable, a single electrode was selected for further analysis. The Cz electrode was chosen, as this electrode is relatively unaffected by muscle artifact (Saunders, 1984). Data were corrected offline for eye movements using a method based on that of Gratton et al. (1983). A 100 Hz low-pass filter was applied to two minutes of relatively artifact-free EEG. The spectrum was calculated at intervals of 0.25 Hz by averaging the spectra of successive 4 s epochs multiplied by a Welch win-

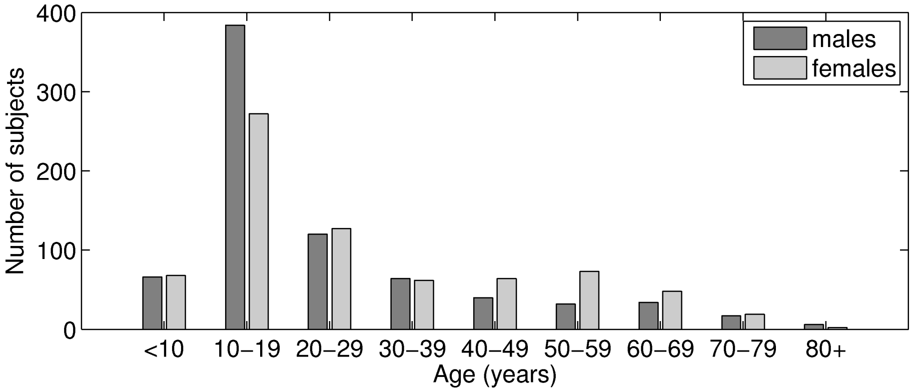

Figure C.1: Numbers of males and females in each age bin.

dow. Two minutes of EEG were considered sufficient for two reasons. First, the large number of subjects allows reliable estimation of average age trends even with relatively short recordings. Second, the reproducibility of spectral parameters is not greatly improved by using longer recordings (Gasser et al., 1985; Salinsky et al., 1991; van Albada et al., 2007).

C.2.2 Theoretical model

A schematic diagram of the neuronal populations included in the model, and their interconnections, is given in Fig. C.2. Within the cortex, the model includes excitatory pyramidal cells, which project both intracortically and to the thalamus, and short-range inhibitory interneurons. The subscripts e and i are used to represent the excitatory and inhibitory cortical populations. The thalamic relay and reticular nuclei are respectively denoted by the subscripts s and r. Input from the brainstem to the thalamus is indicated by the subscript n. With each connection is associated a gain G_{ab} quantifying the number of additional pulses out per additional pulse in with respect to the steady state, where b is the sending and a is the receiving population. Loop gains are combined into the products $G_{srs} = G_{sr}G_{rs}$ for the loop between thalamic reticular and relay nuclei; $G_{ese} = G_{es}G_{se}$ for the thalamocortical loop passing only through the relay nuclei; and $G_{esre} = G_{es}G_{sr}G_{re}$ for the thalamocortical loop also passing through the reticular nucleus. These gains and the corresponding loops are illustrated in Fig. C.2.

Full details of the model have been published elsewhere (Robinson et al., 1997, 1998, 2001b, 2002); however, for completeness, the equations are given in the appendix to this appendix. These enable frequency spectra to be computed from basic physiological quantities, of which we consider those that were allowed to vary when fitting the model to empirical EEG spectra. Besides the gains listed above, these quantities are: t_0, the axonal delay associated with the direct

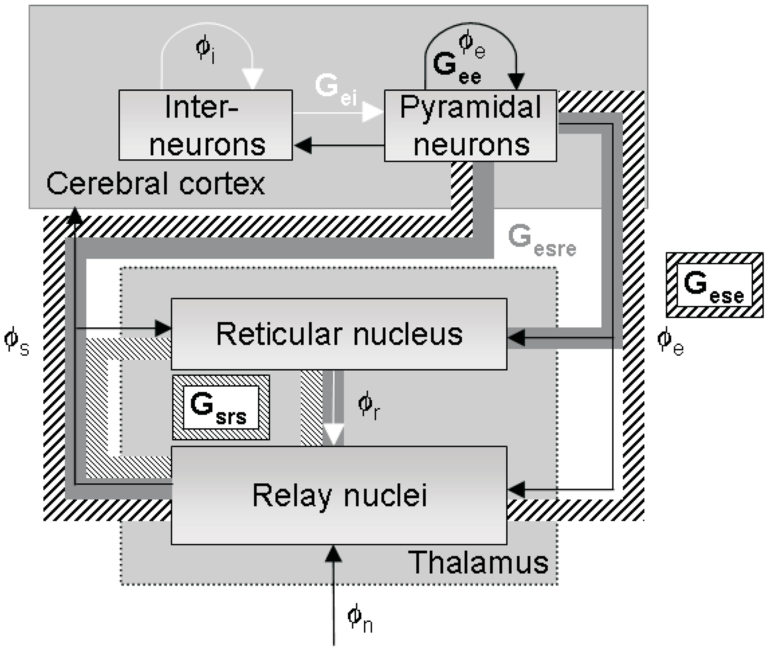

Figure C.2: Schematic representation of the model components and their interconnections: e = cortical excitatory (pyramidal) neurons, i = cortical inhibitory neurons, s = thalamic (specific and secondary) relay nuclei, r = thalamic reticular nucleus. External input to the thalamus is given by ϕ_n. The connections or loops associated with each gain are also indicated: intracortical excitatory and inhibitory connections (G_{ee} and G_{ei}), the direct and indirect thalamocortical loops (G_{ese} and G_{esre}), and the intrathalamic loop (G_{srs}). Black arrows indicate excitatory connections; white arrows inhibitory ones.

thalamocortical loop; α, a characteristic decay rate of the cell-body potential after synaptic input (an average or effective value across neural populations); γ, a damping rate associated with propagation of waves of activity along the cortex; and p_0, a normalization for the frequency spectrum. All parameters are listed in Table C.1.

Parameter	Unit	Description	Value	Min.	Max.
$*\alpha$	s^{-1}	Decay rate of cell-body potential	—	10	200
β	s^{-1}	Rise rate of cell-body potential	4α	—	—
r_e	mm	Range of pyramidal axons	80	—	—
v_e	m s^{-1}	Propagation speed along pyramidal axons	γr_e	—	—
$*\gamma$	s^{-1}	Cortical damping rate	—	40	280
$*t_0$	ms	Thalamocortical axonal latency	—	60	130
$*G_{ee}$	—	Excitatory cortical gain	—	0	20
$*G_{ei}$	—	Inhibitory cortical gain	—	−35	1
$*G_{ese}$	—	Gain for direct thalamocortical loop	—	0	20
$*G_{esre}$	—	Gain for indirect thalamocortical loop	—	−30	2
$*G_{srs}$	—	Gain for intrathalamic loop	—	−15	0.5
$*p_0$	—	Normalization for spectrum	—	No limits	
k_0	m^{-1}	Cut-off wavenumber for spatial filtering	37.5	—	—
L_x, L_y	m	Linear dimensions of cortex	0.5	—	—
A_{EMG}	μV^2 Hz^{-1}	Amplitude of EMG component	—	0	10
ω_{EMG}	s^{-1}	Peak frequency of EMG component	$2\pi\times40$	—	—

Table C.1: Parameters of the thalamocortical model used to fit theoretical predictions to empirical EEG spectra. Parameters considered in this study are marked by an asterisk. The minimum and maximum values are soft boundaries created by imposing a smoothly increasing penalty for smaller or larger values.

The parameters considered here differ from traditional qEEG measures in their direct connection with physiological quantities. As such, they can provide a useful complement to traditional qEEG, especially if physiological models of EEG generation are further developed. Apart from physiological interpretations, an advantage of the model parameters is that they capture spectral shape within frequency bands, which is not captured by band powers.

C.2.3 Model fitting

As described in Rowe et al. (2004) and van Albada et al. (2007), the natural logarithm of the dimensionless version of the spectral power (otherwise measured in μV^2/Hz) was fitted to the empirical log-transformed spectrum using the Levenberg-Marquardt method (Press et al., 1995), which minimizes the χ^2 error defined by

$$\chi^2 = \sum_{i=1}^{N} \frac{[\ln(P_{emp,i}) - \ln(P_{the,i})]^2}{\sigma_i^2}, \tag{C.1}$$

where $P_{emp,i}$ is the empirical spectrum, and σ_i is the standard deviation of $\ln P_{emp}$ for frequency index i. Frequencies up to 50 Hz were taken into account, but the power around 50 Hz was weighted with large σ to downplay the contribution of points contaminated by mains power. Fitting followed a Monte Carlo method in which the ten fitted parameters were repeatedly initialized randomly and the model fitted, until 30 convergent fits were obtained. The stopping criterion for the fitting routine was $\Delta\chi^2 < 10^{-5}$ for six successive iterations. Of 1661 subjects' spectra, 1568 were successfully fitted (94%). To obtain a single subject set for which model parameters, EPs (Chapters c4++Fix and c5++Fix), and alpha peak data across sites (Chiang et al., in preparation) could be investigated, we selected from the set of 1568 subjects the 1498 subjects with EP data for a large number of electrodes. All these subjects also had EEG spectral data across sites, from which alpha peak parameters could be extracted. Figure C.3 gives illustrative examples of fits with different values of χ^2. The values of χ^2 were larger than those reported in Rowe et al. (2004) due to a different normalization of weights, but this did not substantially affect the fits obtained.

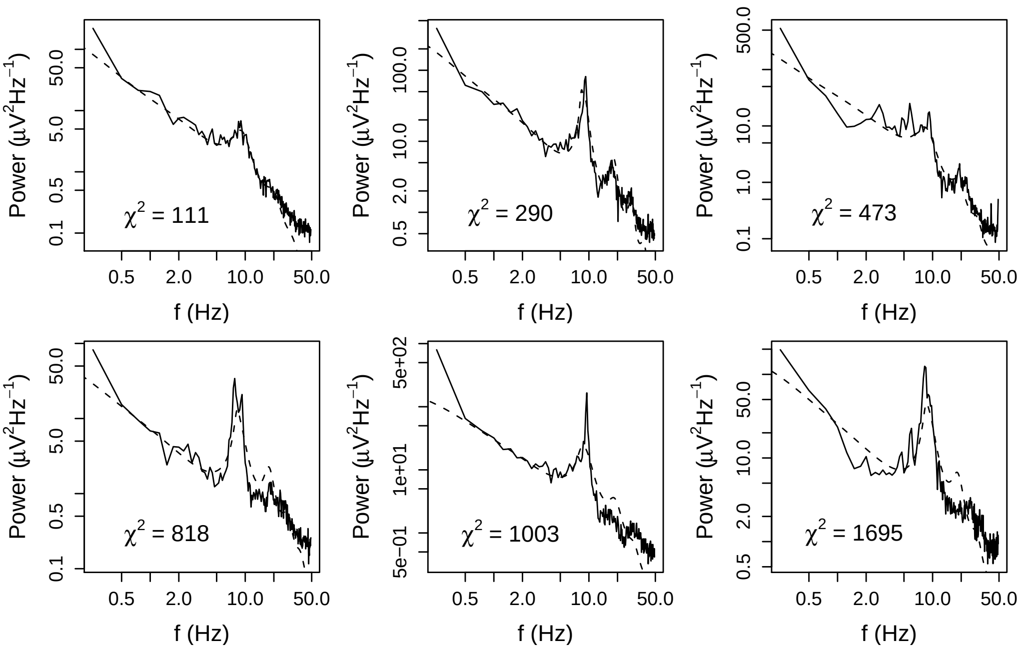

Figure C.3: Examples of experimental (solid) and corresponding model spectra (dashed) from single subjects with varying goodness of fit.

C.2.4 Statistical analysis

The statistical analysis was carried out using R Version 2.7.0 (R Development Core Team, 2008). Visual inspection of histograms and a Shapiro-Wilk test for normality (Shapiro and Wilk, 1965) revealed that none of the parameters were normally distributed ($p < 1.0 \times 10^{-7}$). Furthermore, the residuals of parametric linear regression of model parameters versus age were nonnormal ($p < 1.0 \times 10^{-14}$). Therefore, nonparametric methods were used except where indicated otherwise.

First, the robustness of fits was investigated by refitting empirical spectra with noise added. White Gaussian noise with standard deviation 0.2 was added to log-transformed spectra (using the dimensionless version of power in $\mu\mathrm{V}^2\mathrm{Hz}^{-1}$). This process was repeated to obtain spectra with ten different noise levels. Robustness analysis was restricted to the 1126 cases for which refitting was successful at all noise levels. The standard deviation of the first set of noisy spectra approximates the standard error of ln power of 2-minute spectra computed from 4-second segments (not shown), which corresponds to the method used here (cf. Sec. C.2.1). Thus, the robustness of model parameters was assessed by calculating Spearman correlations between parameters for the original fits and those for the first set of noisy spectra. Spearman correlations for between-fit differences were also determined for each pair of parameters. This gave an indication of correlations induced by fitting (in the presence of uncertainty or noise) rather than physiology. To check for any consistent bias introduced by uncertainty or noise, parametric linear regression was performed of mean parameter values versus noise level.

For the original fits, sex differences in model parameters were assessed using the Mann-Whitney test for independent samples (Hollander and Wolfe, 1973). We compared means and distributions of model parameters with those obtained using a previous version of the fitting routine (Rowe et al., 2004), and those reported in a longitudinal study of healthy males in the age range 18–28 years (van Albada et al., 2007).

Age trends were approximated using a functional form that was chosen based on the following observations: (i) trends were often approximately linear in young and old age; (ii) there was substantial variation in the age ranges over which trends were nonlinear; (iii) the transition from "development" to "aging" occurs gradually, with intermediate slopes in early adulthood; and (iv) the median did not clearly show more than one turning point for any of the parameters. This motivated a fitting function that is smooth, asymptotically linear, and has a second derivative of constant sign. A functional form that meets these criteria and has only a small number of parameters is given by

$$\begin{aligned} y &= Cx + (C - A)\tau \ln\left(1 + \exp[-(x - I)/\tau]\right) + D, && \text{(C.2)} \\ I &= \frac{B - D}{C - A}, && \text{(C.3)} \end{aligned}$$

where x is the age, τ is a width parameter quantifying the age range over which the slope changes considerably, and A, B, C, and D are parameters representing asymptotic slopes and intercepts. Since fits were relatively insensitive to τ, this parameter was fixed at 3 years, which yielded good fits. Equation (C.2) represents a smooth interpolation between two straight lines, $y = Ax + B$ for $x \to -\infty$ and $y = Cx + D$ for $x \to \infty$. These lines intersect at I, which is also the point of maximum rate of change in slope for the interpolated fit. The fits display a minimum or maximum at

$$x = I - \tau \ln\left(-\frac{C}{A}\right), \tag{C.4}$$

if A and C have opposite sign. More than one turning point is excluded, because the second derivative of (C.2) is always negative when $A > C$, strictly positive when $A < C$, and zero when $A = C$. The function (C.2) is illustrated in Fig. C.4.

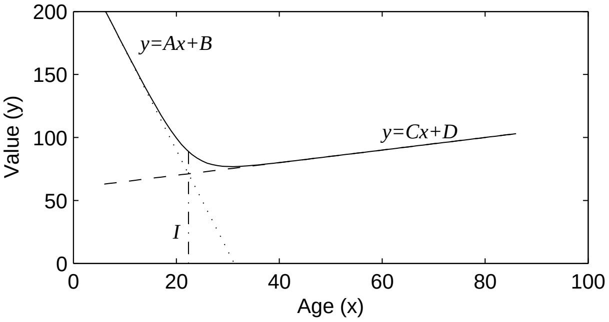

Figure C.4: Example of a function of the form (C.2) with negative A and positive C (solid line). The asymptotic linear trends $y = Ax + B$ (dotted) and $y = Cx + D$ (dashed) intersect at $x = I$ (dash-dotted).

In order to track the median, fits were performed by minimizing the mean absolute difference between fitted and measured values. Optimization was achieved using a downhill simplex method (Nelder and Mead, 1965), with starting conditions fine-tuned to obtain close fits to moving medians computed for groups of 100 subjects with steps of 10 subjects. Confidence intervals for the parameters and fits were obtained by bootstrapping with 1000 resamplings.

For comparison with the literature, we also considered age trends of the form

(C.2) in "raw" empirical spectra. Band powers were determined in the ranges 0.5–4 Hz (delta), 4.25–8 Hz (theta), 8.25–12 Hz (alpha), 12.25–30 Hz (beta), and 30.25–49.5 Hz (gamma). Total power was the sum of these band powers, and relative powers were absolute power divided by total power. Dominant alpha frequencies were determined from spectra at a range of electrodes using the method of Chiang et al. (2008). We consider mainly the Cz electrode, for which 1212 subjects exhibited a clear peak, but we compare with other sites where relevant.

We also investigated the sensitivity of qEEG parameters to model parameters. Normally distributed values with mean zero and standard deviation 0.25 times the sample standard deviation were added to fitted model parameters, and spectra were recomputed. Differences between qEEG parameters for the original and modified spectra were computed, where 0.01 Hz resolution was used to determine alpha peak frequencies. We then calculated Spearman correlations between differences in model parameters and differences in qEEG parameters. The sensitivity of alpha peak frequencies was only investigated for the 1212 subjects whose empirical Cz spectra showed clear peaks. The use of fitted, rather than randomly chosen, parameters ensured that physiologically representative spectra were considered. Artificially varied spectra have the advantage over spectra taken directly from the sample under study that qEEG-model parameter correlations are not confounded by age trends and noise.

C.3 Results

The robustness of fitted model parameters is discussed in Sec. C.3.1. Parameter distributions are given in Sec. C.3.2 and compared to previously published results. Age trends in fitted and model-free spectral parameters are presented in Sec. C.3.3.

C.3.1 Robustness of fits

Figure C.5 shows the noise dependence of mean parameter values for the 1126 subjects whose spectra were successfully fitted at all noise levels. To a good approximation, all means depend linearly on the noise variance. The absolute values of all parameters except α tend to be overestimated in the presence of noise. However, the degree of overestimation is about two orders of magnitude smaller than the standard deviation of each parameter, so spectral uncertainty does not substantially bias fitted parameter values.

Table C.2 shows the results of comparing original parameter values with those obtained after adding noise to empirical spectra. The last column of

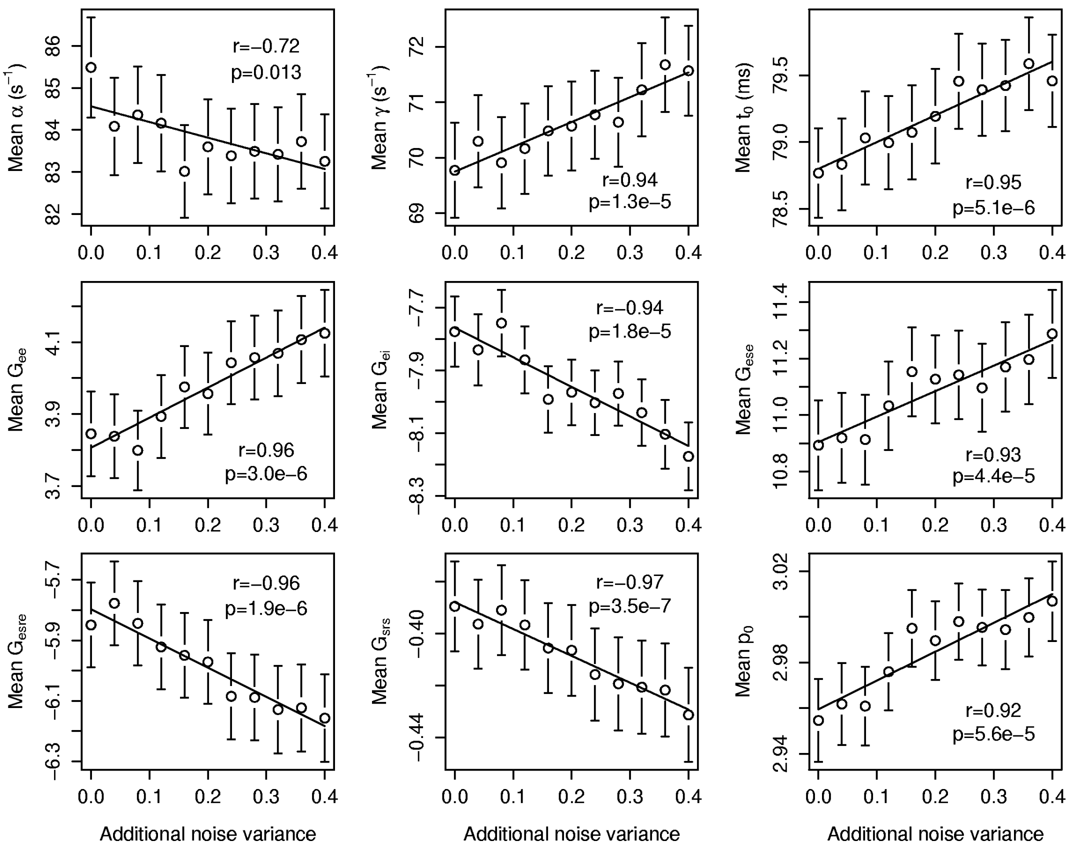

Figure C.5: Dependence of mean parameter values on noise in spectra. Data for the original fits are plotted at zero noise variance. Error bars indicate SEMs. Linear regression fits and Pearson correlation coefficients are shown, with corresponding significance values.

Table C.2 lists correlations between parameter values for the original fits and those obtained from the first set of noisy spectra. These correlations indicate that, overall, parameters are robustly fitted. The most robust parameter is G_{srs} ($\rho = 0.96$), while G_{ei} is the least robust ($\rho = 0.79$). The thalamocortical loop delay t_0 shows the least interaction with other parameters.

It is seen from Table C.2 that almost all parameter pairs show interactions due to noise. Consequently, age trends of physiological origin in some parameters may cause artificial age trends in other (especially less robust) parameters. Particularly strong correlations are found for between-fit differences in p_0 and G_{ei} ($\rho = -0.86$), G_{ese} and G_{esre} ($\rho = -0.74$), and G_{ee} and G_{ei} ($\rho = -0.62$). This should be kept in mind when interpreting the results in the following sections.

Parameter	α	γ	t_0	G_{ee}	G_{ei}	G_{ese}	G_{esre}	G_{srs}	p_0	ρ
α	1	−0.40	0.059	−0.23	0.22	0.011	−0.19	0.59	−0.41	0.91
γ	***	1	−0.078	0.22	−0.14	−0.29	0.36	−0.29	0.010	0.85
t_0	*	**	1	−0.015	0.020	−0.00087	−0.017	0.038	−0.004	0.92
G_{ee}	***	***	n.s.	1	−0.62	0.29	−0.37	−0.34	0.49	0.90
G_{ei}	***	***	n.s.	***	1	−0.59	0.33	0.076	−0.86	0.79
G_{ese}	n.s.	***	n.s.	***	***	1	−0.74	0.082	0.60	0.82
G_{esre}	***	***	n.s.	***	***	***	1	−0.13	−0.27	0.87
G_{srs}	***	***	n.s.	***	*	**	***	1	−0.20	0.96
p_0	***	n.s.	n.s.	***	***	***	***	***	1	0.88

Table C.2: Robustness of model parameters, assessed by adding noise to empirical spectra and refitting. The second through tenth columns contain rank correlations for differences in parameters between the original fits and those obtained from spectra with added Gaussian noise with standard deviation 0.2 on a log scale (in upper triangular form). Corresponding significance values are listed below the diagonal. These correlations obey $\rho(x_1-x_2, y_1-y_2) = \rho(y_1-y_2, x_1-x_2)$ for parameters x and y, and fits 1 and 2. The last column indicates rank correlations between fits before and after adding noise. Significance levels: n.s., not significant; *, 0.05; **, 0.01; ***, 0.001.

C.3.2 Parameter values

Parameter distributions are shown in Fig. C.6. Table C.3 lists parameter means and standard deviations, and χ^2-values The thalamocortical loop gains G_{ese} and G_{esre} were both stronger (i.e., larger in magnitude) in males. The intrathalamic loop, represented by the gain G_{srs}, was stronger in females. The thalamocortical loop delay t_0 was on average slightly longer in females. No significant differences were found in the intracortical gains G_{ee} and G_{ei}, or in the parameters α, γ, and p_0. Fits were on average slightly better for females than for males, as indicated by lower values of χ^2.

Dominant alpha frequencies are expected to be approximately inversely proportional to t_0 (Robinson et al., 2002). However, the sex difference in t_0 did not translate into a significant sex difference in alpha peak frequencies averaged across age (males, 9.5 Hz; females, 9.4 Hz; $p = 0.30$). Boys up to age 16 did show significantly higher peak frequencies than girls in this age range (boys, 9.6 Hz; girls, 9.3 Hz; $p = 0.0045$), and had significantly lower values of t_0 (boys, 77 ms; girls, 81 ms; $p = 1.0e-5$). In contrast, females aged 16–24 years had higher peak frequencies (females, 9.7 Hz; males, 9.4 Hz; $p = 0.0028$), despite a lack of difference in t_0 (females, 78 ms; males, 77 ms; $p = 0.76$). The same pattern of sex differences in alpha peak frequencies was found at occipital sites. We did not find significant sex differences in t_0 or Cz alpha peak frequencies in aged individuals, but frontal rhythms occurred at significantly lower frequencies in women than in men above about age 70. These issues are explored further by

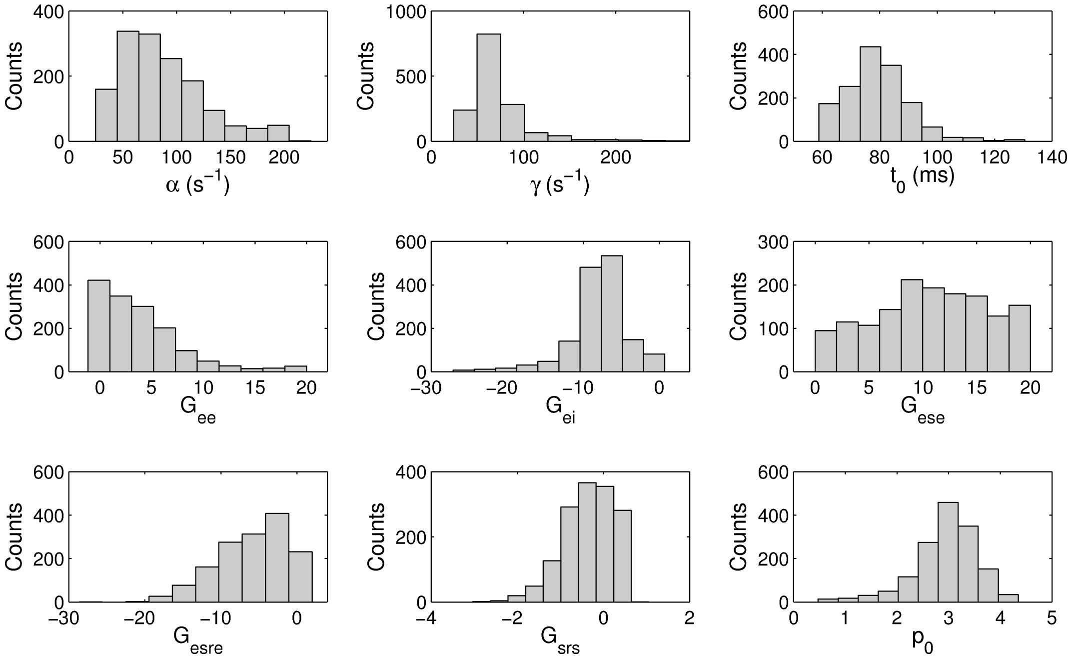

Figure C.6: Histograms of model parameters.

Chiang et al. (in preparation).

Param.	Mean	Mean$_R$	Males	Females	p-value
α	88±1	75	88±1	87.3±1.0	0.98
γ	71.8±0.8	140	71.6±0.8	72.1±0.8	0.22
t_0	79.2±0.3	84	78.1±0.3	80.3±0.3	1.2×10^{-5}
G_{ee}	3.8±0.1	5.8	3.9±0.1	3.8±0.1	0.67
G_{ei}	−8.0±0.1	−7.5	−8.0±0.10	−7.9±0.1	0.14
G_{ese}	10.8±0.1	5.4	11.2±0.1	10.3±0.1	2.5×10^{-4}
G_{esre}	−5.7±0.1	−3.3	−6.3±0.1	−5.2±0.1	3.0×10^{-6}
G_{srs}	−0.34±0.02	−0.50	−0.29±0.01	−0.40±0.02	1.5×10^{-4}
p_0	2.94±0.02	2.49	2.92±0.02	2.96±0.02	0.079
χ^2	360±10		370±10	340±10	1.7×10^{-4}

Table C.3: Means and SEMs for model parameters and χ^2. Units are as in Table C.1. Standard deviations are about 39 times as large as the standard errors listed. Mean$_R$ denotes means for the eyes-closed state from Rowe et al. (2004). The column labeled 'p-value' lists results of the Mann-Whitney test comparing males and females.

Rowe et al. (2004) reported distributions of model parameters for eyes-open and eyes-closed spectra of 100 healthy subjects (49 females, mean age 44 years, SD 15 years; and 51 males, mean age 45 years, SD 16 years) using an earlier version of the fitting routine. Compared to the eyes-closed distributions in that paper, our sample yielded larger standard deviations for all parameters except t_0 and γ. The mean values of γ, t_0, G_{ee}, and $|G_{srs}|$ were smaller than those in Rowe et al. (2004), whereas α, $|G_{ei}|$, G_{ese}, $|G_{esre}|$, and p_0 were found to be larger on average. We attribute this to the different fitting algorithms used, since the new algorithm runs through a range of initial values, whereas the version used by Rowe et al. (2004) initialized parameters at a single set of values. The new fitting algorithm is an improvement over the old one because it reduces bias introduced by the choice of initialization.

We previously reported classic and model-based spectral parameters for 32 healthy males aged 18–28, whose eyes-closed EEGs were obtained in six consecutive weeks, followed for some subjects by intervals of several months (van Albada et al., 2007). Mean values for males in the range 18–28 years from the present study are compared with those from van Albada et al. (2007) in Table C.3. Overall, differences between the two studies are small, and only G_{ee} and p_0 differ substantially.

C.3.3 Age trends

Sec. C.3.3 considers changes in model parameters across age. For comparison, trends in qEEG parameters are described in Sec. C.3.3.

Model parameters

Figure C.7 shows scatter plots and fitted nonlinear age trends of the form (C.2) for model parameters. The fits closely follow moving medians. Age trends for males and females are compared in Fig. C.8. The parameters for each of these fits are listed along with their standard errors in Table C.4. The parameter I is also indicated, corresponding to the age of the bend in the regression. Note that the slopes listed are asymptotic values, and differ somewhat from slopes during development and aging.

Trends in α and t_0 are characterized by steep decreases followed by more gradual increases after age $\sim$15 years. The cortical wave decay rate γ increases up to about age 20 years, after which the trend levels off. All gains except G_{srs} decrease in absolute value with age, changes occurring most rapidly during childhood. The power normalization parameter p_0 shows a rapid decline up to age $\sim$20 years, with much slower reductions thereafter.

These trends are similar for males and females, although there are some differences (cf. Fig. C.8). Girls have slightly larger values of t_0 than boys, but the values reconverge after adolescence. Females show an increase in G_{ese} at least up to age 20, whereas males show a decrease in this parameter over the same age range. Almost the reverse is true for G_{esre}, which becomes weaker

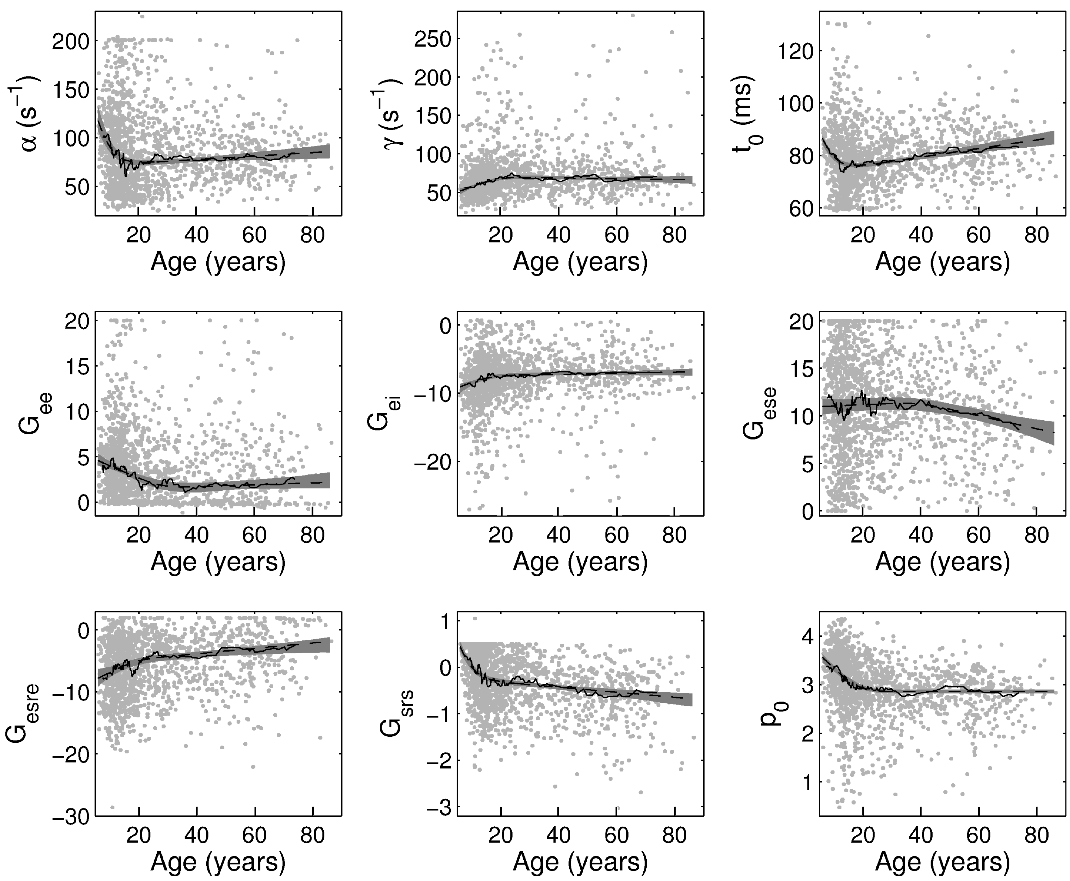

Figure C.7: Scatter plots and age trends of model parameters. Solid lines indicate moving medians, while dashed lines indicate fits of the form (C.2). The gray patches represent 95% confidence intervals for the fits, obtained by bootstrapping.

in boys but remains approximately constant in girls. Recalling that spectral uncertainty links changes in G_{ese} to opposite changes in G_{esre} (cf. Table C.2), some of these differences may not properly reflect the underlying physiology. Similarly, G_{srs} declines more with age in females than in males, while p_0 shows a greater decline in males, although the sex difference in correlation coefficients after age 20 was not found to be statistically significant [z-test (Olkin and Finn, 1995); $p = 0.32$]. Spectral uncertainty also induces a negative correlation between these quantities, albeit to a lesser extent than between G_{ese} and G_{esre} (cf. Table C.2). Figure C.8 shows that p_0 levels off to higher values in females than in males, and average values of this parameter in subjects >18 years differ significantly across sex (males, 2.7; females, 2.9; $p = 4.3\text{e}{-5}$).

	Param.	A	B	C	D	I
All subjects	α	**−12 ± 4**	180 ± 20	**0.18 ± 0.06**	71 ± 3	9 ± 3
	γ	**1.4 ± 0.4**	43 ± 4	−0.06 ± 0.05	71 ± 2	19 ± 5
	t_0	**−4 ± 1**	104 ± 4	**0.16 ± 0.02**	72.8 ± 0.8	8 ± 2
	G_{ee}	**−0.14 ± 0.03**	5.4 ± 0.5	0.01 ± 0.01	1.3 ± 0.7	28 ± 9
	G_{ei}	**0.17 ± 0.07**	−10.1 ± 0.7	0.008 ± 0.005	−7.6 ± 0.2	15 ± 8
	G_{ese}	0.01 ± 0.02	10.9 ± 0.6	**−0.07 ± 0.02**	14 ± 2	40 ± 30
	G_{esre}	**0.2 ± 0.1**	−9 ± 2	**0.04 ± 0.01**	−5.6 ± 0.5	20 ± 20
	G_{srs}	**−0.22 ± 0.06**	1.5 ± 0.2	**−0.005 ± 0.001**	−0.21 ± 0.05	8 ± 2
	p_0	**−0.059 ± 0.009**	3.91 ± 0.09	5e−5 ± 3e−5	2.85 ± 0.02	18 ± 3
Males	α	**−16 ± 5**	210 ± 20	**0.35 ± 0.08**	65 ± 3	9 ± 3
	γ	**1.2 ± 0.8**	48 ± 7	0.03 ± 0.04	67 ± 2	20 ± 10
	t_0	**−13** ± 3	111 ± 8	**0.15 ± 0.03**	72.7 ± 0.9	3.0 ± 1.0
	G_{ee}	**−0.11 ± 0.03**	5.1 ± 0.5	**0.08 ± 0.03**	−3 ± 2	40 ± 10
	G_{ei}	**0.17 ± 0.06**	−10.2 ± 0.6	0.001 ± 0.001	−7.4 ± 0.1	16 ± 7
	G_{ese}	**−0.05 ± 0.01**	13.1 ± 0.5	**0.31 ± 0.07**	−16 ± 4	80 ± 20
	G_{esre}	**0.23 ± 0.09**	−10 ± 1	0.03 ± 0.02	−4.7 ± 0.9	30 ± 10
	G_{srs}	**−0.3 ± 0.1**	1.8 ± 0.3	**−0.004 ± 0.002**	−0.20 ± 0.06	6 ± 2
	p_0	**−0.05 ± 0.01**	3.9 ± 0.1	−0.001 ± 0.001	2.83 ± 0.05	19 ± 5
Females	α	**−5 ± 3**	140 ± 20	0.10 ± 0.07	73 ± 3	12 ± 7
	γ	**1.7 ± 0.4**	39 ± 4	**−0.10 ± 0.05**	74 ± 2	19 ± 5
	t_0	**−1.2 ± 0.5**	93 ± 3	**0.18 ± 0.03**	72 ± 1	15 ± 6
	G_{ee}	**−0.20 ± 0.06**	6.2 ± 0.8	0.0005 ± 0.0007	1.9 ± 0.3	21 ± 8
	G_{ei}	**0.9 ± 0.4**	−14 ± 2	**0.012 ± 0.005**	−7.6 ± 0.3	7 ± 4
	G_{ese}	**0.09 ± 0.06**	8.6 ± 0.9	**−0.09 ± 0.03**	15 ± 2	40 ± 20
	G_{esre}	0.008 ± 0.010	−4.6 ± 0.3	**0.2 ± 0.1**	−20 ± 10	60 ± 60
	G_{srs}	**−0.10 ± 0.03**	1.0 ± 0.2	**−0.006 ± 0.002**	−0.28 ± 0.09	13 ± 5
	p_0	**−0.06 ± 0.01**	3.9 ± 0.1	0.0003 ± 0.0002	2.92 ± 0.02	17 ± 5

Table C.4: Parameters (A–D) and their standard errors for age trends of the form (C.2). The parameter $I = (B - D)/(C - A)$, representing the age (in years) of the turning point in each age trend, is also given along with its standard error. The numbers of figures reported are adapted to the corresponding standard errors. Slopes that differ significantly from zero based on 95% bootstrapping intervals are indicated in bold.

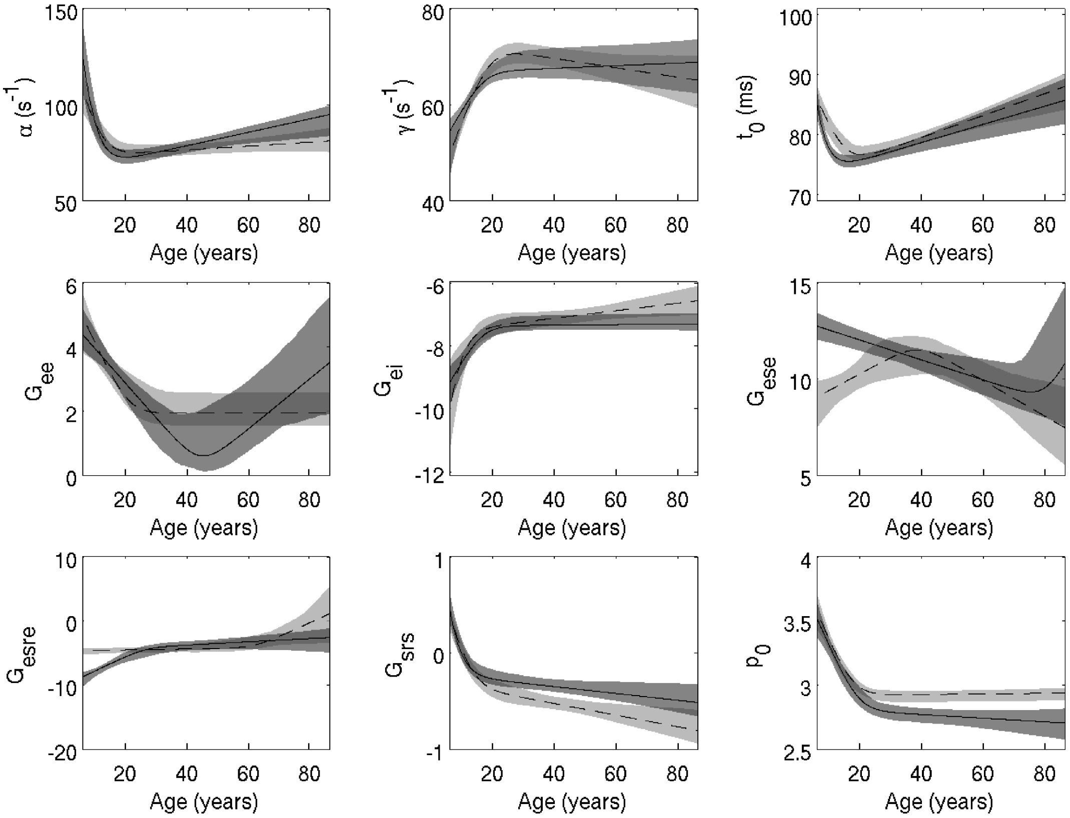

Figure C.8: Age trends in model parameters for males (solid lines) and females (dashed lines), with corresponding 95% confidence intervals.

Comparison with model-free spectral measures

Empirical and fitted model spectra across age are shown in Fig. C.9. For the contour plots in Figs C.9(a) and (c) one-year intervals were used between ages 6 and 20, five-year intervals from 20 to 80, and a single band for age ≥ 80. Figures C.9(b) and (d) show empirical and fitted model spectra for a coarser set of age bands. Figure C.10 contains age trends of the form (C.2) in empirical qEEG parameters.

Total power, and especially that at low frequencies, decreases with age at a gradually diminishing rate. Thus, relative low-frequency power is reduced, and relative high-frequency power is enhanced. Relative alpha power increases approximately until age 30 and then decreases. The frequency of the alpha peak rises until adolescence and then decreases into old age. Since some alpha peaks, particularly in children and the elderly, appear in what has been defined here to be the theta range (i.e., corresponding to adult theta frequencies), this will contribute to the observed trends in relative theta and alpha power. Figure C.9 shows that a small beta peak develops from about age 40, when alpha

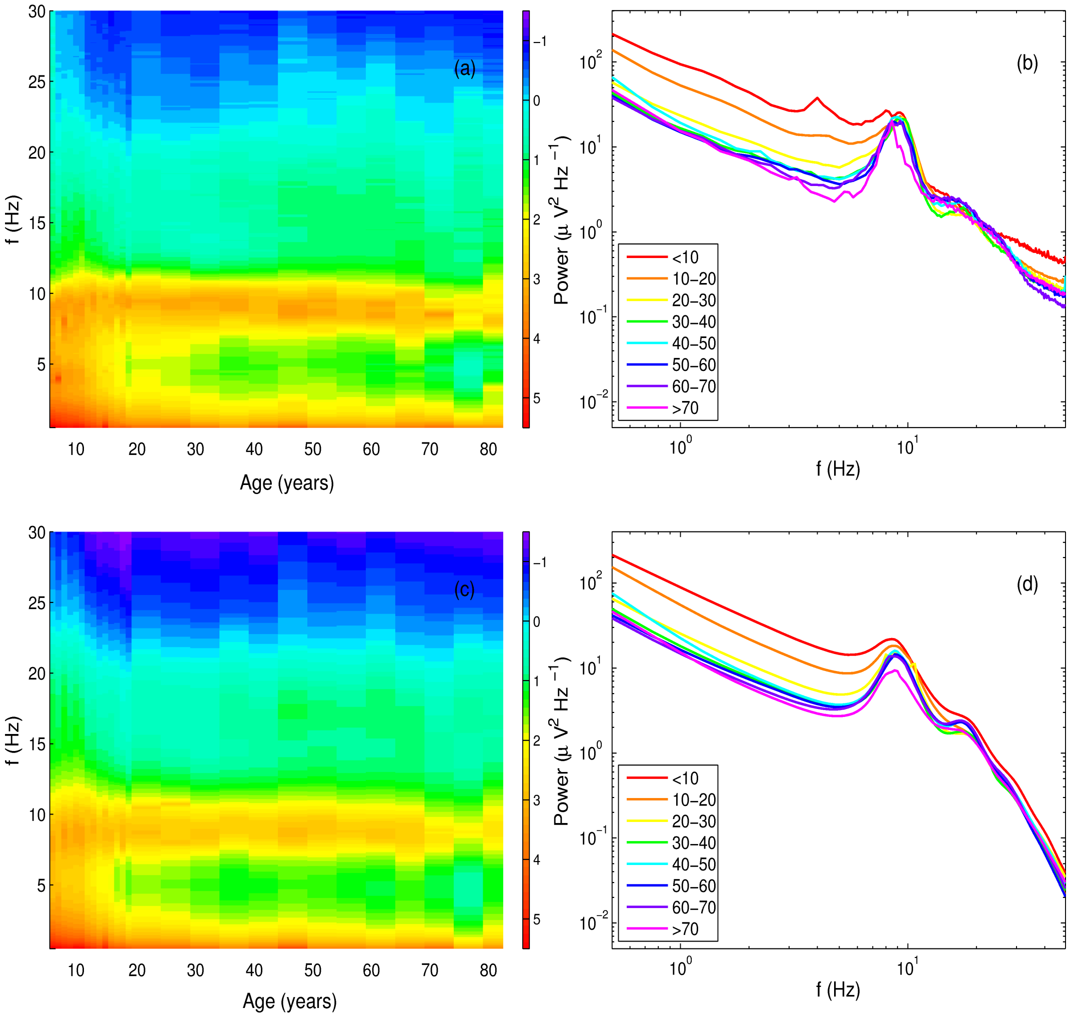

Figure C.9: Changes across age in empirical and fitted spectra. (a) Empirical spectral power averaged across individuals for frequencies up to 30 Hz; (b) double logarithmic plots of averaged empirical spectra; (c) and (d) corresponding plots for fitted spectra. The color bars indicate the logarithm of the dimensionless version of spectral power in μV^2 Hz^{-1}, and the legends of (b) and (d) indicate age in years. The model spectra show a rapid fall-off at high frequencies because the fitted EMG component is not plotted.

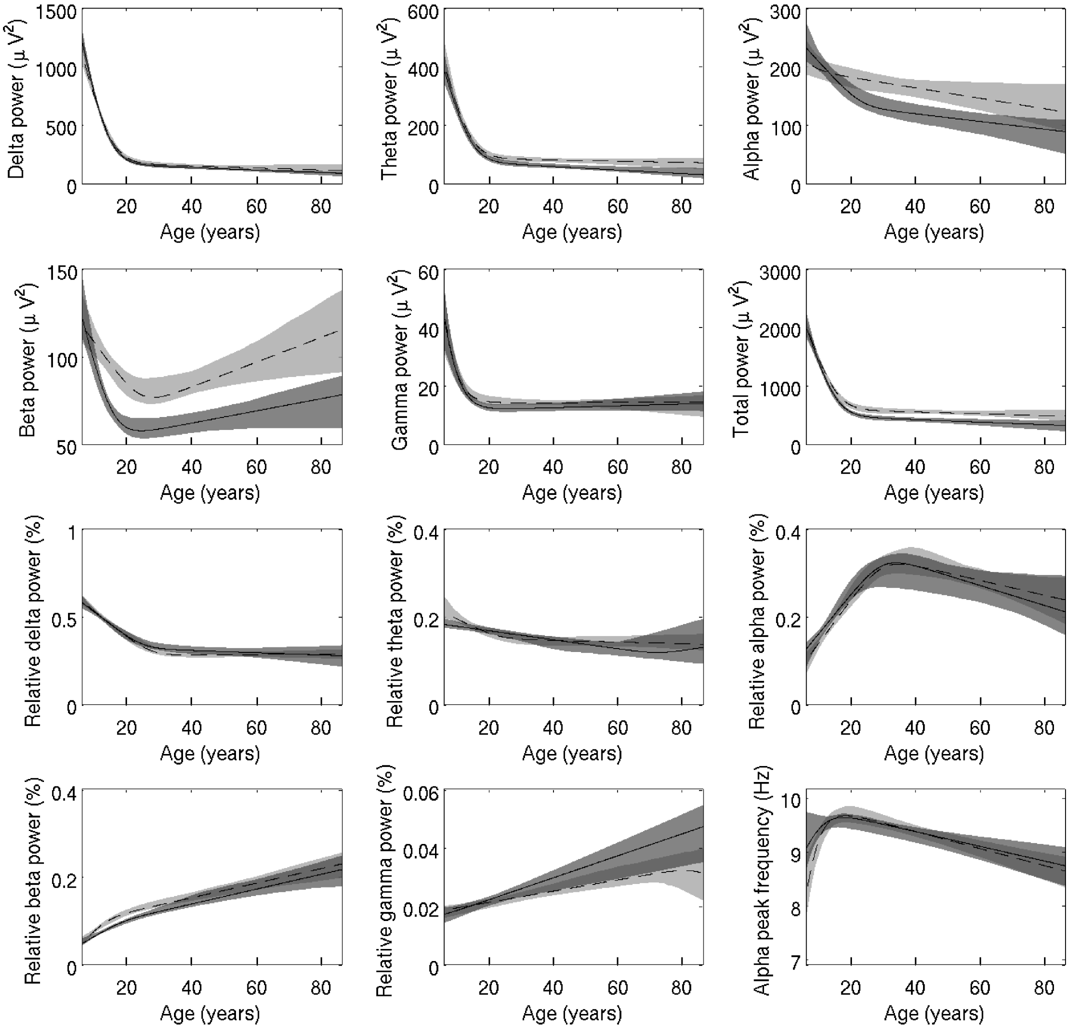

Figure C.10: Age trends in qEEG parameters determined using the functional form (C.2), with 95% confidence intervals. Solid lines, males; dashed lines, females.

peaks are sharper than in early life. The parallel development of beta peaks and sharper alpha peaks supports the hypothesis, implied by our model, that beta is an approximate harmonic of alpha (Robinson et al., 2001b). Note from Fig. C.9(b) that there is even a hint of a third harmonic between 20 and 30 Hz in older subjects.

Table C.5 illustrates the sensitivity of model spectra to model parameters, based on variations around fitted values. Higher synaptodendritic and cortical decay rates α and γ are associated with more power in the alpha through gamma bands. Thus, larger α and γ increase relative high-frequency power and reduce relative low-frequency power. Greater intracortical excitation, quantified by G_{ee}, has the opposite effect. As expected, p_0 does not affect any of the relative band powers, but is positively correlated with absolute power in all bands. The correlations are not perfect because all parameters were varied simultaneously. Of model parameters besides p_0, G_{ei} is most strongly correlated with absolute power in the delta through beta bands. Stronger intracortical inhibition is associated with less power in all bands. Stronger G_{ese} enhances relative alpha power, since the model describes alpha resonances that arise in thalamocortical loops. Relative delta power depends most consistently on the intrathalamic gain G_{srs}: less negative G_{srs} is associated with more relative delta power. Higher rates α and γ, and shorter thalamocortical axonal loop delays t_0, are predictive of higher alpha peak frequencies (cf. Sec. C.2.2). The gains G_{ee}, G_{esre}, and G_{srs} have a significant negative correlation with alpha peak frequency. Thus, stronger intrathalamic interactions and weaker intracortical excitation are associated with higher peak frequencies. Relative theta power has a significant positive correlation with t_0, since sufficiently large t_0 can move alpha peaks to the theta range.

C.4 Discussion

This study considered age trends in parameters obtained by model fits to empirical EEG spectra of a large sample (1498 subjects) of healthy males and females aged 6–86 years. Theoretical spectra were generated from a mean-field model of the thalamocortical system, describing interactions between excitatory and inhibitory cortical populations, and thalamic relay and reticular nuclei. Fitting to these spectra provided physiologically meaningful information on the neuronal substrates underlying the EEG. Fitted parameters were an average synaptodendritic decay rate (α), a damping rate for cortical propagating waves (γ), an average axonal delay for a full thalamocortical loop (t_0), an overall power normalization parameter (p_0), and gains for excitatory and inhibitory cortical interactions (G_{ee} and G_{ei}, respectively), a direct loop between cortex and relay nuclei (G_{ese}), an indirect thalamocortical loop passing through the

	$\Delta\alpha$	$\Delta\gamma$	Δt_0	ΔG_{ee}	ΔG_{ei}	ΔG_{ese}	ΔG_{esre}	ΔG_{srs}	Δp_0
Δ Power (μV^2)									
Δ Delta	0.0071	**0.098**	−0.025	**0.20**	**0.38**	**−0.15**	**−0.11**	**0.30**	**0.50**
Δ Theta	−0.011	**0.088**	**0.085**	**0.15**	**0.42**	−0.038	**0.068**	**0.21**	**0.63**
Δ Alpha	**0.19**	**0.24**	−0.0080	0.036	**0.50**	**0.13**	0.050	−0.027	**0.53**
Δ Beta	**0.37**	**0.26**	0.013	−0.024	**0.40**	−0.019	0.039	**−0.091**	**0.60**
Δ Gamma	**0.44**	**0.43**	0.015	−0.043	**0.29**	−0.017	0.033	**−0.055**	**0.50**
Δ Total	**0.11**	**0.18**	0.013	**0.14**	**0.47**	−0.037	−0.016	**0.16**	**0.58**
Δ Relative power (%)									
Δ Delta	**−0.23**	**−0.19**	**−0.090**	**0.24**	−0.046	**−0.28**	**−0.25**	**0.43**	−0.028
Δ Theta	**−0.29**	**−0.26**	**0.19**	0.0058	**−0.13**	0.0094	**0.23**	**0.060**	0.0078
Δ Alpha	**0.19**	**0.22**	−0.024	**−0.18**	**0.19**	**0.36**	**0.13**	**−0.33**	0.026
Δ Beta	**0.44**	**0.16**	0.026	**−0.25**	**−0.17**	−0.027	0.044	**−0.43**	0.020
Δ Gamma	**0.48**	**0.40**	−0.0083	**−0.20**	**−0.15**	−0.021	0.031	**−0.27**	0.012
Δ Alpha peak frequency (Hz)									
	0.44	**0.18**	**−0.27**	**−0.15**	−0.0069	−0.013	**−0.17**	**−0.30**	−0.022

Table C.5: Relationships between model parameters and qEEG parameters determined from model spectra. Model parameters were varied around their fitted values, and Spearman correlations were calculated between differences in model parameters and differences in qEEG parameters. Absolute values >0.050 for correlations were significant at the 0.05 level, those >0.065 at the 0.01 level, and those >0.085 at the 0.001 level. Significant correlations ($p < 0.05$) are shown in bold. Band limits were: delta, 0.5–4 Hz; theta, 4.25–8 Hz; alpha, 8.25–12 Hz; beta, 12.25–30 Hz; gamma: 30.25–49.5 Hz. Total power was calculated over the range 0.5–49.5 Hz. Alpha peak frequencies correspond to the frequencies where power was maximal in the range 5–13 Hz.

reticular nucleus (G_{esre}), and an intrathalamic loop (G_{srs}). Net inhibitory connections or loops were represented by negative gains (G_{ei}, G_{esre}, and G_{srs}), whereas net excitatory interactions had positive gains (G_{ee} and G_{ese}). The robustness of fits was assessed by refitting empirical spectra with noise added, and comparing old and new parameter values.

Age trends were approximated by smooth asymptotically linear functions with a single turning point. In the literature, age trends for EEG parameters have been described using linear functions (e.g., John et al., 1980; Matoušek et al., 1967; Polich, 1997), piecewise linear functions (e.g., Duffy et al., 1993; Hughes and Cayaffa, 1977; Somsen et al., 1997), or polynomials (e.g., Aurlien et al., 2004a; Duffy et al., 1993). The functions proposed here have the advantage that (i) they are smooth and hence more physiologically realistic than piecewise linear functions; (ii) they are able to follow both fast trends during "development" and slower trends during "aging", unlike single linear functions; (iii) they have only four parameters (or five, including the characteristic age range over which slopes change considerably, which was fixed here), which have a simple interpretation in terms of asymptotic slopes and intercepts, in contrast to polynomial functions with variable numbers of parameters and no clear interpretation.

Since EEG trends in the literature are often reported in terms of absolute and relative band powers and alpha peak frequencies, results on these quantitative EEG (qEEG) measures and their age trends were also presented. Furthermore, the relationships between model parameters and qEEG parameters were investigated. Aided by the large sample size, many significant results were found, which we summarize here and interpret in the light of the relevant literature. For each parameter, we first discuss significant sex differences when present, then summarize age trends, relate these trends to qEEG changes, and finally discuss possible relationships with physiological changes in childhood and adulthood.

General findings

The most robustly fitted parameter was G_{srs}, followed, respectively, by t_0, α, G_{ee}, p_0, G_{esre}, γ, and G_{ese}. We found the least robust parameter to be G_{ei}, consistent with the earlier result that this gain varied widely within individuals in a study of males aged 18–28 years (van Albada et al., 2007).

Between-fit differences in parameters were significantly correlated for a large number of parameter pairs. This occurs both because different sets of parameters can yield identical spectra, and because of the differential dependence of the goodness of fit on the parameters. The former introduces uncertainty in fitted parameters even if the spectrum is perfectly known, whereas the latter introduces additional uncertainty due to the presence of noise. Associations between parameters due to these effects may cause age trends that are not physiological in origin, so trends in parameters that are not highly robust should be interpreted with particular caution.

Averaged across age, there were significant sex differences in t_0, G_{ese}, G_{esre}, and G_{srs}: t_0 and $|G_{srs}|$ were larger in females, whereas G_{ese} and $|G_{esre}|$ were smaller. These sex differences were small compared to changes across the life span in either sex. Similarly, EEGs depended less on sex than on age in a study of a large group of healthy children and young adults (Matsuura et al., 1985). Average values of α, γ, G_{ee}, G_{ei}, and p_0 did not differ significantly between males and females. Although no significant sex difference in p_0 was found across age, trends in females clearly leveled off to higher values than in males during adulthood.

Parameter changes occurred most rapidly during childhood, and trends generally leveled off and sometimes reversed around adolescence. There were some sex differences in age trends besides those in p_0, which are more fully described below.

Synaptodendritic rate α

The average decay rate α for cell-body potentials in response to synaptic inputs, and by implication also the rise rate β (since $\beta = 4\alpha$ was imposed), decreased until about age 18, followed in males by a slight increase.

Smaller values of α enhance the low-pass filter properties of the synapses and dendrites, and correspond to less high-frequency ($\gtrsim$30 Hz) activity in the EEG (Rowe et al., 2004). The relative constancy of α for adults in our study suggests that increases in relative high-frequency power with age in adulthood (Dustman et al., 1999b) are largely independent of changes in synaptodendritic rates.

Several factors may contribute to the observed trends in α. First, a number of studies have found the total length of dendrites in the human cortex to increase in childhood, over longer periods in frontal than in visual areas (Becker et al., 1984; Huttenlocher, 1990), a process that may continue even into old age in some areas (Buell and Coleman, 1979, 1981). Unless the dendritic thickness increases proportionally to the square of the length, this is expected to increase the electrotonic length of neurons (Hill et al., 1994), leading to larger effective time constants (Ascoli, 2003). Unfortunately, investigations of dendritic thickness are sparse and rarely quantitative, at best allowing the conclusion that dendritic thickness of pyramidal neurons in certain cortical layers and areas increases slightly at least until age 5 years (Koenderink and Uylings, 1995; Petanjek et al., 2008).

Alterations in intrinsic membrane properties and numbers of neurotransmitter receptors are also expected to affect α. Expanded membrane surface and reduced capacitance have been suggested to contribute to decreases in membrane time constants during maturation (Tennigkeit et al., 1998; Warren and Jones, 1997), in contrast with the trend in α until age 18 found here (note that α is an inverse time constant). The expression of subunits of the NMDA receptor, which mediates slow glutamatergic transmission, reaches a peak in early development, after which it declines at a decreasing rate (Magnusson et al., 2002; Ontl et al., 2004). This decline is also expected to increase α.

A number of studies have reported shrinkage of the dendritic trees of some neuronal types in adulthood (de Brabander et al., 1998; Esiri, 2007; Jacobs et al., 1997; Uylings and de, 2002), which may contribute to slight increases in α in this age range. On the other hand, Luebke and Rosene (2003) reported significantly longer decay times of inhibitory postsynaptic currents in hippocampal cells of aged compared to young monkeys. This was tentatively attributed to changes in the subunit composition of GABA_A receptors, as found by Gutiérrez et al. (1997) in rat cerebellum and cerebral cortex. These effects would tend to decrease α, and thus cannot account for the trends in adults seen in our study. Therefore, these results merit further investigation.

Cortical damping rate γ

A damped-wave equation for cortical activity was included in the model based on experimental observations of spreading waves of neuronal activity in response to localized stimulation (Chervin et al., 1988; Nunez, 1974; Schiff et al., 2007; Xu et al., 2007). The parameter γ, representing the characteristic damping rate of such waves, increased in both sexes until about age 20, after which the trends leveled off, and even reversed in females.

Larger values of γ are associated with sharper, larger-amplitude, and slightly higher-frequency peaks in the EEG spectrum (Rowe et al., 2004). Thus, changes in the damping rate of cortical waves may contribute to the shift of alpha peaks to higher frequencies during childhood (Hughes, 1987; Kooi, 1971; Niedermeyer and Lopes da Silva, 1998; Somsen et al., 1997), and the narrowing of alpha peaks that was found by Amador et al. (1989) at the C3 electrode. Power augmentation due to larger γ was offset by other parameter changes, including reduced p_0 (see below), to yield a net decline in peak amplitudes, in agreement with the literature (Niedermeyer and Lopes da Silva, 1998).

Since γ is the ratio of the average axonal propagation speed and the typical range of cortical pyramidal axons, increased γ is associated with faster transmission and/or shorter effective ranges (although the characteristic range of pyramidal axons was fixed in this study). Ongoing cortical myelination (Perrin et al., 2008; Sowell et al., 2003) may contribute to increases in γ throughout childhood and adolescence by increasing axonal transmission speeds. However, the more rapid growth of white matter in boys than in girls (Caviness et al., 1996; De et al., 2001; Perrin et al., 2008) did not translate into greater slopes for γ in our study.

A number of studies have found reductions in white matter volume during aging, especially from the fifth decade onward (Ge et al., 2002; Miller et al., 1980; Piguet et al., 2009). Even in myelin sheaths that continue to grow during aging, defects accumulate, and thick sheaths are prone to splitting (Peters, 2002,b). Myelin defects reduce conduction velocities along nerve fibers (Felts et al., 1997; Gutiérrez et al., 1995; Xi et al., 1999). These effects may have contributed to decreases in damping rates in women.

Thalamocortical loop delay t_0

Averaged across the entire age span, the axonal delay t_0 was slightly longer in females than in males. This delay depends on the distance between cortex and thalamus, and velocities along thalamocortical and thalamocortical fibers. Since females have smaller brains on average (Caviness et al., 1996; Dekaban and Sadowsky, 1978), our finding suggests that the propagation speed along axons is more than proportionately smaller in females. This may be related to the smaller percentage of white matter in female compared to male brains (Cosgrove et al., 2007). Since the location of the alpha peak in model spectra depends on the inverse of t_0, this is expected to correspond to higher alpha peak frequencies in males than in females. Males did consistently show slightly higher peak frequencies across age and sites, except around age 20, when females had higher peak frequencies (not shown). Averaged across age, we did not find significant sex differences in alpha peak frequencies at the Cz electrode.

Our results contrast with the finding that alpha peak frequencies are on average slightly higher in females than in males up to age 12–13 (Petersén and Eeg-Olofsson, 1971), as well as averaged over the entire life span (Aurlien et al., 2004a). This discrepancy may be partly explained by the fact that neither Petersén and Eeg-Olofsson (1971) nor Aurlien et al. (2004a) used spectral analysis, and instead relied on time series (which leads to less precise estimates, particularly since traces are modulated by lower-frequency activity). Furthermore, Aurlien et al. studied patients with various pathologies (mostly epilepsy), and selected the highest alpha frequency for each subject. All these factors make it difficult to compare their findings with ours.

The decline in t_0 observed in males up to age ∼15, and in females up to age ∼20, paralleled accelerated alpha rhythms. This corresponds well with findings reported in the literature, as summarized for instance by Petersén et al. (1975) and Klimesch (1999). An increase in the frequency of the alpha peak from about 5–6 Hz to 10 Hz is observed in children between ages 1 and 15 years (Hughes, 1987; Kooi, 1971; Niedermeyer and Lopes da Silva, 1998; Somsen et al., 1997). Our data appear to confirm the finding by Petersén and Eeg-Olofsson (1971) that the alpha rhythm increased in frequency faster in girls than in boys. However, white matter volume has been reported to increase faster in boys than in girls after age 6 (Caviness et al., 1996; De et al., 2001; Perrin et al., 2008), in agreement with more marked reductions in t_0 in boys found here. This suggests that developmental changes in alpha peak frequencies depend not only on white matter growth, but also on other factors. Our results show less marked reductions in synaptodendritic rates in girls than in boys, as well as greater increases in the interaction strength between the thalamic relay and reticular nuclei ($|G_{srs}|$); both tend to enhance increases in alpha peak frequency.

In both sexes t_0 increased into old age, associated with a gradual reduction in the frequency of the alpha peak. These trends may be linked to loss of white matter and accumulating damage to myelin sheaths in adulthood (Peters, 2002,b; Piguet et al., 2009). Decreased alpha peak frequencies are consistent with some early studies of aged individuals without organic brain disease (Hughes and Cayaffa, 1977; Obrist, 1954), but were either not found in more tightly controlled samples, or attributed to age-related pathologies (Duffy et al., 1984, 1993; Katz and Horowitz, 1982). However, Klimesch (1999) noted that the absence of a significant trend in alpha peak frequency reported by Duffy et al. (1984) was due to a relative lack of change between 30 and 50 years, whereas this frequency diminished by about 1 Hz between the ages of 60 and 80. We also observe that slight decreases in the frequency of the alpha peak may not have reached statistical significance due to the relatively small sample (63 subjects) used by Duffy et al. (1984). In agreement with our results, Aurlien et al. (2004a) found dominant alpha frequencies to decrease after age 45.

Gains

All gains except that for the loop between thalamic relay and reticular nuclei, G_{srs}, had larger average absolute values in males. More negative G_{srs} corresponds to differences in qEEG measures including greater absolute and relative beta power. Thus, the greater absolute and relative beta power in women than in men found here and reported in the literature (Veldhuizen et al., 1993) may be related to stronger interactions between the thalamic relay and reticular nuclei in women.

On average, the absolute values of all gains except G_{srs} diminished with age. The cortical excitatory gain G_{ee} decreased in childhood in both males and females, after which it increased in males but stayed about constant in females. The greatest reduction in the cortical inhibitory gain $|G_{ei}|$ occurred up to age ∼20, and trends in both sexes leveled off thereafter. Boys and girls showed opposite trends in the thalamocortical loop gain G_{ese}, which decreased in the former but increased in the latter. The trend for females reversed around age 40. The gain for the thalamocortical loop passing through the thalamic reticular nucleus, $|G_{esre}|$, decreased mostly at young ages in males, but mostly during old age in females.

Relative delta and theta power gradually diminished during childhood, as also reported in the literature (Amador et al., 1989). Sensitivity analysis suggested that stronger interactions between the thalamic relay and reticular nuclei (quantified by G_{srs}) contribute to reductions in relative low-frequency power and increases in relative beta and gamma power. Reductions in G_{ee} tend to decrease relative delta power and increase relative beta and gamma power, while reductions in $|G_{ei}|$ decrease relative theta power. Increases in G_{ese} in girls, and decreases in $|G_{esre}|$ in boys, may contribute to reductions in relative delta power.

Reductions in G_{ee} may have a variety of causes. Extensive pruning of excitatory synapses occurs in primate cortex during adolescence (Gonzalez-Burgos et al., 2008). The density of NMDA glutamate receptors decreases with age, and reduced cortical glutamate content has been observed in aged animals (Segovia et al., 2001). Although decreased glutamate uptake may compensate partly for the decline in glutamate release, these findings appear to support a reduction in G_{ee}. It is particularly striking that G_{ee} decreases until about age 40, found by Jacobs et al. (1997) to be the age at which dendritic spine numbers in two cortical areas approximately stabilize after marked reductions. These findings do not explain the observed sex differences in trends in G_{ee}, so this issue deserves further exploration.

The observed decline in $|G_{ei}|$ during childhood is surprising, since the number of GABAergic synapses increases in this period of life (Heinen et al., 2003), and the brain becomes less vulnerable to epileptic seizures (Camfield et al., 1996). Furthermore, Luebke et al. (2004) found synaptic inhibition in the monkey prefrontal cortex to increase with age. On the other hand, the open times of $\mathrm{GABA_A}$ receptors shorten during development, impairing inhibitory synaptic transmission (Bosman et al., 2005). There is some experimental evidence supporting the reduction in inhibitory cortical interactions in adulthood found here. Poe et al. (2001) described an age-related reduction in the numbers of putative inhibitory synapses in layer 2 of rat somatosensory cortex. Furthermore, some studies with transcranial magnetic stimulation have revealed reduced excitability of cortical inhibitory circuits with aging (Hortobágyi et al., 2006; Peinemann et al., 2001).

Early increases in $|G_{srs}|$ may be related to the growing ability of reticular neurons to sustain bursts of activity (Tennigkeit et al., 1998; Warren and Jones, 1997). In addition, substantial growth of dendritic arbors occurs during maturation (Warren and Jones, 1997), possibly enabling more synaptic contacts to be established. However, dendritic growth cannot account for continued increases in $|G_{srs}|$ during adulthood, which is characterized by regressive processes (Abe et al., 2008). Enhanced expression of metabotropic glutamate receptors in the thalamus during aging (Simonyi et al., 2005) may play a role in the observed trends in G_{srs}. Loss of synapses may explain the significant reductions in G_{ese} and $|G_{esre}|$ in adults found here.

Spectral power normalization p_0

We found that the power normalization parameter p_0 was slightly larger on average in females than in males, although this difference was not significant at the 0.05 level. This accords with the finding that the skulls of white males are slightly thicker at the vertex throughout life than those of white females (Adeloye et al., 1975), since thicker skulls cause greater attenuation of the signal. However, no such differences were found in black subjects, and females had thicker skulls than males at parietal and parieto-occipital sites in the third decade and after age 60. Thus, different findings for p_0 may be expected at electrode sites other than Cz.

The parameter p_0 diminished until age ∼20, after which it showed a slower decrease that was slightly more pronounced in males. The negative trend in p_0 agrees with the decrease in EEG amplitude with age found here and reported in the literature (Aurlien et al., 2004a; Hartikainen et al., 1992; Matoušek et al., 1967; Polich, 1997). EEG amplitude has been reported to increase until 6–11 years and then diminish (Hughes, 1987; Petersén and Eeg-Olofsson, 1971; Petersén et al., 1975). Similarly, closer inspection of our data revealed that p_0 only decreased systematically from about age 10 onward. Due to the relatively small number of subjects aged >80 years, it was not possible to verify from our data if power increased again in the very old, as reported by Aurlien et al. (2004a).

Increases in skull thickness in the first two decades of life (Adeloye et al., 1975) may account for substantial decreases in EEG power recorded on the scalp (Eshel et al., 1995). The reduction in brain volume across the life span is also likely to be linked to negative trends in p_0. Most studies find that age-related atrophy is more extensive in men than in women (Coffey et al., 1998; Cowell et al., 1994; Gur et al., 1991; Tomlinson et al., 1968; Xu et al., 2000), although the onset may be earlier in women (Hatazawa et al., 1982;

Hubbard and Anderson, 1983). Greater changes in peripheral and lateral fissure cerebrospinal fluid volume were also observed in men than in women between 65 and 95 years of age (Coffey et al., 1998). These results accord with the steeper slope in p_0 for males compared to females aged $\gtrsim 20$ in our study, although the difference in age correlations was not statistically significant. Reductions in total power across the life span were also slightly greater in men than in women.

Outlook

This study has shown that mean-field modeling of brain electrical activity presents a viable alternative to classical qEEG, enabling physiological information to be extracted from EEG spectra. The large number of subjects (1498) allowed reliable estimation of average age trends, even with large inter-individual scatter. The average parameter values for healthy individuals across age provide a standard against which clinical groups may be compared.

The model parameters describe large-scale properties of the brain, and as such provide different information than that afforded by most invasive techniques. Moreover, the connection with physiology is an advantage over many other non-invasive techniques. Furthermore, model spectra match most features of empirical spectra, and thus capture most of the information present in absolute and relative band powers and alpha peak frequencies, but contain additional information about spectral shape within bands. Thus, the method presented allows questions about age-related changes in the properties of the brain to be answered that are not readily addressed using other methods.

The cross-sectional design has the potential disadvantage that the results are affected by differences across generations, for instance due to changes in nutrition or education. However, a longitudinal study of the age range considered here would take at least 80 years to complete, rendering this approach highly impractical.

Parallels between age trends in fitted model parameters and known physiological trends provide evidence that the physiological interpretations made of model parameters are plausible. For instance, decreases followed by increases in axonal delays accord with white matter growth during childhood and subsequent accumulation of myelin defects. Similarly, acceleration of axonal conduction due to myelination may account for increases in the damping rate of cortical waves during development. Furthermore, reductions in absolute gain values plausibly reflect synaptic pruning processes. However, there are also discrepancies between parameter trends and known physiological changes. For instance, a number of empirical studies suggest increases followed by decreases in synaptodendritic rates, opposite to our findings. It is hoped that the comparisons presented here will help to spur on further development of realistic models of EEG generation.

An identical subject set will be used to compare our results with data on alpha peak morphology (Chiang et al., 2008), model fits to EPs (Chapter c5++Fix), and EP deconvolution parameters (Chapter c4++Fix), eliminating important sources of experimental bias and uncertainty. It would also be desirable to compare the Cz data presented here with data from other electrodes, to assess differences in aging processes across brain regions. In addition, it will be possible to determine links with genetics and measures of general and social cognition using data from the Brain Resource International Database (www.brainresource.com) (Gordon et al., 2005). Great advantages of this standardized database are its size, diversity of recording modalities, and the uniformity of exclusion criteria and experimental conditions. Convergent evidence from different modalities will help to elucidate some of the links between the physiological substrates and functional aspects of brain aging.

Appendix

Mathematical description of model

With each neuronal population we associate a pulse rate field, which is a continuum estimate of the average rate of incoming action potentials for that population. The pulse rate field is denoted $\phi_a(\mathbf{r}, t)$, where $\mathbf{r}$ is a spatial coordinate within each neuronal population, and the subscript a represents the relevant population. For a given receiving population, the contributions of all afferent populations are weighted by the relevant connection strengths and summed. Dendritic and synaptic delays are modeled using a second-order differential equation that incorporates characteristic rise and decay rates of the membrane potential, respectively denoted β and α. The equations for dendritic and synaptic summation and integration are then (Robinson et al., 1997, 2002)

$$D_{\alpha\beta}(t)V_a(\mathbf{r}, t) = \sum_b \nu_{ab}\phi_b(\mathbf{r}, t - \tau_{ab}), \tag{C.5}$$

$$D_{\alpha\beta}(t) = \frac{1}{\alpha\beta}\frac{d^2}{dt^2} + \left(\frac{1}{\alpha} + \frac{1}{\beta}\right)\frac{d}{dt} + 1, \tag{C.6}$$

where V_a is the average cell-body potential of population a, $\nu_{ab} = N_{ab}s_b$ are connection strengths consisting of the unitary synaptic strength s_b and the number of synapses N_{ab} from neurons of type b per type a neuron, and τ_{ab} is the relevant axonal delay. The axonal delay for a full loop between cortex and thalamus is denoted t_0. The total delay necessary to complete a thalamocortical loop depends also on dendritic and synaptic integration times, and is slightly longer than t_0. In our model, the inverse of this total delay determines the location of the alpha peak in the frequency spectrum (Robinson et al., 2002).

When fitting to empirical spectra, a reduction in the number of independent parameters is achieved by setting $\alpha = \beta/4$, which agrees roughly with experimental results (Rowe et al., 2004). The number of fitted parameters is further reduced using the proportionality of the total number of synapses between two populations to the numbers of sending and receiving neurons, which holds approximately in the cortex (Braitenberg and Schuüz, 1998; Robinson et al., 2001b; Wright and Liley, 1995). Hence, the number of synapses *per cortical neuron* depends only on the afferent population, implying $N_{eb} = N_{ib}$ and $G_{eb} = G_{ib}$ for $b = e, i, s$ (note that we have approximated unitary synaptic strengths s_b as depending only on the sending population).

The outgoing firing rate field depends on the cell-body potential via a sigmoidal function, which results from the contribution of neurons with different firing thresholds. We use (Robinson et al., 1997, 1998, 2001b, 2003a),

$$Q_a(\mathbf{r}, t) = S[V_a(\mathbf{r}, t)] = \frac{Q_{\max}}{1 + \exp[-(V_a - \theta)/\sigma']}, \tag{C.7}$$

where $Q_{\max}$ is the maximum firing rate, θ is the average threshold potential, and $\sigma'\pi/\sqrt{3}$ is the standard deviation of firing thresholds (Wright and Liley, 1995). The version of the model used in the present study imposes equal values of $Q_{\max}$, θ, and σ' for all components, which may be interpreted as average or effective values.

The cortex is modeled as a two-dimensional sheet (parameterized by $\mathbf{r}$) owing to its relative thinness. Many experimental studies have shown that localized cortical stimulation leads to waves of neuronal activity spreading across the cortex (Chervin et al., 1988; Nunez, 1974; Schiff et al., 2007; Xu et al., 2007), a feature included in a number of earlier models (Beurle, 1956; Bressloff, 2001; Bressloff et al., 2003; Jirsa and Haken, 1996, 1997; Nunez, 1995). We use a damped-wave equation for the excitatory pulse rate field (Robinson et al., 1997, 1998, 2001b, 2003a),

$$\left[\frac{1}{\gamma^2}\frac{\partial^2}{\partial t^2} + \frac{2}{\gamma}\frac{\partial}{\partial t} + 1 - r_e^2\nabla^2\right]\phi_e(\mathbf{r}, t) = Q_e(\mathbf{r}, t), \tag{C.8}$$

where isotropy and homogeneity have been assumed, r_e is the characteristic range of pyramidal axons, $\gamma = v_e/r_e$ is the damping rate of cortical waves, and v_e represents the axonal propagation speed. The typical range of axons within the remaining populations is taken to be short enough to ignore wave propagation effects, allowing us to set $\phi_a(\mathbf{r}, t) = Q_a(\mathbf{r}, t)$ for $a = i, s, r$, which has been termed the local activity approximation (Robinson et al., 2004). The signals from these populations therefore influence their targets via delayed one-to-one mappings.

Setting the spatial and temporal derivatives in Eqs. (C.5) and (C.8) to zero yields an odd number of uniform fixed points $\phi_a^{(0)} = Q_a^{(0)}$, usually one or three (Robinson et al., 2002). Stable fixed points represent steady states to which the system settles down unless perturbed. For physiological parameters we expect a low-firing-rate steady state, around which small perturbations can be described using a linear approximation,

$$Q_a(\mathbf{r},t) = Q_a^{(0)} + \rho_a \left[V_a(\mathbf{r},t) - V_a^{(0)}\right], \tag{C.9}$$

$$\rho_a = \frac{dQ_a(\mathbf{r},t)}{dV_a(\mathbf{r},t)}\Big|_{V_a^{(0)}}, \tag{C.10}$$

$$= \frac{Q_a^{(0)}}{\sigma'}\left[1 - \frac{Q_a^{(0)}}{Q_{\max}}\right], \tag{C.11}$$

where $V_a^{(0)}$ is the steady-state value of the mean membrane potential (Robinson et al., 2004), and ρ is the derivative of the sigmoid at steady state. Henceforth denoting $V_a - V_a^{(0)}$ simply by V_a, and similarly for Q_a and ϕ_a, Fourier transformation of Eqs. (C.5), (C.8), and (C.9) yields (Robinson et al., 2001b)

$$Q_a(\mathbf{k},\omega) = \rho_a V_a(\mathbf{k},\omega), \tag{C.12}$$

$$= L(\omega)\sum_b G_{ab}\phi_b(\mathbf{k},\omega)e^{i\omega\tau_{ab}}, \tag{C.13}$$

$$= \begin{cases} \left[\left(1 - \frac{i\omega}{\gamma}\right)^2 + \frac{k^2{v_e}^2}{\gamma^2}\right]\phi_e(\mathbf{k},\omega) & (a = e), \\ \phi_a(\mathbf{k},\omega) & (a \neq e), \end{cases} \tag{C.14}$$

where

$$L(\omega) = \left(1 - \frac{i\omega}{\alpha}\right)^{-1}\left(1 - \frac{i\omega}{\beta}\right)^{-1}. \tag{C.15}$$

Here, $\mathbf{k}$ and ω denote wavenumbers and angular frequencies, and $G_{ab} = \rho_a \nu_{ab}$ are linear gains representing the number of additional pulses out per additional pulse in. Equations (C.13) and (C.14) allow us to derive a linear transfer function $\phi_e(\mathbf{k},\omega)/\phi_n(\mathbf{k},\omega)$ describing the cortical response to input from underlying structures. For the neuronal connections in Fig. C.2, the transfer function is

(Robinson et al., 2002, 2004)

$$\frac{\phi_e(\mathbf{k},\omega)}{\phi_n(\mathbf{k},\omega)} \equiv T(\mathbf{k},\omega) = \frac{1}{(k^2+q^2)r_e^2}\frac{G_{es}G_{sn}L^2e^{i\omega t_0/2}}{(1-G_{srs}L^2)(1-G_{ei}L)}, \tag{C.16}$$

$$q^2r_e^2 = \left(1-\frac{i\omega}{\gamma}\right)^2 - \frac{L}{1-G_{ei}L}\left[G_{ee}+\frac{(G_{ese}L+G_{esre}L^2)e^{i\omega t_0}}{1-G_{srs}L^2}\right], \tag{C.17}$$

where we have defined $G_{ese} = G_{es}G_{se}$ for the direct thalamocortical loop, $G_{esre} = G_{es}G_{sr}G_{re}$ for the indirect thalamocortical loop passing through the reticular nucleus, and $G_{srs} = G_{sr}G_{rs}$ for the intrathalamic loop between relay nuclei and the reticular nucleus. We see that the cortical signal depends only on these gain products, which can be interpreted as being distributed around loops rather than localized to single populations.

Frequency spectra

The EEG is the result of dendritic and synaptic currents of many cortical neurons firing in partial synchrony (Nunez, 1995; Ray, 1990). Excitatory pyramidal neurons are the largest and most aligned among cortical neuronal types, and are thus expected to dominate the signal (Nunez, 1995; Robinson et al., 2001b). Furthermore, the EEG is thought to depend much more strongly on excitatory synaptic input to apical dendrites of pyramidal cells than on inhibitory input to basal dendrites.

One reason for this is that the basal dendrites are closer to the relatively conductive cell body, causing dipoles to arise only over small distances. In addition, basal dendrites are less aligned than apical dendrites, and their synaptic actions are less layer-specific (Mitzdorf, 1985; Towe, 1966). We can therefore approximate the dendritic and synaptic currents responsible for EEG fluctuations as being roughly proportional to the pulse rate field ϕ_e.

The frequency spectrum measured on the scalp is a low-pass filtered version of that on the cortical surface, due to volume conduction attenuating the large-wavenumber content of the signal, and the association of large wavenumbers with high frequencies. Furthermore, the signal measured on the scalp contains a contribution from the muscles. For the purpose of model fitting, input from underlying structures is approximated as spatiotemporal white noise, represented by a constant modulus and random phase in the Fourier domain, $|\phi_n(\mathbf{k},\omega)|^2 = |\phi_n|^2$. This is consistent with evidence that EEG activity often has the properties of filtered noise (Lopes da Silva et al., 1974; Stam et al., 1999), and has proven to yield realistic spectra in previous works (Robinson et al., 2001b, 2003a). Although boundary conditions have only small effects on the cortical spectrum (Robinson et al., 2001a), they were found to improve fits in some cases (Rowe et al., 2004). For a two-dimensional rectangular cortex of size $L_x \times L_y$, the spectrum can be written as a sum over a discrete set of wavenumbers taking the form (Rennie et al., 2002; Rowe et al., 2004; van Albada et al., 2007)

$$\begin{aligned}
P_{the}(\omega) &= P_{EEG}(\omega) + P_{EMG}(\omega), && \text{(C.18)}\\
P_{EEG}(\omega) &= \frac{\pi|\phi_n|^2}{r_e^2} G_{es}^2 G_{sn}^2 \left| \frac{L^2 e^{i\omega t_0/2}}{(1-G_{srs}L^2)(1-G_{ei}L)} \right|^2 \mathcal{P}, && \text{(C.19)}\\
&\equiv 10^{p_0} \left| \frac{L^2 e^{i\omega t_0/2}}{(1-G_{srs}L^2)(1-G_{ei}L)} \right|^2 \mathcal{P}, && \text{(C.20)}\\
\mathcal{P} &= \frac{4\pi r_e^2}{L_x L_y} \times \sum_{m,n=-M,-N}^{M,N} \frac{e^{-k_{mn}^2/k_0^2}}{|k_{mn}^2 r_e^2 + q^2 r_e^2|^2}, && \text{(C.21)}\\
P_{EMG}(\omega) &= A_{EMG} \frac{(\omega/\omega_{EMG})^2}{[1+(\omega/\omega_{EMG})^2]^2}, && \text{(C.22)}
\end{aligned}$$

where the theoretical spectrum $P_{the}(\omega)$, which is a sum of EEG and electromyographic (EMG) components, is matched to the empirical spectrum via $1\ \mu\mathrm{V}^2\mathrm{Hz}^{-1}\mathrm{m}^{-2} \equiv 1$. Furthermore, k_0 is a cut-off wavenumber for filtering by cerebrospinal fluid, skull, and scalp, which is taken into account via $\exp[-k_{mn}^2/k_0^2]$, and the discrete wavenumbers are given by

$$\mathbf{k}_{mn} = \left(\frac{2\pi m}{L_x}, \frac{2\pi n}{L_y} \right). \tag{C.23}$$

The EMG component has a maximum of $A_{EMG}/4$ at ω_{EMG}, taken to be $2\pi \times$ (40 Hz). The amplitude A_{EMG} is determined along with the other model parameters, but is not further considered here since we are interested in the activity of the brain itself. The parameter p_0 appearing in Eq. (C.20) provides a normalization for the spectrum without affecting its shape.

Bibliography

Abe O, Yamasue H, Aoki S, Suga M, Yamada H, Kasai K, Masutani Y, Kato N, Kato N, Ohtomo K (2008). Aging in the CNS: Comparison of gray/white matter volume and diffusion tensor data. *Neurobiol Aging* **29**:102–116.

Adeloye A, Kattan KR, Silverman FN (1975). Thickness of the normal skull in the American blacks and whites. *Am J Phys Antropol* **43**:23–30.

Akay M (ed.) (1998). *Time Frequency and Wavelets in Biomedical Signal Processing*. IEEE Press.

Amador A Alvarez, Sosa PA Valdés, Marqui RD Pascual, Garcia L Galan, Lirio R Biscay, Bayard J Bosch (1989). On the structure of EEG development. *Electroencephalogr Clin Neurophysiol* **73**:10–19.

Amaral D, Lavenex P (2006). Hippocampal neuroanatomy. In: Andersen P, Morris R, Amaral D, Bliss T, O'Keefe J (eds.), *The Hippocampus Book*. Oxford University Press.

Andrew C, Pfurtscheller G (1997). On the existence of different alpha band rhythms in the hand area of man. *Neurosci Lett* **222**(2):103 – 106.

Arle JE, Simon RH (1990). An application of fractal dimension to the detection of transients in the electroencephalogram. *Electroen Clin Neuro* **75**(4):296 – 305.

Arthurs OJ, Boniface S (2002). How well do we understand the neural origins of the fMRI BOLD signal? *Trends Neurosci* **25**:27–31.

Ascoli GA (2003). Electrotonic effects on spike response model dynamics. *IEEE Neural Networks* **4**:2831–36.

Aurlien H, Gjerde IO, Aarseth JH, Eldøen G, Karlsen B, Skeidsvoll H, Gilhus NE (2004a). EEG background activity described by a large computerized database. *Clin Neurophysiol* **115**:665–73.

Aurlien H, Gjerde IO, Aarseth JH, Elden G, Karlsen B, Skeidsvoll H, Gilhus NE (2004b). EEG background activity described by a large computerized database. *Clin Neurophysiol* **115**(3):665 – 673.

Bahramali H, Gordon E, Lagopoulos J, Lim CL, Leslie J, Wright J (1999). The effects of age on late components of the ERP and reaction time. *Exp Aging Res* **25**:69–80(12).

Barnea-Goraly N, Menon V, Eckert M, Tamm L, Bammer R, Karchemskiy A, Dant CC, Reiss AL (2005). White matter development during childhood and adolescence: A cross-sectional diffusion tensor imaging study. *Cereb Cortex* **15**:1848–54.

Beaumont JG, Mayes AR, Rugg MD (1978). Asymmetry in eeg alpha coherence and power: Effects of task and sex. *Electroen Clin Neuro* **45**(3):393 – 401.

Becker LE, Armstrong DL, Chan F, Wood MM (1984). Dendritic development in human occipital cortical neurons. *Develop Brain Res* **13**:117–24.

Bengston VL, Schaie KW (eds.) (1999). *Handbook of theories of aging.* New York: Springer Publishing Company, Inc.

Benninger C, Matthis P, Scheffner D (1984). EEG development of healthy boys and girls. Results of a longitudinal study. *Electroencephalogr Clin Neurophysiol* **57**(1):1 – 12.

Berger H (1929). Über das elektrenkephalogramm des menschen. *Archiv für Psychiatrie und Nervenkrankheiten* **87**:527–570.

Beurle RL (1956). Properties of a mass of cells capable of regenerating pulses. *Phil Trans R Soc Lond* **240**:55–87.

Binnie CD (ed.) (2003). *Clinical neurophysiology: EEG, paediatric neurophysiology, special techniques and applications.* Elsevier Health Sciences.

Bosman LWJ, Heinen K, Spijker S, Brussaard AB (2005). Mice lacking the major adult $\mathrm{GABA_A}$ receptor subtype have normal number of synapses, but retain juvenile IPSC kinetics until adulthood. *J Neurophysiol* **94**:338–346.

Braitenberg V, Schuüz A (1998). *Cortex: Statistics and Geometry of Neuronal Connectivity, 2nd ed.* Berlin: Springer.

Breakspear M, Roberts JA, Terry JR, Rodrigues S, Mahant N, Robinson PA (2006). A unifying explanation of primary generalized seizures through nonlinear brain modeling and bifurcation analysis. *Cereb Cortex* **16**:1296–313.

Bressloff PC (2001). Traveling fronts and wave propagation failure in an inhomogeneous neural network. *Physica D* **155**:83–100.

Bressloff PC, Folias SE, Prat A, Li Y-X (2003). Oscillatory waves in inhomogeneous neural media. *Phys Rev Lett* **91**:178101.

Buell SJ, Coleman PD (1979). Dendritic growth in the aged human brain and failure of growth in senile dementia. *Science* **206**:854–6.

Buell SJ, Coleman PD (1981). Quantitative evidence for selective dendritic growth in normal human aging but not in senile dementia. *Brain Res* **214**:23–41.

Bullock TH (2002). Grades in neural complexity: how large is the span?

Buxton RB, Frank LR (1997). A model for the coupling between cerebral blood flow and oxygen metabolism during neural stimulation. *J Cereb Blood Flow Metab* **17**:64–72.

Camfield CS, Camfield PR, Gordon K, Wirrell E, Dooley JM (1996). Incidence of epilepsy in childhood and adolescence: A population-based study in Nova Scotia from 1977 to 1985. *Epilepsia* **37**:19–23.

Carlson NR (ed.) (1999). *Foundation of Physiological Psychology*. Allyn & Bacon.

Carlson NR, Baskiet W (eds.) (1997). *Psychology, The Science of Behaviour*. Allyn & Bacon.

Caviness VS, Kennedy DN, Richelme C, Rademacher J, Filipek PA (1996). The human brain age 7–11 years: A volumetric analysis based on magnetic resonance images. *Cereb Cortex* **6**:726–36.

Chervin RD, Pierce PA, Connors BW (1988). Periodicity and directionality in the propagation of epileptiform discharges across neocortex. *J Neurophysiol* **60**:1695–713.

Chiang AKI, Rennie CJ, Robinson PA, Roberts JA, Rigozzi MK, Whitehouse RW, Hamilton RJ, Gordon E (2008). Automated characterization of multiple alpha peaks in multi-site electroencephalograms. *J Neurosci Meth* **168**(2):396 – 411.

Clark CR, Veltmeyer MD, Hamilton RJ, Simms E, Paul R, Hermens D, Gordon E (2004). Spontaneous alpha peak frequency predicts working memory performance across the age span. *Int J Psychophysiol* **53**(1):1 – 9.

Coben LA, Danziger WL, Berg L (1983). Frequency analysis of the resting awake eeg in mild senile dementia of alzheimer type. *Electroen Clin Neuro* **55**(4):372 – 380.

Coffey C, Lucke J, Saxton J, Ratcliff G, Unitas L, Billig B, Bryan R (1998). Sex differences in brain aging. *Arch Neurol* **55**:169–79.

Cohn NB, Kircher J, Emmerson RY, Dustman RE (1985). Pattern reversal evoked potentials: Age, sex and hemispheric asymmetry. *Electroencephalogr Clin Neurophysiol* **62**(6):399 – 405.

Comon P (1994). Independent component analysis, a new concept? *Signal Process* **36**(3):287 – 314. Higher Order Statistics.

Cook IA, O'Hara R, Uijtdehaage SHJ, Mandelkern M, Leuchter AF (1998). Assessing the accuracy of topographic eeg mapping for determining local brain function. *Electroen Clin Neuro* **107**(6):408 – 414.

Cosgrove K, Mazure C, Staley J (2007). Evolving knowledge of sex differences in brain structure, function, and chemistry. *Biol Psychiatry* **62**:847–55.

Cowell P, Turetsky B, Gur R, Grossman R, Shtasel D, Gur R (1994). Sex differences in aging of the human frontal and temporal lobes. *J Neurosci* **14**:4748–55.

Davidson RJ (2004). What does the prefrontal cortex "do" in affect: perspectives on frontal eeg asymmetry research. *Biol Psychol* **67**(1-2):219 – 234. Frontal EEG Asymmetry, Emotion, and Psychopathology.

De Bellis, Keshavan M, Beers S, Hall J, Frustaci K, Masalehdan A, Noll J, Boring AM (2001). Sex differences in brain maturation during childhood and adolescence. *Cereb Cortex* **11**:552–7.

de Brabander JM, Kramers RJK, Uylings HBM (1998). Layer-specific dendritic regression of pyramidal cells with ageing in the human prefrontal cortex. *Eur J Neurosci* **10**:1261–9.

Dekaban AS (1977). Tables of cranial and orbital measurements, cranial volume, and derived indexes in males and females from 7 days to 20 years of age. *Ann Neurol* **2**:485–91.

Dekaban A, Sadowsky D (1978). Changes in brain weights during the span of human life: relation of brain weights to body heights and body weights. *Ann Neurol* **4**:345–56.

Delorme A, Makeig S (2004). Eeglab: an open source toolbox for analysis of single-trial eeg dynamics including independent component analysis. *J Neurosci Meth* **134**(1):9 – 21.

Deuschl G, Eisen A (eds.) (2000). *Recommendations for the Practice of Clinical Neurophysiology: Guildlines of the International Federation of Clinical Neurophysiology*. Elsevier Science B.V.

Díaz de León AE, Harmony T, Marosi E, Becker J, Alvarez A (1988). Effect of different factors on EEG spectral parameters. *Int J Neurosci* **43**:123–131.

Duffy FH, Albert MS, McAnulty G, Garvey AJ (1984). Age-related differences in brain electrical activity of healthy subjects. *Ann Neurol* **16**(4):430–438.

Duffy FD, Iyer VG, Survillo WW (1989). *Clinical Electroencephalography and Topographic Brain Mapping : Technology and Practice*. Springer-Verlog.

Duffy FH, McAnulty GB, Albert MS (1993). The pattern of age-related differences in electrophysiological activity of healthy males and females. *Neurobiol Aging* **14**:73–84.

Dustman RE, Shearer DE, Emmerson RY (1999a). Life-span changes in EEG spectral amplitude, amplitude variability and mean frequency. *Clin Neurophysiol* **110**(8):1399 – 1409.

Dustman RE, Shearer DE, Emmerson RY (1999b). Life-span changes in EEG spectral amplitude, amplitude variability and mean frequency. *Clin Neurophysiol* **110**:1399–1409.

Eichorn DH, Bayley N (1962). Growth in head circumference from birth through young adulthood. *Child Develop* **33**:257–71.

Ergenoglu T, Demiralp T, Bayraktaroglu Z, Ergen M, Beydagi H, Uresin Y (2004). Alpha rhythm of the eeg modulates visual detection performance in humans. *Cognitive Brain Res* **20**(3):376 – 383.

Eshel Y, Witman S, Rosenfeld M, Abboud S (1995). Correlation between skull thickness asymmetry and scalp potential estimated by a numerical model of the head. *IEEE Biomed Eng* **42**:242–9.

Esiri MM (2007). Ageing and the brain. *J Pathol* **211**:181–7.

Felts PA, Baker TA, Smith KJ (1997). Conduction along segmentally demyelinated mammalian central axons. *J Neurosci* **17**:7267–77.

Feshchenko VA, Reinsel RA, Veselis RA (2001). Multiplicity of the alpha rhythm in normal humans. *J Clin Neurophysiol* **18**:331–344.

Finger S (ed.) (2001). *Origins of Neuroscience.* Oxford University Press.

Fox PT, Mintun MA (1989). Noninvasive Functional Brain Mapping by Change-Distribution Analysis of Averaged PET Images of H215O Tissue Activity. *J Nucl Med* **30**(2):141–149.

Freeman W (2001). Making Sense of Brain Waves: The Most Baffling Frontier in Neuroscience.

Freyer F, Aquino K, Robinson PA, Ritter P, Breakspear M (2009). Bistability and Non-Gaussian Fluctuations in Spontaneous Cortical Activity. *J Neurosci* **29**(26):8512–8524.

Gallagher M, Colombo P (1995). Ageing: The cholinergic hypothesis of cognitive decline. *Curr Opin Neurobiol* **5**:161–8.

Gasser T, Bächer P, Steinberg H (1985). Test-retest reliability of spectral parameters of the EEG. *Electroencephalogr Clin Neurophysiol* **60**:312–9.

Gasser T, Verleger R, Bächer P, Sroka L (1988). Development of the EEG of school-age children and adolescents. I. Analysis of band power. *Electroencephalogr Clin Neurophysiol* **69**:91–99.

Ge Y, Grossman RI, Babb JS, Rabin ML, Mannon LJ, Kolson DL (2002). Age-related total gray matter and white matter changes in normal adult brain. Part I: Volumetric MR imaging analysis. *Am J Neuroradiol* **23**:1327–33.

Gener NG, Acar CE (2004). Sensitivity of eeg and meg measurements to tissue conductivity. *Phys Med Biol* **49**(5):701.

Ghez C, Fahn S (1985). *Principles of Neural Science*, chap. The cerebellum, pp. 502–522. 2nd edition. Elsevier.

Giedd JN, Blumenthal J, Jeffries NO, Castellanos FX, Liu H, Zijdenbos A, Paus T, Evans AC, Rapoport JL (1999). Brain development during childhood and adolescence: a longitudinal MRI study. *Nat Neurosci* **2**:861–3.

Gleitman H (ed.) (1993). *Psychology.* New York: Norton.

Gonzalez-Burgos G, Kroener S, Zaitsev AV, Povysheva NV, Krimer LS, Barrionuevo G, Lewis DA (2008). Functional maturation of excitatory synapses in layer 3 pyramidal neurons during postnatal development of the primate prefrontal cortex. *Cereb Cortex* **18**:626–37.

Gordon E, Cooper N, Rennie C, Hermens D, Williams LM (2005). Integrative neuroscience: The role of a standardized databse. *Clin Eeg Neurosci* **36**(2):64–75.

Gratton G, Coles MG, Donchin E (1983). A new method for off-line removal of ocular artifact. *Electroencephalogr Clin Neurophysiol* **55**(4):468 – 484.

Guo T, Parrent AG, Peters TM (2007). Automatic target and trajectory identification for deep brain stimulation (dbs) procedures. In: *MICCAI'07: Proceedings of the 10th international conference on Medical image computing and computer-assisted intervention*, pp. 483–490. Berlin, Heidelberg: Springer-Verlag.

Gur RC, Mozley PD, Resnick SM, Gottlieb GL, Kohn M, Zimmerman R, Herman G, Atlas S, Grossman R, Berretta D, Erwin R, Gur RE (1991). Gender differences in age effect on brain atrophy measured by magnetic resonance imaging. *Proc Nat Acad Sci USA* **88**:2845–9.

Gutiérrez A, Khan ZU, Miralles CP, Mehta AK, Ruano D, Araujo F, Vitorica J, De Blas (1997). $\mathrm{GABA_A}$ receptor subunit expression changes in the rat cerebellum and cerebral cortex during aging. *Mol Brain Res* **45**:59–70.

Gutiérrez R, Bioson D, Heinemann U, Stoffel W (1995). Decompaction of CNS myelin leads to a reduction of the conduction velocity of action potentials in optic nerve. *Neurosci Lett* **195**:93–6.

Gutnick MJ, Mody I (eds.) (1993). *The Cortical Neuron.* Oxford: Oxford University Press.

Hagemann D (2004). Individual differences in anterior eeg asymmetry: methodological problems and solutions. *Biol Psychol* **67**(1-2):157 – 182. Frontal EEG Asymmetry, Emotion, and Psychopathology.

Hallez H, Vanrumste B, Grech R, Muscat J, De Clercq W, Vergult A, D'Asseler Y, Camilleri K, Fabri S, Van Huffel S, Lemahieu I (2007). Review on solving the forward problem in eeg source analysis. *J Neuroeng Rehabil* **4**(1):46.

Harmony T, Marosi E, de León AE Díaz, Becker J, Fernández T (1990). Effect of sex, psychosocial disadvantages and biological risk factors on EEG maturation. *Electroencephalogr Clin Neurophysiol* **75**(6):482 – 491.

Hartikainen P, Soininen H, Partanen J, Helkala EL, Riekkinen P (1992). Aging and spectral analysis of EEG in normal subjects: A link to memory and CSF AChE. *Acta Neurol Scand* **86**:148–55.

Hatazawa J, Ito M, Yamaura H, Matsuzawa T (1982). Sex differences in brain atrophy during aging: a quantitative study with computed tomography. *J Am Geriatr Soc* **30**:235–9.

Haug H (1987). Brain sizes, surfaces, and neuronal sizes of the cortex cerebri: a stereological investigation of man and his variability and a comparison with some mammals (primates, whales, marsupials, insectivores, and one elephant). *Am J Anat* **180**:126–42.

Heinen K, Baker RE, Spijker S, Rosahl T, van Pelt J, Brussaard AB (2003). Impaired dendritic spine maturation in $\mathrm{GABA_A}$ receptor $\alpha 1$ subunit knock out mice. *Neuroscience* **122**:699–705.

Hennig J, Koch O Speck MA (2003). Functional magnetic resonance imaging: A review of methodological aspects and clinical applications. *Journal of Magnetic Resonance Imaging* **18**(1):1–15.

Herrmann CS, Arnold T, Visbeck A, Hundemer H-P, Hopf HC (2001). Adaptive frequency decomposition of eeg with subsequent expert system analysis. *Comput Biol Med* **31**(6):407 – 427.

Hill AAV, Edwards DH, Murphey RK (1994). The effect of neuronal growth on synaptic integration. *J Comp Neurosci* **1**:239–54.

Hjorth B (1970). Eeg analysis based on time domain properties. *Electroen Clin Neuro* **29**(3):306 – 310.

Hollander M, Wolfe DA (1973). *Nonparametric Statistical Methods.* New York: Wiley.

Holmes GL, Moshé SM, Royden Jones H(Jr) (eds.) (2006). *Clinical Neuropysiology of Infancy, Childhood, and Adolescence.* Butterword Heinemann Elsevier.

Hortobágyi T, del Fernandez, Rothwell JC (2006). Age reduces cortical reciprocal inhibition in humans. *Exp Brain Res* **171**:322–9.

Hoshi Y, Kobayashi N, Tamura M (2001). Interpretation of near-infrared spectroscopy signals: a study with a newly developed perfused rat brain model. *J Appl Physiol* **90**(5):1657–1662.

Hubbard B, Anderson J (1983). Sex differences in age-related brain atrophy. *Lancet* **321**:1446–8.

Hughes J (1987). Normal limits of the EEG. In: Halliday R, Butler S, Paul R (eds.), *A textbook of Clinical Neurophysiology*, pp. 105–54. New York: Wiley.

Hughes JR, Cayaffa JJ (1977). The EEG in patients at different ages without organic cerebral disease. *Electroencephalogr Clin Neurophysiol* **42**:776–84.

Huttenlocher PR (1990). Morphometric study of human cerebral cortex development. *Neuropsychologia* **28**:517–27.

Huupponen E, Himanen S-L, Vrri A, Hasan J, Saastamoinen A, Lehtokangas M, Saarinen J (2002). Fuzzy detection of eeg alpha without amplitude thresholding. *St Heal T* **24**(2):133 – 147.

Inouye T, Shinosaki K, Yagasaki A, Shimizu A (1986). Spatial distribution of generators of alpha activity. *Electroencephalography and Clinical Neurophysiology* **63**(4):353 – 360.

Jacobs B, Driscoll L, Schall M (1997). Life-span dendritic and spine changes in areas 10 and 18 of human cortex: A quantitative Golgi study. *J Comp Neurol* **386**:661–80.

Jirsa VK, Haken H (1996). Field theory of electromagnetic brain activity. *Phys Rev Lett* **77**:960–3.

Jirsa VK, Haken H (1997). A derivation of a macroscopic field theory of the brain from the quasi-microscopic neural dynamics. *Physica D* **99**:503–26.

John ER, Ahn H, Prichep L, Trepetin M, Brown D, Kaye H (1980). Developmental equations for the electroencephalogram. *Science* **210**:1255–8.

Jueptner M, Weiller C (1995). Review: Does measurement of regional cerebral blood flow reflect synaptic activity?–implications for pet and fmri. *Neuroimage* **2**(2, Part 1):148 – 156.

Kandel ER, Schwartz JH, Jessell TM (2000). *Principles of Neural Science, Fourth Edition*. London: Prentice Hall International.

Karson CN, Coppola R, Daniel DG (1988). Alpha frequency in schizophrenia: an association with enlarged cerebral ventricles. *Am J Psychiatry* **145**(7):861–864.

Katz RI, Horowitz GR (1982). Electroencephalogram in the septuagenarian: studies in a normal geriatric population. *J Am Geriatr Soc* **30**:273–5.

Kemper TL (1994). Neuroanatomical and neuropathological changes during aging and dementia. In: Albert ML, Knoefel JE (eds.), *Clinical Neurology of Aging*. New York: Oxford University Press.

Klimesch W (1997). Eeg-alpha rhythms and memory processes. *Int J Psychophysiol* **26**(1-3):319 – 340.

Klimesch W (1999). EEG alpha and theta oscillations reflect cognitive and memory performance: a review and analysis. *Brain Res Rev* **29**(2-3):169 – 195.

Klimesch W, Schimke H, Pfurtscheller G (1993). Alpha frequency, cognitive load and memory performance. *Brain Topogr* **5**:241–251.

Klimesch W, Sauseng P, Hanslmayr S (2007). EEG alpha oscillations: The inhibition-timing hypothesis. *Brain Res Rev* **53**(1):63 – 88.

Koch C (1999). *Biophysics of Computation.* New York: Oxford University Press.

Koenderink MJT, Uylings HBM (1995). Postnatal maturation of layer V pyramidal neurons in the human prefrontal cortex. A quantitative Golgi analysis. *Brain Res* **678**:233–43.

Kolev V, Yordanova J, Basar-Eroglu C, Basar E (2002). Age effects on visual eeg responses reveal distinct frontal alpha networks. *Clin Neurophysiol* **113**(6):901 – 910.

Kooi KA (1971). *Fundamentals of Electroencephalography.* New York: Harper & Row.

Kropotov JD (2009). *Quantitative EEG, event-related potentials and neurotherapy.* Elsevier.

Kuhl D, Metter E, Riege W, Phelps M (1982). Effects of human aging on patterns of local cerebral glucose utilization determined by the [18F]fluorodeoxyglucose method. *J Cereb Blood Flow Metab* **2**:163–171.

Lindsley DB (1936). Brain potentials in children and adults. *Science* **84**(2181):354–354.

Llinas RR, Walton KD, Lang EJ (2004). *The Synaptic Organization of the Brain.*, chap. Ch. 7 Cerebellum. Oxford University Press.

Lopes da Silva FH, Hoeks A, Smits H, Zetterberg LH (1974). Model of brain rhythmic activity. The alpha rhythm of the thalamus. *Kybernetik* **15**:27–37.

Luebke JI, Rosene DL (2003). Aging alters dendritic morphology, input resistance, and inhibitory signaling in dentate granule cells of the rhesus monkey. *J Comp Neurol* **460**:573–84.

Luebke JI, Chang Y-M, Moore TL, Rosene DL (2004). Normal aging results in decreased synaptic excitation and increased synaptic inhibition of layer 2/3 pyramidal cells in the monkey prefrontal cortex. *Neurosci* **125**:277–88.

Magnusson KR, Nelson SE, Young AB (2002). Age-related changes in the protein expression of subunits of the NMDA receptor. *Mol Brain Res* **99**:40–45.

Marshall PJ, Bar-Haim Y, Fox NA (2002). Development of the EEG from 5 months to 4 years of age. *Clin Neurophysiol* **113**(8):1199 – 1208.

Matoušek M, Volavka J, Roubíček J, Roth Z (1967). EEG frequency analysis related to age in normal adults. *Electroencephalogr Clin Neurophysiol* **23**:162–7.

Matsuura M, Yamamoto K, Fukuzawa H, Okubo Y, Uesugi H, Moriiwa M, Kojima T, Shimazono Y (1985). Age development and sex differences of various EEG elements in healthy children and adults. Quantification by a computerized wave form recognition method. *Electroencephalogr Clin Neurophysiol* **60**:394–406.

Matthis P, Scheffner D, Benninger Chr, Lipinski Chr, Stolzis L. (1980). Changes in the background activity of the electroencephalogram according to age. *Electroencephalogr Clin Neurophysiol* **49**(5-6):626 – 635.

McEntee W, Crook T (1991). Serotonin, memory, and the aging brain. *Psychopharmacology* **103**:143–9.

Miller A, Alston R, Corsellis J (1980). Variation with age in the volumes of grey and white matter in the cerebral hemispheres of man — measurements with an image analyzer. *Neuropath Appl Neurobiol* **6**:119–32.

Mitzdorf U (1985). Current source-density method and application in cat cerebral cortex: Investigation of evoked potentials and EEG phenomena. *Physiol Rev* **65**:37–100.

Moosmann M, Ritter P, Krastel I, Brink A, Thees S, Blankenburg F, Taskin B, Obrig H, Villringer A (2003). Correlates of alpha rhythm in functional magnetic resonance imaging and near infrared spectroscopy. *Neuroimage* **20**(1):145 – 158.

Moretti DV, CB, GB, Cassetta E, Dal Forno G, Ferreric F, Ferri R, Lanuzza B, Miniussi C, Nobili F, Rodriguez G, Salinari S, Rossini PM (2004). Individual analysis of eeg frequency and band power in mild alzheimer's disease. *Clin Neurophysiol* **115**(2):299 – 308.

Morrison J, Hof P (1997). Life and death of neurons in the aging brain. *Science* **278**:412–9.

Mosher JC, Spencer ME, Leahy RM, Lewis PS (1993). Error bounds for eeg and meg dipole source localization. *Electroen Clin Neuro* **86**(5):303 – 321.

Nagai M, Endo N, Kumada T (2007). Measuring brain activities related to understanding using near-infrared spectroscopy (nirs). In: *Proceedings of the 2007 conference on Human interface*, pp. 884–893. Berlin, Heidelberg: Springer-Verlag.

Naik GR, Kumar DK (2009). Determining number of independent sources in undercomplete mixture. *Eurasip J Adv Sig Pr* p. 694850.

Nakamura M, Shibasaki H, Imajoh K, Nishida S, Neshige R, Ikeda A (1992). Automatic eeg interpretation: a new computer-assisted system for the automatic integrative interpretation of awake background eeg. *Electroen Clin Neuro* **82**(6):423 – 431.

Nelder JA, Mead R (1965). A simplex method for function minimization. *The Computer Journal* **7**(4):308–313.

Niedermeyer E (1997). Alpha rhythms as physiological and abnormal phenomena. *Int J Psychophysiol* **26**(1-3):31 – 49.

Niedermeyer E, Lopes da Silva FH (1998). *Electroencephalography, Basic Principles, Clinical Applications, and Related Fields*. Baltimore, Md: Urban & Schwarzenberg.

Niedermeyer E, Lopes da Silva FH (2004). *Electroencephalography: Basic Principles, Clinical Applications, and Related Fields*. Lippincott Williams & Wilkins.

Nolte J (ed.) (1993). *The Human Brain*. Missouri: Moshy.

Nunez PL (1974). Wave-like properties of the alpha rhythm. *IEEE Trans Biomed Eng* **21**:473–82.

Nunez PL (1995). *Neocortical Dynamics and Human EEG Rhythms*. New York: Oxford University Press.

Nunez PL, Srinivasan R (2006). *Electric Fields of the Brain: The Neurophysics of EEG*. Oxford University Press.

Nuwer MR (1988). Quantitative eeg: I. techniques and problems of frequency analysis and topographic mapping. *J Clin Neurophysiol* **5**.

Obrist WD (1954). The electroencephalogram of normal aged adults. *Electroencephalogr Clin Neurophysiol* **6**:235–44.

O'Connor S. C., Robinson P. A. (2004). Spatially uniform and nonuniform analyses of electroencephalographic dynamics,with application to the topography of the alpha rhythm. *Phys. Rev. E* **70**(1):011911.

Olkin I, Finn JD (1995). Correlations redux. *Psychol Bull* **118**:155–64.

Ontl T, Xing Y, Bai L, Kennedy E, Nelson S, Wakeman M, Magnusson K (2004). Development and aging of N-methyl-D-aspartate receptor expression in the prefrontal/frontal cortex of mice. *Neurosci* **123**:467–79.

Pakkenberg B, Gundersen HJG (1997). Neocortical neuron number in humans: Effect of sex and age. *J Comp Neurol* **384**:312–20.

Pantano P, Baron J-C, Lebrun-Grandié P, Duquesnoy N, Bousser M-G, Comar D (1984). Regional cerebral blood flow and oxygen consumption in human aging. *Upd Int Car* **15**:635–41.

Pascual-Marqui RD (1999). Review of methods for solving the eeg inverse problem. *International Journal of Bioelectromagnetism* **1**:75–86.

Pascual-Marqui RD, Esslen M, Kochi K, Lehmann D (2002). Functional imaging with low resolution brain electromagnetic tomography (loreta): a review. *Methods & Findings in Experimental & Clinical Pharmacology* **24C**:91–95.

Passe TJ, Rajagopalan P, Tupler LA, Byrum CE, MacFall JR, Krishnan RR (1997). Age and sex effects on brain morphology. *Prog Neuro-Psychopharmacol & Biol Psychiat* **21**:1231–7.

Peinemann A, Lehner C, Conrad B, Siebner HR (2001). Age-related decrease in paired-pulse intracortical inhibition in the human primary motor cortex. *Neurosci Lett* **313**:33–36.

Perrin JS, Hervé P-Y, Leonard G, Perron M, Pike GB, Pitiot A, Richer L, Veillette S, Pausova Z, Paus T (2008). Growth of white matter in the adolescent brain: Role of testosterone and androgen receptor. *J Neurosci* **28**:9519–24.

Petanjek Z, Judaš M, Kostović I, Uylings BM (2008). Lifespan alterations of basal dendritic trees of pyramidal neurons in the human prefrontal cortex: A layer-specific pattern. *Cereb Cortex* **18**:915–929.

Peters A (2002). Structural changes that occur during normal aging of primate cerebral hemispheres. *Neurosci Biobehav Rev* **26**:733–41.

Peters A (2002b). The effects of normal aging on myelin and nerve fibers: A review. *J Neurocytol* **31**:581–93.

Petersén I, Eeg-Olofsson O (1971). The development of the electroencephalogram in normal children from the age of 1 through 15 years. non-paroxysmal activity. *Neuropadiatrie* **2**(3):247–304.

Petersén I, Eeg-Olofsson O (1971). The development of the electroencephalogram in normal children from the ages of 1 through 15 years. *Neuropädiatrie* **2**:247–304.

Petersén I, Selldén U, Eeg-Olofsson O (1975). The evolution of the EEG in normal children and adolescents from 1 to 21 years. In: Rémond A, Lairy GC (eds.), *Handbook of Electroencephalography and Clinical Neurophysiology*, pp. 31–68. Amsterdam: Elsevier.

Pfurtscheller G, Stancàk A, Edlinger G (1997). On the existence of different types of central beta rhythms below 30 hz. *Electroen Clin Neuro* **102**(4):316 – 325.

Piccolino Marco (2006). Luigi galvani's path to animal electricity. *Cr Biol* **329**(5-6):303 – 318. Aspects de l'histoire des neurosciences.

Piguet O, Double KL, Kril JJ, Harasty J, Macdonald V, McRitchie DA, Halliday GM (2009). White matter loss in healthy ageing: A postmortem analysis. *Neurobiol Aging* **30**:1288–95.

Pineda JA (2005). The functional significance of mu rhythms: Translating seeing and hearing into doing. *Brain Res Rev* **50**(1):57 – 68.

Poe BH, Linville C, Brunso-Bechtold J (2001). Age-related decline of presumptive inhibitory synapses in the sensorimotor cortex as revealed by the physical disector. *J Comp Neurol* **439**:65–72.

Polich J (1997). EEG and ERP assessment of normal aging. *Electroencephalogr Clin Neurophysiol* **104**:244–56.

Posthuma D, Neale MC, Boomsma DI, , de Geus EJC (2001). Are smarter brains running faster? heritability of alpha peak frequency, iq, and their interrelation. *Behav Genet* **31**(6):567–579.

Press WH, Teukolsky SA, Vettering, WTand Flannery BP (1995). *Numerical recipes in C: The art of scientific computing.* Cambridge University Press.

Pritchard WS (1992). The brain in fractal time: 1/f-like power spectrum scaling of the human electroencephalogram. *Int J Neurosci* **66**:119–129.

Purves D (ed.) (2000). *Body and Brain: a Trophic Theory of Neural Connections*. Cambridge, Massachusettes: Harvard University Press.

Purves D, Augustine GJ, Fitzpatrick D, Hall WC, LaMantia A-S, McNamara JO, White LE (2007). *Neuroscience*. 4th edition. Sunderland, MA: Sinauer Associates.

R Development Core Team (2008). *R: A Language and Environment for Statistical Computing*. R Foundation for Statistical Computing, Vienna, Austria.

Rapp P, Gallagher M (1996). Preserved neuron number in the hippocampus of aged rats with spatial learning deficits. *Proc Nat Acad Sci USA* **93**:9926–30.

Rasmussen T, Schliemann T, Sørensen J, Zimmer J, West M (1996). Memory impaired aged rats: no loss of principal hippocampal and subicular neurons. *Neurobiol Aging* **17**:143–47.

Ray W (1990). The electrocortical system. In: Cacioppo J, Tassinary LG (eds.), *Principles of Psychophysiology*, pp. 385–412. Cambridge: Cambridge University Press.

Rennie CJ, Robinson PA, Wright JJ (1999). Effects of local feedback on dispersion of electrical waves in the cerebral cortex. *Phys Rev E* **59**:3320–9.

Rennie CJ, Wright JJ, Robinson PA (2000). Mechanisms of cortical electrical activity and emergence of gamma rhythm. *J Theor Biol* **205**:17–35.

Rennie CJ, Robinson PA, Wright JJ (2002). Unified neurophysical model of EEG spectra and evoked potentials. *Biol Cybern* **86**:457–71.

Roberts JA, Robinson PA (2008a). Modeling absence seizure dynamics: Implications for basic mechanisms and measurement of thalamocortical and corticothalamic latencies. *J Theor Biol* **253**:189–201.

Roberts J. A., Robinson P. A. (2008b). Modeling distributed axonal delays in mean-field brain dynamics. *Phys. Rev. E* **78**(5):051901.

Robinson PA (2003a). Brain waves. *The Physicist* **40**:132–7.

Robinson PA (2003b). Neurophysical theory of coherence and correlations of electroencephalographic signals. *J Theor Biol* **222**:163–75.

Robinson PA, Rennie CJ, Wright JJ (1997). Propagation and stability of waves of electrical activity in the cerebral cortex. *Phys Rev E* **56**:826–40.

Robinson PA, Rennie CJ, Wright JJ, Bourke PD (1998). Steady states and global dynamics of electrical activity in the cerebral cortex. *Phys Rev E* **58**:3557–71.

Robinson PA, Loxley PN, O'Connor SC, Rennie CJ (2001a). Modal analysis of corticothalamic dynamics, electroencephalographic spectra, and evoked potentials. *Phys Rev E* **63**(4):041909.

Robinson PA, Rennie CJ, Wright JJ, Bahramali H, Gordon E, Rowe DL (2001b). Prediction of EEG spectra from neurophysiology. *Phys Rev E* **63**:021903.

Robinson PA, Rennie CJ, Wright JJ, Bahramali H, Gordon E, Rowe DL (2001c). Prediction of electroencephalographic spectra from neurophysiology. *Phys Rev E* **63**(2):021903.

Robinson PA, Rennie CJ, Rowe DL (2002). Dynamics of large-scale brain activity in normal arousal states and epileptic seizures. *Phys. Rev. E* **65**(4):041924.

Robinson PA, Rennie CJ, Rowe DL, O'Connor SC, Wright JJ, Gordon E, Whitehouse RW (2003a). Neurophysical modeling of brain dynamics. *Neuropsychopharmacol* **28**(Suppl. 1):74–9.

Robinson PA, Whitehouse RW, Rennie CJ (2003b). Nonuniform corticothalamic continuum model of electroencephalographic spectra with application to split-alpha peaks. *Phys Rev E* **68**(2):021922.

Robinson PA, Rennie CJ, Rowe DL, O'Connor SC (2004). Estimation of multiscale neurophysiologic parameters by electroencephalographic means. *Hum Brain Mapp* **23**:53–72.

Rocca J (2003). Galen on the brain: anatomical knowledge and physiological speculation in the second century ad. *Stud Anc Med* **26**.

Rossini PM, Rossi S, Babiloni C, Polich J (2007). Clinical neurophysiology of aging brain: From normal aging to neurodegeneration. *Prog Neurobiol* **83**:375–400.

Rowe DL, Robinson PA, Rennie CJ (2004). Estimation of neurophysiological parameters from the waking EEG using a biophysical model of brain dynamics. *J Theor Biol* **231**:413–33.

Salinsky MC, Oken BS, Morehead L (1991). Test-retest reliability in EEG frequency analysis. *Electroencephalogr Clin Neurophysiol* **79**:382–92.

Samson-Dollfus D, Delapierre G, Do Marcolino C, Blondeau C (1997). Normal and pathological changes in alpha rhythms. *Int J Psychophysiol* **26**(1-3):395 – 409.

Sanei S, Chambers JA (2007). *EEG signal processing.* Wiley-Interscience.

Saunders MG (1984). Artifacts: Activity of noncerebral origin in the EEG. In: DW Klass DD Daly (ed.), *Current Practice of Clinical Electroencephalography*, pp. 37–67. New York: Raven.

Scahill R, Frost C, Jenkins R, Whitwell J, Rossor M, Fox N (2003). A longitudinal study of brain volume changes in normal aging using serial registered magnetic resonance imaging. *Arch Neurol* **60**:989–94.

Schiff SJ, Aldroubi A, Unser M, Sato S (1994). Fast wavelet transformation of eeg. *Electroen Clin Neuro* **91**(6):442 – 455.

Schiff SJ, Huang X, Wu J-Y (2007). Dynamical evolution of spatiotemporal patterns in mammalian middle cortex. *Phys Rev Lett* **98**:178102.

Schoppenhorst M, Brauer F, Freund G, Kubicki St (1980). The significance of coherence estimates in determining central alpha and mu activities. *Electroen Clin Neuro* **48**(1):25 – 33.

Scott DF, Heathfield KWG, Toone B, Margerison JH (1972). The EEG in Huntington's chorea: a clinical and neuropathological study. *Journal of Neurology, Neurosurgery & Psychiatry* **35**(1):97–102.

Segovia G, Porras A, Del Arco, Mora F (2001). Glutamatergic neurotransmission in aging: a critical perspective. *Mech Ageing Develop* **122**:1–29.

Shapiro SS, Wilk MB (1965). An analysis of variance test for normality (complete samples). *Biometrika* **52**:591–611.

Shaw JC (2003). *The Brain's Alpha Rhythms and the Mind.* Elsevier.

Simonyi A, Ngomba RT, Storto M, Catania MV, Miller LA, Youngs B, DiGiorgi-Gereveni V, Nicoletti F, Sun GY (2005). Expression of groups I and II metabotropic glutamate receptors in the rat brain during aging. *Brain Res* **1043**:95–106.

Smith JR (1941). The frequency growth of the human alpha rhythms during normal infancy and childhood. *J Psychol* **11**:177 – 198.

Somsen RJM, van't Klooster BJ, van der Molen MW, van Leeuwen HMP, Licht R (1997). Growth spurts in brain maturation during middle childhood as indexed by EEG power spectra. *Biol Psychol* **44**:187–209.

Sowell ER, Trauner DA, Gamst A, Jernigan TL (2002). Development of cortical and subcortical brain structures in childhood and adolescence: a structural MRI study. *Develop Med & Child Neurol* **44**:4–16.

Sowell ER, Peterson BS, Thompson PM, Welcome SE, Henkenius AL, Toga AW (2003). Mapping cortical change across the human life span. *Nat Neurosci* **6**:309–15.

Sowell ER, Thompson PM, Leonard CM, Welcome SE, Kan E, Toga AW (2004). Longitudinal mapping of cortical thickness and brain growth in normal children. *J Neurosci* **24**:8223–31.

Stam CJ, Pijn JPM, Suffczynski P, da Lopes (1999). Dynamics of the human alpha rhythm: evidence for non-linearity. *Clin Neurophysiol* **110**:1801–13.

Steriade M, Jones EG, McCormick DA (1997). *Thalamus Volume I Organisation and Function.* Elsevier Science.

Stroganova TA, Orekhova EV, Posikera IN (1999). EEG alpha rhythm in infants. *Clin Neurophysiol* **110**(6):997 – 1012.

Stuart G, Spruston N, Hausser M (2008). *Dendrites.* Oxford University Press.

Suhara T, Fukuda H, Inoue O, Itoh T, Suzuki K, Yamasaki T, Tateno Y (1991). Age-related changes in human D1 dopamine receptors measured by positron emission tomography. *Psychopharmacology* **103**:41–45.

Sullivan EV, Rosenbloom M, Serventi KL, Pfefferbaum A (2004). Effects of age and sex on volumes of the thalamus, pons, and cortex. *Neurobiol Aging* **25**:185–92.

Surwillo WW (1961). Frequency of the ‘Alpha’ Rhythm, Reaction Time and Age. *Nature* **191**:823–824.

Swartwood JN, Swartwood MO, Lubar JF, Timmermann DL (2003). Eeg differences in adhd-combined type during baseline and cognitive tasks. *Pediatr Neurol* **28**(3):199 – 204.

Tennigkeit F, Schwarz DWF, Puil E (1998). Postnatal development of signal generation in auditory thalamic neurons. *Develop Brain Res* **109**:255–263.

Thompson PM, Giedd JN, Woods RP, MacDonald D, Evans AC, Toga AW (2000). Growth patterns in the developing brain detected by using continuum mechanical tensor maps. *Nature* **404**:190–193.

Tomlinson B, Blessed G, Roth M (1968). Observations on the brains of non-demented old people. *J Neurol Sci* **7**:331–356.

Towe AL (1966). On the nature of the primary evoked response. *Exp Neurol* **15**:113–39.

Tsai AC, Liou M, Jung T-P, Onton JA, Cheng PE, Huang C-C, Duann J-R, Makeig S (2006). Mapping single-trial eeg records on the cortical surface through a spatiotemporal modality. *Neuroimage* **32**(1):195 – 207.

Uylings HBM, de Brabander (2002). Neuronal changes in normal human aging and Alzheimer's disease. *Brain Cogn* **49**:268–76.

Valdés-Hernández PA, Ojeda-González A, Martnez-Montes E, Lage-Castellanos A, Virués-Alba T, Valdés-Urrutia L, Valdes-Sosa PA (2010). White matter architecture rather than cortical surface area correlates with the EEG alpha rhythm. *Neuroimage* **49**(3):2328 – 2339.

van Albada SJ, Rennie CJ, Robinson PA (2007). Variability of model-free and model-based quantitative measures of EEG. *J Integ Neurosci* **6**:279–307.

van Albada SJ, Kerr CC, Chiang AKI, Rennie CJ, Robinson PA (2010). Neurophysiological changes with age probed by inverse modeling of eeg spectra. *Clin Neurophysiol* **121**(1):21 – 38.

Van Der Werf YD, Tisserand DJ, Visser PJ, Hofman PAM, Vuurman E, Uylings HBM, Jolles J (2001). Thalamic volume predicts performance on tests of cognitive speed and decreases in healthy aging: A magnetic resonance imaging-based volumetric analysis. *Cogn Brain Res* **11**:377–85.

Veldhuizen RJ, Jonkman EJ, Poortvliet DCJ (1993). Sex differences in age regression parameters of healthy adults — normative data and practical implications. *Electroencephalogr Clin Neurophysiol* **86**:377–84.

Volkow N, Logan J, Fowler J, Wang G-J, Gur R, Wong C, Felder C, Gatley S, Ding Y-S, Hitzemann R, Pappas N (2000). Association between age-related decline in brain dopamine activity and impairment in frontal and cingulate metabolism. *Am J Psychiatry* **157**:75–80.

Warren RA, Jones EG (1997). Maturation of neuronal form and function in a mouse thalamo-cortical circuit. *J Neurosci* **17**:277–95.

Wassermann EM, Epstein CM, Zieman U, Walsh V, Paus T, Lisanby SH (eds.) (2008). *The Oxford Handbook of Transcranial Stimulation.* OXford University Press.

Williams LM, Gatt JM, Hatch A, Palmer DM, Nagy M, Rennie C, Cooper NJ, Morris C, Grieve S, Dobson-Stone C, Schofield P, Clark CR, Gordon E, Arns M, Paul RH (2008). The Integrate model of emotion, thinking, and self regulation: An application to the "paradox of aging". *J Int Neurosci* **7**:367–404.

Wilson HR, Cowan JD (1972). Excitatory and inhibitory interactions in localized populations of model neurons. *Biophys J* **12**:1–24.

Wilson HR, Cowan JD (1973). A mathematical theory of the functional dynamics of cortical and thalamic nervous tissue. *Kybernetik* **13**:55–80.

Wright JJ, Liley DTJ (1995). Simulation of electrocortical waves. *Biol Cybern* **72**:347–56.

Wright JJ, Liley DTJ (1996). Dynamics of the brain at global and microscopic scales: Neural networks and the eeg. *Behavioral and Brain Sciences* **19**:285–295.

Xi M-C, Liu R-H, Engelhardt KK, Morales FR, Chase MH (1999). Changes in the axonal conduction velocity of pyramidal tract neurons in the aged cat. *Neurosci* **92**:219–25.

Xu J, Kobayashi S, Yamaguchi S, Iijima K, Okada K, Yamashita K (2000). Gender effects on age-related changes in brain structure. *Am J Neuroradiol* **21**:112–8.

Xu W, Huang X, Takagaki K, Wu J-Y (2007). Compression and reflection of visually evoked cortical waves. *Neuron* **55**:119–29.

Yao D, Wang L, Oostenveld R, Nielsen KD, Arendt-Nielsen L, Chen A C N (2005). A comparative study of different references for eeg spectral mapping: the issue of the neutral reference and the use of the infinity reference. *Physiological Measurement* **26**(3):173.

Zemcov A, Barclay L, Blass J (1984). Regional decline of cerebral blood flow with age in cognitively intact subjects. *Neurobiol Aging* **5**:1–6.